UNIVERSITAT POLITÈCNICA DE VALÈNCIA

Departamento de Máquinas y Motores Térmicos

DOCTORAL THESIS:

"Experiments and Modelling of Automotive Turbochargers under Unsteady Conditions"

Presented by: D. LUIS MIGUEL GARCÍA-CUEVAS GONZÁLEZ
Supervised by: DR. D. ANDRÉS OMAR TISEIRA IZAGUIRRE

in fulfillement of the requisites for the degree of

Doctor of Philosophy

Valencia, December 2014

PhD. Thesis

“Experiments and Modelling of Automotive Turbochargers under Unsteady Conditions”

AUTHORS

Presented by: D. Luis Miguel García-Cuevas González
Supervised by: Dr. D. Andrés Omar Tiseira Izaguirre

DEFENSE COMMITTEE

Chairman: Dr. D. Francisco Payri González
Secretary: Dr. D. Pedro Acisclo Rodríguez Aumente
Member: Dr. D. Gregorio López Juste

Valencia, December 2014

Experiments and Modelling of Automotive Turbochargers under Unsteady Conditions

Luis Miguel García-Cuevas González

Abstract

The current global scenario, in which an ever increasing population with an ever growing transportation needs is coupled with a reduction in the fossil fuel production and increasing human-made pollution derived problems, leads automotive engine manufacturers to constant struggles for fuel consumption and emission reductions while keeping engine performance. One-dimensional simulation codes have become a key tool towards these objectives, but require continued accuracy refinements. Phenomena that were previously thought of a limited importance and could be extremely easily modelled now require the development of new methods to be accounted for. Among these phenomena are the turbocharger mechanical losses and the turbine behaviour under highly pulsating boundary conditions. This work is focused on the improvement of current one-dimensional models, for both mechanical losses prediction and high frequency pulsating flow turbine performance.

After reviewing the state-of-the-art in experimental measurement and fast simulation of automotive turbochargers, this work presents first a experimental study of several turbochargers working under both steady-state and unsteady operating conditions, focusing on the general performance of the turbine and the losses in the power transmission between it and the compressor, even including internal pressure measurements in one of the tested units. All the measurements are corrected due to heat transfer, getting the purely adiabatic behaviour. Furthermore, a CFD simulation campaign of a radial turbine has been performed, thus obtaining a detailed description of its internal behaviour under highly pulsating flow.

In the light of both the experimental and CFD-simulated results, a quasi-steady mechanical losses and a quasi-bidimensional turbine model have been developed. Both models have been validated using all the experimental and simulated data, proving a prediction accuracy improvements from the results of previous methods. The mechanical losses model offers a clear advantage over the usual practice of using a constant mechanical efficiency value for correcting the manufacturer's turbocharger map, whereas the turbine model has demonstrated potential for turbine map extrapolation and has improved the instantaneous results over classic one-dimensional turbine volute models for frequencies higher than 1000 Hz. Both models have been developed trying to keep a reduced computational cost, ensuring to exploit the specific characteristics of the processors where they are going to be run.

Resumen

El escenario actual, en el que el crecimiento constante de la población y sus necesidades de transporte se une a una reducción en la capacidad de producción de combustibles fósiles y cada vez mayores problemas derivados de la contaminación producida por el hombre, lleva a los fabricantes de motores para automoción a una constante lucha por la reducción del consumo y las emisiones contaminantes de sus productos manteniendo las prestaciones. Para lograrlo, los códigos de simulación unidimensionales se han convertido en una herramienta fundamental, pero requieren un refinamiento constante para lograr niveles cada vez mayores de precisión en los cálculos. Fenómenos que antaño tenían una importancia limitada y podían ser modelados de forma extremadamente sencilla, hoy día requieren del desarrollo de nuevos métodos de cálculo para ser tenidos en cuenta. Entre estos fenónemos se encuentran las pérdidas mecánicas del turbogrupo y el comportamiento de la turbina bajo condiciones de funcionamiento altamente pulsantes. Este trabajo busca mejorar los modelos actuales unidimensionales, tanto para la predicción de las pérdidas mecánicas como para el comportamiento de la turbina bajo flujo pulsante a altas frecuencias.

Tras estudiar los últimos avances en la medida experimental y la simulación rápida de turbocompresores, el presente documento cuenta primero con un estudio experimental del comportamiento bajo condiciones de contorno estacionarias y no estacionarias de varios turbocompresores de automoción, tanto del comportamiento general de la turbina como de las pérdidas mecánicas, incluyendo medidas de presión interna en una de las unidades probadas. Todas las medidas cuentan con correcciones por flujo de calor, reduciendo su comportamiento al puramente adiabático. Así mismo, se ha desarrollado una campaña de simulación CFD de una turbina radial, obteniendo una descripción detallada de su comportamiento interno bajo flujo altamente pulsante.

A la vista de los resultados experimentales y de simulaciones CFD, se han desarrollado un modelo cuasi-estacionario de pérdidas mecánicas y un modelo pseudo-bidimensional de turbina. Ambos modelos han sido validados usando los datos de las campañas experimentales y de CFD, probando una gran mejora en las precisión de las predicciones al comparar sus resultados con los de métodos anteriores. El modelo de pérdidas mecánicas ofrece una clara ventaja frente a la práctica habitual de utilizar un rendimiento mecánico constante para corregir el comportamiento del turbocompresor frente al mapa de funcionamiento dado por el fabricante, mientras que el modelo de turbina ha demostrado tener potencial para la extrapolación de mapas y ha mejorado los resultados instantáneos para frecuencias mayores a 1000 Hz frente a los modelos clásicos de turbina con volutas totalmente unidimensionales. Ambos modelos han sido desarrollados teniendo en cuenta el mantener un reducido coste computacional, procurando explotar en lo posible las características de los procesadores en los que van a ser simulados.

Resum

L'escenari actual, en què el creixement constant de la població i les seues necessitats de transport s'uneix a una reducció en la capacitat de producció de combustibles fòssils i cada vegada majors problemes derivats de la contaminació produïda per l'home, porta als fabricants de motors d'automoció a una constant lluita per la reducció del consum i les emissions contaminants dels seus productes mantenint les prestacions. Per aconseguir-ho, els codis de simulació unidimensionals s'han convertit en una eina fonamental, però requereixen un refinament constant per aconseguir nivells cada vegada majors de precisió en els càlculs. Fenòmens que abans tenien una importància limitada i podien ser modelats de forma extremadament senzilla, avui en dia requereixen del desenvolupament de nous mètodes de càlcul per a ser tinguts en compte. Entre aquests fenònems es troben les pèrdues mecàniques del turbogrup i el comportament de la turbina sota condicions de funcionament altament polsants. Este treball busca millorar els models actuals unidimensionals, tant per a la prediccio de les pèrdues mecàniques com el comportament de la turbina sota condicions de funcionament polsants a altes freqüències

Després d'estudiar els últims avanços en la mesura experimental i la simulació ràpida de turbocompressors, el present document compta primer amb un estudi experimental del comportament sota condicions de contorn estacionàries i no estacionàries de diversos turbocompressors d'automoció, tant del comportament general de la turbina com de les pèrdues mecàniques, incloent mesures de pressió interna en una de les unitats provades. Totes les mesures compten amb correccions per fluxe de calor, reduint el seu comportament al purament adiabàtic. Així mateix, s'ha desenvolupat una campanya de simulació CFD d'una turbina radial, obtenint una descripció detallada del seu comportament intern baix fluxe altament polsant.

A la vista dels resultats experimentals i de simulacions CFD, s'ha desenvolupat un model quasi-estacionari de pèrdues mecàniques i un model pseudo-bidimensional de turbina. Tots dos models han estat validats utilitzant les dades de les campanyes experimentals i de CFD, provant una gran millora en la precisió de les prediccions en comparar els seus resultats amb els de mètodes anteriors. El model de pèrdues mecàniques ofereix un clar avantatge enfront de la pràctica habitual d'utilitzar un rendiment mecànic constant per corregir el comportament del turbocompressor davant del mapa de funcionament donat pel fabricant, mentre que el model de turbina ha demostrat tindre potencial per a l'extrapolació de mapes i ha millorat els resultats instantanis per a freqüències superiors a 1000 Hz comparat amb els models clàssics de turbina amb volutes totalment unidimensionals. Tots dos models han estat desenvolupats tenint en compte el mantenir un reduït cost computacional, procurant explotar en lo possible les característiques dels processadors amb els que seran simulats.

List of publications

The following papers form the basis of this thesis:

- "Theoretical and experimental study of mechanical losses in automotive turbochargers" by Serrano, Olmeda, Tiseira, García-Cuevas, and Lefebvre [1].
- "Importance of Mechanical Losses Modeling in the Performance Prediction of Radial Turbochargers under Pulsating Flow Conditions" by Serrano, Olmeda, Tiseira, García-Cuevas, and Lefebvre [2].
- "Characterization of a radial turbocharger turbine in pulsating flow by means of CFD and its application to engine modeling" by Galindo, Fajardo, Navarro, and García-Cuevas [3].
- "Development and validation of a radial variable geometry turbine model for transient pulsating flow applications" by Galindo Lucas, Tiseira Izaguirre, Fajardo Peña, and García-Cuevas [4].
- "Effect of the numerical scheme resolution on quasi-2D simulation of an automotive radial turbine under highly pulsating flow" by Galindo, Climent, Tiseira, and García-Cuevas [5].

Division of work between authors

These publications have been done in collaboration with other researchers, being the author signatures in order of seniority. The respondent performed the experimental measurements, results post-processing and developed the models presented here. Methodologies and results discussions were done in collaboration with his supervisor, Assist. Prof. Tiseira, as well as with the rest of co-authors. The setup of the CFD cases were performed by Assist. Prof. Fajardo and Assist. Prof. Navarro.

Other publications

The following is a list of other publications in which the author of this thesis has been involved during the researches leading to the present work. Although not directly present in this document, they have provided a deeper insight in the behaviour of automotive turbochargers.

- "Optimization of the inlet air line of an automotive turbocharger" by Serrano, Margot, Tiseira, and García-Cuevas [6].

- “Uncertainties in power computations in a turbocharger test bench” by Olmeda, Tiseira, Dolz, and García-Cuevas [7].

Acknowledgements

First of all, my most sincere acknowledgement to the whole CMT-Motores Térmicos team for giving me the opportunity of being part of it. All the students, technicians, researchers, professors and the rest of the staff have contributed in one way or another to the successful completion of my research, and I truly thank them form that. Specially, I would like to thank my fellow grad students (and the ones that have successfully obtained their PhD title during these years), specially Jaime Sánchez, Miguel Andrés López, Petar Kleut, Lucía Royo, Miguel Reyes, Pablo Fajardo, Roberto Navarro and Artem Dombrovsky: the future is ours. Also, my special acknowledgements are for Francisco José "Paco" Arnau, who is doing a great job developing `OpenWAM`; Pablo Olmeda and Vicente Dolz, who have worked with me during my first steps in the journal publishing world; Sergio Hoyas, for the occasional conversations about the present and future; and Miguel Ortiz, Valentín Ucedo and José "Lathe Man" Gálvez: the goodness of the experimental results are all their merit. I would like to thank professor José Ramón Serrano and professor José Galindo, who have done all their best to guide me during the last four years. And, above them all, I owe my sincerest thanks to my thesis supervisor, professor Andrés Tiseira, who not only has guided me, but also has always believed in my work even when, due to my novice mistakes, the results were not as clear as they are today.

Eventually, I would like to thank my parents, my brother, my grandparents and all my family, for being there during my whole life. Also, I feel emotionally in debt with my friends for tolerating all my weirdness: the old ones like José Ángel García and Juan Luis Gonzalo, and the new ones, like Luis Fernando Moraga and the whole Comando Pascua and Javier Carrasco and all the Alulums.

And, of course, I owe all to my partner, Mari Carmen, for her patience and love through all these years of hard work.

Contents

List of Figures

List of Tables

Nomenclature

$\dot{m}$	Mass flow rate
$\dot{Q}$	Heat flow
$\dot{W}$	Power
A	Area
a	Speed of sound
A_A	Entropy level
c	Specific heat capacity
c_p	Specific heat capacity at constant pressure
c_v	Specific heat capacity at constant volume
e	Specific internal energy
F	Force
f	Frequency, objective function
g	Gravitational acceleration
h	Specific enthalpy, clearance or thickness
K	Thermal conductance
k	Coefficient, parameter, turbulent kinetic energy
L	Kinetic energy loss
l	Length
N	Number of elements or cases
n	Rotational speed, polytropic coefficient
P	Load per unit of projected area
p	Pressure
Pr	Prandtl number
q	Kinetic energy recovery factor
R	Gas constant, radius
r	Ratio of successive gradients, radius
Re	Reynolds number
$RMSE$	Root-mean-square error
S	Sommerfield number
T	Temperature
u	Absolute speed, uncertainty
V	Volume
w	Relative speed
x	Distance, variable

Z	Measurand
z	Estimate of a measurand
BMEP	Brake mean effective pressure
CFL	Courant–Friedrichs–Lewy condition
DES	Detached eddy simulation
FLOP	Floating point operations per cycle
HIL	Hardware-in-the-loop
LES	Large eddy simulation
MRF	Multiple reference frame
RANS	Reynolds-averaged Navier-Stokes
SMM	Sliding mesh model
SPL	Sound pressure level
SQP	Sequential quadratic programming
SST	Shear stress transport
URANS	Unsteady Reynolds-averaged Navier-Stokes
VGT	Variable geometry turbine

Greek Symbols

α	Absolute flow angle, VGT position
β	Relative flow angle
Δ	Difference
ϵ	Turbulent dissipation
η	Efficiency
Γ	Vortex strength
γ	Heat capacities ratio
λ	Eigenvalue, characteristic
μ	Dynamic viscosity
ν	Kinematic viscosity, Courant number
ω	Angular velocity, specific rate of turbulence dissipation
ϕ	Velocity potential
π	Pressure ratio
ρ	Density
σ	Standard deviation
σ	Blade speed ratio
τ	Torque
θ	Geometric angle
ε	Error
φ	Limiter value
ξ	Thrust bearing geometrical parameter
Δ	Difference operator

Vectors and matrices

$\boldsymbol{AIC}$	Aerodynamic influence coefficients matrix
$\boldsymbol{\tau}'$	Viscous stresses tensor
$\boldsymbol{I}$	Inertia tensor
$\boldsymbol{C}$	Source terms vector

$\boldsymbol{F}$	Flow terms vector
$\boldsymbol{n}$	Unitary normal vector
$\boldsymbol{o}$	Stator reference frame origin
$\boldsymbol{p}$	Point position
$\boldsymbol{s}$	Point position
$\boldsymbol{w}$	State vector

Overbar and others

$\hat{}$	Measured value
$\bar{}$	Mean value
*	Reduced or corrected quantity

Subscripts

$0, 1, \ldots$	Stations, coefficient number
θ	Tangential component
a	Axial component
amb	Ambient
at	Axial thrust
bc	Boundary condition
bl	Blocked, blade
ch	Choked conditions
cl	Clearance
$comp$	Compressor
df	Disc friction
eff	Effective
end	Duct end
exp	Experimental results
$exposed$	Exposed surface
$housing$	Turbocharger housing
in	Inlet
jb	Journal or radial bearing
$left$	Left
max	Maximum value
$metal$	Metal angle
min	Minimum value
ml	Mechanical losses
$model$	Model results
oil	Oil
opt	Optimum
$origin$	Origin
out	Outlet
$panels$	Panels
$puls$	Pulsating flow
r	Radial component
rel	Relative
$right$	Right
rt	Rotor
s	Ideal or isentropic state
st	Stator
$steady$	Steady-state flow
t	Total or stagnation state

tb Thrust or axial bearing

te Trailing edge

th Throat

tongue Volute tongue

turb Turbine

virtual Virtual

vol Volute

window Volute lateral window

CHAPTER 1

Introduction

Contents

Figures

1.1 Background

Turbocompressors were invented by Alfred Büchi in 1905, porting some of the concepts of the vapour turbine to reciprocating internal combustion engines (ICE). The most successful uses in the first years after its invention were in the aeronautic field: in 1917, a turbocompressor was coupled to a petrol V12 engine by Standford Moss while working for General Electric, improving the engine performance in altitude by reducing the effects of low atmospheric density. Although the first turbocharged aircraft engines had a loss of power output in altitude compared to that at sea-level, their performance was nothing but improved from that without a turbocharger, what enabled higher flight altitudes and reduced the engine weight and frontal area for a given power requisite. Turbocharged or supercharged aircraft ICEs not only led to higher flight ceilings: smaller engines meant less frontal area and, thus, reduced drag, and less engine weight meant less lift-induced drag; less drag reduced the power needed to fly with a given payload at a given speed and altitude, so higher payloads, speeds, ranges and altitudes were achieved without other improvements in the engine. Although nowadays turbofans and turboshafts have displaced the aeronautical use of overcharged ICEs, they are still used in small general aviation, where their low acquisition and maintenance costs are fundamental.

In the 1910's, turbocharged compression-ignition engines were introduced in naval transportation, with noticeable improvements over classic vapour turbine engines. They are still widely used today, although they are displaced in some fields by turboshafts and vapour turbines heated by nuclear reactors. In trains, turbocharged ICEs are used both for direct traction, using gearboxes, as well as for driving electrical generators.

In the automotive industry, engine turbocharging was first introduced in large diesel engines. Their usage was extended in the 1950s in heavy duty applications such as trucks, but they were not used in mass-produced cars due to their low reliability with the highly variable loads typical of cars. Automotive petrol engines were not overcharged until a bit later, as engine knocking is easily produced with high intake pressures unless very high octane fuel is used. In 1952, an overcharged competition petrol engine was used in Indianapolis 500, and, in 1962, the Oldsmobile Cutlass Jetfire was mass-produced with a Garrett turbocharger coupled to a V8 petrol engine. One of the first successful mass-produced diesel cars is the Peugeot 604, launched in 1978. Later energetic crises have led to the imposition of diesel turbocharged engines in some markets, such as in trucks or European cars.

Nowadays, the humanity is putting a strong pressure in the environment due to a never-ending rise in energy and transportation demands. The relative scarcity of oil and the internal and external political and social convulsions of the main producers are coupled with the astounding economic rise of some

Asian giants such as China or India, producing constant price increases with sudden spikes. Also, new oil fields are becoming more and more expensive to gather, as easier fields are depleted. As the times of cheap fuel are far in the past and only price surges are expected, the market forces are pushing towards more efficient vehicles: transportation now accounts for around 55 % of oil used. Also, the health issues derived from pollutant emissions, that range from more incidence of allergies and asthma to higher prevalence of cancer, as well as the high economic and social impact of human-made climatic change and the effects of pollutants in the wider biosphere, are rising concerns in the society that are translated into tighter environmental regulations that put stringent limits in CO_2, NO_x and particulate emissions. And, although fuel cell and electric vehicles might be a solution in the long term, reciprocating internal combustion engines are the only feasible solution for the vast majority of current transportation needs.

In Europe, there have been several moves and regulations to improve vehicle fleet efficiencies and lower their emissions. There were a voluntary agreement in 1999 between the European Automobile Manufacturers Association, the Japanese Automobile Manufacturers Association and the Korean Automobile Manufacturers Association, which accounted for 90 % of the European market share, to reduce CO_2 emissions to a fleet-average of $120\,g\,km^{-1}$ in 2014: although this objective has not been reached, large reductions have been produced. More recently, in 2009, the European Commission developed a mandatory CO_2 emission reduction program a bit less ambitious: $130\,g\,km^{-1}$ by 2015 and $95\,g\,km^{-1}$ by 2020 [8]. Meanwhile, engine manufacturers have also to comply with mandatory NO_x and soot emissions, with the latest regulation in application from this very same year [9, 10]. Similar regulations are used in other parts of the world, such as in U.S.A. or Japan.

Lower fuel consumption and pollutant emissions are being achieved using several methods in ICEs:

- General turbine and compressor optimisations, including better stator blades and rotor geometries, better stator actuators, higher turbine operating temperatures, lower friction losses, lower heat transfer losses and wider compressor maps.

- Two-stage boosting systems, which reduce turbo lag, can improve EGR and allow to optimise the turbo operation under broader engine operating conditions.

- Further improvements in the combustion process and new combustion processes, including dual-fuel strategies, which are enabled by very high boosting pressures.

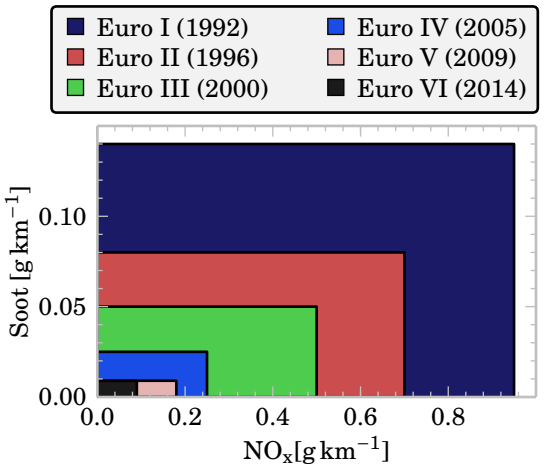

Figure 1.1: European emission limits for diesel light-duty vehicles

- Further engine size reductions (downsizing), also enabled by higher engine boosting pressures.
- Further engine downspeeding.
- Lower moving parts friction, obtained by mechanism and bearing optimisations and lower viscosity lubrication.
- Higher pressure direct injection systems, even in petrol engines.
- More advanced injectors and multiple-injection strategies.
- Higher EGR ratios.
- More sophisticated engine control, including advanced sensors for online engine diagnosis and model-based control systems.
- Advanced thermal management systems, reducing engine loses during the warm-up phase.
- More advanced aftertreatment systems, including NO_x traps, improved particulate filters and selective catalytic reduction filters.
- Usage of new and cleaner fuels, that lack some components and ease the operation of the aftertreatment systems.
- Generalisation of energy recovery systems, being them kinetic energy recovery systems during engine braking or waste heat recovery systems such as organic rankine cycles coupled to large engines.

- Aerodynamic optimisations and weight reductions in case of vehicle applications.

From this list, it is clear that turbocharging improvements play a key role in future engine developments, and is expected that in the near future even 50 % of petrol engines for automotive application will use a turbocharger. Engine manufacturers allocate a large amount of efforts to engine simulations using fast one-dimensional codes, and as such great improvements are being produced in the area of fast and accurate turbocharger modelling, even in areas that were discarded as of having lesser importance, such as pulsating performance, heat transfer and mechanical losses.

The research institute CMT-Motores Térmicos, in which the respondent has done the work leading to his dissertation, has a long history of turbocharger research and one-dimensional ICE code development. The first studies carried out in this area date back to 1973, in the form of a Ph.D. thesis by Payri [11]. More recently, in 1999 Serrano [12] wrote a dissertation about modelling load transients in automotive turbochargers. During the last decade, the research continued in the work by Cervelló [13], in 2005, who wrote a thesis about variable geometry turbine modelling, and in the work by Tiseira Izaguirre [14], in 2008, whose thesis versed about compressor surge and its modelling for automotive engine simulations. In the last couple of years, turbocharger research has accelerated and several theses have been produced. Lang [15] wrote about compressor surge and methods to improve the surge margin in 2011. Varnier [16] studied the current state of the art in two-stage diesel engine boosting systems in 2012. The Ph.D. thesis by Fajardo Peña [17] (2012) is an excellent research work about pulsating flow characterisation of radial turbines using current computational fluid dynamics (CFD) methods. Last year, Reyes-Belmonte [18] successfully defended a very broad dissertation about one-dimensional modelling of automotive turbochargers, taking into account heat flows, pulsating performance and turbine map extrapolation. Finally, this same year, López Hidalgo [19] introduced a novel field of study in the research institute with his work about turbocharger rotor dynamics experimental studies and modelling, while Navarro [20] presented a method for predicting flow-induced acoustics at near-stall conditions in a radial compressor. The institute is now widening its research area about waste energy recovery systems in engine exhaust gases, as with the Ph.D. dissertation by Serrano Sánchez [21], which will be defended this year.

1.2 Motivation

As it has been already said, engine manufacturers rely in fast but accurate computational methods during engine development. The methods employed in

the industry vary in their grade of complexity, with a clear trade-off between potential accuracy and computational cost. Also, the time-resolution is increased for more complex and time-consuming methods.

- Look-up tables-based methods are the faster, and require a large database of different engine configurations. They can be used as a first step in the global optimisation process, combined with the general insight of the engineers that are developing the new engine. They have low accuracy and low time-resolution, giving average results that are valid only in the several seconds time-scale.

- Mean value engine models are slightly slower, but can still be used in real time, so they are a good tool for hardware in the loop (HIL) problems as well as for the second optimisation phase, when a large amount of variables are still used and the complexity of the problem, even when using a very well chosen mathematical programming algorithm, requires fast objective function evaluations. They produce cycle-averaged results.

- Filling and emptying models have time resolutions within the crank angle scale, and are used with phenomenological models that have varying degrees of predictive performance. Their higher computational cost means that can only be used in real time when they are not too complex, and they can be used for optimisations with a reduced number of variables. Their nonlinear acoustic performance is limited to only low frequencies. Filling and emptying methods model the momentum conservation between elements instead of simulating it.

- One-dimensional methods have better time resolution and nonlinear acoustic performance than filling and emptying models, as the momentum conservation equation is simulated. They can be used for frequencies in the kHz scale. As their computational cost is somehow higher than filling and emptying models, are usually used with more sophisticated models for some of the phenomena, such as multi-zone combustion models. They are used during the optimisation process with an even lower amount of variables.

- Three-dimensional methods are what are nowadays considered as truly computational fluid dynamics (CFD) methods. They simulate even more phenomena, and model some aspects such as turbulence. The level of simulation is growing with the years, directly computing some of the largest turbulent structures in some cases. Their computational cost makes them prohibitive but for small optimisation problems or when the accuracy of the method is small (i.e., using coarse meshes) and only tendencies are required.

A large part of the engine development is done using one-dimensional codes, as the nonlinear acoustics are becoming more and more important. Engine acoustic tuning is key to get high volumetric efficiencies, and acoustic pollution regulations are becoming more and more strict. Turbochargers are modelled with a varying degree of complexity in one-dimensional codes, with the most simple approach being using a simple look-up table based in manufacturer's maps. Look-up tables lack, however the accuracy expected for one-dimensional codes, and as such are usually corrected using tuning parameters (i.e., turbocharger efficiency is multiplied by a value different from one to take into account levels of mechanical losses, heat transfer or internal unsteady behaviour different from that found during the measurement of the maps). Heat transfer, mechanical losses and unsteady behaviour were relatively easily corrected in the past, but today turbochargers and engines are becoming too small and these effects are becoming more and more important, above all during the engine warm-up phase and urban driving conditions, with constant engine tip ins and tip outs and partial loads. As today and future regulations are becoming more focused in these operations, notable efforts have been made to get better accuracy while keeping the computational cost low, with very smart approaches for mechanical losses, heat transfer and unsteady performance modelling. A constant evolution of the current methods is needed, however, as the level of engine refinement is constantly rising.

1.3 Objectives

The general objective of the present work is the development of a mechanical losses and a turbine model able to be used during unsteady pulsating flow simulations of an internal combustion engine. These models should be able to predict the turbocharger performance not only under conditions similar to that that were found during the experimental characterisation, but also far from that conditions. They have to improve the current fast simulation models that are used nowadays in the automotive industry, and they should be based as much as possible in first principles in order to reduce the amount of experimental information needed to calibrate them.

1.4 Employed method

The main phenomena that take place in an automotive turbocharger have been studied in order to develop an improved radial turbine and mechanical losses model. They have been studied as follows:

- Study of the turbine performance under steady-state conditions in a tur-

bocharger gas-stand. As the model should be decoupled from heat transfer phenomena, it has been measured under quasi-adiabatic conditions. Despite typically assumed adiabatic, turbochargers are affected by heat flows when working under urban driving conditions and during the warm-up phase: these heat flows can be taken into account as shown in the work by Serrano et al. [22].

- Study of the internal pressure of both the turbine and the compressor, as it affects the axial thrust and, thus, the mechanical losses and this information can be useful during the validation phase of the turbine model.

- Study of the turbine performance under pulsating flow conditions in a turbocharger gas-stand. Both the pressure decomposition and the internal pressure have been studied in order to validate the turbine model.

- Experimental study of the mechanical losses of several turbochargers. The mechanical losses become very important in urban driving conditions and during the warm-up phase due to high oil viscosities, and can substantially reduce the performance of the turbocharger. As it will be seen later, the oil outlet temperature can be affected to a great degree due to heat fluxes, so they have to be measured in order to properly estimate the mechanical losses using internal energy differences in the gas stand.

- Three-dimensional unsteady CFD simulation of a radial turbine. Although the global performance of the turbine can be characterised with high accuracy using experimental studies, its internal behaviour is almost impossible to measure in detail except for some variables in a very limited set of points, such as the pressure at the rotor inlet. The simulated results have proven to be very valuable to develop the radial turbine model and to assess its validity and advantages against a more simplistic approach.

After these studies, the current work has been focused in the development and validation of both the radial turbine and the mechanical losses models.

Chapter 2 has been dedicated to the literature review on turbocharger measurement and modelling. Different proposals for turbine and mechanical losses modelling have been studied, taking care of the decoupling of the adiabatic performance and the heat flow phenomena. CFD approaches to radial turbine simulation have been studied, too.

Chapter 3 has been dedicated to the experimental campaigns performed for turbocharger characterisation. The general method for global turbocharger characterisation is described, as well as the specific improvements carried out in order to measure the specific values needed for the development and validation of the proposed models. In particular, a method for mechanical losses

characterisation using the oil internal energy difference between the oil inlet and outlet ports is presented, discriminating between the dissipated power in the shaft and the internal heat flow, as well as a method for the characterisation of the turbine stator and the turbine rotor with minimal flow disturbance.

Chapter 4 has been dedicated to the study of three-dimensional unsteady simulations of a radial turbine. These simulations are highly valuable to characterise the performance of the different parts of the turbine, giving additional information to that acquired by means of experimentation that is otherwise impossible to obtain. With these results, the total pressure losses at different parts of the turbine can be quantified and phenomena such as flow deviations from the blades can be measured. The circumstances that produce the main differences from the ideal behaviour are qualitatively described in this chapter, and the main challenges that the model will face are determined.

Chapter 5 presents the development of the proposed models, and is divided into two main sections: radial turbine modelling and mechanical losses modelling. The radial turbine modelling is also divided into different submodels, as the turbine has been split in different logical and physical parts: the mainly one-dimensional elements, the stator and the rotor. A finite-volume approach has been used for one-dimensional modelling due to its simplicity at adapting to different geometries and its robustness when introducing source terms. To get high accuracy with a relatively low computational cost, a high resolution method has been used. The volute has been also modelled using a finite-volumes method, with source terms that represent its outlet flow through its lateral window. The stator is modelled using several non-ideal nozzles attached to the volute, coupled with a bi-dimensional boundary elements model to get its outlet flow angle. The rotor is computed using a non-ideal, constant rothalpy element. For the mechanical losses model, the computation is split into two different bearing losses submodels: a radial bearing and an axial bearing. Although the flow inside the bearings is supposed to be mainly one-dimensional, a simple method to account for three-dimensional behaviour is used. The modifications for modelling floating radial journal bearings and coupled radial and thrust bearings are presented.

Chapter 6 is focused in the calibration and the validation of the different models developed in this work. It is divided into two main parts, one for the mechanical losses submodel and other for the turbine flow submodel. The mechanical losses submodel is tested against experimental data and an analysis of its behaviour under different oil feeding conditions is performed. The turbine submodel is tested against CFD data and experimental results at both steady-state and pulsating flow conditions. The internal pressure prediction is validated and the improvements of a quasi-bidimensional method for computing the turbine is assessed. A study of the influence of different numerical schemes in the performance prediction at different frequencies is also performed.

Chapter 7 summarises the main findings and contributions of this Ph.D. dissertation, presenting the main limitations of the models and the recommendations for future work that could improve them.

1.5 Measurement stations

Hereinafter, the variables measured in different stations will be identified by their identification code as subscripts. These codes are:

$comp,in$ Duct upstream of the compressor.

$comp,out$ Duct downstream of the compressor.

oil,in Oil inlet.

oil,out Oil outlet.

$vol,1$ Turbine volute, initial section.

$vol,2$ Turbine volute, middle section.

rot,out Compressor rotor outlet.

0 Duct upstream of the turbine.

1 Turbine inlet.

2 Turbine stator inlet.

3 Turbine stator outlet.

4 Turbine rotor outlet.

5 Turbine outlet.

6 Duct downstream of the turbine.

The measurement stations upstream and downstream of the compressor and the turbine are measured following [23] and [24], keeping the required distances upstream and downstream of the sensors to get proper flow development. The oil inlet station is measured close to the turbocharger oil inlet port, and the oil outlet station is measured close to the turbocharger oil outlet port, using a special arrangement that is described in chapter 3. The turbine internal stations are described in chapter 3, chapter 4 and chapter 5, but their names are self-explanatory.

1.6 References

[8] European Parliament, Council of the European Union. “Regulation (EU) No 510/2011 of the European Parliament and of the Council of 11 May 2011 setting emission performance standards for new light commercial vehicles as part of the Union’s integrated approach to reduce CO 2 emissions from light-duty vehicles (Text with EEA relevance)”. In: *Official Journal of the European Union* 54 (May 2011), pp. 1–15. DOI: 10.3000/17252555.L_2011.145.eng (cit. on p. 3).

[9] European Parliament, Council of the European Union. “Regulation (EC) No 715/2007 of the European Parliament and of the Council of 20 June 2007 on type approval of motor vehicles with respect to emissions from light passenger and commercial vehicles (Euro 5 and Euro 6) and on access to vehicle repair and maintenance information (Text with EEA relevance) ”. In: *Official Journal of the European Union* 50 (June 2007), pp. 1–16. ISSN: 1725-2555. URL: http://eur-lex.europa.eu/legal-content/EN/TXT/?uri=OJ:L:2007:171:TOC (cit. on pp. 3, 15, 73).

[10] European Parliament, Council of the European Union. “Regulation (EC) No 595/2009 of the European Parliament and of the Council of 18 June 2009 on type-approval of motor vehicles and engines with respect to emissions from heavy duty vehicles (Euro VI) and on access to vehicle repair and maintenance information and amending Regulation (EC) No 715/2007 and Directive 2007/46/EC and repealing Directives 80/1269/EEC, 2005/55/EC and 2005/78/EC (Text with EEA relevance) ”. In: *Official Journal of the European Union* 52 (July 2009), pp. 1–13. DOI: 10.3000/17252555.L_2009.188.eng (cit. on pp. 3, 15, 73).

[11] F. Payri. “Predicción de las actuaciones de los grupos de sobrealimentación para motores diesel de automoción”. PhD thesis. Universidad Politécnica de Madrid, 1973 (cit. on p. 5).

[12] J. R. Serrano. “Análisis y modelado de transitorios de carga en MEC turboalimentados”. PhD thesis. Universitat Politècnica de València, 1999 (cit. on p. 5).

[13] C. Cervelló. “Contribución a la caracterización experimental y al modelado de turbinas de geometría variable en grupos de sobrealimentación”. PhD thesis. Universitat Politècnica de València, 2005 (cit. on p. 5).

[14] A. O. Tiseira Izaguirre. “Caracterización experimental y modelado de bombeo en compresores centrífugos de sobrealimentación”. PhD thesis. Universitat Politècnica de València, 2008 (cit. on pp. 5, 18, 252).

[15] R. Lang. “Contribución a la mejora del margen de bombeo en compresores centrífugos de sobrealimentación”. PhD thesis. Universitat Politècnica de València, 2011 (cit. on p. 5).

[16] O. Varnier. “Trends and Limits of Two-Stage Boosting System for Automotive Diesel Engines”. PhD thesis. Universitat Politècnica de València, 2012 (cit. on p. 5).

[17] P. Fajardo Peña. “Methodology for the Numerical Characterization of a Radial Turbine under Steady and Pulsating Flow”. PhD thesis. Universitat Politècnica de València, July 2012 (cit. on pp. 5, 114, 117).

[18] M. Á. Reyes-Belmonte. “Contribution to the Experimental Characterization and 1-D Modelling of Turbochargers for IC Engines”. PhD thesis. Universitat Politècnica de València, Dec. 2013 (cit. on pp. 5, 24, 202).

[19] M. A. López Hidalgo. “Estudio teórico-experimental de la dinámica rotacional de un turbocompresor de MCIA. Aplicación al diagnóstico de fallos”. PhD thesis. Universitat Politècnica de València, 2014 (cit. on p. 5).

[20] R. Navarro. “A numerical approach for predicting flow-induced acoustics at near-stall conditions in an automotive turbocharger compressor”. PhD thesis. Universitat Politècnica de València, 2014 (cit. on pp. 5, 21, 252).

[21] J. Serrano Sánchez. “Contribución a la implementación de ORCs en MCIAs”. PhD thesis. Universitat Politècnica de València, 2014 (cit. on p. 5).

[22] J. R. Serrano, P. Olmeda, A. Páez, and F. Vidal. “An experimental procedure to determine heat transfer properties of turbochargers”. In: *Measurement Science and Technology* 21.3 (3 2010), pp. 035–109. DOI: 10.1088/0957-0233/21/3/035109 (cit. on pp. 8, 18, 41, 68).

[23] SAE. *Supercharger Testing Standard*. SAE J1723. Society of Automotive Engineers, Aug. 1995 (cit. on pp. 10, 18, 59, 77).

[24] SAE. *Turbocharger gas stand test code*. SAE J1826. Society of Automotive Engineers, Mar. 1995 (cit. on pp. 10, 18, 59, 77).

CHAPTER 2

Literature review

Contents

Figures

2.1 Introduction

Nowadays internal combustion engines, ICE, are facing two main problems, the pollutants emission and the fuel consumption reduction, in order to fulfil new regional regulations such as the European norm Euro VI [9], [10] while maintaining the engine performance. The new engine design paradigm used to reach these objectives is based in a reduction of the engine size while incrementing the inlet pressure, an action known as downsizing. This is usually done using a turbocharger placed in the intake and in the exhaust line, and engine efficiency is highly affected by the turbocharger efficiency.

Engine manufacturers are growing their usage of one-dimensional codes during engine development, as they provide accurate results while keeping their computational costs low enough to be used during intensive and broad simulation campaigns. As pulsating flow becomes more important with further engine downsizing and urban driving emission regulations become more stringent, the importance of one-dimensional accurate predictions of turbocharger performances under high amplitude and frequency boundary conditions and high viscous oil grow in importance.

In this chapter, a literature review of the most relevant works about radial turbocharger modelling focused in turbine performance and mechanical losses prediction is presented.

2.2 Turbine behaviour

The data needed to simulate turbochargers in one-dimensional engine codes is obtained from experimental steady-state maps, usually provided by the turbocharger manufacturer. In the turbine side, these maps provide information about its mass flow rate parameter $\dot{m}^*_{turb}$ versus its total to static pressure ratio π_{turb} and about the turbine efficiency η_{turb}:

$$\dot{m}^*_{turb} = \dot{m}_{turb} \cdot \frac{\sqrt{T_{0t}}}{p_{0t}} \tag{2.1}$$

$$\pi_{turb} = \frac{p_{0t}}{p_6} \tag{2.2}$$

where $\dot{m}_{turb}$ is the real mass flow rate, T_{0t} is the total temperature at the turbine inlet, p_{0t} is the total pressure at the turbine inlet and p_6 is the static pressure at the turbine outlet.

Sometimes, the mass flow rate parameter $\dot{m}^*_{turb}$ is called corrected mass flow rate and is defined as:

$$\dot{m}^*_{turb} = \dot{m}_{turb} \cdot \frac{\sqrt{T_{0t}}}{\sqrt{T_{ref}}} \cdot \frac{p_{ref}}{p_{0t}} \tag{2.3}$$

where T_{ref} and p_{ref} are reference temperatures and pressures. The mass flow rate parameter data points are grouped by a turbine speed parameter ω^*_{turb}:

$$\omega^*_{turb} = \frac{\omega}{\sqrt{T_{0t}}} \tag{2.4}$$

where ω is the physical rotational speed. Again, sometimes it is called corrected speed and is expressed as:

$$\omega^*_{turb} = \omega \cdot \frac{\sqrt{T_{ref}}}{\sqrt{T_{0t}}} \tag{2.5}$$

The data points are also grouped by vanes position, in case of variable geometry turbines (VGT). The map is provided in this form to take advantage of the Buckingham π theorem while not giving full non-dimensional values, as some variables that affect the turbine behaviour are almost constant, such as the flow composition.

The turbine efficiency η_{turb} is usually provided as a global turbocharger efficiency, the ratio between the compressor power $\dot{W}_{comp}$ and the turbine isentropic power $\dot{W}_{turb,s}$, instead of the ratio between the turbine power $\dot{W}_{turb}$ and the turbine isentropic power output.

$$\eta_{turb} = \frac{\dot{W}_{comp}}{\dot{W}_{turb,s}} \tag{2.6}$$

This turbocharger efficiency contains the mechanical power and, as the power is not directly measured, is probably affected by heat transfer effects. The compressor power is estimated using its mass flow rate $\dot{m}_{comp}$, its mean specific heat capacity $\bar{c}_{p,comp}$ and its inlet and outlet total temperatures $T_{comp,in,t}$ and $T_{comp,out,t}$, without subtracting the compressor heat flow $\dot{W}_{comp}$:

$$\dot{W}_{comp} \simeq \dot{m}_{comp} \cdot \bar{c}_{p,comp} \cdot \left(T_{comp,out,t} - T_{comp,in,t}\right) \tag{2.7}$$

The turbine isentropic power is defined as:

$$\dot{W}_{turb,s} = \dot{m}_{turb} \cdot \bar{c}_{p,turb} \cdot T_{0t} \cdot \left[1 - \left(\frac{p_6}{p_{0t}}\right)^{\frac{\gamma-1}{\gamma}}\right] \tag{2.8}$$

where γ is the specific heat capacities ratio. This isentropic power is computes supposing that the ideal evolution is from the total pressure at the turbine inlet to a total pressure equal to the static pressure at the turbine outlet. This efficiency is sometimes given versus the total to static expansion ratio, while other times is given versus the turbine blade speed ratio σ_{turb}:

$$\sigma_{turb} = \frac{\omega \cdot r_{rt,in}}{\sqrt{2 \cdot \bar{c}_{p,turb} \cdot T_{0t} \cdot \left[1 - \left(\frac{p_6}{p_{0t}}\right)^{\frac{\gamma-1}{\gamma}}\right]}} = \frac{\omega \cdot r_{rt,in}}{u_s} \tag{2.9}$$

where $r_{rt,in}$ is the turbine wheel inlet radius. This blade speed ratio is a ratio between the turbine blade tip speed and the speed obtained from an isentropic evolution from the turbine inlet total conditions to the turbine outlet static pressure (u_s).

Turbine manufacturer's maps are obtained using the compressor as a brake for the turbine. This way, the range of points provided for each iso-speed line is quite narrow, as the compressor has very limited braking range due to surge and choke. High mass flow rate parameters are obtained for high rotational speeds, where the compressor drains high amounts of power, while low mass flow rate parameters are only obtained for low rotational speeds. As this information can be too limited for engine simulations, specific experimental tests and models are used to get broader data ranges, as it will be explained in the following sections.

Other limitation of these steady-state maps comes from the fact that the turbine is operating under pulsating flow in an internal combustion engine, with rising levels of pulsation as engine downsizing techniques progress. Some authors, such as Iwasaki et al. [25] and Luján et al. [26], have found big differences of even 20 % between steady-state maps and pulsating flow performance, with some studies dating back to the 60s [27]. Some of the most recent work has been focused on CFD simulations, as in [28, 29, 3], while other researchers have been working in fast one-dimensional codes [30, 31, 32], as well as meanline models to better extrapolate the turbine behaviour far from the data found in experimental maps [33, 34].

The map also lacks internal pressure data that is valuable to validate the model proposed later in this work.

Experimental characterisation

Usually, turbocharger turbines are measured in a gas stand using the compressor as a brake. A mass flow meter is placed usually downstream of the turbine, and the inlet and outlet pressure and temperatures are measured. Pressure and temperature transducers are placed 6 diameters upstream and downstream of

the turbine to ensure developed flow. As the turbine temperature may reach high values, it is usually measured using thermocouples. Four thermocouples are normally used in each measurement section: one submerged half diameter, two submerged a third part of a diameter and the last submerged only a quarter of a diameter. The rotational speed can be measured by several means, but it is common to use an inductive sensor placed at the compressor side. The position of the vanes, when using a variable geometry turbine, is measured using a displacement sensor. These measurement recommendations are found in several testing codes and standards, and maybe the most used are *Supercharger Testing Standard* [23] and *Turbocharger gas stand test code* [24].

The turbine can be powered by the exhaust gases of an internal combustion engine (ICE) or by an auxiliary air compressor [35], [36], [22]. Pulsating flow can be obtained directly from the exhaust gases of an ICE or by using a rotating valve [37], [14]. The turbine inlet temperature can be controlled using heat exchangers, electrical heaters and burners.

Heat flow effects are neglected using several approaches. First, external heat flow can be reduced by using thermal insulation. Then, quasi-adiabatic tests can be performed by keeping the turbine inlet temperature very close to the compressor outlet temperature and the oil inlet temperature, as described in [38], thus minimising heat transfer.

Pulsating flow is sometimes studied using pressure wave decomposition, as shown in [39]. Using this technique, the inlet pressure can be split into an incident and a reflected wave, while the outlet pressure can be split into a transmitted wave and a second reflection. Using sensible assumptions, even the instantaneous mass flow rate in the measuring sections can be computed. This information can be later used during the validation of one-dimensional codes [40], [41], as will be shown in following chapters.

When using the turbocharger compressor as a brake, the measuring range is limited by surge at low expansion ratios and by choke at high expansion ratios, and the braking capabilities of the compressor at a given rotational speed are controlled by means of a back-pressure valve. To widen the measurable range for lower and higher expansion ratios, the compressor power consumption has to be lowered or risen accordingly. The most simple technique is to connect the outlet of the compressor line to its inlet in a closed loop: this way, the compressor inlet pressure and density can be lowered using a vacuum pump and can be risen using a pressurised air line. Near the surge line, the compressor power can be further lowered using the vacuum pump, and it can be risen near choke using pressurised air. Further lowering and rising of the compressor power can be achieved by changing the compressor wheel, with obvious shaft balancing issues that have to be addressed. Also, changing the compressor inlet density or its wheel can produce axial force unbalance and higher thrust bearing stresses. The turbine operating range can be further extended by replacing the

compressor with an electric brake, coupled with a reduction gear. In this case, the measurable range is limited due to high rotating speeds. Map extension using a closed loop at the compressor was adopted for this work, as it could be performed without wheel modifications and balancing issues.

No information about internal flow measurement was found in the literature, probably due the very small size of automotive turbochargers.

CFD characterisation and modelling

CFD simulations of radial turbines are done using several approaches for the boundary conditions. First, the boundary conditions are applied sometimes far from the turbine, with long inlet and outlet ducts that ensure flow development before reaching the turbine, as in [3]. In other works, however, the boundary conditions are imposed directly in the turbine inlet and outlet, as done by Aymanns et al. [29]. The boundary conditions usually consist in a total pressure and temperature boundary at the inlet and a static pressure at the outlet, as these variables can be measured in a gas stand and they provide good numerical stability and convergence rates in radial turbine simulations, as seen in [42].

One of the main differences between different approaches in turbine modelling by means of CFD is in how the impeller movement is taken into account. Two main methods apply:

- Use a frozen mesh, simulating the movement by using a rotating coordinate system. Coriolis and centrifugal forces are introduced as source terms and the rotor is solved in its rotating coordinate system. The rest of the turbine is computed using an inertial reference frame. This approach is usually called a Multiple Reference Frame (MRF) method or frozen rotor (although there are other MRF methods, such as circumferential averaging). Its main advantage is its low computational cost, as the mesh doesn't need to be rebuilt at each time-step. Of, course, it neglects blade passing effects and stator-rotor interactions.

- Modify the mesh at each time-step, rotating it as the rotor moves. This approach is called a Sliding Mesh Model (SMM) and involves much higher computational costs than the MRF method. Its main advantage is that it can compute blade passing effects and stator-rotor interactions.

Although some authors have conducted simulations using a MRF approach with a high level of accuracy, such as Lam et al. [28], the general understanding is that the benefits of SMM are needed to correctly model the detailed behaviour of the turbine. Palfreyman et al. [43] considered that the frozen rotor approach may have some impact on the results. Different turbocompressors were simulated by Liu et al. [44], finding that the mesh motion model has an important

role in the reproduction of the stator-rotor interaction results: they analysed two different MRF methods, a frozen rotor model and a circumferential averaging model, and found better results with the latter. In a work from 1999, Hillewaert et al. [45] found that the frozen rotor model was suboptimal for centrifugal compressors. More recently, Hellström [46] has gotten good results while simulating unsteady flow in turbochargers using SMM, and Galindo et al. [47] used MRF and SMM to simulate a centripetal turbine under steady-state conditions, and found better results using SMM when comparing with experimental data.

As for the viscous model, there is an ever growing number of research works dealing with viscous models for turbomachinery CFD simulations. Direct Numerical Simulation (DNS) of the Navier-Stokes equations is unaffordable nowadays but for very simple cases, so the current research is focused in Unsteady Reynolds Averaged methods (URANS), Detached Eddy Simulations (DES) or Large Eddy Simulations (LES).

In RANS, the Navier-Stokes equations are time-averaged and their different terms are composed by a time-averaged quantity and a fluctuating quantity: the averaged quantities are directly solved, while the fluctuating quantities are modelled. These fluctuating quantities form the Reynolds stresses, and are usually modelled using a Boussinesq approach or a Reynolds Stress Model (RSM) approach. In the Boussinesq approach, there is a proportionality between the mean velocity gradient and the Reynolds stresses, while in RSM there is an equation for each element of the Reynolds stresses tensor, which is a better approximation with high turbulence anisotropies but has higher computational costs. Boussinesq-based models have low overhead over the totally laminar solution, and usually consist in two equations for internal flow problems such as in turbine modelling, as seen in [48]. Typical examples of two-equation models are the $k-\epsilon$ model, based on the turbulent kinetic energy k and the turbulence dissipation rate ϵ; and the $k-\omega$ model, based on the specific dissipation rate ω, more accurate in the near-wall layers but very sensitive to the free stream properties. Amongst all the two-equation models, the SST turbulence model developed by Menter [49] is probably the most used in turbomachinery applications. The SST model combines the robust and accurate formulation of the $k-\omega$ model in the near-wall region with the free-stream independence of the $k-\epsilon$ model in the far field. The SST model is used over a wide range of validation cases [50] and in turbomachinery simulations [51], showing good agreement between the simulations and experimental data and being able to capture the effects of the variation of Reynolds number and flow separation. Simpson et al. [42] simulated vaned and vaneless radial turbines using the SST model, obtaining good results.

In LES, the largest eddies are explicitly solved, only modelling the small scales. This leads to potentially more accurate results, as small scales are more isotropic and less affected by macroscopic flow effects. DES can be seen

as a mix between LES and RANS, simulating the largest eddies in the free stream and modelling the boundary layer using RANS. Both LES and DES have larger computational costs than RANS, however, and were seldom used until recently in radial turbine simulations. Mendonça et al. [52] used DES to analyse the aeroacoustics of a radial compressor, obtaining SPL spectra at the inlet and outlet ducts and even assessing rotating stall as the source of a narrow band noise at a frequency about 70 % of rotational speed. In a recent work by Broatch et al. [53], simulations of compressor aeroacoustics are performed using URANS and DES, showing similar results but with better reproduction of the experimental data with DES. More results about DES simulation of a radial compressor can be found in the Ph.D. thesis by Navarro [20].

During CFD simulations, the volute is found to account for the vast majority of wave and accumulation effects in the turbine, with the stator presenting a small hysteretical behaviour due to accumulation effects and the rotor behaving almost totally quasi-steady, as shown in [3].

Fast models

Fast turbine models are split into two different categories: steady-state models and unsteady models. Usually, steady-state models are coupled with one-dimensional codes to compute the unsteady behaviour.

Steady-state models

Steady-state modelling of radial turbines are done with different levels of complexity and interpolation and extrapolation capabilities. First of all, the most simple way to model a radial turbine is to treat it as a punctual map interpolating black box. In this approach, the turbine behaviour is obtained from interpolating the turbine map. The interpolation can be done with different levels of complexity, from simple linear interpolation in expansion ratio and turbine speed parameter to more complex transfinite interpolators. The problem with this approach is that it provides no extrapolation capabilities.

A bigger level of complexity is achieved by means of semi-empirical models. These models approximate the performance of the turbine using simple functions such as polynomials, and have some success in both mass flow rate [54] and efficiency [55], and are useful when very fast computations are needed such as in real time simulations. The extrapolation capabilities of these semi-empirical models is somewhat limited, as they are not based in sound physical principles. A very simple but very fast approach to these kind of models aimed to control processes can be found in the work by Eriksson et al. [56], where the mass flow

rate parameter is a function of the expansion ratio and two parameters, k_1 and k_2:

$$\dot{m}^*_{turb} = k_1 \cdot \sqrt{1 - \pi^{k_2}_{turb}} \tag{2.10}$$

Eriksson [57] also presents a simple model of turbine efficiency, using a quadratic function in blade speed ratio σ_{turb} and depending on the maximum turbine efficiency $\eta_{turb,max}$, the blade speed ratio for maximum efficiency $\sigma_{turb,max}$ and a fitting parameter:

$$\eta_{turb} = \eta_{turb,max} \cdot \left[1 - k_1 \cdot \left(\sigma_{turb} - \sigma_{turb,max}\right)^2\right] \tag{2.11}$$

Sieros et al. [58] proposed a more complex model, using a quadratic polynomial, but has problems at very high expansion ratios where the turbine should become choked. Also, it is developed for axial turbines.

$$\dot{m}^*_{turb} = k_1 + k_2 \cdot \pi_{turb} + k_3 \cdot \omega^*_{turb} + k_4 \cdot \pi_{turb} \cdot \omega^*_{turb} + k_5 \cdot \pi^2_{turb} + k_6 \cdot \omega^*_{turb} \tag{2.12}$$

A similar model that also tries to somehow take into account choking conditions is due to Orkisz et al. [59], also developed for axial turbines:

$$\begin{aligned} \pi_{turb} = & k_1 + k_2 \cdot \dot{m}^*_{turb} \cdot \omega^*_{turb} + k_3 \cdot \left(\dot{m}^*_{turb} \cdot \omega^*_{turb}\right)^2 \\ & + k_4 \cdot \dot{m}^*_{turb} \cdot \omega^*_{turb} \cdot Z_{turb} + k_5 \cdot Z_{turb} + k_6 \cdot Z^2_{turb} \end{aligned} \tag{2.13}$$

$$Z_{turb} = \left(\frac{\pi_{turb}}{\dot{m}^*_{turb} \cdot \omega^*_{turb}}\right)_{ch} \cdot \left(\frac{\dot{m}^*_{turb} \cdot \omega^*_{turb}}{\pi_{turb}}\right) - 1 \tag{2.14}$$

In this equation, the mass flow rate and expansion ratio are needed at choking conditions, and the equation has to be solved iteratively.

The model developed by Fang et al. [54] depends on four parameters per VGT position, and supposes that all the curves for different speeds collapse, and gives better results than the previous models:

$$\dot{m}^*_{turb} = k_1 + k_2 \cdot \mathrm{e}^{k_3 \cdot \omega \cdot (\pi_{turb} - 1)} \tag{2.15}$$

while the turbine efficiency model was presented a year later in [55], using a turbine efficiency defined as the turbine power output divided by the isentropic turbine power output:

$$\eta_{turb} = k_1 + \frac{\ln \pi_{turb}}{\frac{\gamma - 1}{\gamma}} \cdot \left(k_2 + k_3 \cdot \sigma_{turb} + k_4 \cdot \sigma^2_{turb}\right) \tag{2.16}$$

Again, the parameters change when changing the VGT position. These correlations showed good results at performance prediction for control models, where computational speed is critical.

A method that is currently used by a large fraction of the engine industry is that of GT-Power™, which relates the reduced mass flow rate with the blade speed ratio σ_{turb} and four parameters:

$$\dot{m}^*_{turb} = k_1 \cdot \left[k_2 + (1-k_2) \cdot (k_3 \cdot \sigma_{turb})^{k_4} \right] \tag{2.17}$$

where k_1 is the mass flow rate parameter at maximum efficiency, k_2 is the reduced mass flow rate at a blade speed ratio equal to zero, k_3 is the inverse of the blade speed ratio at maximum efficiency and k_4 is an adjusting parameter that ranges from 2 to 4. Turbine efficiency is modelled as:

$$\eta_{turb} = \eta_{turb,max} \cdot \left[1 - (1 - k_3 \cdot \sigma_{turb})^{k_5} \right] \tag{2.18}$$

where k_5 varies between 1.4 and 2.2.

Other authors model the turbine using a single equivalent nozzle element, varying its geometry depending on the operating point. This approach can be found in [60], and although it gave good results for small expansion ratios, the equivalent nozzle became choked at high expansion ratios typical of radial turbines. An enhancement from this model can be found in the works by Payri et al. [61], [62], where the turbine is modelled using two nozzles in series, connected by an internal plenum. The first nozzle represented the stator, while the second nozzle represented the rotor, and their effective areas were obtained by supposing that half the expansion happened in the stator and the other half in the rotor. Although this model showed good results for interpolating the mass flow rate, it had some limitations, as in reality the rotor can't be modelled as an ideal nozzle as the energy is not conserved inside it, as it is extracting power from the air.

Jensen et al. [63] models the turbine as a single ideal nozzle, but uses a correlation to modify its effective throat section A_{eff}:

$$\dot{m}^*_{turb} = A_{eff} \cdot \pi_{turb}^{\frac{-1}{\gamma}} \cdot \sqrt{\frac{2 \cdot \gamma}{R \cdot (\gamma - 1) \cdot \left(1 - \pi_{turb}^{\frac{1-\gamma}{\gamma}} \right)}} \tag{2.19}$$

$$A_{eff} = k_1 + k_2 \cdot \pi_{turb} + k_3 \cdot \omega^*_{turb} + k_4 \cdot \pi_{turb} \cdot \omega^*_{turb} \tag{2.20}$$

Also, when the expansion ratio is bigger than the one that produces sonic flow in the nozzle throat, the mass flow parameter is maintained equal to that

at choking conditions. They also propose a semi-empirical model for turbine efficiency:

$$\eta_{turb} = k_1 + k_2 \cdot \omega^*_{turb} + \left(k_3 + k_4 \cdot \omega^*_{turb}\right) \cdot \sigma_{turb} + \left(k_5 + k_6 \cdot \omega^*_{turb}\right) \cdot \sigma^2_{turb} \tag{2.21}$$

A similar approach is found in the work by Canova [64], [65], but with a constant effective section A_{eff} and a polytropic coefficient n smaller than γ:

$$\dot{m}^*_{turb} = A_{eff} \cdot \pi_{turb}^{\frac{-1}{n}} \cdot \sqrt{\frac{2 \cdot \gamma}{R \cdot (\gamma - 1) \cdot \left(1 - \pi_{turb}^{\frac{1-n}{n}}\right)}} \tag{2.22}$$

These two coefficients are obtained by least-square fitting experimental data.

Other correlation for A_{eff} for Equation 2.19 is presented by Serrano et al. [66], supposing a linear trend between this effective area and the blade speed ratio σ_{turb}:

$$A_{eff} = k_1 + k_2 \cdot \sigma_{turb} \tag{2.23}$$

A set of parameters is obtained for each iso-speed line, as well as for each position of the vanes when working with VGTs.

Serrano et al. [31] propose a two-nozzle model, each one solved using Equation 2.19, with an intermediary plenum. The effective area of each nozzle was computed using semi-empirical correlations, and the VGT position was taken into account.

A further development of the two-nozzles model is presented in the Ph.D. dissertation by Reyes-Belmonte [18]. The proposed model uses two expansions in series to compute an equivalent one-nozzle effective section:

$$A_{eff} = \frac{A_{st} \cdot \sqrt{1 + k_1 + \sigma^2 \cdot \left[\left(\frac{r_{rt,out}}{r_{rt,in}}\right)^2 - 1\right]}}{\sqrt{1 + \left(\frac{A_{rt}}{A_{st}}\right)^2 \cdot \left\{\frac{k_2 \cdot IER}{1 - \eta_{turb} \cdot \left[1 - (k_2 \cdot IER)^{\frac{\gamma-1}{\gamma}}\right]}\right\}^2}} \tag{2.24}$$

$$IER = \frac{2}{\pi_{turb} + 1} \tag{2.25}$$

$$k_1 = \left(\frac{u_{st} \cdot \sin \alpha_3}{u_s}\right)^2 + \left(\frac{w_3}{u_s}\right)^2 \tag{2.26}$$

where the definition of the different speeds is shown in Figure 2.1. k_1, k_2, A_{st} (stator throat area) and A_{rt} (rotor outlet throat area) are fitted for each VGT position.

The turbine efficiency is computed assuming conservation of rothalpy. Using the speed, radius and angle definitions seen in Figure 2.1:

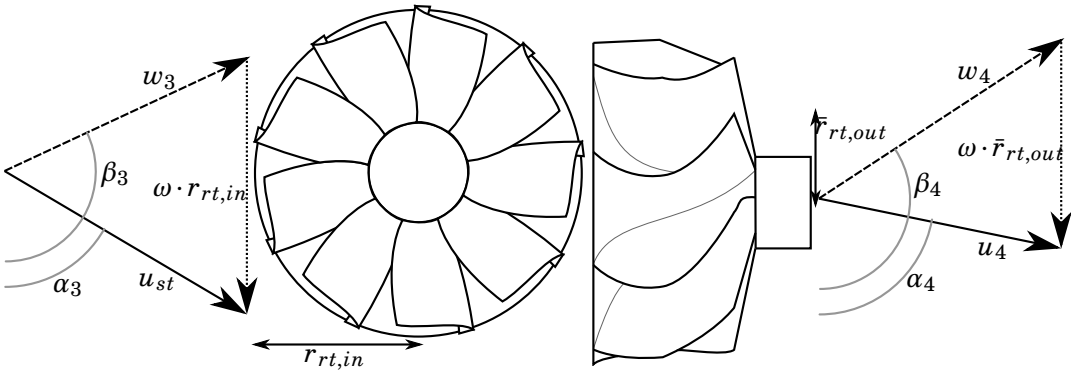

Figure 2.1: Rotor velocity triangles

$$\begin{aligned}\eta_{turb} &= \frac{-\left(\omega \cdot \bar{r}_{rt,out}\right)^2 + \omega \cdot r_{rt,in} \cdot u_{st} \cdot \sin\alpha_3 \cdot \left[\operatorname{cotan}\alpha_3 + \left(\frac{\bar{r}_{rt,out}}{r_{rt,in}}\right) \cdot \left(-\operatorname{cotan}\beta_4\right)\right]}{\bar{c}_{p,turb} \cdot T_{0t} \cdot \left[1 - \left(\frac{p_6}{p_{0t}}\right)^{\frac{\gamma-1}{\gamma}}\right]} \\ &= -2 \cdot \left(\frac{\bar{r}_{rt,out}}{r_{rt,in}}\right)^2 \cdot \sigma_{turb}^2 + \frac{2 \cdot \left[\operatorname{cotan}\alpha_3 - \frac{\bar{r}_{rt,out}}{r_{rt,in}} \cdot \operatorname{cotan}\beta_4\right]}{u_s} \cdot u_{st} \cdot \sin\alpha_3 \cdot \sigma_{turb} \\ &= -k_3 \cdot \sigma^2 + k_4 \cdot \sigma \cdot \frac{u_s t \cdot \sin\alpha_3}{u_s}\end{aligned} \tag{2.27}$$

$$k_3 = 2 \cdot \left(\frac{\bar{r}_{rt,out}}{r_{rt,in}}\right)^2 \tag{2.28}$$

$$k_4 = 2 \cdot \left[\operatorname{cotan}\alpha_3 - \frac{\bar{r}_{rt,out}}{r_{rt,in}} \cdot \operatorname{cotan}\beta_4\right] \tag{2.29}$$

The rotor outlet axial speed has been supposed to be equal to the rotor inlet radial speed in Equation 2.27, and it is further simplified, supposing to be equal

to the mean flow speed at the volute tongue u_{tongue}, just before the air starts to leave the volute:

$$u_{st} \cdot \sin \alpha_3 \simeq \frac{\dot{m}_{turb} \cdot R \cdot T_{tongue}}{p_{tongue} \cdot A_{tongue}} \tag{2.30}$$

The rotor inlet absolute flow angle is supposed to maintain a linear relationship with the rotor blade speed ratio:

$$\alpha_3 = k_5 \cdot \sigma + k_6 \tag{2.31}$$

Finally, the rotor outlet angle is set to be equal to the metal angle. The expression in Equation 2.27 is further expressed in terms of nozzle effective area and turbine expansion ratio in his work, leading to a final equation that has the following form:

$$\eta_{turb} = -k_3 \cdot \sigma^2 + k_4 \cdot \sigma \cdot \frac{A_{eff}}{A_{tongue}} \cdot (\pi_{turb})^{\frac{-1}{\gamma}} \tag{2.32}$$

The parameters of the model (k_1, k_2, A_{st}, A_{rt}, k_5 and k_6) are fitted for each VGT position.

Other authors compute the turbine performance using several losses submodels that account for a power output reduction from the ideal one. The highly recommendable introductory book about turbomachinery by Japikse et al. [67] has a whole chapter about turbine losses modelling, describing techniques that can be seen as industry standards in meanline turbine modelling. Chiong et al. [68] use this approach, where the rotor power output is computed in several phases: first, a one-dimensional model is used to get the rotor inlet conditions (total pressure, total temperature, radial inlet speed), using a pressure drop boundary condition that produces the same mass flow rate as in experiments, and the rotor inlet flow angle is deduced from conservation of angular momentum in the flow that exits the volute; then, the ideal specific total enthalpy leap across the rotor is computed supposing adiabatic and isentropic flow; finally, four kinetic energy losses submodels are applied to reduce the ideal specific total enthalpy leap and thus obtain its final value. The losses submodels are due to non-ideal incidence at the rotor inlet, passage losses due to secondary flow, tip clearance recirculation losses and disk friction losses behind the rotor. The incidence losses model, popularly known as NASA shock losses model, is due to Futral et al. [69], and produces a kinetic energy loss L_{inc} that in its original form was expressed as:

$$L_{inc} = \frac{1}{2} \cdot \left[w_3 \cdot \cos\left(\beta_3 - \beta_{opt}\right) \right]^2 \tag{2.33}$$

where β_{opt} is the optimum incidence angle. This model supposes that the kinetic energy associated to the flow component normal to a given ideal incidence angle can't be extracted from the flow to produce useful power. A modified version by Mizumachi et al. [70] was used:

$$\begin{gathered} L_{inc} = \frac{k_{loss,inc}}{2} \cdot \left[w_3 \cdot \cos\left(\beta_3 - \beta_{opt}\right) \right]^2 \\ if\ \left(\beta_3 - \beta_{opt}\right) < \frac{\pi}{4} \\ L_{inc} = \frac{k_{loss,inc}}{2} \cdot w_3^2 \cdot \left(0.5 + \left| \beta_3 - \beta_{opt} \right| - \frac{\pi}{4} \right) \\ if\ \left(\beta_3 - \beta_{opt}\right) > \frac{\pi}{4} \end{gathered} \tag{2.34}$$

In this case however, some of the physical meaning of the losses mechanism is lost.

The second losses submodel is proportional to the mean kinetic energy of the flow inside the rotor passage, without the flow component that was subtracted with the previous submodel [71]:

$$L_{psg} = \frac{k_{loss,psg}}{2} \cdot \left\{ \left[w_3 \cdot \sin\left(\beta_3 - \beta_{opt}\right) \right]^2 + w_4^2 \right\} \tag{2.35}$$

Finally, tip clearance recirculation losses and rotor friction losses are modelled as in [72]:

$$L_{cl} = \frac{2 \cdot \Delta h_{3,4s} \cdot \dfrac{h_{cl}}{2 \cdot r_{4,max}}}{1 - \left(\dfrac{r_{4,min}}{r_{4,max}} \right)} \tag{2.36}$$

where h_{cl} is the tip clearance and $\Delta h_{3,4}$ is the enthalpy ideal leap between rotor inlet and outlet.

$$L_{df} = \frac{0.02125 \cdot \omega^2 \cdot r_3^2 \cdot \rho_3^2}{\dot{m}_{turb} \cdot \left(\rho_3 \cdot \omega \cdot r_3^2 / \mu_{air} \right)^{0.2}} \tag{2.37}$$

The enthalpy leap is then computed as:

$$\Delta h_{3,4} = \Delta h_{3,4s} - L_{inc} - L_{psg} - L_{cl} - L_{df} \tag{2.38}$$

This approach is used in other works, such as in [34]. Romagnoli et al. [33] also models other losses mechanisms such as losses in the volute and the stator

nozzles, as well as flow deviations and blockage factors (equivalent to discharge coefficients):

$$p_{1t} - p_{2t} = k_{loss,psg,vol} \cdot (p_{2t} - p_2) \tag{2.39}$$

$$u_{tongue,\theta} \cdot r_{tongue} = k_{\theta,vol} \cdot u_{2,\theta} \cdot r_2 \tag{2.40}$$

$$\dot{m}_{turb} = \rho_2 \cdot A_2 \cdot C_D \cdot u_{2,r} \tag{2.41}$$

$$p_{2t} - p_{3t} = k_{loss,psg,st} \cdot \rho_3 \cdot u_3^2 \tag{2.42}$$

$$\alpha_3 = \alpha_{st,metal} + \cos^{-1} \frac{l_{st,th}}{l_{st,te}} \tag{2.43}$$

$$u_{\theta,3} = \left(1 - k_{st,cl}\right) \cdot u_{\theta,3} + k_{st,cl} \cdot u_{\theta,3,cl} \tag{2.44}$$

where $k_{loss,psg,vol}$ is a constant, $k_{loss,psg,st}$ is a function of the Reynolds number in the stator nozzles, $k_{\theta,vol}$ is also a constant, $\alpha_{st,metal}$ is the angle formed by the vanes, $l_{st,th}$ is the length of the stator throat, $l_{st,te}$ is the circumferential distance between two blades at the trailing edge, $k_{st,cl}$ is the fraction of mass flow rate that goes through the stator clearance and $u_{\theta,3,cl}$ is the tangential speed at the stator clearance, that can be estimated supposing angular momentum conservation. The rotor is supposed to perform ideal guiding of the flow, so $\beta_4 = \beta_{4,metal}$. The model is solved iteratively until the mass flow rate is the same at the stator inlet and outlet and at the rotor outlet.

A comprehensive study of several losses prediction methods for 1D turbine models is found in Dahlquist's MSc thesis [73], but it was done for axial turbines. He used an interesting approach, however, that will be used in the present work: as it is simpler to measure total pressure losses in a gas stand, he proposed to relate the losses models to those total pressure losses instead of to a reduced enthalpy leaps.

More advanced losses models are found in the literature, as in the works by Benner et al. [74] and Benner et al. [75], in which a linear cascade to get pressure loss data and a better secondary losses model is obtained taking into account the spanwise flow behaviour differences. This model, however, is obtained for an axial linear cascade, and more work is needed to adapt it to radial turbines.

A similar approach as in [33] is used in this work, but using total pressure losses not only in the stator but also in the rotor, as in [73]. The rotor inlet angle is estimated using a bidimensional potential model instead of using a correlation, using a fast boundary elements model (BEM) as described in classic aerodynamic tests, such as the one by Katz et al. [76].

Unsteady models

The most simple proposals use steady-state models with some correction, and only compute the mean turbine performance. The correction factors reduce the steady-state turbine performance, as experimental studies show these reductions [26]. The most simple correction is as follows:

$$\frac{\eta_{turb,puls}}{\eta_{turb,steady}} = k_1 + k_2 \cdot \frac{p_{max} - p_{min}}{\bar{p}} \cdot \omega \tag{2.45}$$

where p_{max} is the maximum pressure, p_{min} the minimum pressure and $\bar{p}$ the mean pressure. The coefficients have to be adjusted to each engine.

Payri et al. [77] encountered that, for a VGT, there wasn't a simple linear correlation, possibly due to the presence of the stator vanes. Torregrosa et al. [78] proposed a more complex correction factor that takes into account the pulse frequency f and amplitude $p_{max} - p_{min}$, as well as the VGT position α:

$$\frac{\eta_{turb,puls}}{\eta_{turb,steady}} = k_1 + k_2 \cdot \alpha + k_3 \cdot \omega + k_4 \cdot \frac{p_{max} - p_{min}}{p_{max} - p_{amb}} + k_5 \cdot (p_{max} - p_{min}) + k_6 \cdot f \tag{2.46}$$

The set of parameters have to be adjusted for each turbine [77].

A more complex approach uses filling and emptying models attached to the steady-state turbine model. These 0-D models can predict the flow characteristics at low engine regimes and pulse frequencies, when wave effects are small and the main effects are due to mass and energy accumulation in the volute, as shown in [62] and [79]. At higher engines regimes and pulse frequencies, however, wave effects become important and 0-D models fall sort in accuracy.

To overcome the limitations of 0-D models while still providing fast simulation speeds, one-dimensional codes are used. In these codes, the main wave-action effects are supposed to happen in the volute, as it is the larger element of the turbine, just as is observed in CFD simulations [3].

Several paradigms can be used to simulate one-dimensional ducts, such as finite-differences, finite-volumes or spectral methods. The most used methods in one-dimensional engine simulation are, probably, finite-differences and finite-volumes. A comprehensive description of one-dimensional solvers based on finite-differences and finite-volumes can be found in [80], and more detailed aspects of the methods can be found in more specific books such as [81] (with a special chapter about solving hyperbolic equations with finite-differences methods) and [82] (focused on finite volumes).

In one-dimensional codes, the volute is solved as an equivalent one-dimensional duct of a given length and area distribution, what can be called a classical one-dimensional volute model. The main philosophy behind these models is shown in [83], where the volute is modelled using two tapered pipes. The first

tapered pipe represents the turbine inlet duct, from the very beginning of the turbine to the volute tongue, with a length, inlet diameter and outlet diameter equal to the real ones. The second duct had a length equal to the length of the volute from the tongue to a point at 180°, passing through the central point of each section, setting the duct area to get the correct volute volume. This length selection was done supposing that half the mass flow enters the rotor at this point.

Abidat et al. [30] refined the method developed by Chen et al. [83], setting the volute outlet area to that at the mean volute section, using a linear variation from the tongue to the exit node.

Costall et al. [32] used constant section ducts, with the same volume as the real volute and stator volume, and a length equal to the real length from the turbine inlet to a point 180° from the volute tongue. This one-dimensional volute was connected to a punctual rotor model. The length of the simplified volute was supposed to depend on mass flow consumption criteria, but as the distribution of mass flow at the volute outlet window is unknown, it would be much harder to implement.

More complex models connect some or all of the volute channels to the rotor. Chiong et al. [84] present a model where the volute is simulated as a one-dimensional duct of the full length and area law than the real volute, with three sections connected to a common exit set to ambient boundary conditions. These three sections are placed at 90° from the volute tongue, at 180° and at 270°. The volute end is modelled as a closed end. During pulsating flow, the duct is computed using an adiabatic pressure loss boundary downstream of the common exit. This pressure loss boundary condition is set to get the same mean swallowing capacity for the one-dimensional ducts as the measured one at that turbine speed. The results of the one-dimensional simulation are saved and used as an input for a mean-line model of the rotor, using the flow characteristics at the three aforementioned sections as inputs for the rotor after averaging them. The rotor model is used to compute the power output, and uses four different losses submodels. The results of the model are compared with experimental data, showing a good level of agreement. The results are also compared to a quasi-steady simulation, showing better reproduction of the experimental data than with the one-dimensional model.

Hu [85] and King [86] present a turbine model where the stator and rotor channels are also computed using a one-dimensional method. The volute is simulated as a one-dimensional duct with a length and a section distribution equal to that of the real volute. The inlet of each one-dimensional stator channel is connected to the volute, interpolating its inlet values with the results of several volute cells. The rotor passages are modelled with axial and radial components, and its flow evolution is solved in its relative reference frame, while the rest of the turbine is solved using an inertial reference frame. Non-ideal

behaviour is computed using source terms in the rotor. This approach, although potentially more accurate than the others, have several problems. First, it is not easy to relate turbine losses to the source terms used in this method. Second, perfect stator guiding is supposed, which leads to problems when computing vaneless turbines or when stator outlet flow deviation can't be neglected. Finally, it has inherently higher computational costs than the other methods, while some of the accuracy advantages are questionable, as it has been shown than the rotor can be supposed to behave in a quasi-steady manner.

Bellis et al. [87] present an interesting approach: first, the turbine is solved under steady-state conditions using five one-dimensional ducts: the turbine inlet, the volute, the stator, the rotor and the turbine outlet. The rotor duct is solved including inertial forces as source terms, as well as general losses source terms. The steady-state one-dimensional equations are solved and a wheel extended map is obtained. The volute is computed as an equivalent tapered pipe, as well as the stator. After obtaining the wheel extended map, the unsteady simulations are carried out using a constant section pipe for the turbine inlet, a tapered pipe of a given length for the volute, a pipe with the same length and volume as the rotor ducts and a constant section duct for the rotor. No information is given about the details of the volute, but is presumed to have a geometry as in [83]. Their results are compared with that of using a classical volute as in [32] connected to the real turbine map, and they show better accuracy at predicting experimental data. This accuracy improvement is assumed to be due to their use of a wheel-only map instead of a general turbine map, as well as to their use of a duct for rotor accumulation and wave effects. However, other researchers tend to suppose a very small contribution of the rotor to the turbine overall accumulation and wave effects, so their improvements may be mainly produced by their use of a wheel map.

Chiong et al. [34] use the same losses models described in [68], solving in parallel the one-dimensional ducts to get the instantaneous mass flow rate evolution and to feed with data the meanline model to compute the turbine power output. Again, a pressure drop boundary condition is used to get the same mass flow rate as the experimental average value, and four ducts are connected at four points of the volute, computing it in a quasi-bidimensional manner. The rotor speed evolution is also computed at each time-step, modifying the braking torque applied to the rotor wheel if its acceleration exceeds a predefined threshold. An investigation of the number of rotor entries is performed, finding an optimum value at four rotor entries.

2.3 Mechanical losses

During turbocharger operation, some of the power produced by the turbine is dissipated instead of integrally transmitted to the compressor. These mechanical losses are produced in the bearings placed at the shaft due to viscous stresses inside the thin oil film. Small automotive turbochargers usually have two sets of radial journal bearings, as well as a thrust bearings near the compressor wheel that damps the axial movement due to force unbalances between the turbine and the compressor rotors. The power dissipation inside the bearings can become a considerable fraction of the total turbine power output at low rotational speeds and low oil temperatures [88].

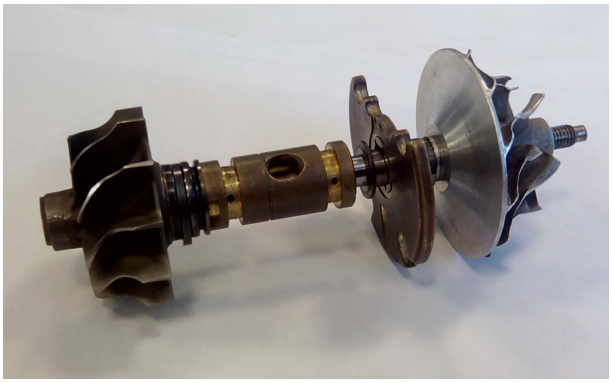

Figure 2.2: Turbocharger bearings. The radial bearings are visible as well as the axial bearing washers. The oil seals are also present

Large turbochargers, on the other hand, use other kind of bearings, such as multi-lobed bearings with and without squeeze film dampers, as described in [89], and they won't be studied in the present work.

Turbocharger mechanical losses are usually used in one-dimensional engine simulation codes as a multiplier of the turbine power output, a mechanical efficiency. This mechanical efficiency η_{mech} is defined as the ratio between the compressor power $\dot{W}_{comp}$ and the turbine power $\dot{W}_{turb}$, and can also be expressed in terms of the mechanical losses power $\dot{W}_{ml}$

$$\eta_{mech} = \frac{\dot{W}_{comp}}{\dot{W}_{turb}} = \frac{W_{turb} - W_{ml}}{W_{turb}} \tag{2.47}$$

This information is not usually available using only manufacturer's maps and has to be measured independently in a turbocharger gas stand. Manufacturer's maps usually collapse all the related information about the power generation, transmission and consumption in a global turbocharger efficiency,

η_{global}, in which heat transfer effects may even be present, using the compressor power and the isentropic turbine power output $\dot{W}_{turb,s}$

$$\eta_{global} = \frac{\dot{W}_{comp}}{\dot{W}_{turb,s}} \tag{2.48}$$

This data is obtained in the manufacturer's gas stand, using hot oil and hot air flow, so it is affected by heat transfer and the oil viscosity has a small value not representative of urban driving conditions during the engine warm-up phase, as seen in the work by Deligant et al. [90]. When simulating the turbocharger with other oil temperatures, engine designers have to use a correction factor for η_{global} or, in the case that it is available, for η_{mech}. It is also a typical assumption to use a value of $\eta_{mech} = 90\,\%$ as a general approximation.

Experimental characterisation

Mechanical losses play an essential role in automotive turbochargers performance at low speeds and during engine warm-up, but are difficult to determine experimentally as very sensitive transducers are needed and the high rotational speed of the shaft. There are two different approximations for measuring mechanical losses: direct and indirect measuring. Direct measuring is done by means of torquemeters, and indirect measuring can be achieved using precision temperature measurements.

Direct measurement

Direct measurement can give the most accurate results for turbocharger mechanical losses. It is done using a torquemeter between the turbine wheel and the bearings, or between a driving rotor and the bearings if the wheel is removed. The main drawbacks of this technique are that the high rotational speeds of the shaft difficult the measurements for points typical of medium to high engine loads, and that the turbocharger have to be profoundly modified in order to be coupled with the torquemeter. The small size of automotive turbochargers complicate the shaft balancing, critical due to its high rotational speeds even at medium equivalent engine loads.

Deligant et al. [90] carried out experiments using a torquemeter placed between the turbine wheel and the rest of the turbocharger. The torquemeter was able to measure at up to 120 krpm. They used the turbine to drive the compressor and used different oil temperatures and pressures during the experiments. They found that the mechanical losses were very important at low rotational speeds, reducing in a non-negligible amount the available power at the compressor side and thus rising pumping losses in the engine. Podevin et al. [91] obtained more experimental results with the same experimental arrangement,

designing a method to better characterise the compressor behaviour under low rotational speeds. Again, mechanical losses were found to play an important role in the turbocharger performance at low rotational speeds typical of urban driving conditions, Deligant et al. [92], [93] modified the experimental arrangement and placed a magnetic axial load, thus being able to control the axial thrust. The turbocharger was tested at 50 krpm, 70 krpm and 90 krpm and low temperatures were used for the oil. It was found that, as the oil mass flow rate increases, the mechanical losses rise due to lower oil temperatures inside the bearings and, thus, higher viscosities. Several axial loads were tested, confirming an increase in power dissipation when applying higher forces: as expected the mechanical losses in the thrust bearing were not negligible, and small but clearly measurable changes in global mechanical losses are produced by changes in axial forces in the shaft. They also removed the axial bearing, thus being able to decouple the radial and the axial bearing contribution to the total mechanical losses. More authors have used a similar technique, using a torquemeter and a magnetic axial load and have found similar results, such as Schmitt et al. [94]. Gjika et al. [95] measure the axial load in a small turbocharger using extensometers placed in the thrust bearing fixed washer: although this technique for axial thrust measurement is easily implemented, it wasn't used in the present work in order to perform the least intrusive measurements.

Initially, measurement of mechanical losses by means of a torquemeter was considered, but the problems associated to it (very problematic shaft balancing, non-viable measurements at rotational speeds higher than 120 krpm at the time of the beginning of this research) led to discard it in favour of indirect measurement.

Indirect measurement

Indirect measurements don't need modifications in the turbocharger body, but are also of lower precision than direct measurements. They can, however, be used at high rotational speeds.

Power difference between compressor and turbine This is probably the most easy to perform, as it only needs a standard turbocharger gas stand capable of measuring turbine and compressor mass flow rates and turbine and compressor inlet and outlet pressures and temperatures. Mechanical losses power $\dot{W}_{ml}$ is obtained subtracting the compressor power $\dot{W}_{comp}$ to the turbine power $\dot{W}_{turb}$, all under steady-state conditions:

$$\dot{W}_{ml} = \dot{W}_{turb} - \dot{W}_{comp} \tag{2.49}$$

Turbine and compressor power can be evaluated using total enthalpy flows if the heat flow is known or negligible:

$$\begin{aligned}\dot{W}_{ml} \simeq & \dot{m}_{turb} \cdot \bar{c}_{p,turb} \cdot \left(T_{turb,t,in} - T_{turb,t,out}\right) \\ & - \dot{m}_{comp} \cdot \bar{c}_{p,comp} \cdot \left(T_{comp,t,out} - T_{comp,t,in}\right) - \dot{Q}_{turb} + \dot{Q}_{comp}\end{aligned} \tag{2.50}$$

where $\bar{c}_p$ is the mean specific heat capacity, $turb$ indicates turbine side, $comp$ indicates compressor side, t indicates total conditions and $\dot{Q}$ is heat flow. This method presents problems due to the uncertainty of the temperature measurement if the flow is not properly developed and due to the estimation of heat flows. The measurements have to be done with thermal insulation in the ducts and the turbocharger, and the temperatures of the compressor outlet, turbine inlet and central housing have to be kept as similar as possible to reduce the uncertainties due to heat flow.

If the compressor wheel is retired, the estimated turbine power output is a direct approximation of the mechanical power losses. There is still a small term, however, due to air whipping in the compressor side, as the shaft is still in contact with air.

When measuring low turbine power points, temperature differences become small enough to get unacceptable mechanical losses uncertainties, so other techniques were investigated.

Free deceleration test This method is done by maintaining the turbocharger running at a constant speed until stabilisation, and then cutting the air feeding at the turbine inlet and accurately measuring the rotational speed ω while the shaft decelerates. The moment of inertia of the shaft and turbine wheel $\boldsymbol{I}$ have to be known to make this test, and the compressor wheel needs to be retired from the shaft:

$$\dot{W}_{ml} = -\boldsymbol{I} \cdot \frac{\mathrm{d}\omega}{\mathrm{d}t} \cdot \omega \tag{2.51}$$

Again, air whipping at the compressor side still affects the results, but also at the turbine side as the rotor is still moving the air even if the turbine mass flow rate is zero. The technical difficulties in reducing instantaneously the turbine mass flow rate to zero make this technique seldom used and the respondent haven't found any source of its use in small automotive turbochargers, but it is a standard technique to get mechanical losses in other types of rotating machinery. It was discarded.

Oil total energy change In this case, oil mass flow rate $\dot{m}_{oil}$, temperatures and pressures have to be measured in the gas stand.

$$\dot{W}_{ml} \simeq \dot{m}_{oil} \cdot \left[\bar{c}_{oil} \cdot \left(T_{oil,out} - T_{oil,in} \right) - \Delta x \cdot g + \frac{u_{oil,out}^2 - u_{oil,in}^2}{2} + \frac{p_{oil,out} - p_{oil,in}}{\bar{\rho}_{oil}} \right] - \dot{Q}_{oil} \tag{2.52}$$

where $\bar{c}_{oil}$ is the mean specific heat capacity of the oil during the process, T_{oil} is its temperature, Δx is the distance between the measurement points, g is the modulus of the gravitational field at the turbocharger (i.e., the gravitational acceleration), u_{oil} its flow speed, p_{oil} is the oil pressure, $\bar{\rho}_{oil}$ is the mean oil density, in refers to inlet conditions, out to outlet conditions and $\dot{Q}_{oil}$ is the heat flow to the oil. The terms due to flow speed can be computed if the duct sections are known, but they are usually neglected, as well as the terms due to pressure drop and gravity:

$$\dot{W}_{ml} \simeq \dot{m}_{oil} \cdot \bar{c}_{oil} \cdot \left(T_{oil,out} - T_{oil,in} \right) - \dot{Q}_{oil} \tag{2.53}$$

The heat flow has to be kept as small as possible, and it should be estimated to correct the experimental results. Heat transfer correction can be made as shown in [96].

Again, if the temperature rise in the oil is too small, the mechanical losses estimation becomes invalid due to high uncertainties. This can happen at very low rotational speeds or too high oil inlet temperatures and, thus, very low oil viscosities. If the oil mass flow rate is very high, the temperature rise may also decrease to impermissible levels for mechanical losses estimation. The problem seams to be of less importance than when estimating the mechanical losses as a difference between the turbine and compressor power as only one temperature difference has to be measured, and high precision temperature sensors can be easily placed in the oil line as the temperature is not as high as in the turbine side, which may reduce their accuracy. This method is successfully used by turbocharger researchers, as seen by Payri et al. [38], or in Sjöber's MSc thesis [97]. The latter not only measured the mechanical losses, but also measured axial displacements and estimated the axial load. The research institute where the respondent was developing this work had experience using this method, so it seemed the most plausible.

CFD characterisation and modelling

CFD studies are used to complete the information obtained by means of experiments. These simulations are done under low Reynolds number flow, and

sometimes are computed using totally laminar flow and other times a special turbulence model for low Reynolds number is used.

Deligant et al. [98] model the radial bearing in 3D, performing several simulations modifying the rotational speed of the shaft and the oil inlet pressure, using both isothermal and thermal calculations (i.e., simulations where the oil temperature is kept constant and where the oil is heated up due to friction) and maintaining laminar flow. No cavitating flow was assumed. The results from isothermal simulations overestimate the friction losses as the viscosity is kept too high, so they are discarded. The frictional torque is found to have relatively small variations for different rotating speeds when the oil temperature evolution is taken into account, what results in an almost linear relationship between the mechanical losses power and the shaft speed for a given oil inlet temperature, but it separates from the linear trend at low oil inlet temperatures. Oil inlet temperature affects to a high degree the simulated results, what is consistent with the oil viscosity behaviour. Variations of oil inlet pressure produced only small variations in oil mass flow rate and dissipated power, probably due to the simplified geometry of the problem. Another interesting result is that the influence of the eccentricity in the dissipated power is very small, so it may be discarded when developing a simplified model. Finally, they compared the CFD simulations with experimental results: while the general tendency is kept, there are some deficiencies in the model and in the experimental results. First, external heat transfer is not measured and the experimental data may be affected by it, while the CFD results don't model heat flows. Also, only the journal bearing is simulated and the thrust bearing power losses are not computed.

Turbulent flow inside bearings can be computed using several models, such as the ones described by Bouard et al. [99] for tilting-pad journal bearings. They found that the influence of turbulent flow at high rotational speeds is not negligible in these kind of bearings, and thus should be taken into account during simulations. For small turbocharger bearings, however, the influence of turbulent flow should be smaller. Maneshian et al. [100] present simulations for journal bearings (although not turbocharger journal bearings) with two different turbulence models, one for very low Reynolds number (low-Reynolds $k-\epsilon$) and another one for more turbulent flows (AKN Low-Reynolds $k-\epsilon$). They validate their results with experimental pressure and temperature data, obtaining a good level of correlation. It is mentioned that turbulent flow may be present in journal bearings under very low viscosity conditions and in zones with very big clearances, which rarely apply to turbocharger bearings.

CFD models can be used to characterise not only the mechanical losses, but also other effects such as the rotordynamics of the shaft. Huiping et al. [101] coupled CFD simulations of the oil inside journal bearings with the elastic deformation of the shaft, taking into account oil cavitation. With these kind

of models, more accurate results may be obtained in cases with a high level of cavitation, as the cavitation zone extension depends on the exact eccentricity of the shaft and elastic deformations have an important role in the shaft final position. Flow cavitation, when present, affects the dissipated power in the oil. Lihua et al. [102] performed CFD simulations of oil film bearings with fluid-structure interaction, and found a high influence of the oil pressure and temperature in the static stiffness, what may affect the final position of the shaft and possibly induce cavitation.

Although a carefully performed CFD simulation campaign would have provided valuable information, it wasn't possible to carry it out during the production of this document, and is recommended for future works.

Fast models

Fast models are needed to compute mechanical losses coupled with one-dimensional engine simulation codes. They fall into two categories: semi-empirical models and first-principles-based models.

An example of an empirical model for mechanical losses determination can be found in the work by Payri et al. [38]. In this work, the dependency between the mechanical losses and some dimensionless numbers is shown. These dimensionless numbers are the oil flow Reynolds number, the Prandtl number and a dimensionless pressure difference, which expression was based on the work of Hu et al. [103]. The last contribution define the axial thrust in the turbocharger as the pressure difference between the end of the compressor impeller and the turbine backplate, which is related to the outlet of the compressor rotor and the inlet of the turbine rotor. This model was developed using a wide experimental campaign of a turbocharger under quasi-adiabatic steady-state flow conditions. The experiments were performed in the low-speed region to ensure quasi-adiabaticity, and different oil temperatures and pressures were used: 60 °C, 70 °C, 80 °C and 90 °C and 200 kPa, 300 kPa and 400 kPa. The study first correlated the mechanical losses with a Reynolds number Re:

$$Re = \frac{\rho_{oil} \cdot \omega \cdot R \cdot h_{jb}}{\mu_{oil}} \tag{2.54}$$

where ρ_{oil} is the density of the oil at the inlet temperature, ω is the shaft rotational speed, R is the shaft radius, h_{jb} is the clearance between the shaft and the internal face of the journal bearing and μ_{oil} is the oil dynamic viscosity at the inlet temperature. After representing mechanical efficiency versus the Reynolds number, it was observed a clear grouping by oil inlet temperatures.

The Prandtl number Pr was used to account for this grouping:

$$Pr = \frac{\mu_{oil}}{\rho_{oil} \cdot \alpha_{oil}} \tag{2.55}$$

where α_{oil} is the thermal diffusivity of the oil at the inlet temperature.

Finally, the effects of the axial thrust in the mechanical efficiency are computed using a special pressure ratio $\Delta p/p$. According to Hu et al. [103], axial thrust in small turbochargers is mostly determined by the static pressure difference between the compressor impeller and the turbine back plate. As these pressures are generally unknown, they are taken into account using the turbine inlet pressure p_3 and the compressor inlet and outlet pressures (p_1 and p_2). The oil inlet pressure $p_{oil,in}$ was also used in this parameter:

$$\frac{\Delta p}{p} = \frac{p_{oil,in} - \left(p_3 - \frac{p_1+p_2}{2}\right)}{p_{oil,in}} \tag{2.56}$$

The final correlation used exponential dependencies since mechanical efficiencies lie between 0 and 1, and contained 6 adjusting parameters:

$$\eta_{mech} = k_1 \cdot \left[1 - \mathrm{e}^{-k_2 \cdot Re^{k_3} \cdot Pr^{k_4}}\right] + (1 - k_1) \cdot \left[1 - \mathrm{e}^{-k_5 \cdot \left(\frac{\Delta p}{p}\right)^{k_6}}\right] \tag{2.57}$$

The coefficients k_1 to k_6 were obtained using least squares fitting with experimental data, and good agreement between the measured and modelled mechanical efficiency was obtained. Although this method proved to produce acceptable results, it was suggested that the actual variable that should be modelled was the power dissipation, not the mechanical efficiency, as a given set of conditions should produce the same mechanical power losses in the bearings regardless of the turbine power output.

First-principles-based models usually part from the generalised Reynolds equation [104], and are used to compute the mechanical losses power in journal bearings. The Reynolds equation is solved for different values of the eccentricity ratio and slenderness ratio of the bearing. A result derived from the generalised Reynolds equation correlates the friction in the bearings (and, thus, the dissipated power) when no cavitation occurs and a bearing characteristic number called the Sommerfield number (S):

$$S = \left(\frac{R}{h_{jb}}\right)^2 \frac{\mu_{oil} \cdot \omega}{P} \tag{2.58}$$

where P is the load per unit of projected bearing area. The results are usually obtained for large bearings. Large bearings spin at a low speed, typically less than 10 krpm, and carry loads as high as 50 kN, while small turbocharger bearings are prepared to spin at even more than 200 krpm and carry loads of a

couple of N. This leads to values of the Sommerfield number that are too high for turbocharger bearings, and the computed power using this method is usually overestimated. Other of the limitations of the solution of the Reynolds equation using Sommerfield's approximation is that it doesn't consider cavitation.

An improvement over the estimation using the generalised Reynolds equation is described in [105], where a finite-differences approach is used to compute the flow inside the journal bearing and the dissipated power is computed. The results overestimate the experimental mechanical losses, however, as the oil evolution is assumed to be isothermal and its viscosity is therefore too high during the flow inside the bearings, instead of reducing its viscosity as it heats up due to friction. A better solution would require to model the temperature variation of the oil. This approximation presents two main drawbacks, however: it doesn't compute the effects of the thrust bearing and the modifications in the dissipated power due to variations in the axial force in the shaft; the computational cost of the method, while still low, is higher than that of a lumped model such as one obtained using a semi-empirical correlation.

More recently, Hung coupled the Reynolds equation with a finite-elements model of the shaft to compute its rotordynamic behaviour. He solved the Reynolds equation taking into account oil cavitation, with a low pressure in the cavitation zone of the bearing. Although his results were used for rotordynamics predictions, they can be used also for mechanical losses computation. Again, the computational cost is higher than with a semi-empirical correlation, this time due to the computation of the shaft deformation.

A fast and reliable lumped model to compute the power dissipation in both the journal and the thrust bearing of small turbochargers wasn't found in the literature, so a first-principles based one was proposed for this work.

2.4 Heat transfer

Although no heat transfer model development has been done for this work, it has to be estimated to get proper experimental results for the development of both mechanical losses and steady-state turbine submodels. Heat transfer effects are usually neglected in large turbomachinery, but have to be taken into account for small automotive turbochargers, mainly during urban driving conditions and turbocharger warm-up, as shown in the works by Shaaban [106], [107], Podevin et al. [108] and Baines et al. [109].

Manufacturer's data are not enough to characterise heat flow inside turbochargers, and thus a specific experimental characterisation has to be done. As the internal heat transfer can't be directly measured, some assumptions have to be done in order to estimate it.

Experimental characterisation and simple modelling

Probably, the most common techniques to characterise heat flow in automotive turbochargers are performed by means of thermal imaging and by using thermocouple arrays attached to the turbocharger body.

Thermal emissivity of turbocharger materials can be obtained using thermal imaging, as was done in [110], and its results can be used to estimate heat transfer due to radiation.

Serrano et al. [22] use an array of thermocouples placed at five different planes in the turbocharger and uses a special thermo-hydraulic test rig to characterise a heat flow lumped model that can be used later to estimate heat flux during normal gas stand operation. The turbocharger is filled with oil and is thermally insulated. The oil is heated to different temperatures at the turbine side, and the test is performed until thermal stabilisation. As the heating power is controlled and known and the temperatures at different planes are measured, internal thermal conductance coefficients can be computed supposing that the heat flow is mainly one-dimensional and that perfect external adiabatic conditions are achieved. Transient tests are also performed, so thermal capacities are also computed. When the thermal conductances are characterised, the model can be applied during turbocharger gas stand tests, provided that the body thermocouple array is kept.

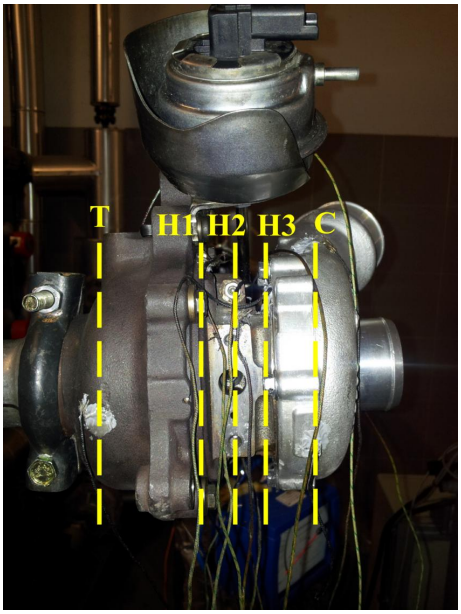

Figure 2.3: Heat transfer planes location, reproduced from [110] with permission from the authors

The method is further refined and tested in [111], [96] and [110], even including external heat flow. If external heat flow is neglected, and using the same nodes defined in Figure 2.3:

$$\dot{Q}_{turb} = K_{T,H1} \cdot (T_T - T_{H1}) \tag{2.59}$$

$$\dot{Q}_{oil} = K_{T,H1} \cdot (T_T - T_{H1}) - K_{H2,H3} \cdot (T_{H2} - T_{H3}) \tag{2.60}$$

where $\dot{Q}_{turb}$ is the heat flow from the turbine to the housing, $K_{T,H1}$ is the thermal conductance between the turbine plane and the plane $H1$, T_T is the

measured temperature at the plane T, T_{H1} is the temperature at the plane $H1$, T_{H2} is the temperature at the central housing node, T_{H3} is the temperature at the housing plane closer to the compressor, $K_{H2,H3}$ is the thermal conductance between planes $H2$ and $H3$ and $\dot{Q}_{oil}$ is the heat flow that goes to the oil.

2.5 References

[3] J. Galindo, P. Fajardo, R. Navarro, and L. M. García-Cuevas. "Characterization of a radial turbocharger turbine in pulsating flow by means of CFD and its application to engine modeling". In: *Applied Energy* 103 (2013), pp. 116–127. ISSN: 0306-2619. DOI: 10.1016/j.apenergy.2012.09.013 (cit. on pp. vii, 17, 19, 21, 29, 117, 202).

[9] European Parliament, Council of the European Union. "Regulation (EC) No 715/2007 of the European Parliament and of the Council of 20 June 2007 on type approval of motor vehicles with respect to emissions from light passenger and commercial vehicles (Euro 5 and Euro 6) and on access to vehicle repair and maintenance information (Text with EEA relevance) ". In: *Official Journal of the European Union* 50 (June 2007), pp. 1–16. ISSN: 1725-2555. URL: http://eur-lex.europa.eu/legal-content/EN/TXT/?uri=OJ:L:2007:171:TOC (cit. on pp. 3, 15, 73).

[10] European Parliament, Council of the European Union. "Regulation (EC) No 595/2009 of the European Parliament and of the Council of 18 June 2009 on type-approval of motor vehicles and engines with respect to emissions from heavy duty vehicles (Euro VI) and on access to vehicle repair and maintenance information and amending Regulation (EC) No 715/2007 and Directive 2007/46/EC and repealing Directives 80/1269/EEC, 2005/55/EC and 2005/78/EC (Text with EEA relevance) ". In: *Official Journal of the European Union* 52 (July 2009), pp. 1–13. DOI: 10.3000/17252555.L_2009.188.eng (cit. on pp. 3, 15, 73).

[14] A. O. Tiseira Izaguirre. "Caracterización experimental y modelado de bombeo en compresores centrífugos de sobrealimentación". PhD thesis. Universitat Politècnica de València, 2008 (cit. on pp. 5, 18, 252).

[18] M. Á. Reyes-Belmonte. "Contribution to the Experimental Characterization and 1-D Modelling of Turbochargers for IC Engines". PhD thesis. Universitat Politècnica de València, Dec. 2013 (cit. on pp. 5, 24, 202).

[20] R. Navarro. "A numerical approach for predicting flow-induced acoustics at near-stall conditions in an automotive turbocharger compressor". PhD thesis. Universitat Politècnica de València, 2014 (cit. on pp. 5, 21, 252).

[22] J. R. Serrano, P. Olmeda, A. Páez, and F. Vidal. “An experimental procedure to determine heat transfer properties of turbochargers”. In: *Measurement Science and Technology* 21.3 (3 2010), pp. 035–109. DOI: 10.1088/0957-0233/21/3/035109 (cit. on pp. 8, 18, 41, 68).

[23] SAE. *Supercharger Testing Standard*. SAE J1723. Society of Automotive Engineers, Aug. 1995 (cit. on pp. 10, 18, 59, 77).

[24] SAE. *Turbocharger gas stand test code*. SAE J1826. Society of Automotive Engineers, Mar. 1995 (cit. on pp. 10, 18, 59, 77).

[25] M. Iwasaki, N. Ikeya, Y. Marutani, and T. Kitazawa. *Comparison of Turbocharger Performance Between Steady Flow and Pulsating Flow on Engines*. Tech. rep. 940839. SAE International, 1994. DOI: 10.4271/940839 (cit. on p. 17).

[26] J. M. Luján, J. Galindo Lucas, and J. R. Serrano. *Efficiency Characterization of Centripetal Turbines under Pulsating Flow Conditions*. Tech. rep. 2001-01-0272. SAE International, 2001. DOI: 10.4271/2001-01-0272 (cit. on pp. 17, 29).

[27] F. J. Wallace and G. P. Blair. “The pulsating-flow performance of inward radial-flow turbines”. In: *Proceedings of the ASME Gas Turbine Conference and Products Show*. 1965, pp. 1–19 (cit. on p. 17).

[28] J. Lam, Q. Roberts, and G. McDonell. “Flow modelling of a turbocharger turbine under pulsating flow”. In: *Seventh International Conference Turbochargers and Turbocharging*. 2002 (cit. on pp. 17, 19).

[29] R. Aymanns, J. Scharf, T. Uhlmann, and D. Lückmann. “A revision of Quasi Steady Modelling of Turbocharger Turbines in the Simulation of Pulse Charged Engines”. In: *16th Supercharging Conference*. 2011 (cit. on pp. 17, 19).

[30] M. Abidat, M. Hachemi, M. K. Hamidou, and N. Baines. “Prediction of the steady and non-steady flow performance of a highly loaded mixed flow turbine”. In: *Proceedings of the Institution of Mechanical Engineers*. Vol. 212. 1998, pp. 173–184. DOI: 10.1243/0957650981536844 (cit. on pp. 17, 30).

[31] J. R. Serrano, F. J. Arnau, V. Dolz, A. Tiseira, and C. Cervelló. “A model of turbocharger radial turbines appropriate to be used in zero- and one-dimensional gas dynamics codes for internal combustion engines modelling”. In: *Energy Conversion and Management* 49 (12 2008), pp. 3729–3745. DOI: 10.1016/j.enconman.2008.06.031 (cit. on pp. 17, 24, 161).

[32] A. W. Costall, R. M. McDavid, R. F. Martínez-Botas, and N. C. Baines. "Pulse performance modelling of a twin-entry turbocharger turbine under full unequal admission". In: *Proceedings of ASME Turbo Expo 2009*. ASME, 2009. DOI: 10.1115/1.4000566 (cit. on pp. 17, 30, 31, 140, 202).

[33] A. Romagnoli and R. Martinez-Botas. "Performance prediction of a nozzled and nozzleless mixed-flow turbine in steady conditions ". In: *International Journal of Mechanical Sciences* 53.8 (2011), pp. 557–574. ISSN: 0020-7403. DOI: 10.1016/j.ijmecsci.2011.05.003 (cit. on pp. 17, 27, 28).

[34] M. Chiong, S. Rajoo, A. Romagnoli, A. Costall, and R. Martinez-Botas. "Integration of meanline and one-dimensional methods for prediction of pulsating performance of a turbocharger turbine". In: *Energy Conversion and Management* 81 (2014), pp. 270–281. ISSN: 0196-8904. DOI: 10.1016/j.enconman.2014.01.043 (cit. on pp. 17, 27, 31, 140).

[35] J. M. Luján, V. Bermúdez, J. R. Serrano, and C. Cervelló. *Test Bench for Turbocharger Groups Characterization*. SAE Technical Paper 2002-01-0163. SAE International, Mar. 2002. DOI: 10.4271/2002-01-0163 (cit. on p. 18).

[36] D. Naundorf, H. Bolz, and M. Mandel. *Design and Implementation of a New Generation of Turbo Charger Test Benches Using Hot Gas Technology*. Tech. rep. 2001-01-0279. SAE International, 2001. DOI: 10.4271/2001-01-0279 (cit. on p. 18).

[37] S. Reuter, A. Koch, and A. Kaufmann. "Extension of performance maps of radial turbocharger turbines using pulsating hot gas flow". In: *9th International Conference on Turbochargers and Turbocharging*. IMechE. 2010 (cit. on p. 18).

[38] F. Payri, J. R. Serrano, P. Olmeda, A. Páez, and F. Vidal. "Experimental Methodology to Characterize Mechanical Losses in Small Turbochargers". English. In: *Proceedings of the ASME Turbo Expo 2010*. Vol. 2010. 44007. Int Gas Turbine Inst. Glasgow, Scotland: ASME, June 2010, pp. 413–423. ISBN: 978-0-7918-4400-7. DOI: 10.1115/GT2010-22815 (cit. on pp. 18, 36, 38, 71).

[39] G. Piñero, L. Vergara, J. M. Desantes, and A. Broatch. "Estimation of velocity fluctuation in internal combustion engine exhaust systems through beamforming techniques". In: *Measurement Science and Technology* 11.11 (2000), p. 1585. DOI: 10.1088/0957-0233/11/11/307 (cit. on pp. 18, 89).

[40] J. R. Serrano, F. J. Arnau, P. Fajardo, and M. Á. Reyes-Belmonte. "Contribution to the Modeling and Understanding of Cold Pulsating Flow Influence in the Efficiency of Small Radial Turbines for Turbochargers". In: *Journal of Engineering for Gas Turbines and Power* 134.10 (Aug. 2012), 102701 (11 pages). DOI: 10.1115/1.4007027 (cit. on pp. 18, 71).

[41] J. R. Serrano, F. J. Arnau, R. Novella, and M. Á. Reyes-Belmonte. *A Procedure to Achieve 1D Predictive Modeling of Turbochargers under Hot and Pulsating Flow Conditions at the Turbine Inlet*. Tech. rep. 2014-01-1080. SAE International, 2014. DOI: 10.4271/2014-01-1080 (cit. on p. 18).

[42] A. T. Simpson, S. W. T. Spence, and J. K. Watterson. "A comparison of the flow structures and losses within vaned and vaneless stators for radial turbines". In: *Journal of Turbomachinery* 131 (2009). DOI: 10.1115/1.2988493 (cit. on pp. 19, 20).

[43] D. Palfreyman and R. Martinez-Botas. "The pulsating flow field in a mixed flow turbocharger turbine: An experimental and computational study". In: *Journal of turbomachinery* 127 (1 2005), pp. 144–155. DOI: 10.1115/1.1812322 (cit. on p. 19).

[44] Z. Liu and D. Hill. "Issues surrounding multiple frames of reference models for turbo compressor applications". In: *Fifteenth International Compressor Engineering Conference*. Purdue University. 2000 (cit. on p. 19).

[45] K. Hillewaert and R. Van den Braembussche. "Numerical simulation of impeller-volute interaction in centrifugal compressors". In: *Journal of Turbomachinery* 121 (1999), pp. 603–608. DOI: 10.1115/1.2841358 (cit. on p. 20).

[46] F. Hellström. "Numerical computations of the unsteady flow in turbochargers". PhD thesis. Royal Institute of Technology KTH Mechanics, 2010 (cit. on p. 20).

[47] J. Galindo, S. Hoyas, P. Fajardo, and R. Navarro. "Set-up analysis and optimization of CFD simulations for radial turbines". In: *Engineering Applications of Computational Fluid Mechanics* 7.4 (2013), pp. 441–460 (cit. on pp. 20, 114).

[48] A. M. Tousi and A. Tourani. "Comparison of turbulence methods in CFD analysis of compressible flows in radial turbomachines". In: *Aircraft Engineering and Aerospace Technology: An International Journal* (2008), pp. 657–665. ISSN: 0002-2667. DOI: 10.1108/00022660810911608 (cit. on p. 20).

[49] F. R. Menter. “Two-equation eddy-viscosity turbulence models for engineering applications”. In: *AIAA journal* 32.8 (1994), pp. 1598–1605. DOI: 10.2514/3.12149 (cit. on p. 20).

[50] F. R. Menter, M. Kuntz, and R. Langtry. “Ten years of industrial experience with the SST turbulence model”. In: *Turbulence, heat and mass transfer* 4 (2003), pp. 625–632 (cit. on p. 20).

[51] F. R. Menter, R. Langtry, and T. Hansen. “CFD simulation of turbomachinery flows - verification, validation and modelling”. In: *European Congress on Computational Methods in Applied Sciences and Engineering*. 2004 (cit. on p. 20).

[52] F. Mendonça, O. Baris, and G. Capon. “Simulation of Radial Compressor Aeroacoustics using CFD”. In: *Proceedings of ASME Turbo Expo*. 2012, pp. 1823–1832. DOI: 10.1115/GT2012-70028 (cit. on p. 21).

[53] A. Broatch, J. Galindo Lucas, R. Navarro, and J. García-Tíscar. “Numerical and experimental analysis of automotive turbocharger compressor aeroacoustics at different operating conditions”. In: *International Journal of Heat and Fluid Flow* (2014) (cit. on p. 21).

[54] X. Fang, Q. Dai, Y. Yin, and Y. Xu. “A compact and accurate empirical model for turbine mass flow characteristics”. In: *Energy* 35.12 (2010), pp. 4819–4823. ISSN: 0360-5442. DOI: 10.1016/j.energy.2010.09.006 (cit. on pp. 21, 22).

[55] X. Fang and Y. Xu. “Development of an empirical model of turbine efficiency using the Taylor expansion and regression analysis”. English. In: *Energy* 36.5 (May 2011), 2937–2942. ISSN: 0360-5442. DOI: 10.1016/j.energy.2011.02.036 (cit. on pp. 21, 22).

[56] L. Eriksson, L. Nielsen, J. Brugård, J. Bergström, F. Pettersson, and P. Andersson. “Modeling of a turbocharged {SI} engine”. In: *Annual Reviews in Control* 26.1 (2002), pp. 129–137. ISSN: 1367-5788. DOI: 10.1016/S1367-5788(02)80022-0 (cit. on p. 21).

[57] L. Eriksson. “Modeling and Control of Turbocharged SI and DI Engines”. In: *Oil & Gas Science and Technology - Rev. IFP* 62.4 (2007), pp. 523–538. DOI: 10.2516/ogst:2007042 (cit. on p. 22).

[58] G. Sieros, A. Stamatis, and K. Mathioudakis. “Jet engine component maps for performance modelling and diagnosis”. In: *Journal of Propulsion and Power* 13 (1997), pp. 665–674. DOI: 10.2514/2.5218 (cit. on p. 22).

[59] M. Orkisz and S. Stawarz. “Modeling of turbine engine axial-flow compressor and turbine characteristics”. In: *Journal of Propulsion and Power* 16 (2000), pp. 336–339. ISSN: 0748-4658. DOI: 10.2514/2.5574 (cit. on p. 22).

[60] N. Watson and S. Janota. *Turbocharging the internal combustion engine*. London: MacMillan Publishers Ltd., 1982 (cit. on p. 23).

[61] F. Payri, J. Benajes, J. Jullien, and Q. Duan. “Non-steady flow behaviour of a supercharger turbine”. In: *Proceedings of the Third EAEC International Conference*. Strasssbourg, 1991 (cit. on p. 23).

[62] F. Payri, J. Benajes, and M. Reyes. “Modelling of supercharger turbines in internal-combustion engines”. In: *Journal of Mechanical Science* 38 (8-9 1996), pp. 835–869. DOI: 10.1016/0020-7403(95)00105-0 (cit. on pp. 23, 29).

[63] J. Jensen, A. Kristensen, S. Sorenson, N. Houbak, and E. Hendricks. *Mean value modeling of a small turbocharged diesel engine*. Tech. rep. 910070. SAE International, 1991. DOI: 10.4271/910070 (cit. on p. 23).

[64] M. Canova. “Development and validation of a control-oriented library for the simulation of automotive engines”. In: *International Journal of Engine Research* 5.3 (2004), pp. 219–228. ISSN: 1468-0874. DOI: 10.1243/1468087041549625 (cit. on p. 24).

[65] M. Canova, S. Midlam-Mohler, Y. Guezennec, and G. Rizzoni. “Mean value modeling and analysis of HCCI diesel engines with external mixture formation”. In: *Journal of Dynamic Systems, Measurement and Control* 131.1 (2008). DOI: 10.1115/1.2977465 (cit. on p. 24).

[66] J. R. Serrano, B. Pla, D. Ospina, and R. Gonzalbo. *Estimation of the Extended Turbine Maps for a Radial Inflow Turbine*. Tech. rep. 2010-01-1234. SAE International, 2010. DOI: 10.4271/2010-01-1234 (cit. on p. 24).

[67] D. Japikse and N. C. Baines. *Introduction to turbomachinery*. Concepts ETI, 1997. ISBN: 978-0933283107 (cit. on p. 26).

[68] M. S. Chiong, S. Rajoo, A. Romagnoli, and R. F. Martínez-Botas. “Single Entry Mixed Flow Turbine Performance Prediction With 1-D Gas Dynamic Code Coupled With Mean Line Model”. In: *International Journal of Gas Turbine, Propulsion and Power Systems* 4.2 (June 2012), pp. 8–16. ISSN: 1882-5079 (cit. on pp. 26, 31).

[69] S. Futral, C. Wasserbauer, U. S. N. Aeronautics, and S. Administration. *Off-design performance prediction with experimental verification for a radial-inflow turbine: Samuel M.Futral Jr. and Charles A. Wasserbauer*. Tech. rep. NASA TN D-2621. NASA, 1965. URL: http://books.google.es/books?id=N1kzLAHfK-IC (cit. on pp. 26, 119, 153).

[70] N. Mizumachi, D. Yoshiki, and T. A. Endoh. "A study on performance of radial turbine under unsteady flow conditions". In: *Report of the Institute of Industrial Science* 28 (1979), pp. 122–130 (cit. on p. 27).

[71] A. Romagnoli. "Aerodynamic and thermal characterization of turbocharger turbines: experimental and computational evaluation". PhD thesis. Imperial College, University of London, June 2010 (cit. on p. 27).

[72] P. L. Meitner and A. J. Glassman. *Computer code for off-design performance analysis of radial-inflow turbines with rotor blade sweep*. Tech. rep. 2199. NASA, 1983 (cit. on p. 27).

[73] A. N. Dahlquist. *Investigation of Losses Prediction Methods in 1D for Axial Gas Turbines*. 2008 (cit. on p. 28).

[74] M. Benner, S. Sjolander, and S. Moustapha. "An empirical prediction method for secondary losses in turbines - Part I: A new loss breakdown scheme and penetration depth correlation". In: *Journal of Turbomachinery* 128.2 (2006). cited By (since 1996)23, pp. 273–280. ISSN: 0889504X. DOI: 10.1115/1.2162593 (cit. on p. 28).

[75] M. Benner, S. Sjolander, and S. Moustapha. "An empirical prediction method for secondary losses in turbines - Part II: A new secondary loss correlation". In: *Journal of Turbomachinery* 128.2 (2006). cited By (since 1996)25, pp. 281–291. ISSN: 0889504X. DOI: 10.1115/1.2162594 (cit. on p. 28).

[76] J. Katz and A. Plotkin. *Low-Speed Aerodynamics*. 2nd. Cambridge University Press, 2001. ISBN: 978-0521665520 (cit. on pp. 28, 145).

[77] F. Payri, J. Benajes, J. Galindo, and J. R. Serrano. "Modelling of turbocharged diesel engines in transient operation. Part 2: Wave action models for calculating the transient operation in a high speed direct injection engine". In: *Proceedings of the Institution of Mechanical Engineers, Part D: Journal of Automobile Engineering* 216.6 (2002), pp. 479–493. DOI: 10.1243/09544070260137507 (cit. on p. 29).

[78] A. Torregrosa, J. Galindo, J. R. Serrano, and A. Tiseira. "A procedure for the unsteady characterization of turbochargers in reciprocating internal combustion engines". In: *Fluid Machinery and Fluid Mechanics, The 4th International Symposium on Fluid Machinery and Fluid Engineering*. Beijing, China: Springer Berlin Heidelberg, Nov. 2009, pp. 72–79. ISBN:

978-3-540-89748-4. DOI: 10.1007/978-3-540-89749-1_10 (cit. on p. 29).

[79] N. Baines, A. Halijouy-Benisi, and J. H. Yeo. "The pulse flow performance and modelling of radial inflow turbines". In: *Proceedings of the Institution of Mechanical Engineers, 5th International Conference on Turbocharging and Turbochargers*. 1994, pp. 209–220 (cit. on p. 29).

[80] D. E. Winterbone and R. J. Pearson. *Theory of Engine Manifold Design: Wave Action Methods for IC Engines*. Wiley-Blackwell, 2000. ISBN: 1860582095 (cit. on p. 29).

[81] S. Larsson and V. Thomée. *Partial Differential Equations with Numerical Methods*. Vol. 45. Texts in Applied Mathematics. Springer, 2003. ISBN: 10.1007/978-3-540-88706-5. DOI: 10.1007/978-3-540-88706-5 (cit. on p. 29).

[82] R. J. LeVeque. *Finite Volume Methods for Hyperbolic Problems*. Cambridge Texts in Applied Mathematics. Cambridge University Press, 2002. ISBN: ISBN 0-521-81087-6. (Cit. on p. 29).

[83] H. Chen and D. Winterbone. "A method to predict performance of vaneless radial turbine under steady and unsteady flow conditions". In: *Turbocharging and Turbochargers*. Institution of Mechanical Engineers. 1990, pp. 13–22 (cit. on pp. 29–31).

[84] M. S. Chiong, S. Rajoo, A. Romagnoli, and R. Martínez-Botas. "Unsteady performance prediction of a single entry mixed flow turbine using 1-D gas dynamic code extended with meanline model". In: *Proceedings of the ASME Turbo Expo*. Vol. 5. ASME. 2012, pp. 781–795. DOI: 10.1115/GT2012-69176 (cit. on p. 30).

[85] X. Hu. "An advanced turbocharger model for the internal combustion engine". PhD thesis. Purdue University, 2000 (cit. on p. 30).

[86] A. King. "A turbocharger unsteady performance model for the GT-Power internal combustion engine simulation". PhD thesis. Purdue University, 2002 (cit. on p. 30).

[87] V. D. Bellis, S. Marelli, F. Bozza, and M. Capobianco. "1D Simulation and Experimental Analysis of a Turbocharger Turbine for Automotive Engines Under Steady and Unsteady Flow Conditions". In: *Energy Procedia* 45 (2014). {ATI} 2013 - 68th Conference of the Italian Thermal Machines Engineering Association, pp. 909–918. ISSN: 1876-6102. DOI: 10.1016/j.egypro.2014.01.096 (cit. on pp. 31, 151).

[88] A. Diango, C. Perilhon, G. Descombes, and E. Danho. “Application of exergy balances for the optimization of non-adiabatic small turbomachines operation”. English. In: *Energy* 36.5 (May 2011), 2924–2936. ISSN: 0360-5442. DOI: 10.1016/j.energy.2011.02.035 (cit. on p. 32).

[89] W. J. Chen. “Rotordynamics and bearing design of turbochargers”. English. In: *Mechanical Systems and Signal Processing* 29.SI (May 2012), pp. 77–89. ISSN: 0888-3270. DOI: 10.1016/j.ymssp.2011.07.025 (cit. on p. 32).

[90] M. Deligant, P. Podevin, G. Descombes, L. Thierry, V. Fabrice, and A. Marche. “Experimental Study of Turbocharger’s Performances at Low Speeds”. English. In: *Proceedings of the ASME Internal Combustion Engine Division Fall Technical Conference*. ASME, Internal Combust Engine Div. Three Park Avenue, New York, NY 10016-5990 USA: AMER SOC MECHANICAL ENGINEERS, 2010, 911–918. ISBN: 978-0-7918-4944-6. DOI: 10.1115/ICEF2010-35071 (cit. on p. 33).

[91] P. Podevin, A. Clenci, and G. Descombes. “Influence of the lubricating oil pressure and temperature on the performance at low speeds of a centrifugal compressor for an automotive engine”. English. In: *Applied Thermal Engineering* 31.2-3 (Feb. 2011), pp. 194–201. ISSN: 1359-4311. DOI: 10.1016/j.applthermaleng.2010.08.033 (cit. on p. 33).

[92] M. Deligant, P. Podevin, G. Descombes, T. Lamquin, F. Vidal, and A. Marchal. “Effect of axial load on turbocharger friction losses”. In: *Proceedings of the 13th EAEC European Congress*. Valencia, Spain, 2011 (cit. on p. 34).

[93] M. Deligant, P. Podevin, and G. Descombes. “Experimental identification of turbocharger mechanical friction losses”. English. In: *Energy* 39.1 (Mar. 2012), 388–394. ISSN: 0360-5442. DOI: 10.1016/j.energy.2011.12.049 (cit. on pp. 34, 81, 235).

[94] S. Schmitt, W. Schmid, G. Hetweck, M. Schlegl, and S. Staudacher. “High-Precision Measurements of Friction Losses in Turbochargers”. In: *Aufladetechnische Konferenz 2007*. Dresden, Germany, 2007 (cit. on p. 34).

[95] K. Gjika and G. D. Larue. “Axial Load Control on High-Speed Turbochargers: Test and Prediction”. In: *Proceedings of the ASME Turbo Expo 2008: Power for Land, Sea and Air*. Berlin, Germany, June 2008, pp. 705–712. ISBN: 978-0-7918-4311-6. DOI: 10.1115/GT2008-50756 (cit. on p. 34).

[96] J. R. Serrano, P. Olmeda, F. J. Arnau, M. Á. Reyes-Belmonte, and A. Lefebvre. “Importance of Heat Transfer Phenomena in Small Turbochargers for Passenger Car Applications”. In: *SAE Int. J. Engines* 6(2) (2 2013), pp. 716–728. DOI: 10.4271/2013-01-0576 (cit. on pp. 36, 41).

[97] E. Sjöber. *Friction Characterization of Turbocharger Bearings*. 2013 (cit. on p. 36).

[98] M. Deligant, P. Podevin, and G. Descombes. “{CFD} model for turbocharger journal bearing performances”. In: *Applied Thermal Engineering* 31.5 (2011). {MNF} 2009 Special Issue, pp. 811–819. ISSN: 1359-4311. DOI: 10.1016/j.applthermaleng.2010.10.030 (cit. on pp. 37, 157, 164).

[99] L. Bouard, M. Fillon, and J. Frêne. “Comparison between three turbulent models — application to thermohydrodynamic performances of tilting-pad journal bearings”. In: *Tribology International* 29.1 (1996). {AUSTRIB} ’94, pp. 11–18. ISSN: 0301-679X. DOI: 10.1016/0301-679X(95)00028-3 (cit. on p. 37).

[100] B. Maneshian and S. Gandjalikhan Nassab. “Thermohydrodynamic Characteristics of Journal Bearings Running Under Turbulent Condition”. In: *IJE Transactions A: Basics* 22 (2009), pp. 181–194 (cit. on p. 37).

[101] L. Huiping, X. Hua, J. E. Peter, and J. Zhongmin. “Application of computational fluid dynamics and fluid-structure interaction method to the lubrication study of a rotor-bearing system”. In: *Tribology Letters* 28 (2010), pp. 325–336. DOI: 10.1007/s11249-010-9612-6 (cit. on p. 37).

[102] L. Lihua, S. Hao, L. Yingchun, and Z. Qiang. “Research on Static Stiffness of Hydrostatic Bearing using Fluid-Structure Interaction Analysis”. In: *Procedia Engineering* 29 (2012). 2012 International Workshop on Information and Electronics Engineering, pp. 1304–1308. ISSN: 1877-7058. DOI: 10.1016/j.proeng.2012.01.131 (cit. on p. 38).

[103] L. Hu, C. Yang, H. Sun, E. Krivizky, L. Larosiliere, J. Zhang, and M. Lai. *Experimental and Computational Analysis of Impact of Self Recirculation Casing Treatment on Turbocharger Compressor*. Tech. rep. 2001-01-0272. SAE International, 2010. DOI: 10.4271/2010-01-1224 (cit. on pp. 38, 39).

[104] O. Reynolds. “On the Theory of Lubrication and Its Application to Mr. Beauchamp Tower’s Experiments, Including an Experimental Determination of the Viscosity of Olive Oil”. In: *Philosophy Transactions of the Royal Society of London* 177 (1886), pp. 157–234 (cit. on p. 39).

[105] M. Deligant, P. Podevin, F. Vidal, W. Tyminski, S. Guilain, and H. Lahjaily. “3D thermal steady-state CFD analysis of power friction losses in a turbocharger’s journal bearing and comparison with finite difference method and experimentation”. In: *12th European Automotive Congress: EAEC 2009, Bratislava*. 2009 (cit. on p. 40).

[106] S. Shaaban. “Experimental Investigation and Extended Simulation of Turbocharger Non-Adiabatic Performance”. PhD thesis. Fachbereich Maschinenbau: Universität Hannover, 2004 (cit. on pp. 40, 71).

[107] S. Shaaban, J. Seume, R. Berndt, H. Pucher, and H. J. Linnhoff. “Part-load performance prediction of turbocharged engines”. In: *Proceedings of 8th International Conference on Turbochargers and Turbocharging*. 2006 (cit. on p. 40).

[108] P. Podevin, M. Toussaint, G. Richarg, and G. Farinole. “Performances of turbocharger at low speed”. In: *Proceedings of the SYMKOM02 congress*. Lodz, Pologne, 2002 (cit. on p. 40).

[109] N. Baines, K. D. Wygant, and A. Dris. “The Analysis of Heat Transfer in Automotive Turbochargers”. English. In: *Journal of Engineering for Gas Turbineas and Power - Transactions of the ASME* 132.4 (Apr. 2010). ISSN: 0742-4795. DOI: 10.1115/1.3204586 (cit. on pp. 40, 68).

[110] F. Payri, P. Olmeda, F. J. Arnau, A. Dombovsky, and L. Smith. “External heat losses in small turbochargers: Model and experiments”. In: *Energy* 71 (2014), pp. 534–546. DOI: 10.1016/j.energy.2014.04.096 (cit. on p. 41).

[111] P. Olmeda, V. Dolz, F. J. Arnau, and M. Á. Reyes-Belmonte. “Determination of heat flows inside turbochargers by means of a one dimensional lumped model”. In: *Mathematical and Computer Modelling* 57.7–8 (2013), pp. 1847–1852. ISSN: 0895-7177. DOI: 10.1016/j.mcm.2011.11.078 (cit. on pp. 41, 71, 105, 248).

CHAPTER 3

Experimental tests in automotive turbochargers

Contents

Figures

Tables

3.1 Introduction

THE information provided by turbocharger manufacturers, usually in the form of compressor and turbine maps, lacks some of the fine details that are needed to successfully compute their behaviour in conditions far from that that were used during the measurement of such maps. To estimate their behaviour, computational models able to extrapolate in other operating conditions are needed. Such models should be able to compute the behaviour of the different physical phenomena that affects a turbocharger:

- Turbine and compressor adiabatic behaviour, decoupling their different parts.
- Mechanical power transmission losses between the turbine and the compressor.
- Heat fluxes inside the turbocharger and between it and the environment.
- Rotational dynamics of the turbocharger.

It is necessary to decouple these different effects during the experimental characterisation to get good information for the development, calibration and validation of the different subsystems that conform a full turbocharger model. Different methods are needed to improve basic turbocharger gas stands to get the extra measurements that are needed to decouple the effects of these physical phenomena.

The experimental campaign done in this work is focused in the adiabatic characterisation of turbochargers, measuring the mechanical power transmission losses, the global behaviour of the turbocharger, its performance under pulsating flow conditions and the behaviour of the different parts of the turbine.

In this chapter, the experimental facilities used to characterise different automotive turbochargers are described in detail. Then, the experimental campaigns used to globally characterise radial turbochargers are presented. The experimental tests needed to get the internal pressure of different parts of a turbocharger are described later. Finally, the experimental method to get the mechanical losses and their experimental results are presented. The next chapter will be focused on the characterisation of a radial turbine by means of CFD simulations.

Gas stand characteristics

First gas stand

The first gas stand used during the experimental campaign performed during the production of this document is described here. Three different turbochargers

were measured using this test bench.

In this test bench, a screw compressor is used to feed the turbine. Its operating speed and, thus, its outlet pressure can be controlled. When the required pressure or mass flow rate is lower than the minimum supplied by the screw compressor, an electronic discharge valve is used; this valve is placed downstream of the screw compressor and the discarded flow is directly discharged to the atmosphere. The screw compressor has its own filters, so the air that enters the turbine is oil and dust-free.

After the compressor, five parallel tube-type electrical heaters rise the temperature of the turbine inlet air up to the desired value. The flow through each of the heaters is regulated and balanced by means of valves placed on the heater inlet ports. This system can reach up to 720 K at the maximum mass flow rate. This hot flow is collected in a plenum and conducted to the turbine inlet.

After passing through the turbine, the air is cooled by means of a heat exchanger in order to allow the mass flow measurement by high accuracy hot film flow meters. Of course, all flow meters in the installation have been previously calibrated.

The turbocompressor sucks air from the atmosphere. The air passes first through a filter and then its flow rate is measured. Downstream of the compressor, there is an electronically driven backpressure valve, a second flow meter and filters to clean the air from oil before discharging it to the atmosphere. The compressor can also be tested in a closed-loop configuration, where the outlet of the loop can be attached to its inlet: this allows to test the compressor with low pressure or high pressure at its inlet, thus lowering or rising the power drawn by it for a given compression ratio and corrected speed.

An independent lubrication system is used to control oil flow rate and pressure (by means of an oil pump and a pressure control valve) and temperature (by using an electrical heater and a cooler). The oil mass flow rate is measured by means of a coriolis flow meter. Lubrication inlet and outlet temperatures are measured by means of low uncertainty platinum resistance temperature detectors. Periodic samples of oil can be taken from the independent lubrication system in order to characterise its properties (viscosity, density and specific heat capacity variations with temperature).

The turbocharger, inlet, outlet and oil ducts are insulated with fibreglass during all the tests in order to make the heat flow to the environment as negligible as possible during the experimental campaign.

Temperature and pressure sensors are installed on the inlet and the outlet pipes of the compressor and the turbine according to *Supercharger Testing Standard* [23] and *Turbocharger gas stand test code* [24]. Small thermocouples all also located on the turbocharger housing and over the insulation to estimate heat fluxes.

General specifications

- Roots compressor
  - Maximum gauge operating pressure: 0.3 MPa
  - Maximum flow rate at maximum pressure: $0.2\,\mathrm{kg\,s^{-1}}$
- Air/water heat exchanger to cool compressor inlet air.
- Turbine inlet electrical heaters.
  - Maximum power output: 40 kW.
- Closed-loop capable compressor circuit.
- High temperature rotating valve pulse-generator at compressor outlet or turbine inlet.
  - Tested up to 900 K.
  - Maximum frequency: 50 Hz.
- Turbocharger lubrication system with pressure and temperature conditioner.
- Turbocharger cooling system with pressure and temperature conditioner.

Transducers

- Temperature
  - 20 type-K thermocouples
    - Diameter: 1.5 mm
    - Position: 4 at compressor inlet, 4 at compressor outlet, 4 at turbine inlet, 4 at turbine outlet, 1 at lubrication inlet, 2 at lubrication outlet, one over the turbocharger.
    - Measurement uncertainty: 1.5 K
  - 21 type-K thermocouples.
    - Diameter: 0.5 mm
    - Position: 15 on the turbocharger surface, 3 on the turbocharger insulation, one on the compressor outlet duct insulation, one on the turbine inlet duct insulation, one on the turbine outlet insulation.
    - Measurement uncertainty: 1.5 K

  - 4 class A, four-wire PT-100 RTDs.
    * Diameter: 3 mm
    * Position: one in the lubrication inlet, one in the lubrication outlet, one in the cooling inlet, one in the cooling outlet.
    * Measurement uncertainty: between 0.21 K (at low temperature) and 0.43 K (at a measured temperature of 410 K)

- Pressure
  - 2 piezoresistive transmitter.
    * Operating range: 0 to 200 kPa
    * Position: Compressor inlet.
    * Measurement uncertainty: 200 Pa
  - 6 piezoresistive transmitters.
    * Operating range: 0 to 500 kPa
    * Position: Compressor outlet, turbine inlet, turbine outlet.
    * Measurement uncertainty: 500 Pa
  - 2 piezoresistive transmitter.
    * Operating range: 0 to 600 kPa
    * Position: Lubrication inlet.
    * Measurement uncertainty: 600 Pa
  - 1 piezoresistive transmitter.
    * Operating range: 0 to 500 kPa
    * Position: Refrigeration inlet.
    * Measurement uncertainty: 500 Pa
  - 3 piezoresistive transducers.
    * Operating range: 0 to 500 kPa
    * Position: compressor outlet and turbine inlet and outlet ducts or turbine inlet and compressor inlet and outlet ducts.
  - 6 piezoelectric transducers.
    * Position: compressor inlet and outlet ducts or turbine inlet and outlet ducts.

- Mass flow rate
  - 2 hot-film mass flow meters.
    * Operating range: 5 to 200 $\mathrm{g\,s^{-1}}$

        - Position: Compressor inlet, turbine outlet.
        - Measurement uncertainty: 1 % of the measured value.
    - One vortex mass flow meter.
        - Operating range: 11 to 167 $g\,s^{-1}$
        - Position: Compressor outlet.
        - Measurement uncertainty: 2 % of the measured value.
    - One coriolis mass flow meter.
        - Position: Lubrication inlet.
    - One magnetic mass flow meter.
        - Position: Refrigeration inlet.

- Rotating speed.
    - Eddy currents sensor.
        - Position: compressor housing.

- Displacement.
    - Inductive sensor.
        - Position: central housing, attached to the VGT lever.

The data acquisition hardware has an expanded uncertainty of 0.25 K for temperature.

Gas stand schematic This gas stand schematic is shown in Figure 3.1. The small thermocouples used to estimate heat transfer have been omitted for clarity's sake. The piezoelectric and piezoresistive transducers used during pulsating flow campaigns are located in the compressor inlet and outlet ducts(when measuring compressor pulsating behaviour) or in the turbine inlet and outlet ducts (when measuring turbine pulsating behaviour). A heat exchanger is located at the turbine outlet to reduce the outlet flow temperature to levels admissible by the turbine outlet mass flow meter.

Second gas stand

General specifications The second gas stand has been used to characterise the internal pressure of a radial turbine during steady and pulsating flow conditions. Albeit being bigger, its implementation is similar to that of the first gas stand. It has a heat exchanger after the screw compressor to lower its outlet temperature when required, seven high pressure electrical heaters of higher power and an air to air heat exchanger between the flow upstream of the

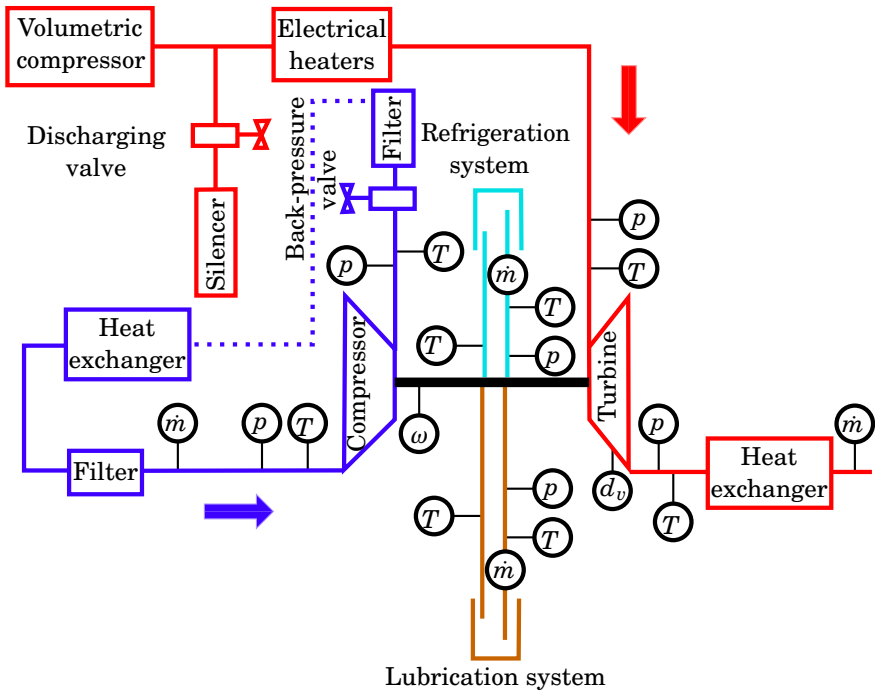

Figure 3.1: Old gas stand schematic

electrical heaters and downstream of the turbine for improved power efficiency during the experimental campaign.

- Roots compressor
  - Maximum gauge operating pressure: 0.4 MPa
- Air/water heat exchanger to cool turbine inlet air.
- Air/water heat exchanger to cool compressor inlet air.
- Turbine inlet electrical heaters.
  - Maximum power output: 70 kW.
- Heat exchanger between the flow upstream of the electrical heaters and downstream of the turbine for improved power efficiency.
- Closed-loop capable compressor circuit.
- Rotating valve pulse-generator at compressor outlet.
  - Maximum operating temperature: 400 K.

  - Maximum frequency: 50 Hz.

- High temperature rotating valve pulse-generator at compressor outlet or turbine inlet.
  - Tested up to 900 K.
  - Maximum frequency: 50 Hz.
- Turbocharger lubrication system with pressure and temperature conditioner.
- Turbocharger cooling system with pressure and temperature conditioner.

Transducers

- Temperature
  - 20 type-K thermocouples
    - Diameter: 1.5 mm
    - Position: 4 at compressor inlet, 4 at compressor outlet, 4 at turbine inlet, 4 at turbine outlet, 1 at lubrication inlet, 2 at lubrication outlet, one over the turbocharger.
    - Measurement uncertainty: 1.5 K
  - 21 type-K thermocouples.
    - Diameter: 0.5 mm
    - Position: 15 on the turbocharger surface, 3 on the turbocharger insulation, one on the compressor outlet duct insulation, one on the turbine inlet duct insulation, one on the turbine outlet insulation.
    - Measurement uncertainty: 1.5 K
  - 4 class A, four-wire PT-100 RTDs.
    - Diameter: 3 mm
    - Position: one in the lubrication inlet, one in the lubrication outlet, one in the cooling inlet, one in the cooling outlet.
    - Measurement uncertainty: between 0.21 K (at low temperature) and 0.43 K (at a measured temperature of 410 K)
- Pressure
  - 2 piezoresistive transmitter.
    - Operating range: 0 to 200 kPa

    - Position: Turbine outlet, turbine internal pressure probes.
    - Measurement uncertainty: 200 Pa
  - 6 piezoresistive transmitters.
    - Operating range: 0 to 500 kPa
    - Position: Compressor inlet, compressor outlet, turbine inlet and turbine internal pressure probes or compressor internal pressure probes.
    - Measurement uncertainty: 500 Pa
  - 2 piezoresistive transmitter.
    - Operating range: 0 to 600 kPa
    - Position: Lubrication inlet, turbine internal pressure probes.
    - Measurement uncertainty: 600 Pa
  - 2 piezoresistive transmitter.
    - Operating range: 0 to 200 kPa
    - Position: Turbine internal pressure probes or compressor internal pressure probes.
    - Measurement uncertainty: 200 Pa
  - 2 piezoresistive transducers.
    - Operating range: 0 to 500 kPa
    - Position: compressor inlet and outlet ducts or turbine inlet and outlet ducts.
  - One piezoresistive transducer.
    - Operating range: 0 to 200 kPa
    - Position: compressor volute or turbine stator outlet.
    - Measurement uncertainty: 400 Pa
  - 2 piezoelectric transducers.
    - Position: compressor volute or turbine volute.

- Mass flow rate
  - 2 hot-film mass flow meters.
    - Operating range: 5 to 200 $g\,s^{-1}$
    - Position: Compressor inlet, turbine outlet.
    - Measurement uncertainty: 1 % of the measured value.
  - One vortex mass flow meter.
    - Operating range: 11 to 167 $g\,s^{-1}$

        - Position: Compressor outlet.
        - Measurement uncertainty: 2 % of the measured value.
    - One coriolis mass flow meter.
        - Position: Lubrication inlet.
    - One magnetic mass flow meter.
        - Position: Refrigeration inlet.

- Rotating speed.
    - Eddy currents sensor.
        - Position: compressor housing.

- Displacement.
    - Inductive sensor.
        - Position: central housing, attached to the VGT lever.

Gas stand schematic This gas stand schematic is shown in Figure 3.2. Again, the small thermocouples used to estimate heat transfer have been omitted. The piezoelectric and piezoresistive transducers used during pulsating flow campaigns are located at the compressor inlet and outlet ducts (when measuring compressor pulsating behaviour) or at the turbine inlet and outlet ducts (when measuring turbine pulsating behaviour). There are several air/water heat exchangers in order to reduce the air temperature at the outlet of the screw compressor, at the inlet of the turbocharger compressor and just upstream of the turbine outlet mass flow meter. Also, an air/air heat exchanger is located upstream of the electric heaters in order to recover some of the turbine outlet gases residual heat.

Uncertainty assessment

Uncertainty in direct measurements is propagated to derived quantities that are of interest such as compressor power or turbine efficiency. To assess the reliability of the measurements of physical quantities, values of their uncertainties should be given in a standardised way. There are different types of methods used to estimate the probability density distribution of values of uncertainty for a multivariable system, some of them comprise “Bootstrapping” and “Monte Carlo” methods. A good alternative is described in [113] by the Joint Committee for Guides in Metrology and is applied in this work. The objective focuses on finding the standard deviation but not the probability density of the results. Moreover, the bootstrapping and Monte Carlo [114] methods require more computational time than the standard method, although generate more information.

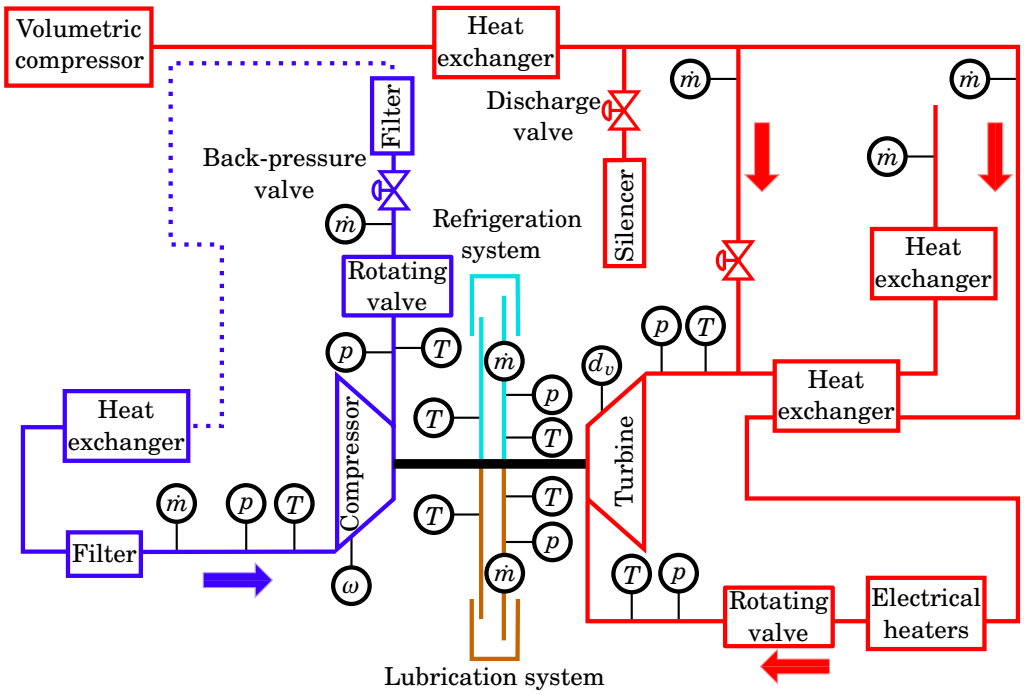

Figure 3.2: New gas stand schematic

Standard deviation is used as a measure of uncertainty, and some information about the probability density function that describes the behaviour of the measurements done by means of each transducer is needed to compute it using manufacturer's data. When there is no information available about the expected probability density function, an uniform distribution should be used.

In the present work, a coverage factor k is used on the basis of a level of confidence of 99.7 % of the real values of the measurands falling inside an interval $z - k \cdot u_z$ to $z + k \cdot u_z$, what gives $k = 3$ in case of normal distributions. In the case of uniform distributions, the real values of the measurands fall inside the interval $z - \sqrt{3} \cdot u_z$ to $z + \sqrt{3} \cdot u_z$ with a level of confidence of 100 %. The value $k \cdot u_z$ is called expanded uncertainty. The standard uncertainty of z, where z is the estimate of the measurand Z and thus the result of the measurement, is obtained by appropriately combining the standard uncertainties of the input estimates $x_1, x_2, ..., x_n$. This combined standard uncertainty of the estimate z is denoted by u_z.

For a given derived quantity z, its uncertainty u_z can be computed as:

$$u_z^2 = \sum_i^n \left(\frac{\partial z}{\partial x_i} \right)^2 u_{x_i}^2, \tag{3.1}$$

where, again u_{x_i} is the uncertainty of the variable x_i and it is assumed that there is no correlation between the measurements.

3.2 Mechanical losses characterisation

Power dissipated at the bearings of three different turbochargers has been measured to get enough data for the development and calibration of a mechanical losses lumped model. The three units have different bearing characteristics, and are used for engines ranging from 75 kW to almost 130 kW. In this section, the experimental method used to characterise the mechanical losses of these three turbochargers is described, as well as the study of the main results obtained during the experimental campaign.

Experimental method

In order to decouple mechanical losses and heat transfer in the turbocharger, the tests, performed over three different turbochargers and whose main characteristics are presented in Table 3.1, have been designed in order to mitigate the influence of heat transfer. These have been performed in the following way:

- Firstly, temperature drops across the turbocharger have been kept as low as possible. This was achieved by means of the so called quasi-adiabatic conditions, which means imposing the same temperature at turbine inlet, lubrication oil inlet and compressor outlet (i.e. $T_3 = T_{oil,in} = T_2$). The main limitation of this procedure is due to the maximum temperature of the lubricating oil, so only low to medium turbocharger compression ratios can be tested as Figure 3.3 shows; also, it is difficult to keep the three temperatures the same as Tables 3.2 to 3.4 show.

- Secondly, the whole turbocharger has been insulated, so heat losses to the ambient have been minimised.

With these two actions, the turbocharger behaviour is expected to be almost adiabatic [109]. In this way, the energy absorbed by the lubrication oil will mainly come from the heat generated by friction [115], i.e. mechanical losses. Albeit conducting the experimental campaign in quasi-adiabatic conditions, the internal heat transfer is computed and the mechanical losses power is corrected following the method described by Serrano et al. [22], measuring the temperature at different parts of the turbocharger body and computing the heat flow inside it using a one-dimensional lumped elements thermal model. The thermal model has been calibrated with experiments done in a special thermo-hydraulic test bench using the same turbocharger units.

The main limit associated to these kind of tests is the range of compressor points where the test requirements can be accomplished. Figure 3.3 shows the range of the quasi-adiabatic tests on a full compressor map. The limit is imposed by compressor outlet temperatures higher than 420 K, a condition that can deteriorate the lubricating oil.

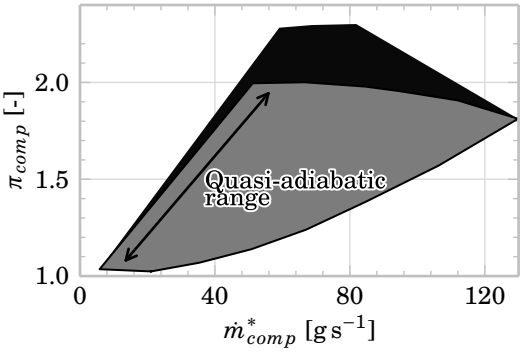

Figure 3.3: Quasi-adiabatic measurement range in compressor map

As Tables 3.2 to 3.4 show, the measurements performed go from 30 krpm to 190 krpm in steps of 20 krpm in compressor corrected speed for the three tested turbochargers, between surge and choke (between 7 and 13 points per corrected speed line). At minimum compression ratios (i.e. 30 krpm and 50 krpm), the quasi-adiabaticity is difficult to achieve [116].

In order to widen the tested turbine expansion ratios, the tests have been done in a closed-loop configuration in the compressor side: the compressor loop has been pressurised in choke conditions and its pressure has been reduced near surge. Doing so, the range of power consumed by the compressor has been widened for each iso-speed line.

As the temperature difference between the oil inlet and outlet ports is used to compute the dissipated power, and as this difference is usually small, a special arrangement of the temperature sensors is needed to reduce the measurement uncertainty. First, four-wire, class A RTDs are used to measure the oil temperature, as thermocouples are inherently less precise. The inlet temperature is measured close to the inlet port, with the sensors fully submerged in the oil flow. At the oil outlet port, there could exist a mixture of oil and blow-by air, with the oil dripping at the duct wall occasionally, difficulting the measurement of its temperature. The outlet temperature is measured using a special PTFE manifold close to the outlet port: it collects the outlet flow in an almost horizontal channel where an RTD lies, thus ensuring that the sensor is fully submerged in oil while the heat flow is reduced at its minimum due to the low thermal conductivity of PTFE. Figure 3.4 shows a schematic representation

Table 3.1: Main characteristics of the employed turbochargers

Parameter	First turbocharger	Second turbocharger	Third turbocharger
Turbine wheel diameter [mm]	41	38	36.5
Compressor wheel diameter [mm]	49	46	40
VGT	yes, vanes	yes, vanes	no
Water cooled	yes	no	yes
Type of journal bearing	fixed	floating ring	floating ring
Engine power [kW]	129	96	75
Engine type	diesel	diesel	petrol
Displacement [L]	2.0	1.6	1.2

Table 3.2: Mean deviations of the adiabatic temperatures. First turbocharger

n [rpm]	$\overline{T_{oil,in}}$ [K]	$\overline{T_{comp,out} - T_{oil,in}}$ [K]	$\overline{T_0 - T_{oil,in}}$ [K]
30 000	299.8	−1.6	2.4
50 000	305.7	0.3	3.3
70 000	317.1	1.1	2.5
90 000	333.1	1.7	3.1
110 000	349.2	0.6	1.3
130 000	369.7	1.5	1.1
150 000	397.4	3.7	0.3
170 000	417.2	12.6	1.5

of the oil temperature measurement arrangement.

The oil mass flow rate is measured using a high accuracy coriolis flowmeter, and its characteristics (specific heat capacity, viscosity) are obtained experimentally or from the manufacturer's data sheet. It is fed to the turbocharger using an independent lubrication system with regulated pressure and temperature.

The three units were disassembled and the geometry of the bearings was measured using high precision outside and inside micrometers. Due to the small values of the clearance between the bearings and the shafts, the measurements were done under a controlled temperature equal to that of the calibration of the gauge blocks that were used to test the micrometers.

Experimental study

All performed measurements are processed in order to obtain mechanical power and mechanical efficiency. Since tests were quasi-adiabatic, heat losses can

Table 3.3: Mean deviations of the adiabatic temperatures. Second turbocharger

n [rpm]	$\overline{T_{oil,in}}$ [K]	$\overline{T_{comp,out} - T_{oil,in}}$ [K]	$\overline{T_0 - T_{oil,in}}$ [K]
30000	297.0	−3.1	4.9
50000	298.8	−0.2	0.8
70000	310.3	−1.7	4.3
90000	321.2	0.6	1.0
110000	343.7	−9.0	0.7
130000	357.8	−1.7	1.5
150000	379.0	3.1	2.0
170000	400.2	3.6	1.4

Table 3.4: Mean deviations of the adiabatic temperatures. Third turbocharger

n [rpm]	$\overline{T_{oil,in}}$ [K]	$\overline{T_{comp,out} - T_{oil,in}}$ [K]	$\overline{T_0 - T_{oil,in}}$ [K]
50000	305.6	1.4	4.1
70000	314.1	1.0	4.3
90000	322.2	0.1	3.0
110000	334.4	−1.6	2.6
130000	345.3	2.0	0.6
150000	362.3	5.0	1.8
170000	386.0	−0.3	−0.6
190000	403.4	3.0	3.3

usually be neglected [38]. Nevertheless, they are taken into account as seen in [40]:

$$\dot{W}_{ml} \simeq \dot{m}_{oil} \cdot c_{oil} \cdot \Delta T_{oil} - \dot{Q}_{oil-housing} \tag{3.2}$$

where $\dot{Q}_{oil-housing}$ represents the convective heat flow from turbocharger central housing to the oil or vice versa, while mechanical efficiency can be obtained as (see [111]):

$$\eta_{mech} = \frac{\dot{W}_{comp}}{\dot{W}_{turb}} = \frac{\dot{W}_{turb} - \dot{W}_{ml}}{\dot{W}_{turb}} = 1 - \frac{\dot{W}_{ml}}{\dot{W}_{turb}} \tag{3.3}$$

where $\dot{W}_{turb}$, in this kind of tests, can be obtained as the enthalpy drop [106] of the gas flowing through the turbine.

Figure 3.5 shows the estimated internal oil heat flow relative to the computed mechanical losses power. As it can be seen, there are big differences depending

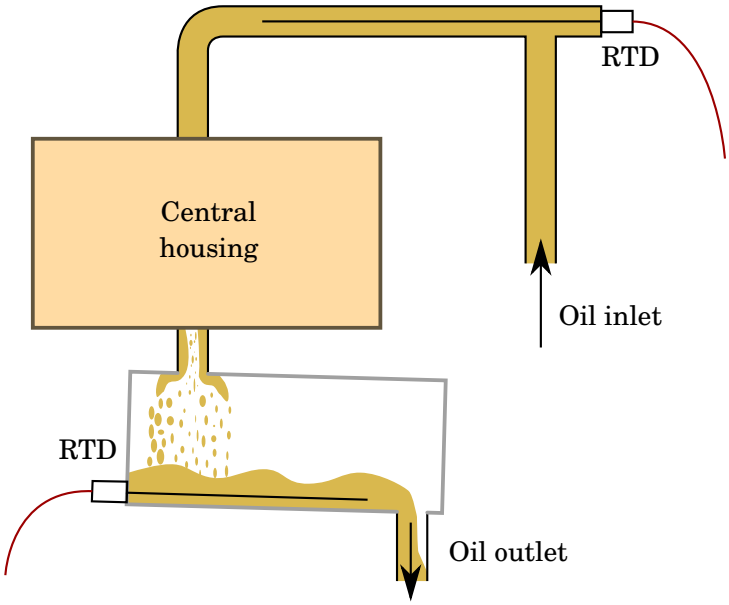

Figure 3.4: Oil temperature measurement scheme

upon the characteristics of the turbocharger. The first turbocharger, which is the biggest one and is water-cooled during normal operations but wasn't during the quasi-adiabatic testing campaign, has a relative heat flow of around 10 % of the computed mechanical losses power. When it was first measured, this led to expect negligible oil heat flow in the general case, but that proved wrong after measuring the second turbocharger. This second turbocharged showed large variations in the specific oil heat flow, probably due to the oil-cooled architecture of this unit. The last turbocharger, again a water-cooled unit, showed smaller differences in the specific heat flow between different experimental points. These results emphasised the importance of the heat flow estimation for mechanical losses computation from oil enthalpy leap, which seems to be higher in oil-cooled units than in water-cooled turbochargers.

Figure 3.6 shows the mechanical efficiency obtained for all three turbochargers in a compressor map, where a clear relationship between this efficiency and the compressor load is observed, i.e. the higher the load, the higher the mechanical efficiency. For low to medium compression ratios (as the tests were performed with the constraints explained in section 3.2, the maximum measured load was approximately two thirds of the turbochargers maximum load), the value of this efficiency is higher than 90 %. So, for higher loads and following the trends shown in Figure 3.6, maximum efficiencies are expected. On the other hand, minimum measured efficiencies down to 50 % at very low compression

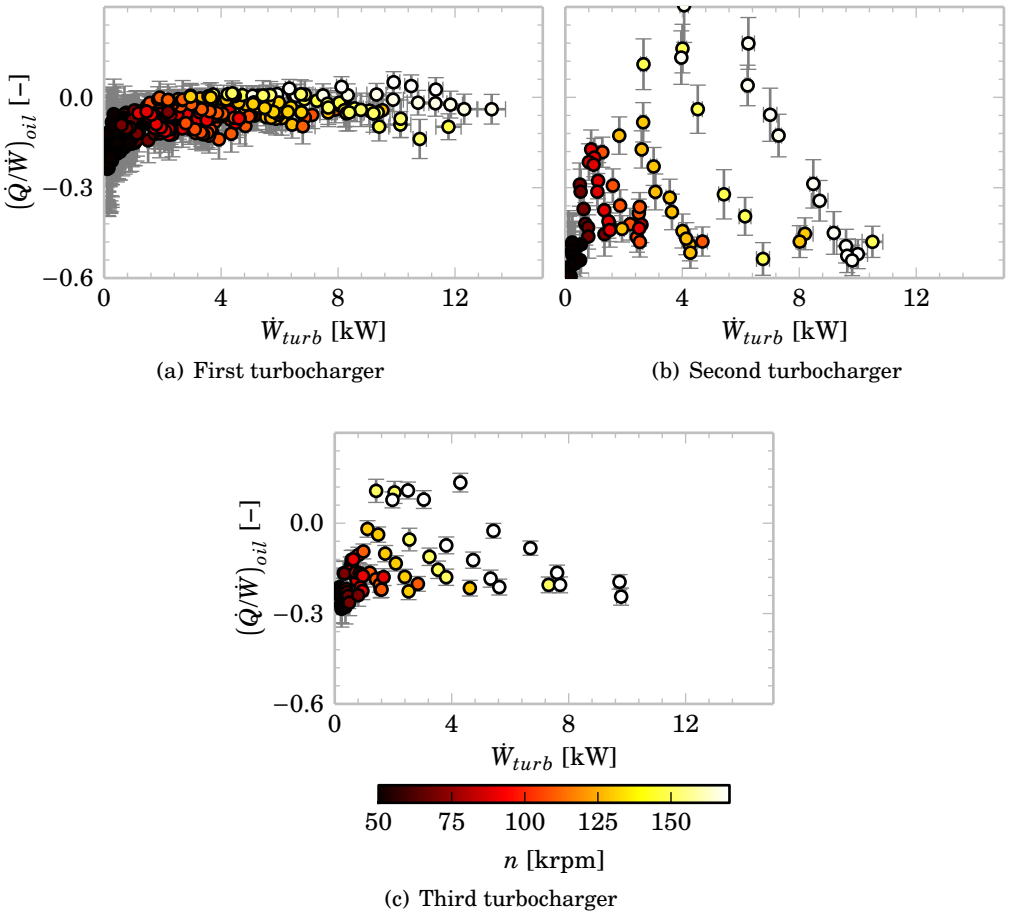

(a) First turbocharger

(b) Second turbocharger

(c) Third turbocharger

Figure 3.5: Estimated oil heat flow.

ratios, that is when the engine is at idle or at very low load that corresponds to a high number of operating conditions in the urban cycle [9, 10, 117]. The power drawn can be seen in Figure 3.7. The mechanical losses power is higher for bigger turbochargers, as expected, and rises with the rotational speed. The overpressure and low-pressure points have not been plotted in these two figures, and only one VGT configuration is shown. In Figure 3.8 the mechanical losses power is plotted against the turbine power output for all VGT positions and also for the low and high pressure points. The expanded uncertainty of the measurements is plotted as errorbars.

So, in these low load points the use of a fixed mechanical efficiency will lead to a very high error in modelling the turbocharger behaviour, and hence if a proper model of the turbocharger is expected, it is imperative to model as good

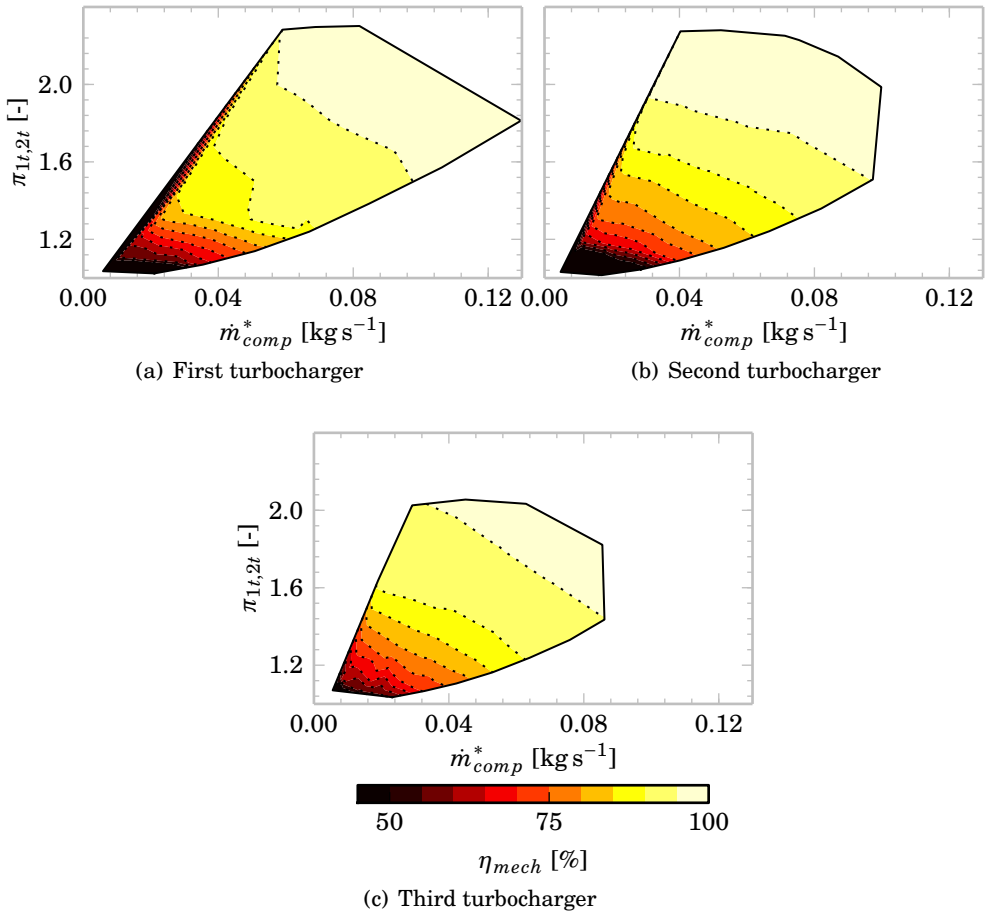

(a) First turbocharger

(b) Second turbocharger

(c) Third turbocharger

Figure 3.6: Measured mechanical efficiencies

as possible this efficiency (or mechanical losses).

Finally, it must be mentioned that oil viscosity has played an important role when obtaining the values of mechanical efficiency: at low compression ratios (due to the constraints in the measurements) oil temperatures are lower than those used at medium compression ratios. On the contrary, these oil temperatures are higher than those used in the beginning of the tests of the European cycle [118]. All the tests have been performed using standard 5W-30 engine oil. Its viscosity has been supposed to follow Vogel's equation (Equation 3.4) and has been calibrated with experimental data (see Figure 3.9). When using a higher viscosity oil, the mechanical losses power should rise accordingly.

$$\mu = \mu(T) = 4.374 \times 10^{-4} \cdot e^{\frac{5.420 \times 10^2}{T - 1.986 \times 10^2}} \tag{3.4}$$

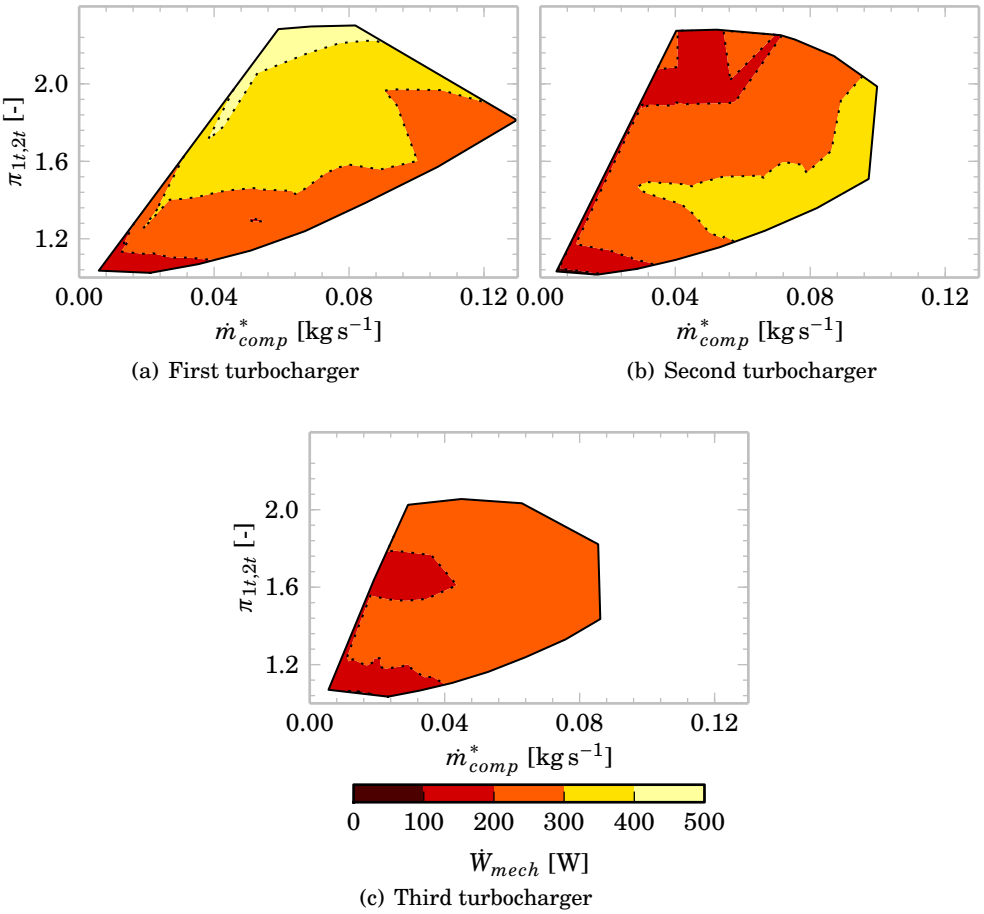

(a) First turbocharger

(b) Second turbocharger

(c) Third turbocharger

Figure 3.7: Measured mechanical losses power

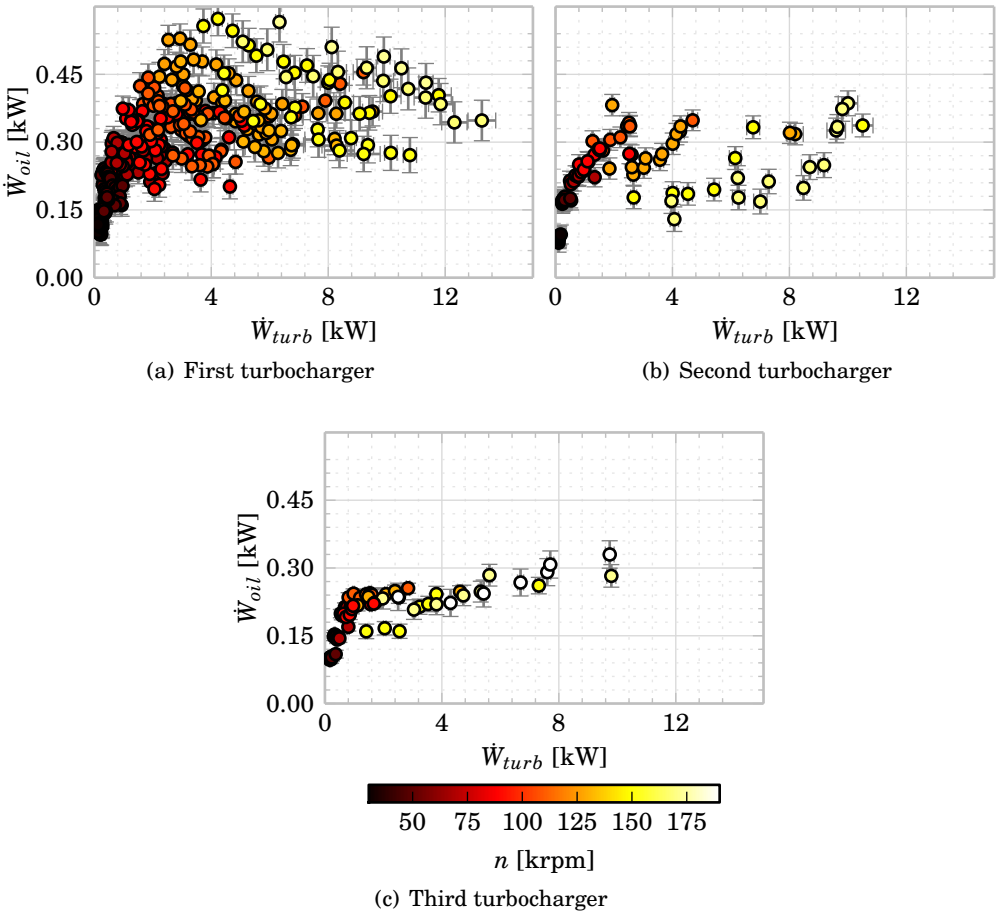

(a) First turbocharger

(b) Second turbocharger

(c) Third turbocharger

Figure 3.8: Measured mechanical losses power vs. turbine power

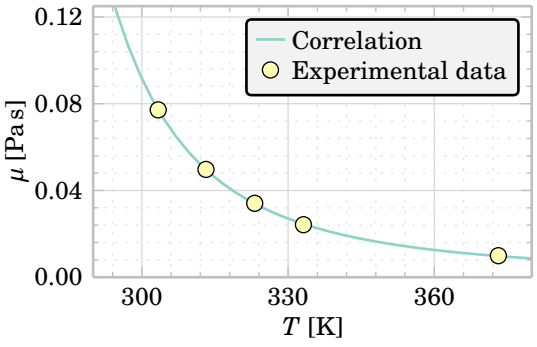

Figure 3.9: Oil viscosity

3.3 Global turbine performance

Experimental method

The turbine is globally characterised in a gas stand following [23] and [24]. When characterising the turbine, the compressor acts as a very limited brake due to surge and choke, so the obtained turbine map is quite reduced. The gas stand that was used during these tests, however, has the capability of working with a closed-loop in the compressor side, allowing to pressurise the compressor air loop to widen its braking performance. Near surge, the compressor inlet density can be lowered, reducing its required power to a minimum. Near choke, the compressor inlet density can be risen, increasing its required power for a given rotational speed. During the experiments, the compressor inlet pressure was lowered to near 50 kPa close to the surge line and was increased to 250 kPa at the highest mass flow rates. Several iso-speed lines were measured, separated by 20 krpm. All the tests were done under quasi-adiabatic conditions, as described in section 3.2. For each iso-speed line, the turbine and oil inlet temperatures were set to the quasi-adiabatic one, and the back-pressure valve of the compressor air loop was closed from choke to the surge line, reducing the turbine feeding pressure to maintain the shaft rotational speed. Each experimental point was measured after stabilisation during 30 s, registering the mean value of each variable during the measuring period.

During the characterisation, the pressures and temperatures at the turbine inlet and outlet were obtained, as well as the mass flow rate and the turbocharger body temperatures that are used to obtain its internal heat flow. The temperature was measured using four standard type K thermocouples per section, and their average value was used as the mean section temperature. The temperature probes that were used hadn't total temperature shields, so the measured temperature laid between the total and the static temperature. A typical kinetic energy recovery factor q 0.5 was used:

$$q = \frac{\widehat{T} - T}{T_t - T} \Rightarrow T = \widehat{T} - \frac{q}{2} \cdot \frac{u^2}{c_p} \tag{3.5}$$

where $\widehat{T}$ is the measured temperature, T is the static temperature, T_t is the total temperature and u is the mean flow speed at the measurement section. The flow speed was obtained by:

$$u = \frac{\dot{m}_{turb}}{\rho \cdot A} = \frac{\dot{m}_{turb} \cdot R \cdot T}{p \cdot A} \tag{3.6}$$

where ρ is the density, p is the pressure, $\dot{m}_{turb}$ is the turbine mass flow rate and A is the area of the measurement section.

The total temperature T_t and pressure p_t were obtained as:

$$T_t = T + \frac{u^2}{2 \cdot c_p} \tag{3.7}$$

$$p_t = p \cdot \left(\frac{T_t}{T} \right)^{\frac{\gamma}{\gamma - 1}} \tag{3.8}$$

Several VGT positions were tested, changing them after measuring each partial turbine map. The VGT position was fixed using a screw and nuts, and it was measured using an inductive displacement sensor.

The mass flow rate was measured downstream of the turbine after passing through a heat exchanger. The heat exchanger was needed to get a flow temperature at the flow meter similar to its calibrated value, thus minimising its measurement uncertainty. As there were a large distance between the turbine inlet measurement station and the flow meter, special care was taken to ensure airtight duct joints, performing leak tests after the gas stand set-up.

The geometry of the turbine was obtained disassembling it and taking photographs to get diameters and angles. The volute was used as a mould to get a silicone negative that was easily measured. The VGT was photographed at different positions to get the angles of their vanes.

Experimental study

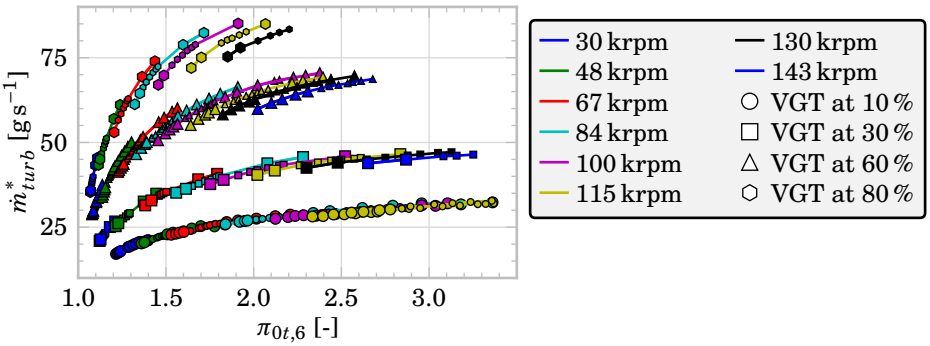

Figure 3.10: First turbocharger, turbine map

The measured turbine map for the first turbocharger is shown in Figure 3.10, where the points measured with a pressurised compressor air loop are highlighted with bigger markers. The width of the measurable map is clearly extended thanks to the pressurisation of the compressor at both low expansion ratios and high expansion ratios for each iso-speed line. More extension could

be achieved modifying the compressor wheel, such as removing its blades or attaching it to an external brake; these modifications, however, would be destructive, while the map extension technique that was employed didn't harm the structural integrity of the measured units.

The turbine corrected mass flow rate $\dot{m}^*_{turb}$ is plotted against its total to static expansion ratio p_{0t}/p_6, where p_{0t} is the total pressure at the turbine inlet duct and p_6 is the static pressure measured downstream of the turbine. The corrected mass flow rate is computed as:

$$\dot{m}^*_{turb} = \dot{m}_{turb} \cdot \frac{p_{ref}}{p_{0t}} \cdot \sqrt{\frac{T_{0t}}{T_{ref}}} \tag{3.9}$$

where $\dot{m}_{turb}$ is the measured turbine mass flow rate and T_{0t} is the total temperature at the turbine inlet duct. p_{ref} and T_{ref} are the reference pressure and temperature, respectively, and are set to 101 325 Pa and 288.15 K.

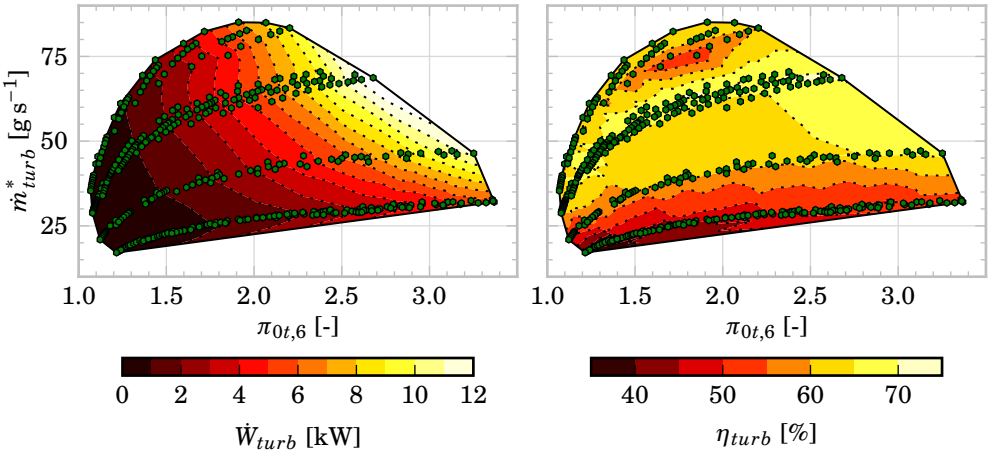

(a) Power output

(b) Efficiency

Figure 3.11: First turbocharger, turbine power output and efficiency

The fourth turbine is also globally characterised, although in this case it wasn't possible to pressurise the compressor air loop and, thus, the turbine map is less extended. This turbine is larger than the former, having a bigger swallowing capacity but a similar power output. The geometry of the stator vanes is also similar, having simple and straight blades. The outlet lacks the small plenum that exists in the first turbine.

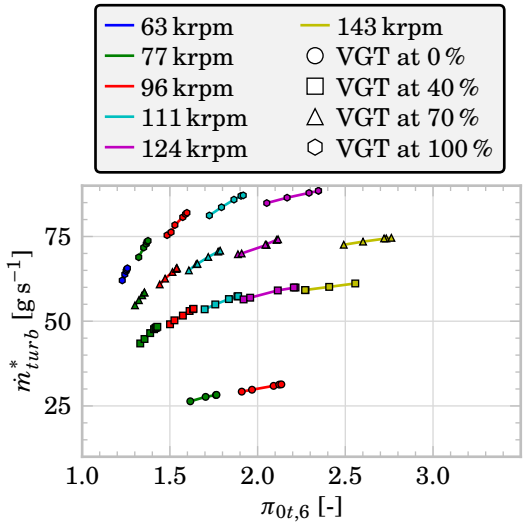

Figure 3.12: Fourth turbocharger, turbine map

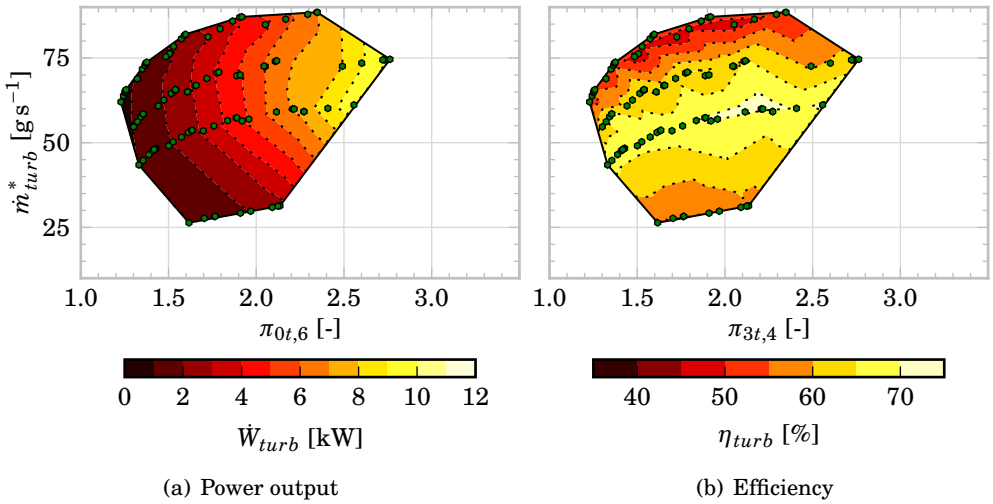

(a) Power output

(b) Efficiency

Figure 3.13: Fourth turbocharger, turbine power output and efficiency

3.4 Internal pressure in the turbocharger

Experimental method

As will be seen in section 5.6, the mechanical losses model needs information about the axial thrust in the shaft to properly estimate the oil film thickness in the thrust bearing and, thus, compute the dissipated power. There are two different approaches to measure this axial thrust: direct measurement or pressure distribution measurement. Both methods are difficult to accomplish due to the small size of automotive turbochargers, but some research is done in this area.

Deligant et al. [93] use a novel approach to measure the axial thrust: two units of the same turbocharger model are modified and coupled with a high speed torquemeter and a magnetic load is used to control the axial thrust. While this method gives accurate results, it needs profound modifications in usual automotive turbocharger research facilities. Also, there are, to the author's knowledge, a very limited supply of very high speed torquemeters (for rotational speeds of 160 krpm and up) in the market, being the shaft balancing a rather critical task that slows down the rapid turbocharger gas stand setup that characterises the typical research done by the institute of which the respondent is a member.

The second experimental technique used to estimate the axial thrust consists in the direct measurement of the air pressure in multiple points in both the compressor and turbine wheels. Again, the small dimensions of automotive turbochargers render this task unworkable. A less ambitious method is possible, however. The pressure distribution at the wheels can be approximated as in Figure 3.14, where the pressure has been supposed to vary linearly in the front side of each wheel, while staying constant in their back.

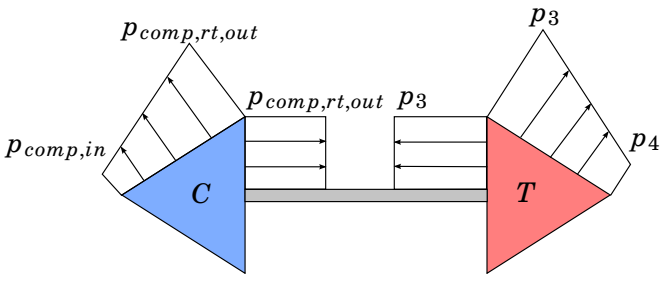

Figure 3.14: Pressure distribution in the wheels

Also, the pressure at the compressor wheel inlet can be supposed to be very similar to the pressure measured upstream, while at the rotor outlet it should be similar to the pressure measured downstream of the turbine. Using these

assumptions, the only unknown quantities are the pressure at the compressor wheel outlet and the turbine rotor inlet.

The measured pressure at the rotor inlet and outlet can vary to a great degree in different azimuthal points due to small differences in the radius at which the probe is set or due to the wake of the stator blades in the turbine case. Several probes should be used in both the compressor and the turbine in order to get a mean value that is representative of the real mean pressure at the rotor outlet or inlet. The realisable number of probes is limited by their diameter and the accessibility of the turbocharger casing.

Unfortunately, the three turbocharger units used during the mechanical losses characterisation were not available at the time these tests were done, so a fourth unit was used. Three pressure probes were used to measure the pressure at the compressor rotor outlet, and four in the turbine rotor inlet. The turbine probes were placed in points immersed in the wake of the vanes, in the wake of the VGT screws and in points free of wakes. All the probes measure 1.5 mm in diameter. The tests were done in quasi-adiabatic conditions, thus minimising the heat flux between the different parts of the turbocharger. The internal pressure tests can also be used to calibrate and validate the quasi-bidimensional turbine model that is presented in chapter 5, so pressure probes were installed not only in the stator outlet, but also across the volute and at the rotor outlet. The instrumented turbine housing is shown in Figure 3.15.

Figure 3.15: Turbine instrumented for internal pressure characterisation

The turbine probes are placed as follows:

- Mean pressure:

  - Seven at different angles in the volute.
  - Four in the stator outlet.
  - One in the turbine rotor outlet.
  - Three in the turbine outlet.

- Instantaneous pressure:
  - Two in the volute.
  - One in the stator outlet.

The mean pressure probes are used to calibrate the model, while the instantaneous pressure signals are used to validate it during pulsating operation similar to that found in real engine applications.

Several probes were used in the volute because, although its pressure should be almost uniform in close to design conditions, it may present non-uniformities far from that ideal conditions. Also, only one instantaneous pressure probe could be set in the stator outlet due to physical accessibility constraints, so its measurements should be taken with care. The mean stator pressure probes, as has been already said, were placed in different points trying to get measurements with and without wakes.

The heat flow has been maintained as low as possible during the experimental campaign, as described in section 3.2. To ensure it, the turbine and lubrication inlet temperatures have been set to be close to the compressor outlet temperature, with a maximum allowed discrepancy of $\pm 6\,\mathrm{K}$ and a mean value of $\pm 2.5\,\mathrm{K}$. Also, as the compressor outlet temperature is relatively low, the heat flow to the ambient is bounded to a small amount of around 2 % of the measured turbine power output, as can be seen in Figure 3.16. This heat flow to the ambient has been estimated using the ambient temperature T_{amb}, the maximum surface temperature of the turbine $T_{exposed}$ and the exposed surface of the ducts and turbine $A_{exposed}$, and assuming a convective heat transfer coefficient h_{conv} of $10\,\mathrm{W\,m^{-2}\,K^{-1}}$:

$$\dot{Q}_{amb} = A_{exposed} \cdot h_{conv} \cdot \left(T_{exposed} - T_{amb}\right) \tag{3.10}$$

The turbine power is estimated using the total enthalpy flow:

$$\dot{W} = \dot{m} \cdot c_p \cdot (T_{6t} - T_{0t}) \tag{3.11}$$

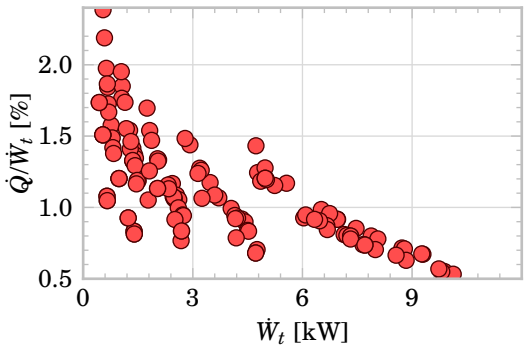

Figure 3.16: Expected error in turbine power output due to external heat flow effects.

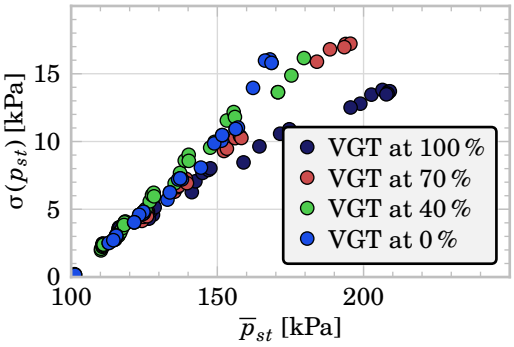

Figure 3.17: $\sigma(p_{st})$ during the experimental campaign

Experimental study

During the first steady-state tests, the pressure was very similar across all the volute probes, with differences in the range of few hPa. As the measurement uncertainty was of the same order, their mean value was used for the calibration and validation phase. Larger fluctuations appeared in the stator and rotor outlets, and mean values were also used. The large variations in the stator outlet are assumed to be due to the presence of wakes: these wakes are produced by the stator vanes and screws. As can be seen in Figure 3.17, the standard deviation of the stator pressure $\sigma(p_{st})$ is more or less linear with the measured pressure and it is higher when the stator is closed. The fluctuations at the rotor outlet are produced by the highly three-dimensional flow present at that section. As the model that is presented in chapter 5 does not cope with these three-dimensional effects, the mean pressure of the section will be used for its validation.

The compressor was also instrumented with pressure probes in the volute, although these results are not used in the present work.

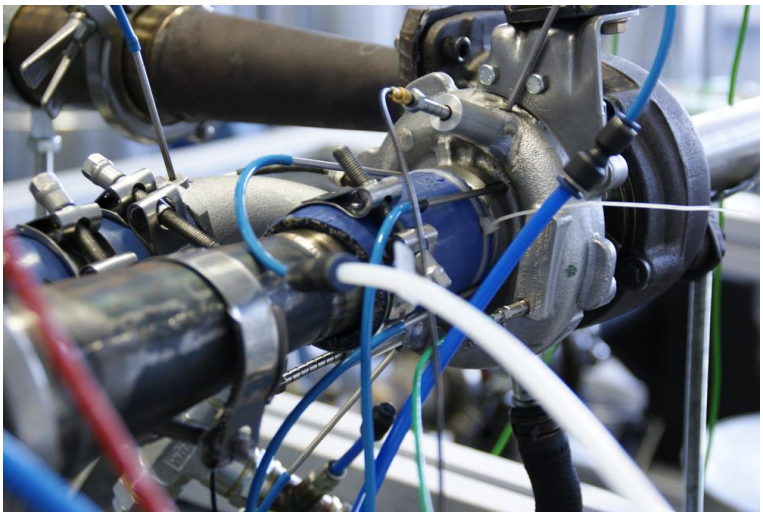

Figure 3.18: Compressor instrumented for internal pressure characterisation

The compressor map is shown in Figure 3.19. It has been measured with leaps of 20 krpm in speed, from the surge line to the maximum achievable mass flow rate. The highest iso-speed line, at 180 krpm, is only measured partially due to the quasi-adiabatic limitations of the test: at that speeds, the needed oil temperature is not safe and produces oil degradation. The high pressures at the compressor outlet were also a concern while using the internal pressure probes, as the little accessibility during their assembly did not provide enough room to properly screw them with the maximum torque.

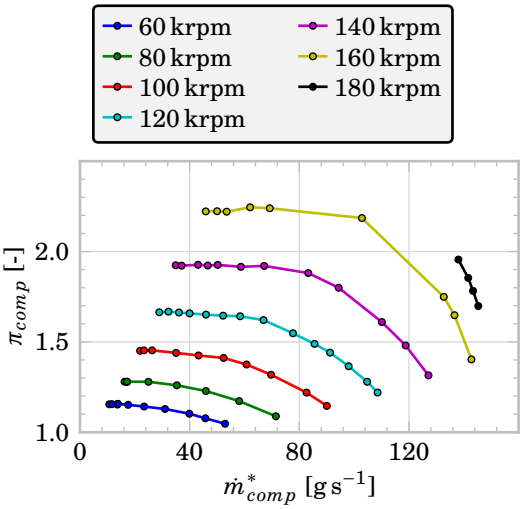

Figure 3.19: Fourth turbocharger, compressor map

The turbine map is shown again in Figure 3.20. Again, it has been measured with leaps of 20 krpm in shaft speed, from the compressor surge line to the maximum mass flow rate, at four different positions of the VGT. In this case, the probes were welded to the turbine case, so the pressure was not a concern, but the maximum speed was again limited due to high temperatures.

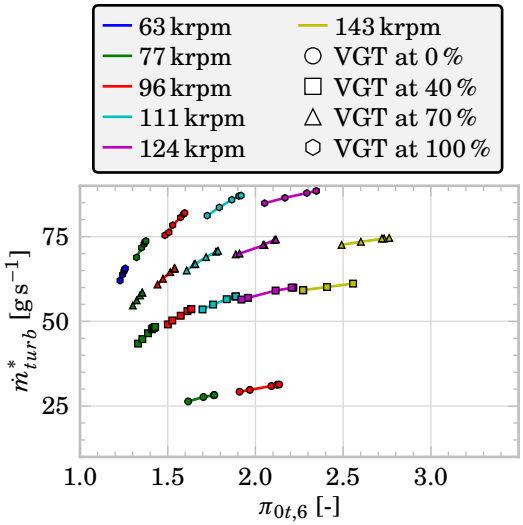

Figure 3.20: Fourth turbocharger, turbine map

The pressure difference between the compressor rotor outlet and the compressor inlet is shown in Figure 3.21, divided by the total pressure leap in the compressor. This pressure difference appears to be a function, above all, of the relative distance to the surge line: near this surge line, the pressure at the wheel outlet has a value similar to that at the compressor outlet, while its level approaches the arithmetic mean between the inlet and outlet pressures when the mass flow rate rises up to near-choke values. The influence of the rotor speed is of a lesser

degree.

The pressure difference between the turbine outlet pressure and the rotor inlet pressure, divided by the whole pressure leap in the turbine, is plotted in Figure 3.22. The mean influence in this pressure difference is due to the position of the stator blades: the stator outlet pressure is closer to the turbine inlet pressure as the VGT opens. These results can be explained by the rising stator pressure losses expected when closing the VGT. The pressure difference also rises with higher mass flow rates.

Further experimental results are needed to extract definitive conclusions, but it seems that, if no information about the internal pressure is available and at a first approximation, the compressor rotor outlet pressure can be supposed to be the mean value between the inlet and the outlet of the whole compressor. For better accuracy, a linear variation between choke and surge is expected to give better accuracy in these cases. The turbine rotor inlet pressure has to be approximated in a similar way when no information is available, varying with the VGT position and the mass flow rate. Of course, more complex computational models can be used when available.

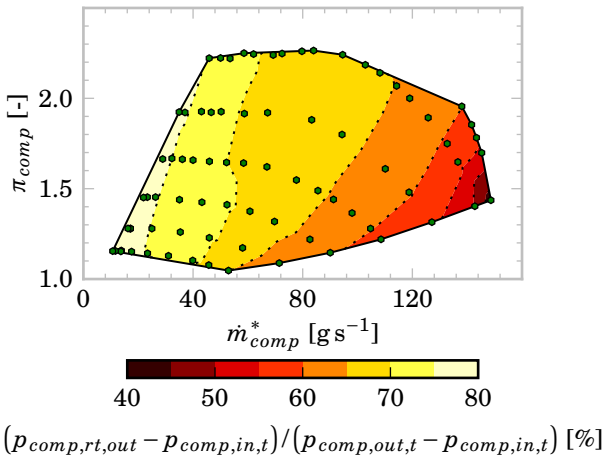

Figure 3.21: Fourth turbocharger, compressor rotor outlet pressure

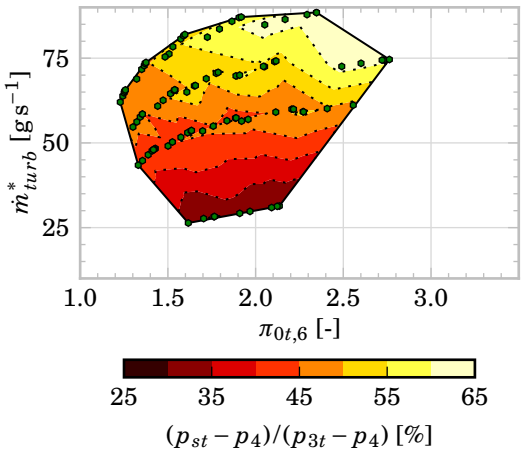

Figure 3.22: Fourth turbocharger, turbine rotor inlet pressure

3.5 Turbine pulsating flow

Pressure decomposition

The first turbocharger was measured under pulsating flow conditions generated by means of a rotating valve placed upstream of the turbine. The law of aperture of the disc was designed to approximate the behaviour of that found in the exhaust manifold of a four cylinder, four strokes reciprocating engine. Several engine configurations were simulated in the gas stand:

- 2000 rpm, 25 % of maximum BMEP.
- 2000 rpm, 100 % of maximum BMEP.
- 3000 rpm, 50 % of maximum BMEP.
- 3000 rpm, 75 % of maximum BMEP.
- 3000 rpm, 100 % of maximum BMEP.
- 3500 rpm, 100 % of maximum BMEP.

The original amplitude of the pulses was obtained in a real two-litre diesel engine.

The rotating valve is a heavily-modified turbocharger. It lacks both the turbine and compressor wheels and volutes, and it is driven by an electrical engine attached to the compressor side. A disc with several windows is placed at the turbine side, which opens and closes the air flow path as it rotates. The shaft

of the valve has oil film bearings fed by the test rig independent lubrication system, and can withstand high temperatures of up to 900 K, although only relatively low temperatures were needed during these tests. The frequency of the pulse was controlled varying the frequency of the electrical engine power supply from 0 Hz to 50 Hz: as the discs had three windows, it was possible to simulate a four-strokes, four cylinder engines running at up to 4500 rpm. A bypass valve was used in parallel with the rotating valve to adjust the pulse amplitude for a given mean turbine mass flow rate. The pulse amplitude was also adjusted by swapping the discs.

Figure 3.23: Rotating valve discs

An array of three piezoelectric transducers was used at both the turbine inlet and outlet for beamforming purposes, so the pressure could be decomposed in an incident and a reflected wave at the turbine inlet and in a transmitted and a second reflection at the turbine outlet, as described in the work by Piñero et al. [39]. This process has been done using the following assumptions:

- The array aperture is small compared with the pressure wavelength.
- The flow speed is equal to the linear superposition of a forward and a backward flow velocities.
- There is a linear propagation of both the pressure and the sound speed.
- The incidence angles of the forward and backward waves are different.

The distance between the sensors was set to 5 cm to get a good compromise between the measurement precision and the linear propagation of the waves between the sensors. Too large apertures can't be used due to loss of linear behaviour, and too small apertures lead to differences between the measurement

of the different sensors that are of the same order of the measurement uncertainty, rendering the method invalid. The sensors used were high sensitivity, acceleration compensated Kistler 7031 transducers, with water cooled adaptors. The water cooled adaptors were needed in order to reduce the effect of the flow temperature in the measurement uncertainty.

The signal of the sensors was measured with a calibrated data acquisition unit operating at a sampling frequency of 100 kHz. As the piezoelectric transducers don't measure the very low frequency components of the pressure, piezoresistive sensors were used to get its mean value.

The test matrix was as follows:

Table 3.5: Pulsating flow test matrix, first turbocharger

Engine speed [rpm]	Load [%]	Pulse frequency [Hz]	Pulse amplitude [kPa]	Mean inlet pressure [kPa]	VGT position [%]	Turbo speed [krpm]
2000	25	66.67	34	141	49	57.50
2000	100	66.67	45.60	261	47	110.60
3000	50	100	55.30	194	80	99
3000	75	100	60	263	58	121.80
3000	100	100	49.20	304	50	123.30
3500	100	116.67	50.50	280	55	124.10

The level of entropy A_A, defined as:

$$A_A = \sqrt{\frac{T}{T_{ref}} \cdot \left(\frac{p_{ref}}{p}\right)^{\frac{\gamma-1}{2\cdot\gamma}}} \tag{3.12}$$

(where T_{ref} is a reference temperature, p_{ref} is a reference pressure and γ is the specific heat capacities ratio) is supposed to be constant during each pulsating flow test, leading to an isentropic relationship between the instantaneous temperature and pressure at the turbine inlet and outlet.

The flow speed associated to the forward wave p_{right} is:

$$u_{right} = \frac{2\cdot a_{ref}}{\gamma-1} \cdot \left[\left(\frac{p_{right}}{p_{ref}}\right)^{\frac{\gamma-1}{2\cdot\gamma}} - 1\right] \cdot A_A \tag{3.13}$$

whereas the flow speed associated to the backwards wave p_{left} is:

$$u_{left} = -\frac{2\cdot a_{ref}}{\gamma-1} \cdot \left[\left(\frac{p_{left}}{p_{ref}}\right)^{\frac{\gamma-1}{2\cdot\gamma}} - 1\right] \cdot A_A \tag{3.14}$$

where a_{ref} is the speed of sound at T_{ref}.

In these conditions, the instantaneous mass flow rate can be estimated:

$$\begin{aligned}\dot{m} &= \rho \cdot A \cdot u = \rho \cdot A \cdot \left(u_{right} + u_{left}\right) \\ &= \frac{p}{R \cdot T} \cdot A \cdot \frac{2 \cdot a_{ref}}{\gamma - 1} \cdot \left[\left(\frac{p_{right}}{p_{ref}} \right)^{\frac{\gamma-1}{2\cdot\gamma}} - \left(\frac{p_{left}}{p_{ref}} \right)^{\frac{\gamma-1}{2\cdot\gamma}} \right] \cdot A_A \end{aligned} \tag{3.15}$$

The instantaneous pressure decomposition can be found in Figures 3.25 to 3.27, whereas Figure 3.28 shows the estimated instantaneous mass flow rate at the turbine inlet and outlet. The sound pressure level is obtained using a reference pressure of 20 µPa, estimating the power spectral density by Welch's periodogram method [119], windowing the data with a Hanning window [120]. An abrupt decrease in the pressure amplitude for frequencies higher than 600 Hz is found at the turbine outlet, which might be caused by a plenum placed at the turbine outlet inside the turbine housing (see Figure 3.24). The amplitude of the instantaneous evolution of the mass flow rate is greatly reduced after passing through the turbine, in part due to the lamination of the pulses done by the turbine and in part due to the length of the ducts. The high frequency oscillations observed in the last case might be caused by electrical noise.

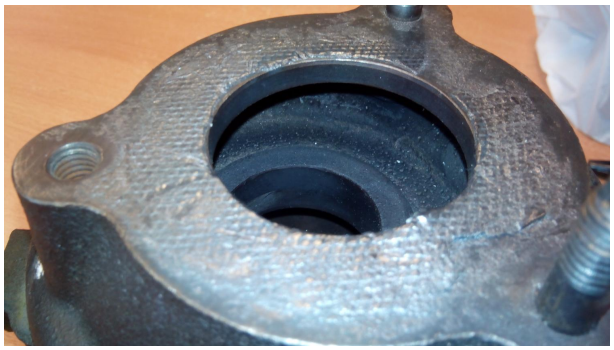

Figure 3.24: Outlet plenum in the first turbocharger

The differences in attenuation between different VGT positions seems to be small, in both pressure waves and instantaneous mass flow rate.

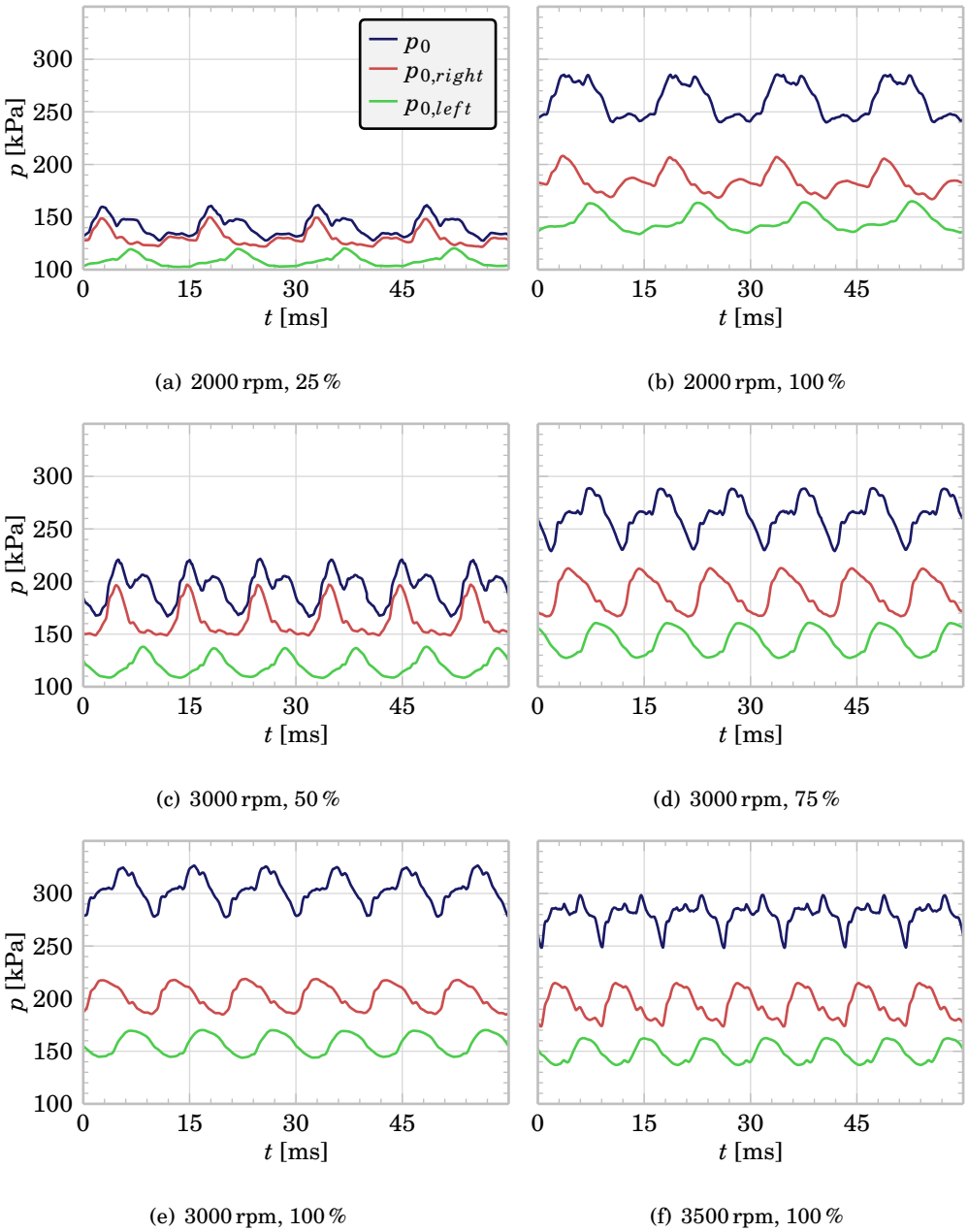

(a) 2000 rpm, 25 %

(b) 2000 rpm, 100 %

(c) 3000 rpm, 50 %

(d) 3000 rpm, 75 %

(e) 3000 rpm, 100 %

(f) 3500 rpm, 100 %

Figure 3.25: First turbocharger instantaneous results, inlet pressure

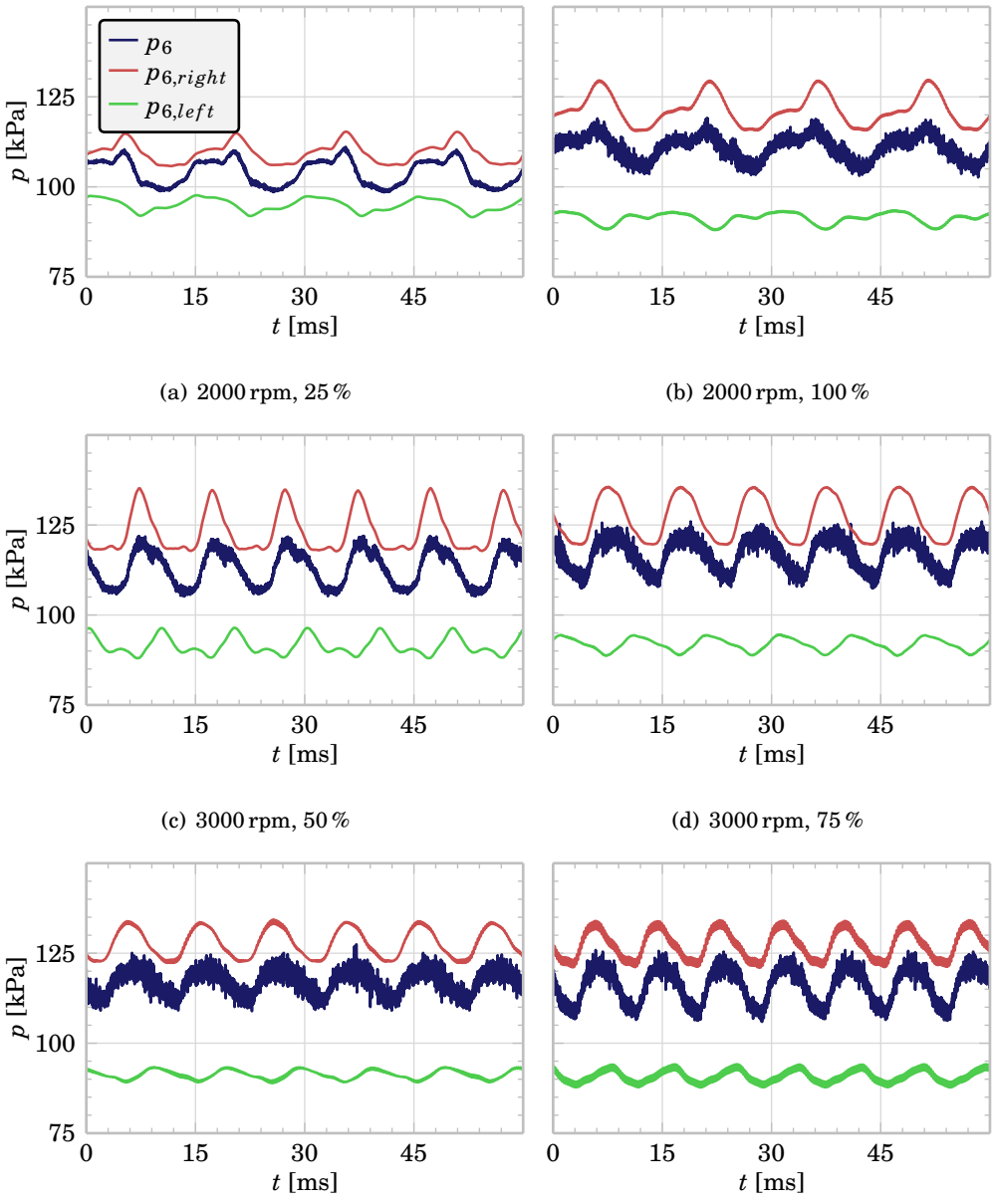

(a) 2000 rpm, 25 %

(b) 2000 rpm, 100 %

(c) 3000 rpm, 50 %

(d) 3000 rpm, 75 %

(e) 3000 rpm, 100 %

(f) 3500 rpm, 100 %

Figure 3.26: First turbocharger instantaneous results, outlet pressure

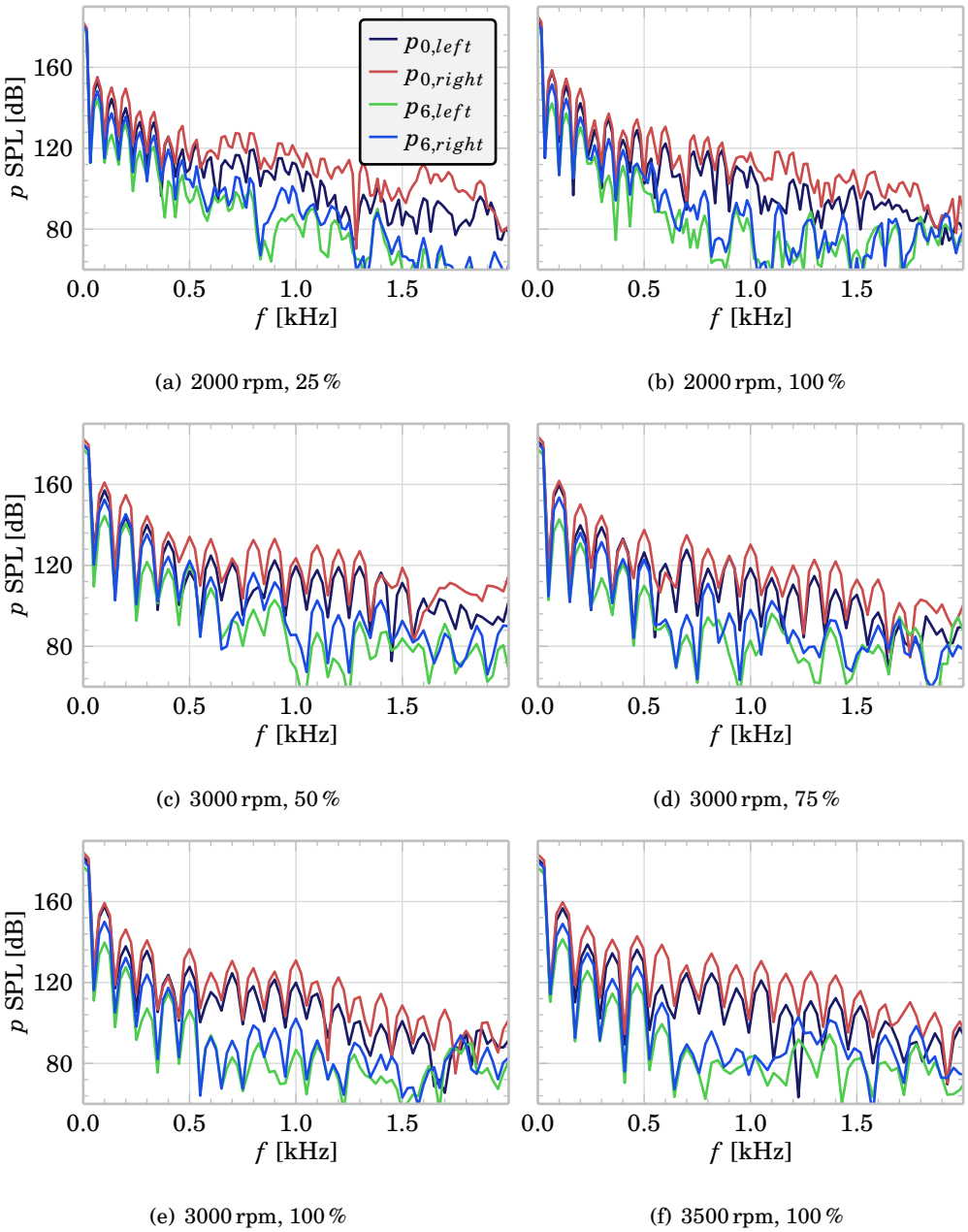

(a) 2000 rpm, 25 %

(b) 2000 rpm, 100 %

(c) 3000 rpm, 50 %

(d) 3000 rpm, 75 %

(e) 3000 rpm, 100 %

(f) 3500 rpm, 100 %

Figure 3.27: First turbocharger instantaneous results, sound pressure level

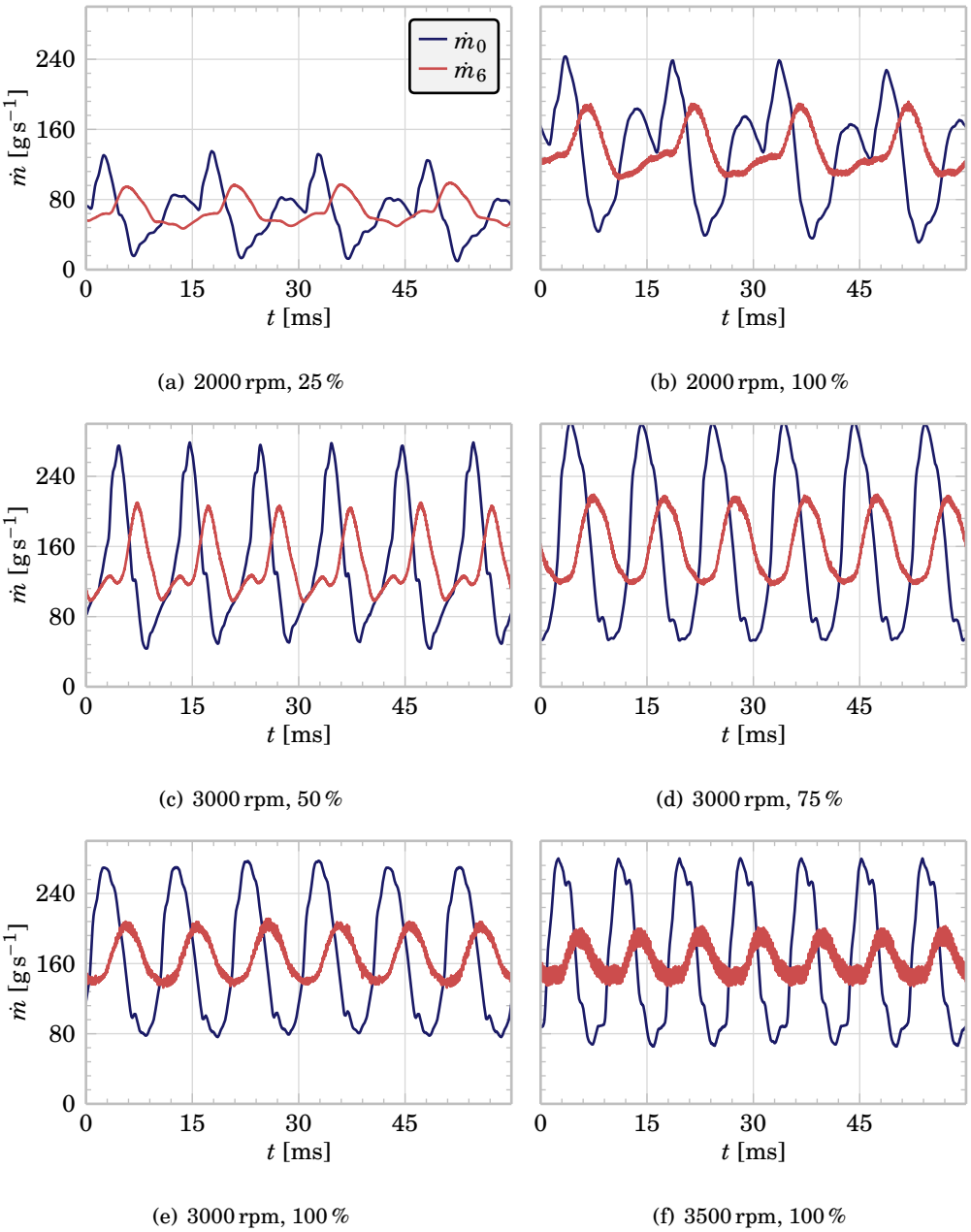

(a) 2000 rpm, 25 %

(b) 2000 rpm, 100 %

(c) 3000 rpm, 50 %

(d) 3000 rpm, 75 %

(e) 3000 rpm, 100 %

(f) 3500 rpm, 100 %

Figure 3.28: First turbocharger instantaneous results, mass flow rate

Pulsating internal pressure

The fourth turbocharger was measured under pulsating flow using a low temperature rotating valve as a pulse generator. The law of aperture of the disc was designed to resemble that of the intake or exhaust ports of a two-stroke engine.

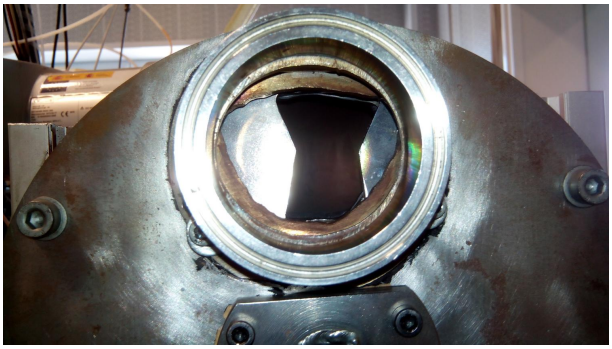

Figure 3.29: Cold flow rotating valve disc

In this case, the shaft is held by two ball bearings, so it can not withstand high temperatures. Flow leakages around the disc clearance are reduced, however, so higher amplitude pulses can be achieved. During these tests, no real engine points were simulated in the gas stand and the maximum pulse amplitude was searched for, so no bypass valve was used. The rotational speed of the disc was controlled by means of an electrical rotor driven by a variable-frequency power supply. The disc had four windows, allowing to generate pulses of up to 200 Hz.

There were no enough sensors available to build a beamforming array during the execution of these experiments, and only the composed pressures were measured. The instantaneous pressure was measured upstream of the turbine, downstream of the turbine, in two different points of the volute and at the stator outlet. The first volute probe, which measures $p_{vol,1}$, is placed near the tongue, while the second volute probe ($p_{vol,2}$) is placed at the central section; these transducers are piezoelectric and can't measure the mean pressure. The transducer at the stator outlet is piezoresistive and can withstand temperatures of up to 573 K, although incurring in increasing uncertainties as the process temperature rises; due to spacing problems, only one instantaneous transducer was placed at the stator outlet, so its measurement might have been affected by wakes.

Figure 3.30 shows the turbine housing. The instantaneous pressure probes location is visible as the two cylinders in the volute and the hole that passes through the turbine outlet flange.

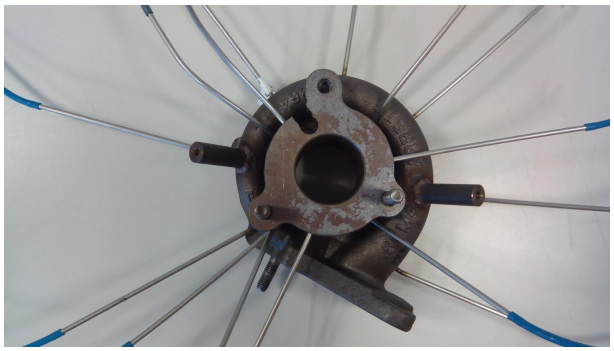

Figure 3.30: Fourth turbocharger, instantaneous pressure probes location

As in the other experiments, the tests were performed under quasi-adiabatic conditions. The test matrix is shown in Table 3.6.

Table 3.6: Pulsating flow test matrix, fourth turbocharger

VGT position [%]	Turbo speed [krpm]	Pulse frequency [Hz]	Pulse amplitude [kPa]	Mean inlet pressure [kPa]
100	100	60	100	166
		100	80	165
	140	60	162	254
		100	125	250
70	100	60	81	160
		100	64	156
	140	60	139	233
		100	103	228
40	100	60	62	166
		100	45	165
	140	60	110	245
		100	80	241

In all cases, a reduction of the pulse amplitude was observed when changing from 60 Hz to 100 Hz. The attenuation between p_0 and p_3 is small compared with the attenuation from p_3 to p_6, but it slowly grows while closing the VGT due to higher flow restrictions. The highest attenuation occurs at the rotor, as the flow losses part of its momentum to move the wheel. Of course, as it was only possible to place a single instantaneous transducer at the stator outlet, the

instantaneous evolution of the average pressure is measured with a high level of uncertainty: this probe might have been affected by wakes in some points and not in others. In this case, as opposite to the first turbocharger results, there is no abrupt pressure attenuation at high frequencies at the turbine outlet. This turbine lacks an outlet plenum, as seen in Figure 3.31, which ostensibly is the responsible of such attenuations.

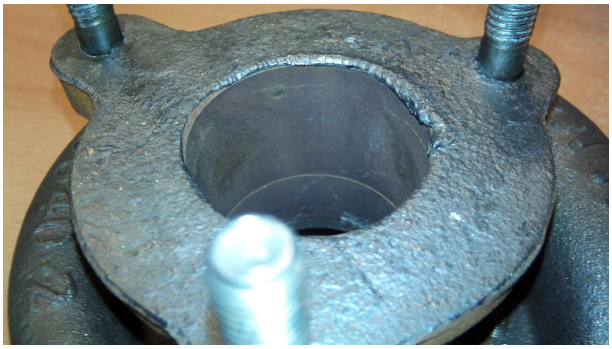

Figure 3.31: Lack of outlet plenum in the fourth turbocharger

It is interesting to note that the pressure amplitude doesn't decrease while travelling the volute: as some mass, momentum and energy is lost as the flow travels it, this effect is compensated with smaller sections. Turbine volutes are designed to have uniform pressure at their design conditions, and it appears to be the case not only for the mean value of the pressure but also for its instantaneous evolution. The most appreciable differences in amplitude appears to be at high frequencies, however, when the wavelength is comparable to the length of the volute.

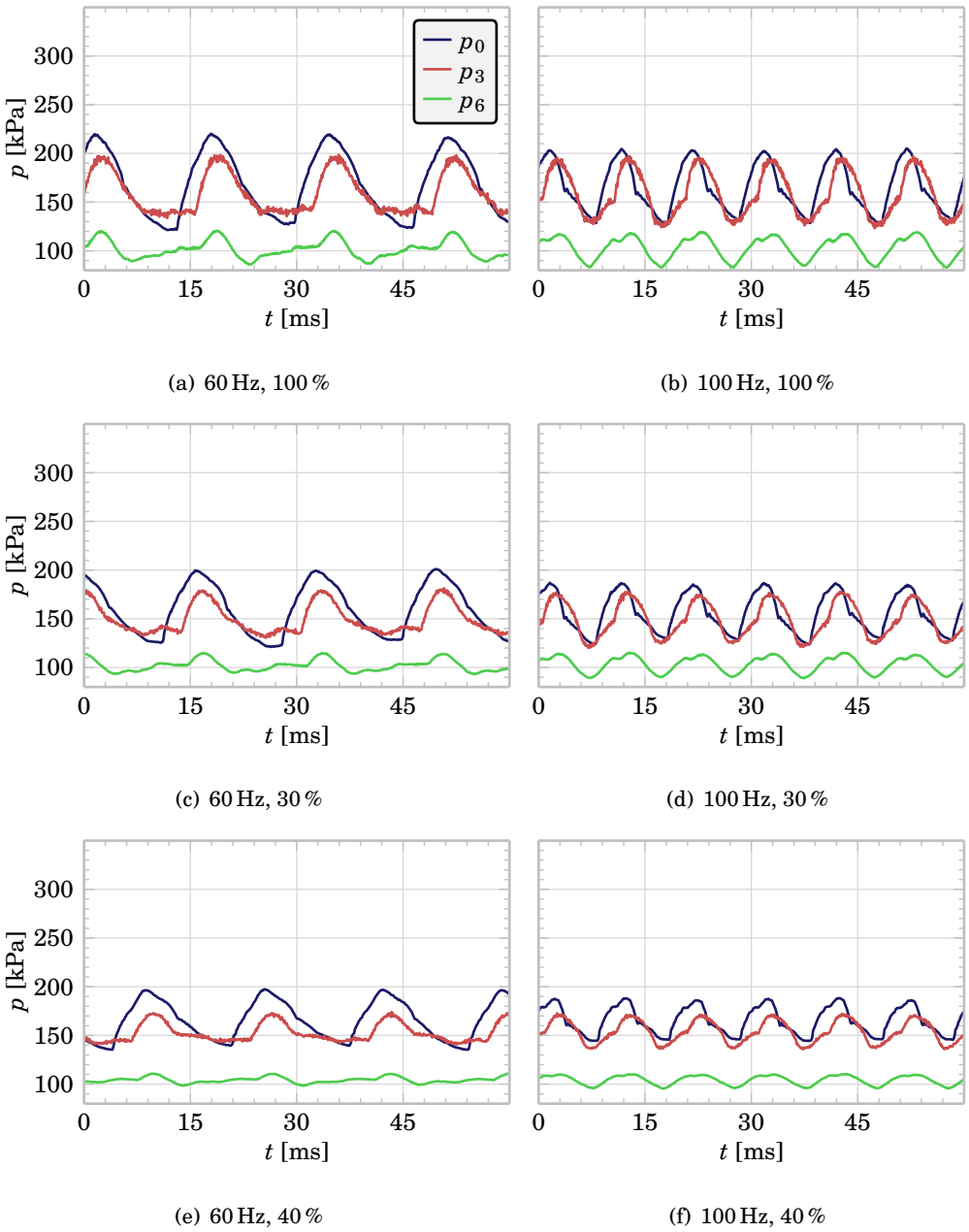

(a) 60 Hz, 100 %

(b) 100 Hz, 100 %

(c) 60 Hz, 30 %

(d) 100 Hz, 30 %

(e) 60 Hz, 40 %

(f) 100 Hz, 40 %

Figure 3.32: Fourth turbocharger instantaneous results at 100 krpm, pressure

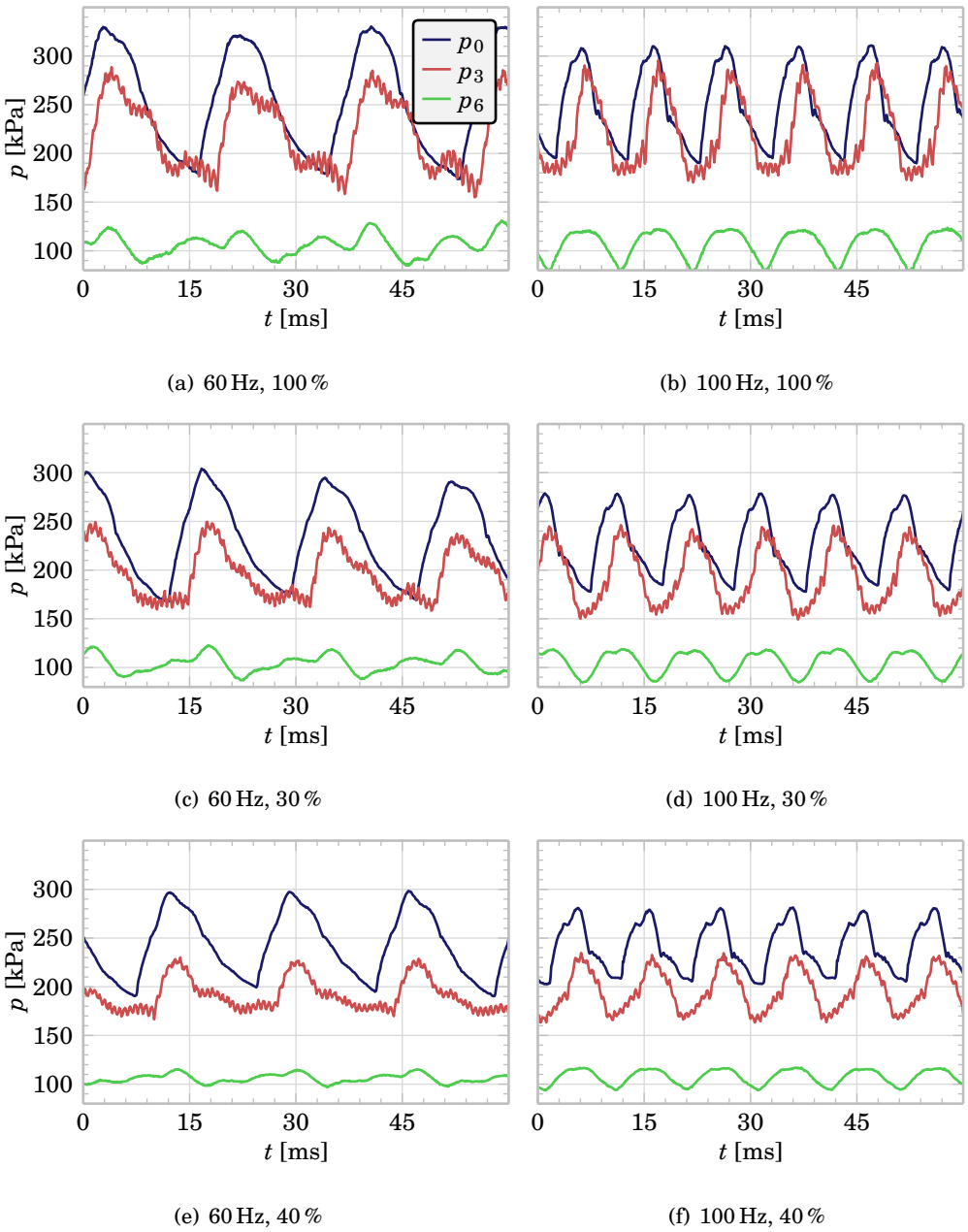

(a) 60 Hz, 100 %

(b) 100 Hz, 100 %

(c) 60 Hz, 30 %

(d) 100 Hz, 30 %

(e) 60 Hz, 40 %

(f) 100 Hz, 40 %

Figure 3.33: Fourth turbocharger instantaneous results at 140 krpm, pressure

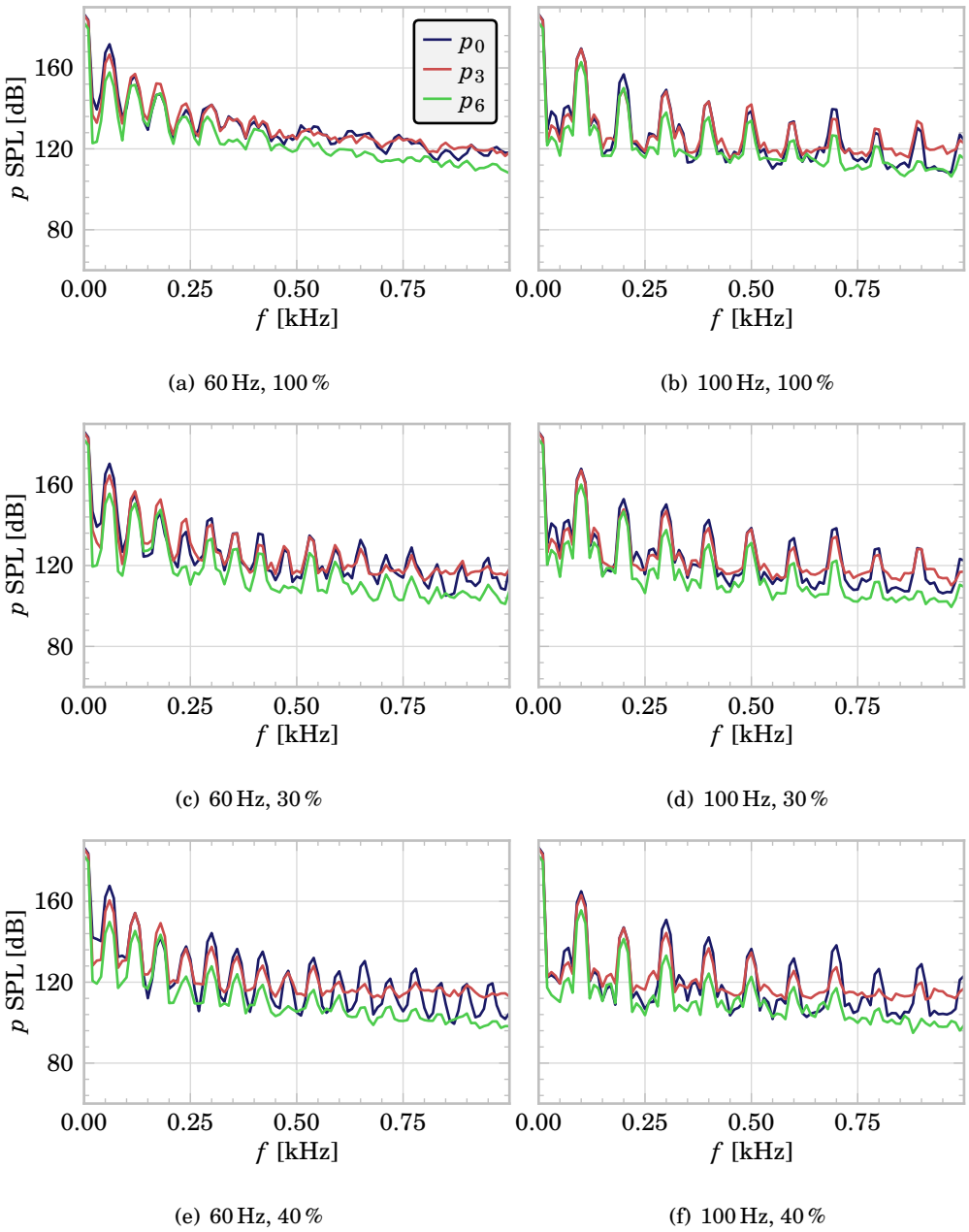

(a) 60 Hz, 100 %

(b) 100 Hz, 100 %

(c) 60 Hz, 30 %

(d) 100 Hz, 30 %

(e) 60 Hz, 40 %

(f) 100 Hz, 40 %

Figure 3.34: Fourth turbocharger instantaneous results at 100 krpm, sound pressure level

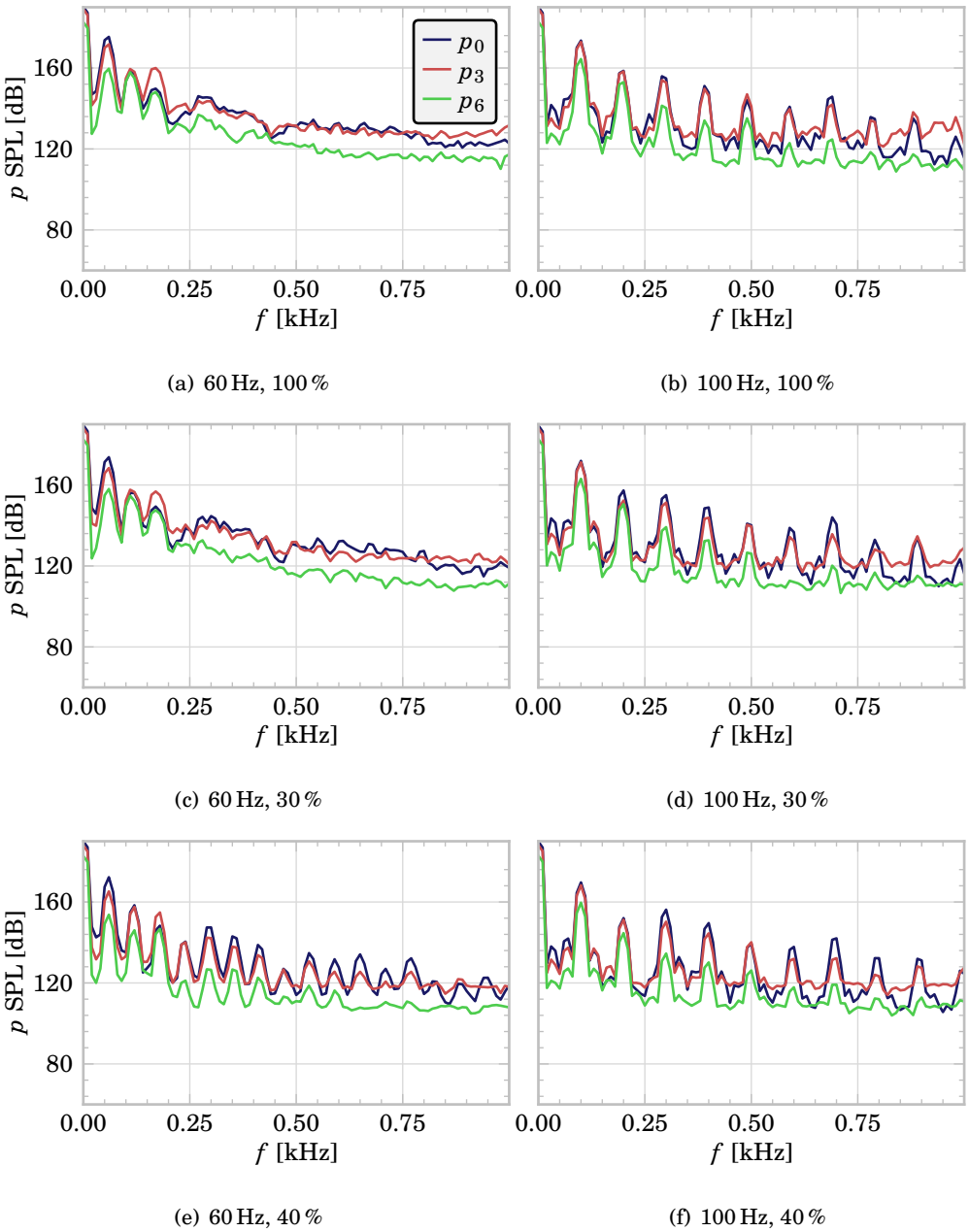

(a) 60 Hz, 100 %

(b) 100 Hz, 100 %

(c) 60 Hz, 30 %

(d) 100 Hz, 30 %

(e) 60 Hz, 40 %

(f) 100 Hz, 40 %

Figure 3.35: Fourth turbocharger instantaneous results at 140 krpm, sound pressure level

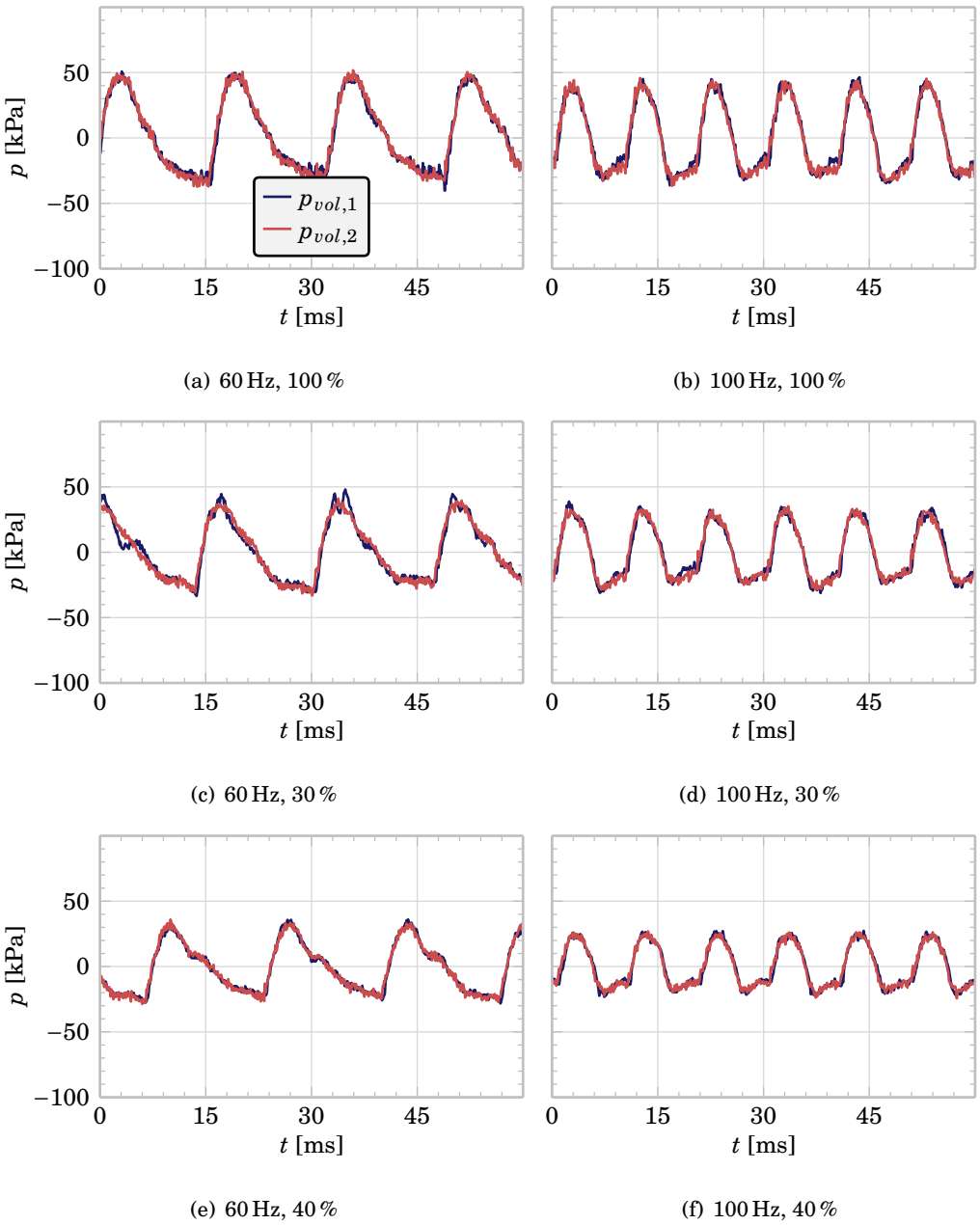

(a) 60 Hz, 100 %

(b) 100 Hz, 100 %

(c) 60 Hz, 30 %

(d) 100 Hz, 30 %

(e) 60 Hz, 40 %

(f) 100 Hz, 40 %

Figure 3.36: Fourth turbocharger instantaneous results at 100 krpm, volute pressure

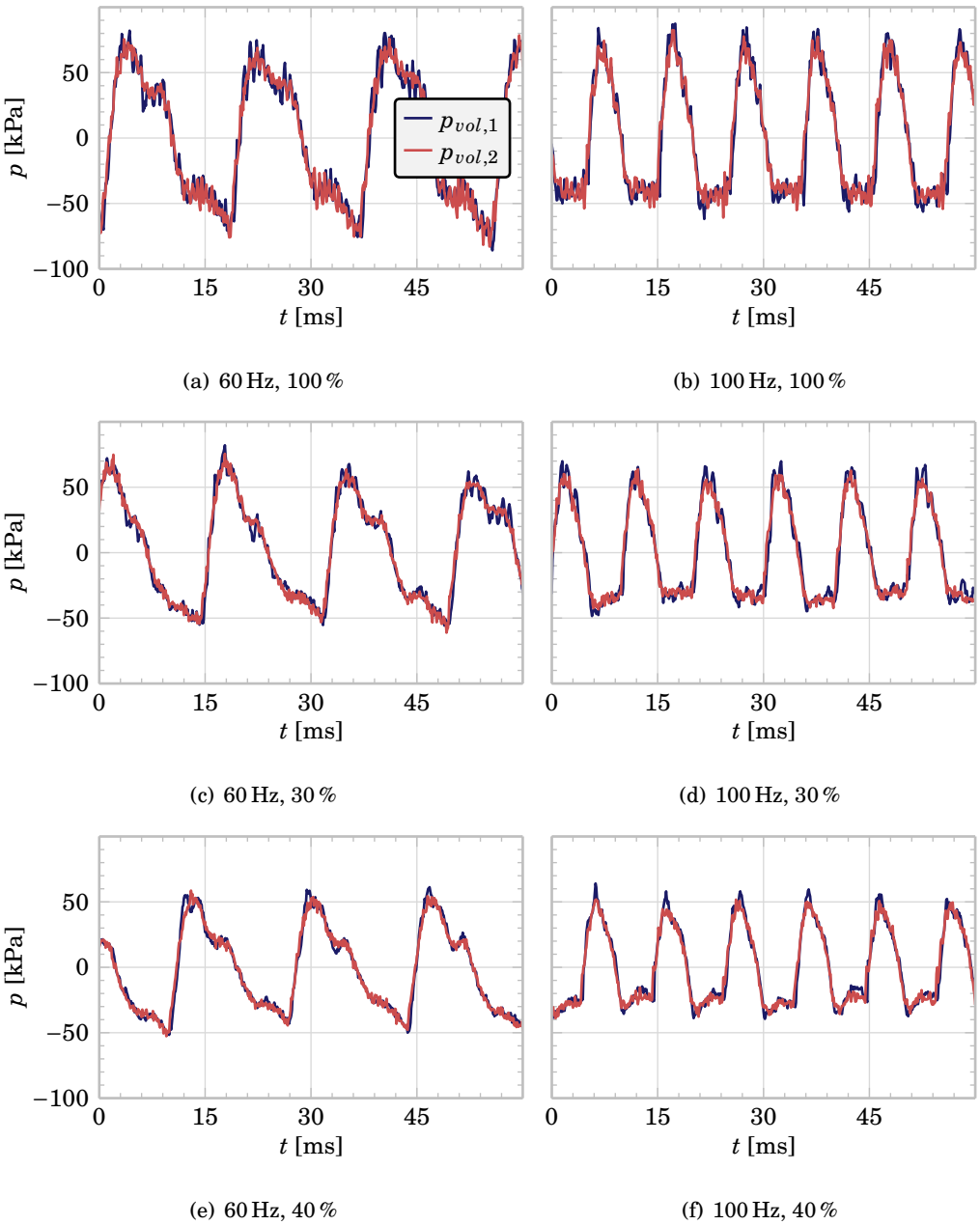

(a) 60 Hz, 100 %

(b) 100 Hz, 100 %

(c) 60 Hz, 30 %

(d) 100 Hz, 30 %

(e) 60 Hz, 40 %

(f) 100 Hz, 40 %

Figure 3.37: Fourth turbocharger instantaneous results at 140 krpm, volute pressure

3.6 Summary

In this chapter, the experimental methods and results used to characterise turbocharger mechanical losses and turbine performances are described and presented. The measurements have been done in two different turbocharger gas stands, properly set up to measure the specific variables needed to calibrate and validate the models that will be presented in chapter 5.

First, three different turbochargers were prepared to measure their internal heat fluxes as described in [111]. Then, after thermally insulating them, they were globally characterised under quasi-adiabatic steady flow. During this characterisation the energy leap in the oil subsystem was measured, using a special arrangement of RTDs to reduce the uncertainty of the measurement. Subtracting the heat flow, the mechanical losses were obtained. The oil was also characterised for further use in the mechanical losses model, as well as the geometry of the bearings. The mechanical power dissipated in the bearings was found to account to a large amount of the turbine power output when the oil was relatively cold, a situation that is found during urban driving conditions. The heat flow accounted for a variable ratio of the oil energy leap, being of lower concern in water-cooled turbochargers and very important in the oil-cooled unit.

The same experiments that were used to characterise the mechanical losses were also used to get the global performance of a turbine under steady-state conditions. Its geometry was also measured to get data for a simplified model. It was also measured under pulsating flow conditions, using a special rotating valve as a pulse generator. The pulsating flow was measured using two beamforming arrays, one at the turbine inlet and other at the turbine outlet, so the pressure pulses were decomposed in incident, reflected, transmitted and second reflection waves. A sharp decrease in pulse amplitude at high frequencies was found at the turbine outlet, probably due to its outlet plenum. The instantaneous mass flow rate was estimated using the instantaneous pressure decomposition.

Finally, a fourth turbine was specially modified to measure its internal pressure at different points. It was tested under steady-state conditions, obtaining the pressure at the rotor inlet. The pressure at the volute was found to be uniform, even at points far from the design conditions. The internal pressure at the compressor rotor outlet was also obtained, as this information is important to properly model the axial thrust in the turbocharger shaft and, thus, estimate the mechanical losses in the thrust bearing. Pulsating flow was also imposed in the turbine, measuring the instantaneous pressure at two different points in the volute and in the stator outlet. Little differences were found across the volute but at high frequencies, and the pulse amplitude was found to decrease with decreasing VGT apertures due to more flow restrictions. The highest pulse attenuation was measured at the rotor. No sharp attenuation in the pulse was found at high frequencies in the turbine outlet pressure, probably due to the

lack of a turbine outlet plenum.

3.7 References

[9] European Parliament, Council of the European Union. “Regulation (EC) No 715/2007 of the European Parliament and of the Council of 20 June 2007 on type approval of motor vehicles with respect to emissions from light passenger and commercial vehicles (Euro 5 and Euro 6) and on access to vehicle repair and maintenance information (Text with EEA relevance) ”. In: *Official Journal of the European Union* 50 (June 2007), pp. 1–16. ISSN: 1725-2555. URL: http://eur-lex.europa.eu/legal-content/EN/TXT/?uri=OJ:L:2007:171:TOC (cit. on pp. 3, 15, 73).

[10] European Parliament, Council of the European Union. “Regulation (EC) No 595/2009 of the European Parliament and of the Council of 18 June 2009 on type-approval of motor vehicles and engines with respect to emissions from heavy duty vehicles (Euro VI) and on access to vehicle repair and maintenance information and amending Regulation (EC) No 715/2007 and Directive 2007/46/EC and repealing Directives 80/1269/EEC, 2005/55/EC and 2005/78/EC (Text with EEA relevance) ”. In: *Official Journal of the European Union* 52 (July 2009), pp. 1–13. DOI: 10.3000/17252555.L_2009.188.eng (cit. on pp. 3, 15, 73).

[22] J. R. Serrano, P. Olmeda, A. Páez, and F. Vidal. “An experimental procedure to determine heat transfer properties of turbochargers”. In: *Measurement Science and Technology* 21.3 (3 2010), pp. 035–109. DOI: 10.1088/0957-0233/21/3/035109 (cit. on pp. 8, 18, 41, 68).

[23] SAE. *Supercharger Testing Standard*. SAE J1723. Society of Automotive Engineers, Aug. 1995 (cit. on pp. 10, 18, 59, 77).

[24] SAE. *Turbocharger gas stand test code*. SAE J1826. Society of Automotive Engineers, Mar. 1995 (cit. on pp. 10, 18, 59, 77).

[38] F. Payri, J. R. Serrano, P. Olmeda, A. Páez, and F. Vidal. “Experimental Methodology to Characterize Mechanical Losses in Small Turbochargers”. English. In: *Proceedings of the ASME Turbo Expo 2010*. Vol. 2010. 44007. Int Gas Turbine Inst. Glasgow, Scotland: ASME, June 2010, pp. 413–423. ISBN: 978-0-7918-4400-7. DOI: 10.1115/GT2010-22815 (cit. on pp. 18, 36, 38, 71).

[39] G. Piñero, L. Vergara, J. M. Desantes, and A. Broatch. “Estimation of velocity fluctuation in internal combustion engine exhaust systems through beamforming techniques”. In: *Measurement Science and Technology* 11.11 (2000), p. 1585. DOI: 10.1088/0957-0233/11/11/307 (cit. on pp. 18, 89).

[40] J. R. Serrano, F. J. Arnau, P. Fajardo, and M. Á. Reyes-Belmonte. "Contribution to the Modeling and Understanding of Cold Pulsating Flow Influence in the Efficiency of Small Radial Turbines for Turbochargers". In: *Journal of Engineering for Gas Turbines and Power* 134.10 (Aug. 2012), 102701 (11 pages). DOI: 10.1115/1.4007027 (cit. on pp. 18, 71).

[93] M. Deligant, P. Podevin, and G. Descombes. "Experimental identification of turbocharger mechanical friction losses". English. In: *Energy* 39.1 (Mar. 2012), 388–394. ISSN: 0360-5442. DOI: 10.1016/j.energy.2011.12.049 (cit. on pp. 34, 81, 235).

[106] S. Shaaban. "Experimental Investigation and Extended Simulation of Turbocharger Non-Adiabatic Performance". PhD thesis. Fachbereich Maschinenbau: Universität Hannover, 2004 (cit. on pp. 40, 71).

[109] N. Baines, K. D. Wygant, and A. Dris. "The Analysis of Heat Transfer in Automotive Turbochargers". English. In: *Journal of Engineering for Gas Turbineas and Power - Transactions of the ASME* 132.4 (Apr. 2010). ISSN: 0742-4795. DOI: 10.1115/1.3204586 (cit. on pp. 40, 68).

[111] P. Olmeda, V. Dolz, F. J. Arnau, and M. Á. Reyes-Belmonte. "Determination of heat flows inside turbochargers by means of a one dimensional lumped model". In: *Mathematical and Computer Modelling* 57.7–8 (2013), pp. 1847–1852. ISSN: 0895-7177. DOI: 10.1016/j.mcm.2011.11.078 (cit. on pp. 41, 71, 105, 248).

[113] *Evaluation of measurement data – Guide to the expression of uncertainty in measurement*. 100:2008. JCGM. Sept. 2008. URL: http://www.bipm.org/utils/common/documents/jcgm/JCGM_100_2008_E.pdf (cit. on p. 66).

[114] D. Baroudi and E. Thibert. "An instrumented structure to measure avalanche impact pressure: Error analysis from Monte Carlo simulations". In: *Cold Regions Science and Technology* 59.2-3 (2009). International Snow Science Workshop (ISSW) 2008, pp. 242–250. ISSN: 0165-232X. DOI: 10.1016/j.coldregions.2009.05.010 (cit. on p. 66).

[115] S. Marelli and M. Capobianco. "Steady and pulsating flow efficiency of a waste-gated turbocharger radial flow turbine for automotive application". In: *Energy* 36.1 (2011), pp. 459–465. ISSN: 0360-5442. DOI: 10.1016/j.energy.2010.10.019 (cit. on pp. 68, 117).

[116] M. V. Casey and M. Schlegel. "Estimation of the performance of turbocharger compressors at extremely low pressure ratios". English. In: *Proceedings of the Institution of Mechanical Engineers Part A - Journal of Power and Energy* 224.A2 (2010), 239–250. ISSN: 0957-6509. DOI: {10.1243/09576509JPE810} (cit. on p. 69).

[117] United Nations Economic Comission for Europe. *E/ECE/324/Rev.2/Add.100/Rev.3 or E/ECE/TRANS/505/Rev.2/ Add.100/Rev.3 (12 April 2013), "Agreement concerning the adoption of uniform technical prescriptions for wheeled vehicles, equipment and parts which can be fitted and/or be used on wheeled vehicles and the conditions for reciprocal recognition of approvals granted on the basis of these prescriptions", Addendum 100: Regulation No. 101, Uniform provisions concerning the approval of passenger cars powered by an internal combustion engine only, or powered by a hybrid electric power train with regard to the measurement of the emission of carbon dioxide and fuel consumption and/or the measurement of electric energy consumption and electric range, and of categories M1 and N1 vehicles powered by an electric power train only with regard to the measurement of electric energy consumption and electric range.* Apr. 2013. URL: http://www.unece.org/fileadmin/DAM/trans/main/wp29/wp29regs/updates/R101r3e.pdf (cit. on p. 73).

[118] A. J. Torregrosa, P. Olmeda, J. Martín, and C. Romero. "A Tool for Predicting the Thermal Performance of a Diesel Engine". In: *Heat Transfer Engineering* 32 (2011), 891–904. DOI: 10.1080/01457632.2011.548639 (cit. on p. 74).

[119] P. Welch. "The Use of Fast Fourier Transform for the Estimation of Power Spectra: A Method Based on Time Averaging Over Short, Modified Periodograms". In: *IEEE Transactions on Audio Electroacoustics* 15 (2 June 1967), pp. 70–73. ISSN: 0018-9278. DOI: 10.1109/TAU.1967.1161901 (cit. on pp. 91, 202, 211).

[120] F. Harris. "On the use of windows for harmonic analysis with the discrete Fourier transform". In: *Proceedings of the IEEE*. Vol. 66. IEEE, Jan. 1978, pp. 51–83. DOI: 10.1109/PROC.1978.10837 (cit. on pp. 91, 202, 211).

CHAPTER 4

Turbocharger modelling by means of CFD

Contents

Figures

Tables

4.1 Introduction

IN the previous chapter, the experimental set-up and investigation is presented. Current state of the art experimental facilities, although very sophisticated, aren't enough to get further insight in the behaviour of the flow inside the turbine, differencing the effects that its different parts produce. The extremely small size of the sensors needed to measure variables as the flow speed or the total pressure in different points of the turbine makes this task almost impossible to achieve except in the largest turbines, but the need of fine-grained distributions of different operational variables across different sections renders this task unrealisable. CFD simulations, in the other hand, impose no limits but time and computational costs in these kind of tests. Current developments in CFD simulations of turbochargers tend towards LES simulations, with very refined meshes, but U-RANS simulations using a sliding mesh approximation for rotor modelling can give results of enough quality if properly set-up.

In this chapter, the results from a CFD study of a radial turbine are presented and discussed, highlighting their applications to simple quasi-bidimensional modelling. A detailed discussion of some of the phenomena found inside the turbine, such as structures found in the secondary flow inside the rotor or detailed pressure distribution in the rotor or stator blades, falls outside the scope of the present work and, thus, will not be presented here, but can be found in the doctoral thesis of Fajardo Peña [17].

4.2 Description of the simulations

As the main motivation of using CFD simulations in the present work is to calibrate and validate the results from a simplified model, the simulations have been done using an U-RANS method, discarding LES due to its higher computational costs. A $k-\omega$ SST model was used for turbulence, maintaining a y^+ equal to one, which is usually the preferred model when computing turbomachinery, as seen in [47]. The convective terms were computed using a second-order upwind scheme and the unsteady terms were integrated using a first-order implicit scheme in time. 1.8° of rotor turning per time-step were used, and the mesh was formed by 2 million cells. In order to take into account the rotor movement, a sliding mesh model was used. A mesh independence analysis was carried out to asses the validity of the results.

The geometry was set as to simulate a turbine in a turbocharger test bench, so long inlet and outlet straight ducts were used. The computational domain was divided as follows:

- A long, straight inlet duct, using a structured mesh.

- The volute, using a non-structured mesh.
- The stator, using a non-structured mesh.
- The rotor, using a non-structured sliding mesh.
- The turbine outlet, using a non-structured mesh.
- A long, straight outlet duct, using a structured mesh.

The following sections were also defined:

Table 4.1: Turbine sections

Section	Description
0	Domain inlet
1	Turbine inlet
2	Stator inlet
3	Rotor inlet
4	Rotor outlet
5	Turbine outlet
6	Domain outlet

A two-views figure of the computational domain can be found in Figure 4.1, where the main sections are highlighted. The inlet and outlet ducts have not been drawn.

The turbine was first simulated using a static mesh using a multiple reference frame (MRF) approximation, also known in the literature as frozen rotor approach. Further simulations with a sliding mesh model (SMM) showed that the MRF was not accurate enough, but aided to initialise the flow field.

The turbine was simulated at two different rotor speeds and different pressure pulses were imposed. At the inlet, a total temperature and total pressure boundary condition was used, while at the outlet a constant static pressure outlet boundary condition was imposed. The inlet total pressure described a sinusoid of a given frequency and amplitude around a mean pressure level, while the total temperature maintained an isentropic relationship with the total pressure:

$$T_{0t} = T_{0t}|_{t=0} \cdot \left(\frac{p_{0t}}{p_{0t}|_{t=0}} \right)^{\frac{\gamma-1}{\gamma}} \tag{4.1}$$

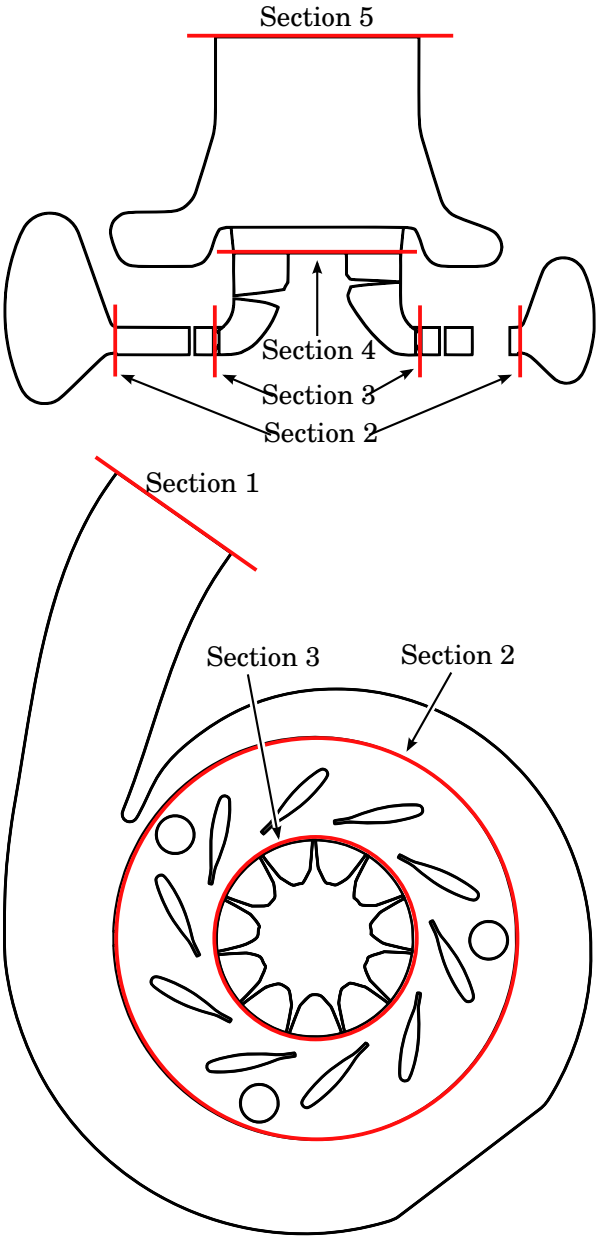

Figure 4.1: CFD model

Table 4.2: CFD boundary conditions

Case	Speed [krpm]	Frequency [Hz]	p_{0t} [kPa]	T_{0t} [K]	p_6 [kPa]
1	90	50	101 to 221	585 to 723	101
2	90	130	101 to 221	585 to 723	101
3	181	50	191 to 291	624 to 699	101
4	181	50	151 to 331	585 to 723	101
5	181	90	191 to 291	624 to 699	101
6	181	90	151 to 331	585 to 723	101
7	181	130	191 to 291	624 to 699	101
8	181	130	151 to 331	585 to 723	101
9	181	750	151 to 331	585 to 723	101

The test matrix is shown in Table 4.2. The amplitude of the pulses is extremely high, ranging from expansion ratios that produce flow detachment to values that produce choked flow. At 750 Hz, the amplitude is the same as at smaller frequencies, to get similar expansion ratio ranges. Also, these extreme results can be used to force the model during its validation in chapter 6, highlighting its limitations for future improvements.

Steady-state simulations were also carried out for 181 krpm, trying to cover the operational range of the pulsating flow cases.

The rotational speed was kept constant for each simulated case. Although it should not remain constant during real pulsating operation, its changes would be in a narrow range, as can be seen in [115].

Some of the results from these simulations were peer-reviewed and published in [3], and the setup and a discussion about the methods and results can be found in a Ph.D thesis by Fajardo Peña [17]. The mesh independence study, and the selection of wheel rotation strategies, viscous model and solver are discussed in detail in the aforementioned work. More simulations were done for the present work using the same mesh and methods.

4.3 Results

The following results are obtained using weighted averages for the different quantities computed in the sections defined in Table 4.1:

$$\bar{x}_j = \frac{\sum_i x_{i,j} \cdot \dot{m}_{i,j}}{\sum_i \dot{m}_{i,j}} \tag{4.2}$$

where $\bar{x}_j$ is the weighted average of the quantity x in section j, $\dot{m}$ is the mass flow rate and i is the cell face index.

The CFD results have been validated against steady-state experimental data. There are two different simulation datasets: one for a sliding mesh model approach for the rotor (SMM), where the mesh is rotated each time-step, and other for a multiple-reference-frame approach (MRF). The best results were obtained with the SMM approach, so that was the model used for the rest of the campaign.

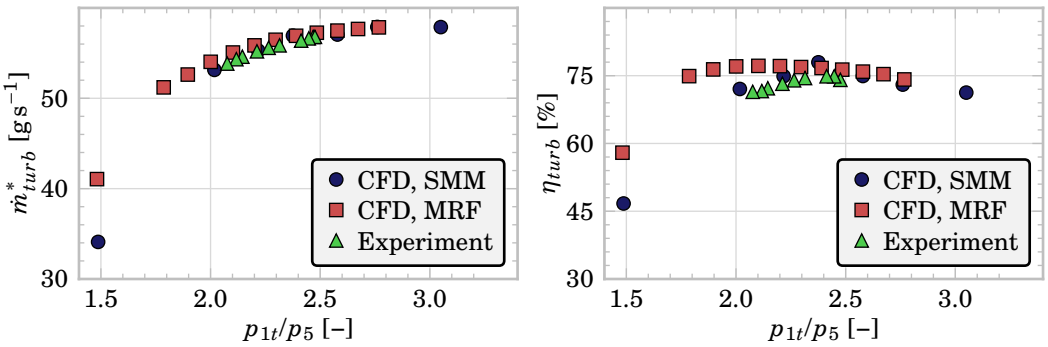

Figure 4.2: CFD results validation

The main objective of doing CFD simulations in the present thesis is to calibrate and validate a quasi-bidimensional model, so the analysis that is presented here is focused in the main results that can be used for that calibration and validation. Some of the details of the flow, such as the specific points where flow detachment is produced under very low expansion ratios or the detailed pressure gradient in the rotor surfaces, although full of interest, fall far from the scope of the present work. As it will be shown later, the model needs several parameters for its calibration such as coefficients of proportionality for the pressure loss modelling at both the stator and the rotor, and can be obtained from the results presented in this chapter.

Figure 4.3 shows the total pressure loss at the volute, plotted against the dynamic pressure at the turbine inlet. The accumulation and wave effects are too big in all pulsating flow cases. For the stator, its total pressure loss is shown in Figure 4.4. It is plotted against the dynamic pressure at the stator inlet and outlet, for different boundary condition frequencies. The mean values at each section are used in these plots. Steady-state results are also plotted as a reference. It is worth noting that the steady-state results were obtained at 181 krpm. There is a linear trend between the pressure loss and the dynamic pressure at both the stator inlet and outlet; this general trend is maintained regardless of the rotor speed. At high frequencies, the accumulation effects become so important that there is no clear correlation between the mean dynamic pressure at the stator inlet or outlet and the average total pressure

loss: there are appreciable differences in the magnitudes in different points of the volute outlet, complicating the use of the average total pressure loss as a representative value; also, the stator becomes less quasi-steady. At low expansion ratios and, thus, low dynamic pressures, the linear trend is lost. The total pressure loss at the stator is bigger than in the volute, due to higher flow speeds and bigger flow restrictions.

The rotor total pressure loss is plotted against the dynamic pressure at the rotor outlet in Figure 4.5. This pressure loss is computed in the relative reference frame, spinning at the same speed as the rotor, so it is defined as the difference between the relative total pressure at the inlet, p_{3tr}, and the relative total pressure at the outlet, p_{4tr}. It shows a clear non-linear relationship between this pressure loss and the dynamic pressure. A simple losses model that takes into account the secondary flow losses due to imperfect incidence at the rotor inlet due to Futral et al. [69] is found to give good results in the literature. This model, which is usually called the NASA shock losses model, is applied to the rotor total pressure losses results and is plotted in Figure 4.6. An ideal incidence angle of $\pi/2\,\mathrm{rad}$ is used to get these results. The vertical axis represents the relative total pressure loss minus the results from the NASA model, $\Delta p_{loss,NASA}$ The non-linear relationship between the dynamic pressure and the total pressure loss at the rotor is reduced, what will ease the implementation of a mean-line model later on.

The stator outlet flow angle α_3 is represented in Figure 4.7. It is plotted against the total to static expansion ratio of the stator, using the average values at its inlet and outlet. Again, the steady-state behaviour is approximated when dealing with pulsating flow if the frequency is low enough, while the results differ to a great degree at 750 Hz. The results at 90 krpm were obtained using a very large range of expansion ratios, even generating flow detachment and recirculation, what may explain their strange behaviour. The stator streamlines are plotted at two different time steps in Figure 4.8, for both a high and a very low expansion ratio points: flow detachment is highlighted, and some streamlines enter the rotor almost tangentially. The detachment and reattachment cycle is of a non-linear and hysteretical nature.

Figure 4.9 shows the rotor outlet relative flow angle β_4. There is an abrupt change in tendency for low mass expansion ratios for a given rotational speed: the flows tends to be more tangential as the mass flow rate drops, while it changes to values similar to the metal angle at higher flow speeds.

The stator outlet discharge coefficient is plotted in Figure 4.10. It is defined as the mass flow rate at the stator outlet divided by the density, the mean outlet radial speed and the stator outlet area:

$$C_{D_3} = \frac{\dot{m}_3}{\rho_3 \cdot u_3 \cdot \sin(\alpha_3) \cdot A_3} \tag{4.3}$$

where C_{D_3} is the discharge coefficient and A_3 is the stator outlet area. Its value grows with the expansion ratio, and it stays almost constant for the most common expansion ratios. Its value grows due to thinner wakes, that produce flow blockage at the rotor inlet, until a maximum value that is limited by the physical blockage produced by the rotor blades.

The discharge coefficient at the rotor outlet, in the other hand, is equal to one in all the simulated cases.

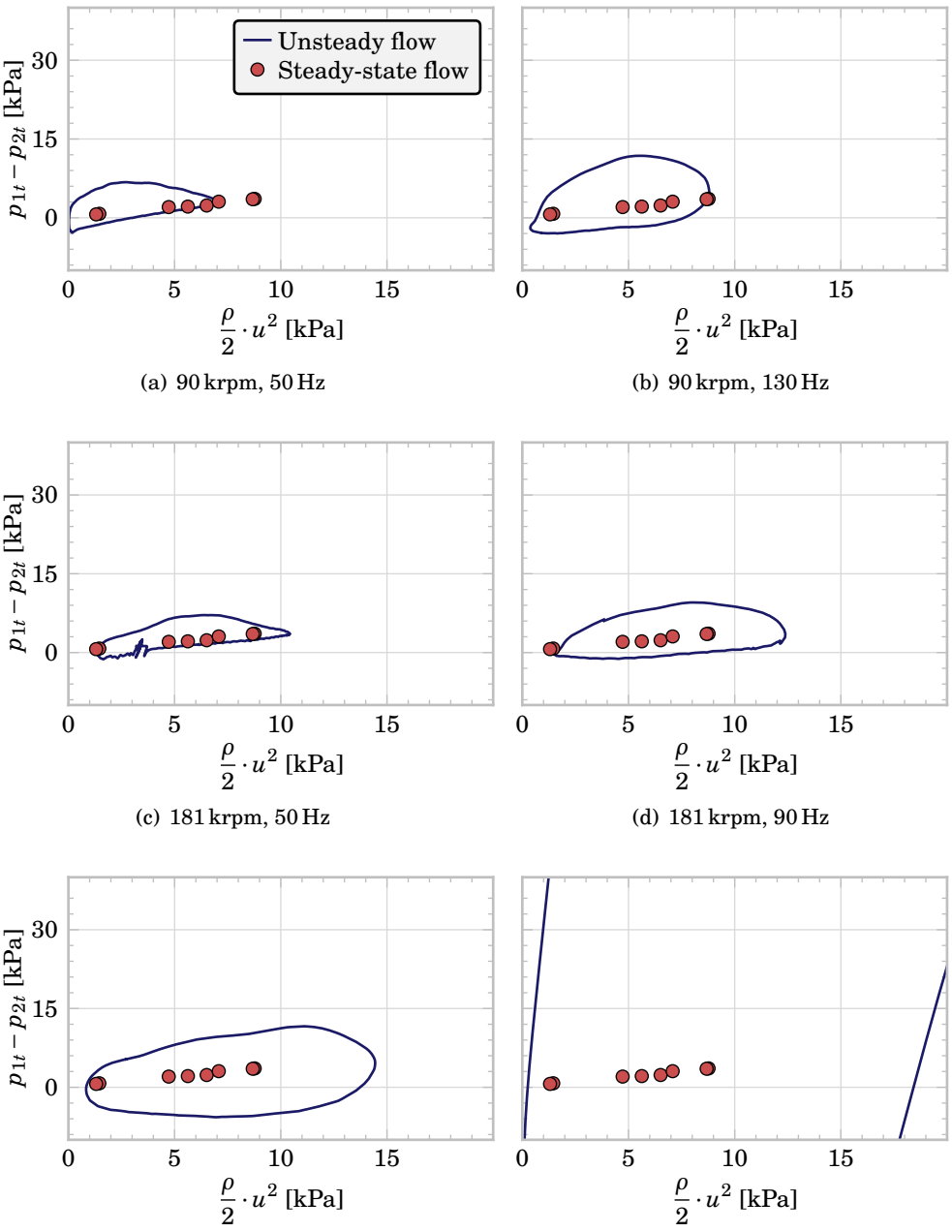

(a) 90 krpm, 50 Hz

(b) 90 krpm, 130 Hz

(c) 181 krpm, 50 Hz

(d) 181 krpm, 90 Hz

(e) 181 krpm, 130 Hz

(f) 181 krpm, 750 Hz

Figure 4.3: Total pressure loss at the volute

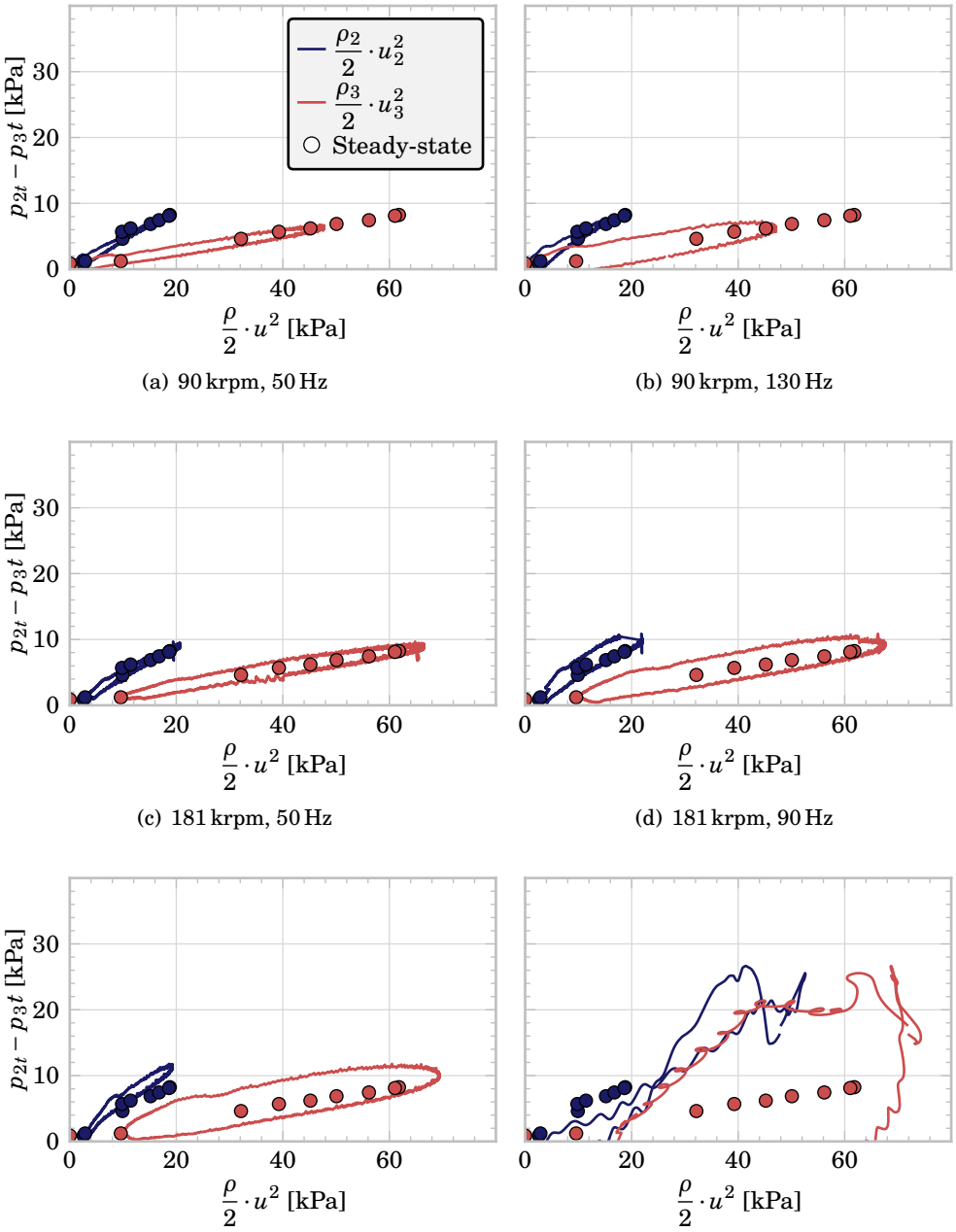

(a) 90 krpm, 50 Hz

(b) 90 krpm, 130 Hz

(c) 181 krpm, 50 Hz

(d) 181 krpm, 90 Hz

(e) 181 krpm, 130 Hz

(f) 181 krpm, 750 Hz

Figure 4.4: Total pressure loss at the stator

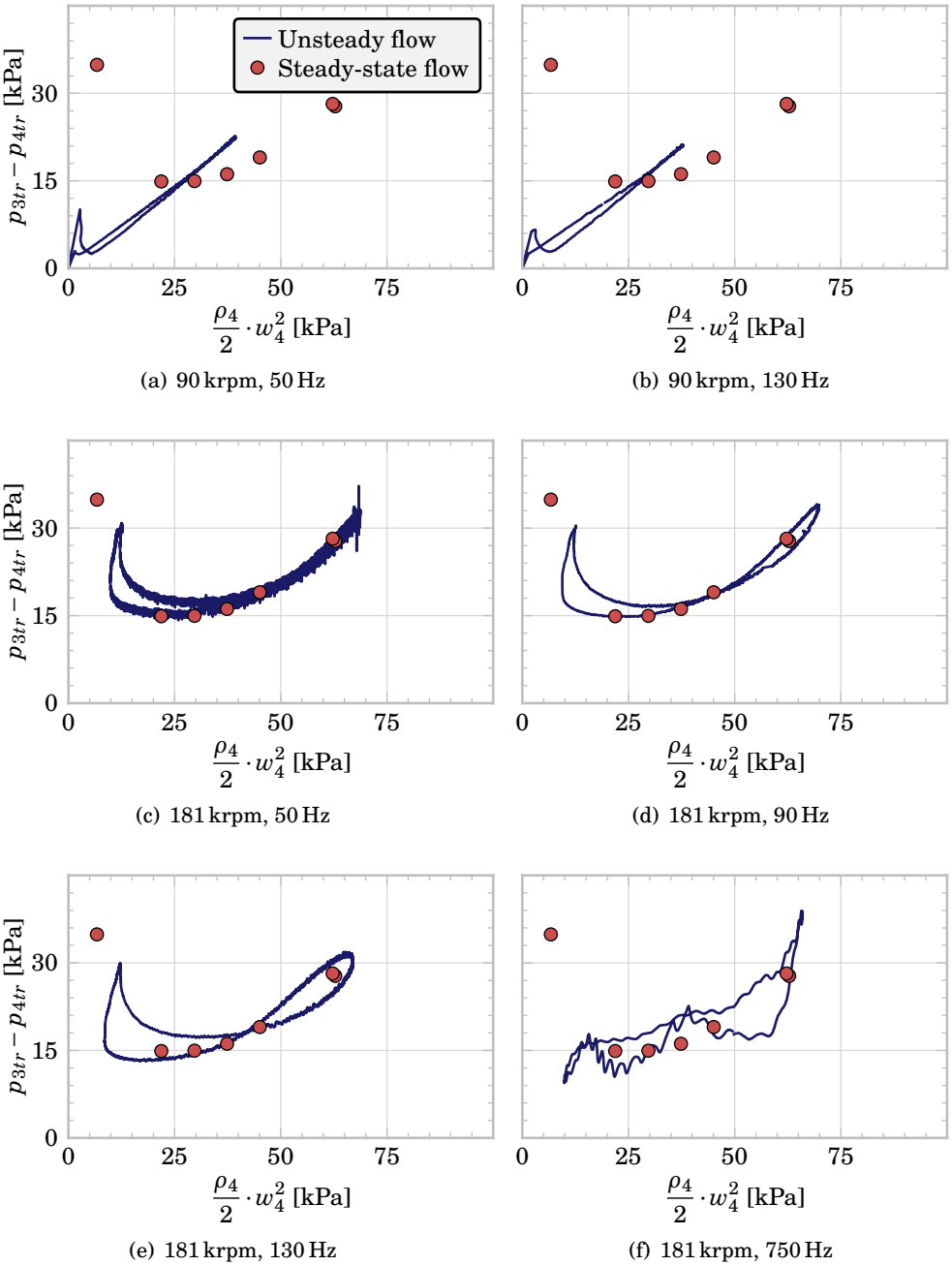

(a) 90 krpm, 50 Hz

(b) 90 krpm, 130 Hz

(c) 181 krpm, 50 Hz

(d) 181 krpm, 90 Hz

(e) 181 krpm, 130 Hz

(f) 181 krpm, 750 Hz

Figure 4.5: Total pressure loss at the rotor

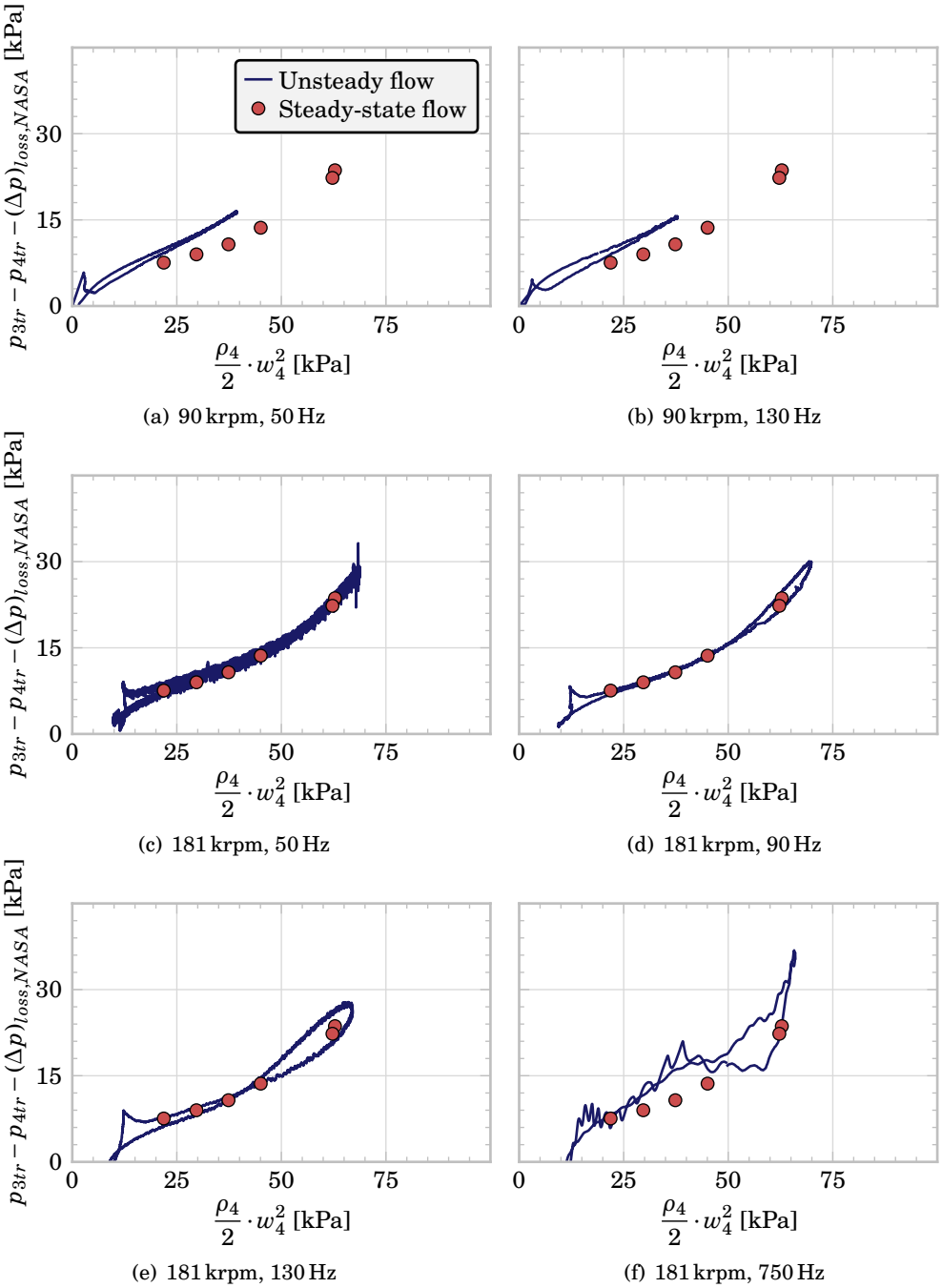

(a) 90 krpm, 50 Hz

(b) 90 krpm, 130 Hz

(c) 181 krpm, 50 Hz

(d) 181 krpm, 90 Hz

(e) 181 krpm, 130 Hz

(f) 181 krpm, 750 Hz

Figure 4.6: Total pressure loss at the rotor, without NASA shock losses due to imperfect incidence

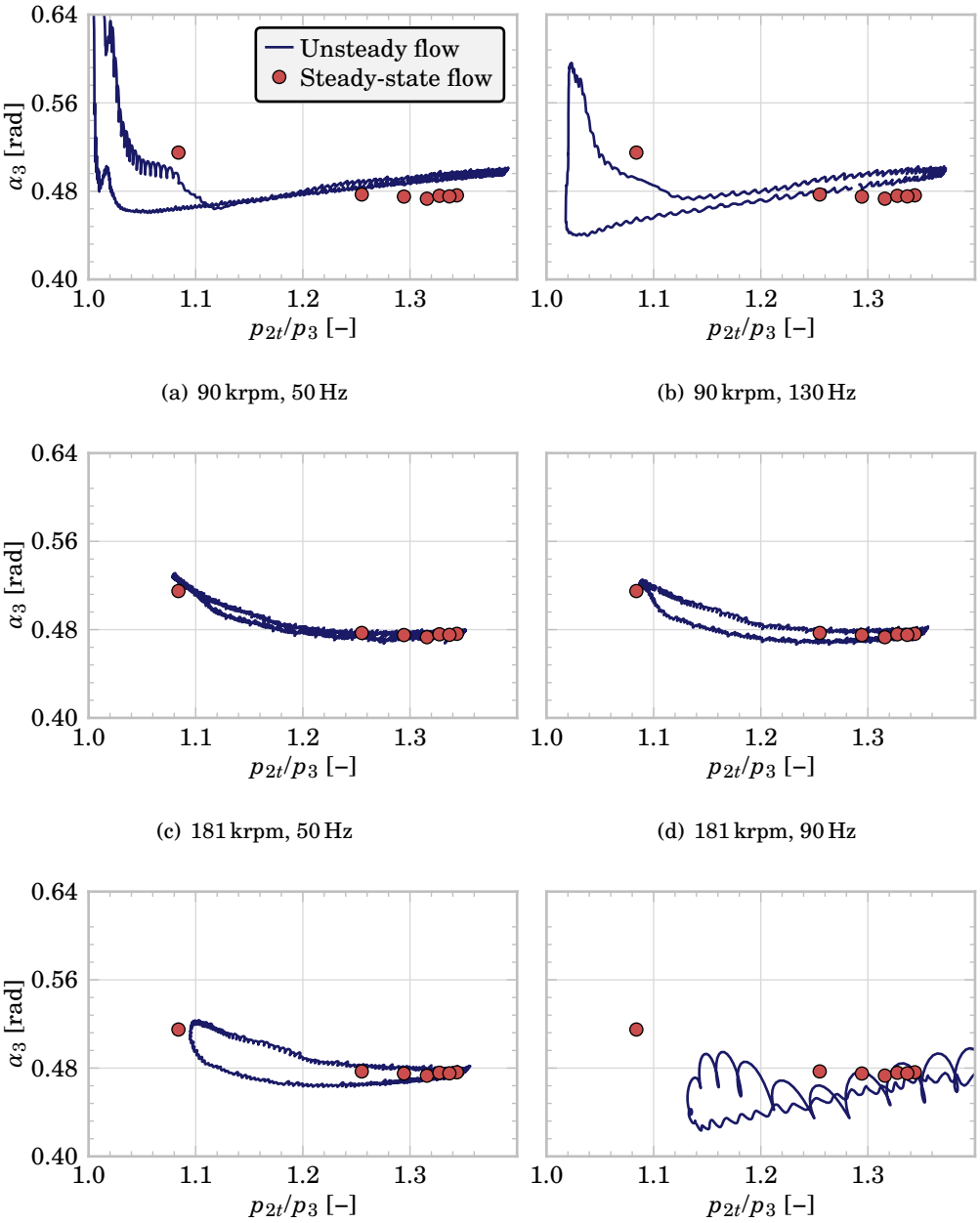

(a) 90 krpm, 50 Hz

(b) 90 krpm, 130 Hz

(c) 181 krpm, 50 Hz

(d) 181 krpm, 90 Hz

(e) 181 krpm, 130 Hz

(f) 181 krpm, 750 Hz

Figure 4.7: Stator outlet absolute flow angle

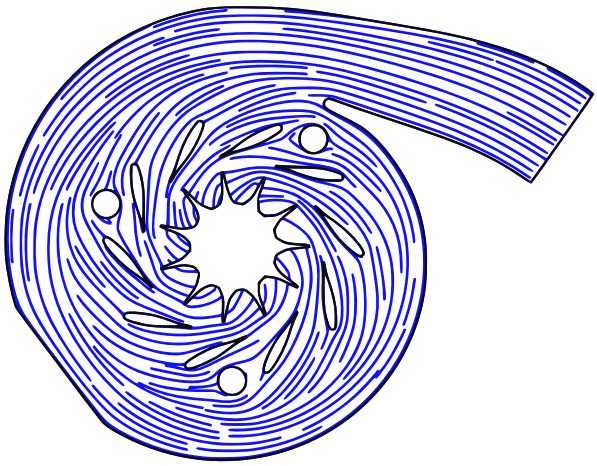

(a) 90 krpm, very high expansion ratio

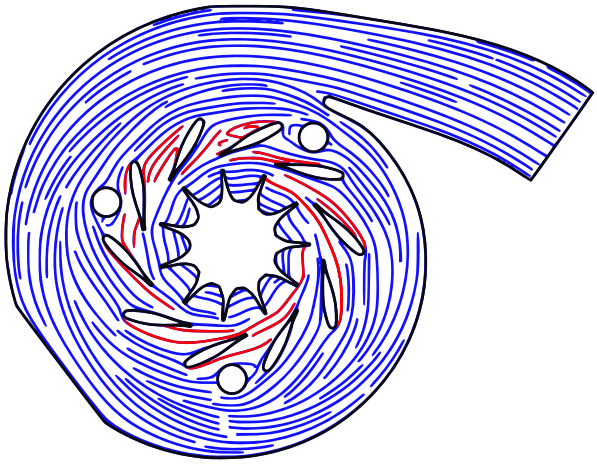

(b) 90 krpm, very low expansion ratio

Figure 4.8: Stator streamlines

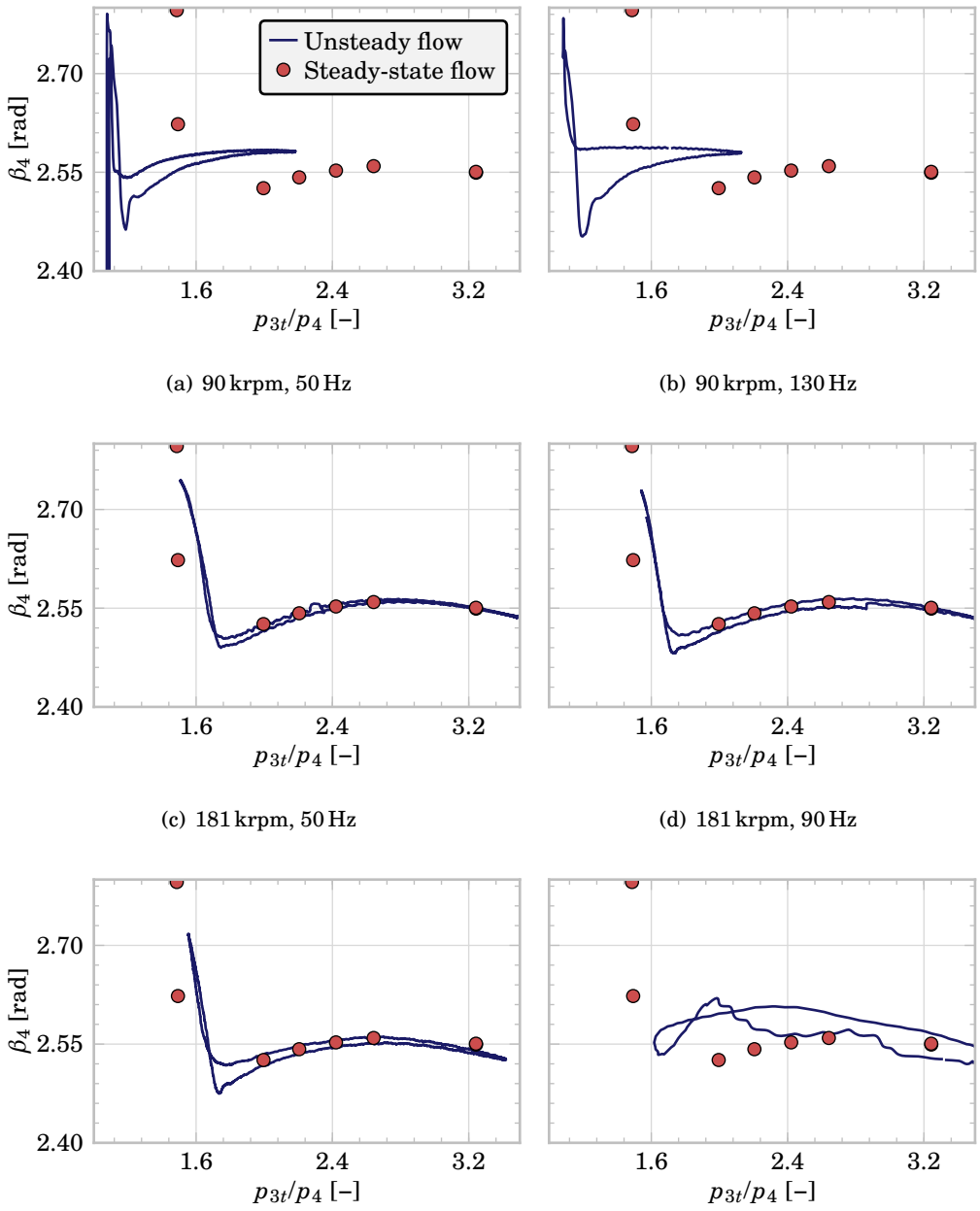

(a) 90 krpm, 50 Hz

(b) 90 krpm, 130 Hz

(c) 181 krpm, 50 Hz

(d) 181 krpm, 90 Hz

(e) 181 krpm, 130 Hz

(f) 181 krpm, 750 Hz

Figure 4.9: Rotor outlet relative flow angle

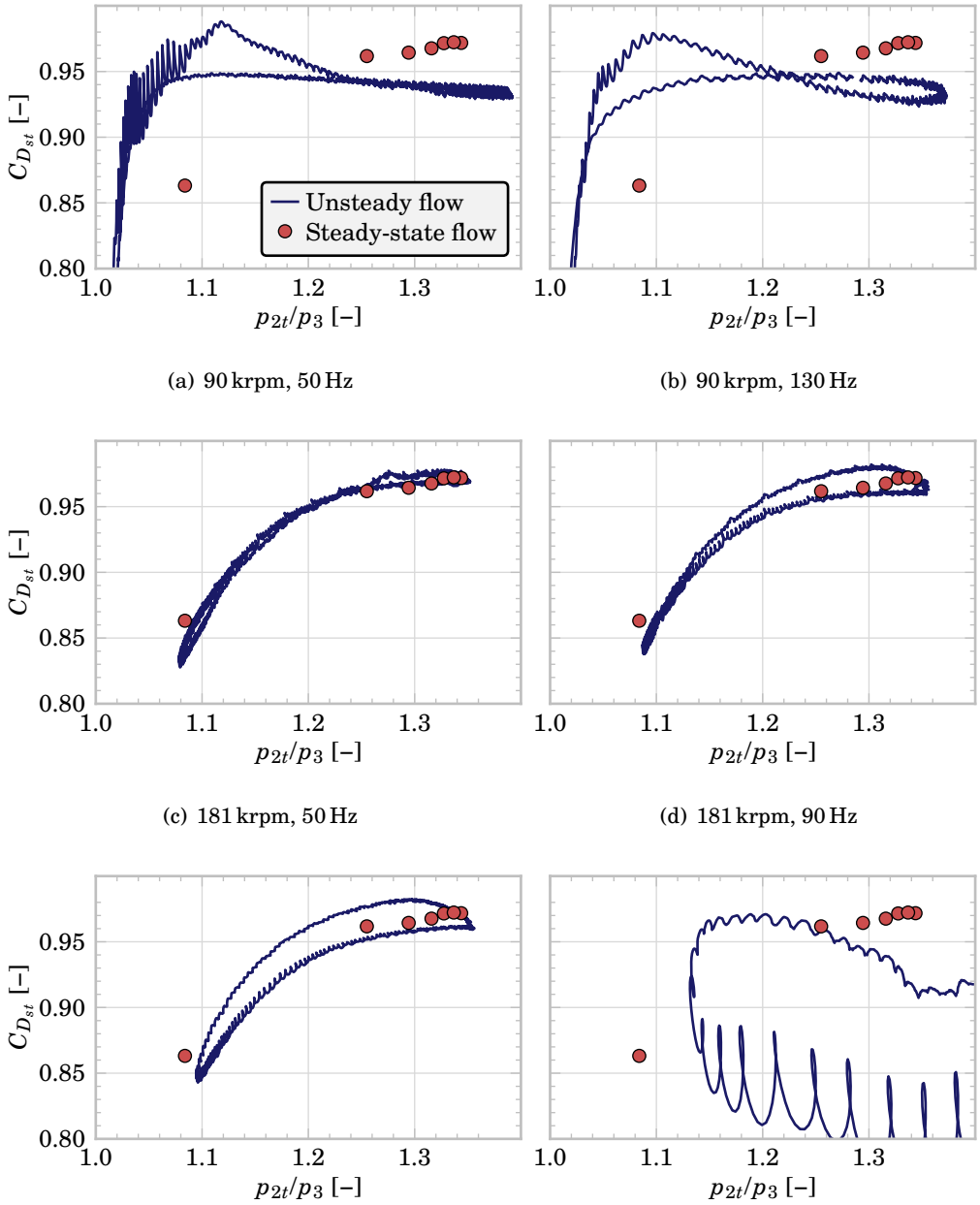

(a) 90 krpm, 50 Hz

(b) 90 krpm, 130 Hz

(c) 181 krpm, 50 Hz

(d) 181 krpm, 90 Hz

(e) 181 krpm, 130 Hz

(f) 181 krpm, 750 Hz

Figure 4.10: Stator outlet discharge coefficient

4.4 Summary

In this chapter, the results from a CFD simulation campaign of an automotive radial turbine are presented and discussed. The simulations show that the biggest accumulation effects are found in the volute, as it was expected. The pressure loss in the volute is affected by the accumulation and wave effects inside it, but its value is less than that found in the stator. The stator pressure losses are also found to depart from the quasi-steady behaviour at the highest frequencies, but that effect is of a lesser degree than that of the volute. The rotor, in the other hand, has the highest pressure losses of all the elements, but it can be supposed to behave in a quasi-steady manner with a very small error.

In the flow angle point-of-view, the stator shows a small hysteretic behaviour due to accumulation effects in both the volute and inside itself when compared to its global expansion ratio. At very low expansion ratios, flow detachment and recirculation occur, leading to strange flow angle changes. Again, the unsteady behaviour can be approximated as a quasi-steady evolution for the rotor outlet flow angle. At low expansion ratios, the flow angle behaviour changes abruptly, producing more tangential streamlines. When the expansion ratio is low enough, the hysteretic cycle grows, as flow recirculation also happens inside the rotor. The rotor performance differs from the quasi-steady solution only at the highest frequencies.

The discharge coefficient of the stator can be approximated as a constant value until small turbine expansion ratios and mass flow rates, when it decreases due to growing blade and screw wakes. Its value is equal to one in the rotor.

The results from simple steady-state CFD simulations can be used to calibrate a simplified model in terms of pressure losses and flow angle models, and, as the main unsteady behaviour is found in the volute, this calibration should give good results as long as the volute is properly computed, at least for the first harmonics of the engine pulse.

4.5 References

[3] J. Galindo, P. Fajardo, R. Navarro, and L. M. García-Cuevas. "Characterization of a radial turbocharger turbine in pulsating flow by means of CFD and its application to engine modeling". In: *Applied Energy* 103 (2013), pp. 116–127. ISSN: 0306-2619. DOI: 10.1016/j.apenergy.2012.09.013 (cit. on pp. vii, 17, 19, 21, 29, 117, 202).

[17] P. Fajardo Peña. "Methodology for the Numerical Characterization of a Radial Turbine under Steady and Pulsating Flow". PhD thesis. Universitat Politècnica de València, July 2012 (cit. on pp. 5, 114, 117).

[47] J. Galindo, S. Hoyas, P. Fajardo, and R. Navarro. "Set-up analysis and optimization of CFD simulations for radial turbines". In: *Engineering Applications of Computational Fluid Mechanics* 7.4 (2013), pp. 441–460 (cit. on pp. 20, 114).

[69] S. Futral, C. Wasserbauer, U. S. N. Aeronautics, and S. Administration. *Off-design performance prediction with experimental verification for a radial-inflow turbine: Samuel M.Futral Jr. and Charles A. Wasserbauer*. Tech. rep. NASA TN D-2621. NASA, 1965. URL: http://books.google.es/books?id=N1kzLAHfK-IC (cit. on pp. 26, 119, 153).

[115] S. Marelli and M. Capobianco. "Steady and pulsating flow efficiency of a waste-gated turbocharger radial flow turbine for automotive application". In: *Energy* 36.1 (2011), pp. 459–465. ISSN: 0360-5442. DOI: 10.1016/j.energy.2010.10.019 (cit. on pp. 68, 117).

CHAPTER 5

0D and quasi-2D turbocharger modelling

Contents

Figures

5.1 Introduction

In this chapter, the models developed during the production of the present thesis are presented. They consist in two main models: a radial turbine model and a mechanical losses model. Each of them is composed by several submodels.

Turbine model The radial turbine model is composed by several one-dimensional and modified one-dimensional elements, as well as the stator and the rotor. The one-dimensional elements are computed using a finite-volume, density based solver, using a high-resolution approach to get high spatial order while avoiding spurious oscillations due to Godunov's theorem. The method is explained in this chapter, as well as the different implemented boundary conditions. The volute is a special one-dimensional case: the flow that goes through its lateral window to the stator is computed at each cell, leading to its quasi-bidimensional characteristics.

The stator is computed using several submodels. First, the flow is estimated using several non-ideal nozzles, each one connected to a volute cell and to a plenum at the stator exit. This plenum represents the volume enclosed by the stator, and gives it some accumulation capabilities, as well as some advantages in computational complexity for the calculation of the stator and rotor mass flow rates. The stator outlet angle is approximated using a bi-dimensional potential model, where each blade is discretised using flat panels, imposing potential vortexes at each panel.

The rotor is computed using a non-ideal, constant-rothalpy model. It is coupled to the stator and to the one-dimensional turbine outlet duct.

The models are adiabatic, but the finite-volumes nature of the one-dimensional ducts makes it trivial to impose new source terms due to heat fluxes.

Mechanical losses model Small automotive turbochargers usually use oil-film bearings, seldom resorting to other kinds such as ball bearings. The mechanical losses model is computed using a radical simplification of the flow characteristics inside the bearing system of the turbocharger. The oil flow is supposed to be mainly one-dimensional, adiabatic and quasi-steady inside each bearing, so its evolution is computed by integrating a simplification of the Navier-Stokes equations over the surface of the bearings. Automotive turbochargers usually use floating or semi-floating journal bearings to avoid metal-to-metal contact due to the radial movement of the shaft, and simple thrust bearing washers for the axial movement. The model is developed for semi-floating ring journal bearings and simple

thrust bearings, each one fed by separate oil channels, but is latter modified to accept floating ring radial bearings and journal bearings with a lateral surface acting as one of the washers of the thrust bearing.

While the flow is supposed to be adiabatic during the evolution inside the bearings system, a method to apply heat fluxes to the oil before and after the bearings is also presented.

The next chapter is focused on the calibration and validation of the models, as well as a discussion of their results.

5.2 One-dimensional approximation

One-dimensional elements such as the inlet and outlet are discretised using a finite-volume approach, dividing each one in computational cells that are described by their state vector:

$$\boldsymbol{w} = \begin{pmatrix} \rho \\ \rho \cdot u \\ \rho \cdot e_t \end{pmatrix} = \begin{pmatrix} \rho \\ \rho \cdot u \\ \rho \cdot c_v \cdot T + \rho \cdot u^2/2 \end{pmatrix} \tag{5.1}$$

where ρ is the density, u is the fluid speed, c_v is the specific heat capacity at constant volume, T is the fluid temperature and p is the fluid pressure. Also, an ideal gas law is used:

$$p = \rho \cdot R \cdot T \tag{5.2}$$

where R is the gas constant. The finite-volume problem is computed using a Godunov's scheme, as first described in the work by the mentioned author [121]:

$$\frac{\mathrm{d}\bar{\boldsymbol{w}}_{\boldsymbol{i}}}{\mathrm{d}t} = \frac{\left(A_{i-1,i} \cdot \boldsymbol{F}_{i-1,i} - A_{i,i+1} \cdot \boldsymbol{F}_{i,i+1} + \boldsymbol{C}_i\right)}{V_i} \tag{5.3}$$

where t is the time, $\bar{\boldsymbol{w}}_i$ represents the mean value of the state vector in the cell i, $A_{i-1,i}$ is the boundary surface between cell $i-1$ and cell i, $\boldsymbol{F}_{i-1,i}$ is the flow vector between cells $i-1$ and i, $\boldsymbol{C}_i$ is the source terms vector affecting cell i and V_i is the volume of the cell.

The source term is computed as:

$$\boldsymbol{C}_i = \begin{bmatrix} 0 \\ p_i \cdot \left(A_{i-1,i} - A_{i,i+1}\right) \\ 0 \end{bmatrix} \tag{5.4}$$

The flow vector is obtained by using an approximation for the inter-cell fluxes: several methods have been implemented to asses their validity for this

particular problem. Equation 5.3 is solved iteratively using a classical ODE solver: again, several solvers have been implemented and tested. The time-step Δt is chosen at each integration step in order to obey the Courant-Friedrichs-Lewy (CFL) condition [122]:

$$\Delta t = \nu \cdot \left. \frac{\Delta x}{\lambda} \right|_{min} = \nu \cdot \left. \frac{\Delta x}{|u| + |a|} \right|_{min} \tag{5.5}$$

where Δx is the cell length, ν is the Courant number, λ is the maximum pressure propagation speed and a is the speed of sound:

$$a = \sqrt{\gamma \cdot R \cdot T} \tag{5.6}$$

where γ is the specific heat capacities ratio. The Courant number is chosen to be less than unity.

In order to improve the spatial accuracy of the integration, a second order Monotone Upstream-centered Schemes for Conservation Laws (MUSCL) scheme has been implemented. In a MUSCL scheme, as described by van Leer in [123], the state vector is reconstructed at each side of the boundary between two cells at the beginning of each time-step using a linear or higher order extrapolation, limiting this extrapolation so the scheme obtains total variation diminishing (TVD) properties. A linear extrapolation has been chosen, so second order accuracy is obtained where the state vector is smooth enough, degrading the solution to first order where sharp discontinuities are present. Like with the inter-cell fluxes solvers and the ODE integration schemes, several limiter functions have been implemented and tested. The limiters are functions of the ratio of successive gradients of the state vector, and multiply the slope of the state vector extrapolation by a value between 0 and 2. The different limiter functions are shown in Figure 5.1, where the second order TVD zone is highlighted. In these plots, φ is the limiter value and r is the ratio of successive gradients. The Minmod limiter is the most conservative one, using the lowest value that conforms to second order TVD properties, while the Superbee limiter is the most aggressive.

The connection between one-dimensional elements is computed using a virtual duct consisting of four cells: two for the ending of the first element and other two for the start of the other element. This way, the flow vector between the second and the third virtual cells is the flow that leaves the last cell of the first element and the one that enters the first cell of the second element, maintaining second order TVD properties in the boundary condition.

Equation 5.3 can be solved exploiting single instruction, multiple data (SIMD) intrinsics and maintaining a high level of data locality. As an example, assuming that the time is t_0 and the time-step is Δt and using Heun's method:

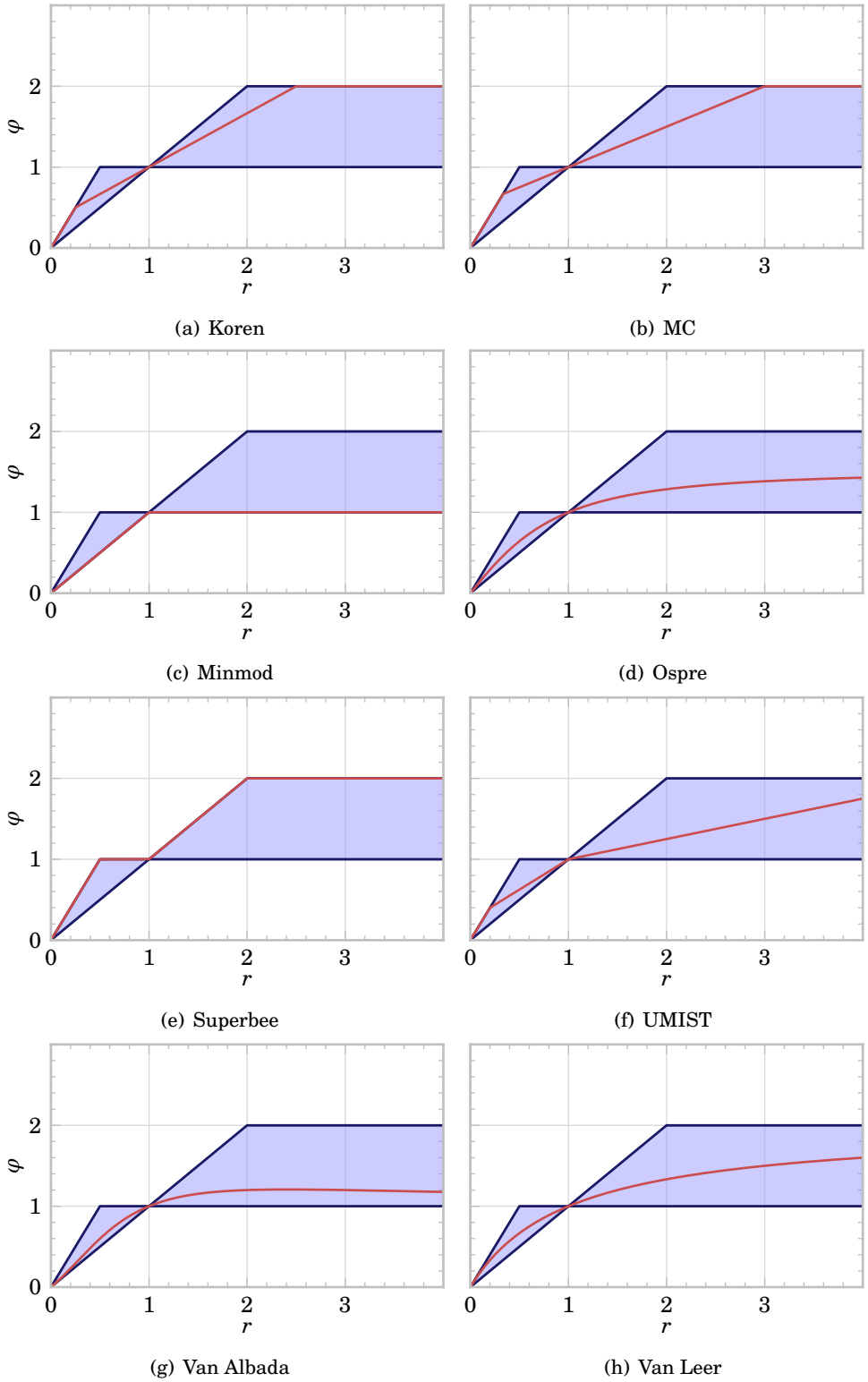

(a) Koren (b) MC

(c) Minmod (d) Ospre

(e) Superbee (f) UMIST

(g) Van Albada (h) Van Leer

Figure 5.1: Limiter functions

- The value of $\Delta t \cdot \dfrac{\left(A_{i-1,i} \cdot \boldsymbol{F}_{i-1,i} - A_{i,i+1} \cdot \boldsymbol{F}_{i,i+1} + \boldsymbol{C}_i\right)}{V_i}$ is obtained for all the cells almost at the same time, aligning all the vectors to 128 bit bounds and using SIMD instructions to compute them. The flux at the boundary conditions is computed at $t = t_0$.

- The result from the previous operation, k_1, is summed to the state vector of the duct. Again, SIMD intrinsics are used to sum several cells at each processor cycle. The sum is safely performed without evaluating temporaries to reduce computational costs.

- The value of $\Delta t \cdot \dfrac{\left(A_{i-1,i} \cdot \boldsymbol{F}_{i-1,i} - A_{i,i+1} \cdot \boldsymbol{F}_{i,i+1} + \boldsymbol{C}_i\right)}{2 \cdot V_i}$ is obtained. The value of the flux at the boundary conditions is computed for $t = t_0 + \Delta t$

- The result from the previous operation, k_2, is summed to the state vector, subtracting the value of $k_1/2$. Again, the sums are performed reducing the number of temporaries to its minimum.

- All the arrays should be allocated in the stack to reduce heap allocation and deallocation overheads.

The respondent has successfully performed all the vectorisation using `Eigen` C++ template library for linear algebra [124].

The stator model also maintains some accumulation effects and it is partly simulated as an equivalent cell with a volume equal to the actual volume occupied by the real stator. The flow vector that enters the stator is computed as:

$$\boldsymbol{F} = \begin{bmatrix} \Sigma \left.\dfrac{\mathrm{d}m}{\mathrm{d}t}\right|_{st,i} \\ 0 \\ \Sigma \left(\left.\dfrac{\mathrm{d}m}{\mathrm{d}t}\right|_{st} \cdot c_p \cdot T_t \right)_i \end{bmatrix} \tag{5.7}$$

and the flow vector that leaves the stator and enters the rotor is:

$$\boldsymbol{F} = \begin{pmatrix} \left.\dfrac{\mathrm{d}m}{\mathrm{d}t}\right|_{rt} \\ 0 \\ \left.\dfrac{\mathrm{d}m}{\mathrm{d}t}\right|_{rt} \cdot c_p \cdot T_{3t} \end{pmatrix} \tag{5.8}$$

where $\left.\frac{\mathrm{d}m}{\mathrm{d}t}\right|_{rt}$ is the mas flow rate that goes through the rotor and T_{3t} is the total temperature at the stator finite-volume cell. The presence of this stator cell not only provides accumulation effects for the stator, but also uncouples the rotor from the stator flow: as this is known at the stator cell at the beginning of each time-step, it can be used as an input for the rotor flow simulation instead of solving the coupled stator-rotor system.

Finally, the flow that enters the boundary between the rotor and the turbine outlet is:

$$\boldsymbol{F} = \begin{pmatrix} \left.\frac{\mathrm{d}m}{\mathrm{d}t}\right|_{rt} \\ \left.\frac{\mathrm{d}m}{\mathrm{d}t}\right|_{rt} \cdot w_4 \cdot \sin\beta_4 + p_4 \\ \left.\frac{\mathrm{d}m}{\mathrm{d}t}\right|_{rt} \cdot c_p \cdot T_{4t} \end{pmatrix} \tag{5.9}$$

where w_4 is the rotor outlet relative speed, β_4 is the rotor outlet relative flow angle and T_{4t} is the total temperature at the rotor outlet.

Several boundary conditions are implemented to simulate the experimental and three-dimensional data that was obtained as described in chapter 3 and chapter 4.

Inlet total pressure boundary condition: A virtual cell is attached to the end of the one-dimensional duct, imposing its total temperature $T_{virtual,t}$ and total pressure $p_{virtual,t}$. The flow speed at the duct cell attached to the virtual cell u_{end} is imposed in the latter, and then the virtual cell density, momentum and total internal energy can be computed. The flow between the virtual cell and the duct end cell is then computed. The temperature at the virtual cell $T_{virtual}$ is:

$$T_{virtual} = T_{virtual,t} - \frac{u_{end}^2}{2 \cdot c_p} \tag{5.10}$$

The static pressure $p_{virtual}$ is:

$$p_{virtual} = p_{virtual,t} \cdot \left(\frac{T_{virtual}}{T_{virtual,t}}\right)^{\frac{\gamma}{\gamma-1}} \tag{5.11}$$

Equations (5.10) and (5.11) and the virtual cell speed, which is equal to u_{end}, are used to compute the state vector.

Outlet pressure boundary condition: Again, a virtual cell is attached to the end of the one-dimensional duct. In this case, its static pressure $p_{virtual}$ is imposed. Its temperature $T_{virtual}$ is computed using an isentropic evolution between the total conditions at the duct end ($p_{end,t}$, $T_{end,t}$) and the pressure at the virtual cell. The cell speed $u_{virtual}$ is set assuming that the total temperature at the virtual cell is the same as the total temperature at the duct end. This way, the density, momentum and total internal energy at the virtual cell can be known and the flow between the virtual cell and the duct end cell can be computed using an inter-cell flux estimator.

$$T_{virtual} = T_{end,t} \cdot \left(\frac{p_{virtual}}{p_{end,t}} \right)^{\frac{\gamma-1}{\gamma}} \tag{5.12}$$

$$u_{virtual} = \sqrt{\frac{T_{end,t} - T_{virtual}}{2 \cdot c_p}} \tag{5.13}$$

The virtual cell static pressure $p_{virtual}$ is used with Equations (5.12) and (5.13) to compute the virtual cell state vector.

Incident pressure: The characteristic that enter the duct from the boundary condition λ_{in} and the characteristic that exits the duct from the duct end cell λ_{out} are used to compute the state vector of a virtual cell. Once its state vector is known, the inter-cell flux is computed. λ_{in} is computing using the incident pressure p_{in}, the reference pressure p_{ref} and the entropy level $A_{A_{in}}$:

$$\lambda_{in} = \left[2 \left(\frac{p_{in}}{p_{ref}} \right)^{\frac{\gamma-1}{2\gamma}} - 1 \right] \cdot A_{A_{in}} \tag{5.14}$$

Assuming that the flow speed at the duct end cell u_{end} is positive when it flows from the boundary condition to the interior of the duct:

$$\lambda_{out} = \frac{a_{end}}{a_{ref}} - \frac{\gamma - 1}{2} \frac{u_{end}}{a_{ref}} \tag{5.15}$$

The speed of sound at the virtual cell $a_{virtual}$ is computed combining the two characteristics:

$$a_{virtual} = a_{ref} \cdot \frac{\lambda_{in} + \lambda_{out}}{2} \tag{5.16}$$

The flow speed at the virtual cell $u_{virtual}$ is computed as:

$$u_{virtual} = a_{ref} \cdot \frac{\lambda_{in} - \lambda_{out}}{\gamma - 1} \tag{5.17}$$

The pressure at the virtual cell $p_{virtual}$ is:

$$p_{virtual} = p_{ref} \cdot \left(\frac{\frac{a_{virtual}}{a_{ref}}}{A_{A_{in}}} \right)^{\frac{2\gamma}{\gamma-1}} \tag{5.18}$$

Finally, the temperature at the virtual cell $T_{virtual}$ is:

$$T_{virtual} = \frac{a_{virtual}^2}{\gamma \cdot R} \tag{5.19}$$

Using Equation 5.17, Equation 5.18 and Equation 5.19, the state vector is easily obtained and the inter-cell flux can be computed.

5.3 Volute model

The majority of the fast radial turbine models described in the literature simulate the volute accumulation and wave propagation effects using an equivalent one-dimensional duct of a certain length, which can be either of constant area or tapered. Usually, the length of this pipe is more or less equal to that of half volute (i.e., from the volute tongue to 180° downstream of it), the initial area is equal to that at the tongue and the final area is equal to that 180° downstream, if the duct is tapered. This one-dimensional equivalent duct has the same volume as the real volute, and an example of such a model can be found in the work from Costall et al. [32]. The pipe end is connected to the rotor or, in some cases, to an equivalent nozzle representing the stator channels. Some authors go further, connecting some of the computational nodes of the volute to the rotor, like Chiong et al. [34]. Some of the authors that simulate the volute using these simplifications get to the conclusion that the equivalent length of the volute should change based on mass flow consumption [32], but it is much harder to implement it that way.

The proposed model takes a slightly different approach:

- While the volute is simulated using a one-dimensional model, the volute end section is not connected to the stator nor the rotor, but instead is connected again to the volute tongue.

- The volute area distribution is taken directly from the real geometry and its real length is also used.

- The lateral window is present and mass, energy and momentum fluxes are computed at each computational cell, what leads to a quasi-bidimensional representation of the volute.

- The flow that leaves each volute cell through its lateral window is computed by coupling the volute with a stator model.

This quasi-bidimensional approach is supposed to give better high-frequency results than the classic model due to a more realistic simulation of the volute while still being simple, easy to implement and non computationally-expensive. One-dimensional models are fast enough to be used in real-time computations such as hardware-in-the-loop (HIL) simulations of full engines in a not so distant future, so maintaining low computational costs in the turbocharger code should be attractive for not pushing this scenario forward in time. Also, maintaining high computational efficiency bounds function evaluation costs during optimisation processes.

As will be seen later, some of the extra information produced by the quasi-bidimensional model can and will be used with the stator model in order to provide means to predict its outlet angle.

The main flow speed inside the volute is the tangential speed, so its state vector becomes:

$$\boldsymbol{w} = \begin{pmatrix} \rho \\ \rho \cdot u_\theta \\ \rho \cdot e_t \end{pmatrix} = \begin{pmatrix} \rho \\ \rho \cdot u_\theta \\ \rho \cdot c_v \cdot T + \rho \cdot u_\theta^2/2 \end{pmatrix} \tag{5.20}$$

The flow vector is computed as in the one-dimensional ducts, using u_θ as the main flow speed. At each time-step the stator is solved as a boundary condition that generates additional source terms in the volute. Each volute cell i is connected to a stator channel, and its additional source term $\boldsymbol{C}_i$ is computed as:

$$\boldsymbol{C}_i = \begin{pmatrix} \left.\dfrac{\mathrm{d}m}{\mathrm{d}t}\right|_{st} \\ \left.\dfrac{\mathrm{d}m}{\mathrm{d}t}\right|_{st} \cdot u_\theta \\ \left.\dfrac{\mathrm{d}m}{\mathrm{d}t}\right|_{st} \cdot c_p \cdot T_t \end{pmatrix}_i \tag{5.21}$$

where $\left.\frac{\mathrm{d}m}{\mathrm{d}t}\right|_{st,i}$ is the mass flow rate that goes through the volute window at cell i to the stator. This source terms vector is summed with the normal source terms vector. The volute has other particularity: its end is connected to its inlet, so some recirculation is possible. The volute inlet is, thus, connected to the volute outlet and to the turbine inlet duct outlet.

The radial flow speed at cell i, $u_{r,i}$, is computed as:

$$u_{r,i} = \frac{1}{A_{window,i} \cdot \rho_i} \cdot \left.\frac{\mathrm{d}m}{\mathrm{d}t}\right|_{st,i} \tag{5.22}$$

5.4 Stator

Stator flow

Each stator channel outlet speed is computed assuming a constant total enthalpy evolution:

$$T_{2ti} = T_{3ti} \;\Rightarrow\; u_{st,i} = \left.\sqrt{2 \cdot c_p \cdot (T_{2t} - T_3)}\right|_i \tag{5.23}$$

$$\left.\frac{T_{2t}}{T_3}\right|_i = \left(\frac{p_{2t}}{p_3}\right)_i^{\frac{n_{st}-1}{n_{st}}} \tag{5.24}$$

$$u_{st,i} = \left.\sqrt{2 \cdot R \cdot \frac{\gamma}{\gamma - 1} \cdot T_{2t} \cdot \left[1 - \left(\frac{p_{2t}}{p_3}\right)^{\frac{1-n_{st}}{n_{st}}}\right]}\right|_i \tag{5.25}$$

where $u_{st,i}$ is the stator outlet speed for the stator channel connected to the volute cell i, n_{st} is the polytropic coefficient of the evolution, the conditions at the stator inlet $T_{2t,i}$ and $p_{2t,i}$ are computed in the cell i at the volute and the pressure p_3 is the pressure computed at the cell that represents the accumulation effects of the stator.

To compute the mass flow rate, the stator outlet density is needed:

$$\begin{aligned} \rho_3 = \frac{p_3}{R \cdot T_3} &= \frac{p_3}{p_{2t,i}} \cdot \frac{T_{2t,i}}{T_3} \cdot \frac{p_{2t,i}}{R \cdot T_{2t,i}} \\ &= \frac{p_{2t,i}}{R \cdot T_{2t,i}} \cdot \left(\frac{p_{2t,i}}{p_3}\right)^{-\frac{1}{n_{st}}} \end{aligned} \tag{5.26}$$

The mass flow rate that flows outside the volute cell i is:

$$\left.\frac{\mathrm{d}m}{\mathrm{d}t}\right|_{st,i} = A_3 \cdot C_{D_{st}} \frac{A_{w,i}}{\sum A_{w,i}} \cdot \sin\alpha_3 \cdot \left[\frac{p_{2t}}{R \cdot T_{2t}} \cdot \left(\frac{p_{2t}}{p_3}\right)^{-\frac{1}{n_{st}}} \cdot u_{st}\right]_i \tag{5.27}$$

where $C_{D_{st}}$ represents a discharge coefficient. It reflects that the area at the compressor outlet is partially blocked by the rotor blades and there are also some wake blockage, $A_{w,i}$ is the volute window surface at cell i and α_3 is the absolute stator outlet angle, i.e., the flow angle measured in an inertial reference frame fixed in the turbine body. α_3 is equal to 0 when the flow is fully tangential and travels in the same direction than the rotor blades, and is equal to $\pi/2$ when the flow is fully radial. The stator outlet mean speed u_{st} can be computed using this mass flow rate:

$$u_{st} = \frac{\sum u_{st,i} \cdot \left.\frac{\mathrm{d}m}{\mathrm{d}t}\right|_i}{\sum \left.\frac{\mathrm{d}m}{\mathrm{d}t}\right|_i} \tag{5.28}$$

$C_{D_{st}}$ is computed as follows in the case of small wakes:

$$C_{D_{st}} = \frac{A_3 - A_{rt,in,bl}}{A_3} = \frac{2 \cdot \pi \cdot r_{rt,in} \cdot x_{st} - A_{rt,bl}}{2 \cdot \pi \cdot r_{rt,in} \cdot x_{st}} \tag{5.29}$$

where A_3 is the stator outlet surface, $A_{rt,in,bl}$ is the surface blocked by the rotor blades at its inlet, $r_{rt,in}$ is the rotor inlet radius and x_{st} is the stator height.

In the case that very large expansion ratio occurs in the stator, the flow will become choked; to compute this situation, the following procedure is used:

- The stator outlet pressure that generates choked flow is computed, see Equation 5.31.
- The evolution is calculated between the stator total inlet pressure and the stator outlet pressure that generates choke.
- The stator outlet speed is computed iteratively in order to comply with the following:
  - The mass flow rate should be that of sonic blockage.
  - The total temperature is conserved.

– Equation 5.2 is obeyed.

In choke conditions, the stator outlet speed is equal to the speed of sound:

$$\begin{aligned} a_{3,i} &= \gamma \cdot R \cdot T_{3,ch,i} = \gamma \cdot R \cdot \left(\frac{p_{2t,i}}{p_{3,ch,i}} \right)^{\frac{1-n_{st,i}}{n_{st,i}}} \\ &= 2 \cdot \frac{\gamma}{\gamma - 1} \cdot R \cdot T_{2t,i} \cdot \left[1 - \left(\frac{p_{2t,i}}{p_{3,ch,i}} \right)^{\frac{1-n_{st,i}}{n_{st,i}}} \right] \end{aligned} \tag{5.30}$$

Solving Equation 5.30:

$$p_{3,ch,i} = p_{2t,i} \cdot \left(\frac{\gamma + 1}{2} \right)^{\frac{n_{st,i}}{1-n_{st,i}}} \tag{5.31}$$

To compute the polytropic coefficient found in Equation 5.27, the real evolution is divided into two effective simple ideal processes, which are shown schematically in Figure 5.2:

- An evolution from p_{2t} to $p_{2t} - \Delta p_{st,loss}$, where some total pressure is dissipated increasing the specific entropy.
- An isentropic evolution from $p_{2t} - \Delta p_{st,loss}$ to p_3.

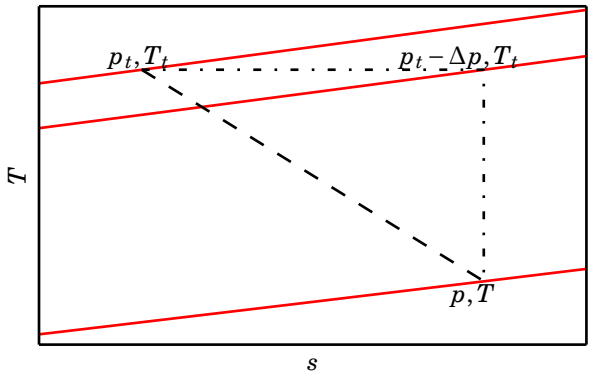

Figure 5.2: Schematic evolution for modelling losses.

This evolution is equivalent to the direct one with a polytropic coefficient:

$$\left(\frac{p_{2t}}{p_3} \right)^{\frac{n_{st}-1}{n_{st}}} = \left(\frac{p_{2t} - \Delta p_{st,loss}}{p_3} \right)^{\frac{\gamma-1}{\gamma}} \tag{5.32}$$

Thus, the polytropic coefficient n_{st} can be computed as:

$$n_{st} = \frac{\ln \dfrac{p_{2t} - \Delta p_{st,loss}}{p_3}}{\frac{1-\gamma}{\gamma} \cdot \ln \dfrac{p_{2t}}{p_3} + \ln \dfrac{p_{2t} - \Delta p_{st,loss}}{p_3}} \tag{5.33}$$

The dissipated stagnation pressure due to losses in the stator is assimilated to the losses in a passage due to turbulence, which are proportional to the dynamic pressure, as described in Equation 5.34. This kind of model is compatible with the results obtained in chapter 4.

$$\Delta p_{st,loss} = k_{st,loss} \cdot \frac{\rho_2 \cdot |\boldsymbol{u}_i|^2}{2} \tag{5.34}$$

where the dynamic pressure is that of the stator inlet, taking into account both components of the speed (tangential and radial):

$$\rho_2 \cdot |\boldsymbol{u}_i|^2 = \rho_2 \cdot {u_{\theta,i}}^2 + \left.\frac{\mathrm{d}m}{\mathrm{d}t}\right|_{st,i} \cdot \frac{1}{A_{w,i}} \tag{5.35}$$

where the tangential speed has been approximated by the mean tangential speed in the volute cell and the radial speed is computed using the mass flow rate that leaves the volute cell by its window. In order to accelerate the computation, the mass flow rate used to compute the losses can be the one from the last time-step.

Finally, the stator flow angle is approximated assuming bidimensional, inviscid, non-compressible and homentropic conditions. It is important to note that these assumptions are only used to compute the stator outlet flow angle. This way, there is potential flow in the stator and the speed can be computed solving Laplace's equation, as it derives from a velocity potential ϕ:

$$\nabla \cdot \boldsymbol{u} = \nabla \cdot \left(\nabla \phi\right) = 0 \tag{5.36}$$

Equation 5.36 can be solved using a boundary elements method (BEM), as can be seen in the work from Katz and Plotkin [76]:

- Each stator blade is discretised as flat panels.
  - A point vortex singularity is placed in the quarter-chord point of each panel.
  - The flow is forced to be tangential to the three-quarter-chord point of each panel.
- The flow has polar periodicity.

- A point vortex singularity is placed in the centre of the stator plane.
- An unitary point sink singularity is placed in the centre of the stator plane.
- The speed is forced to have the same mean angle at the stator inlet as it has at the volute outlet in the last integration step.
- After solving the BEM problem, the speed angle is obtained at the stator outlet control point.

This simplified model can be seen in Figure 5.3. In this figure, the stator blades are descretised as four flat panels and the flow is forced to be tangential to the three-quarter-chord points and to the known stator inlet flow from the last time-step. The blades may be discretised with more panels if a lack of accuracy is observed with only one element per blade, as has been done here. In this figure, several elements are highlighted: the inlet control point, the outlet control point, the blade control point and the blade vortex. Of course, the validity of the method degrades as the assumptions become less valid.

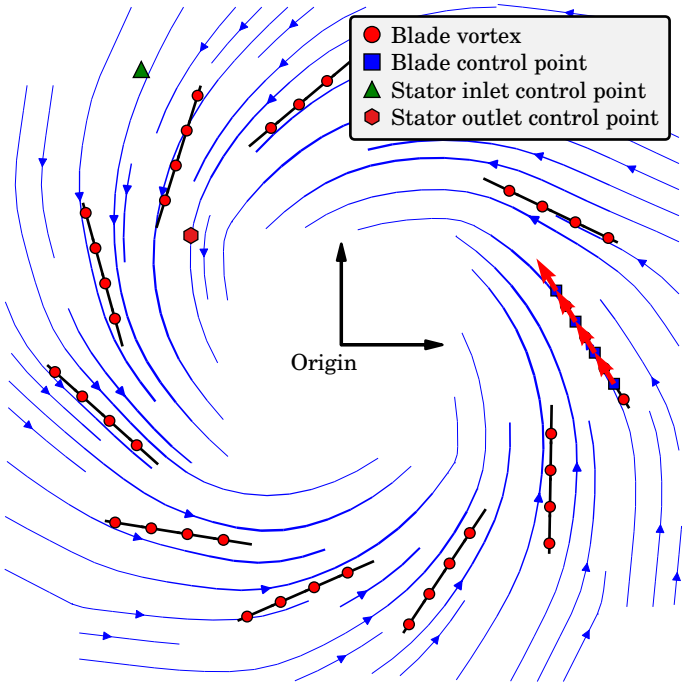

Figure 5.3: Idealised potential stator flow.

The induced speed at point $\boldsymbol{p}$ due to an unitary sink singularity at point $\boldsymbol{s}$ is:

$$\boldsymbol{u}_{sink}(\boldsymbol{p},\boldsymbol{s}) = -\begin{pmatrix} \dfrac{\cos\theta}{2\cdot\pi\cdot|\boldsymbol{p}-\boldsymbol{s}|} \\ \dfrac{\sin\theta}{2\cdot\pi\cdot|\boldsymbol{p}-\boldsymbol{s}|} \end{pmatrix} \tag{5.37}$$

where θ is the angle formed between the radius vector $\boldsymbol{p}$ and the radius vector $\boldsymbol{s}$. The induced speed at point $\boldsymbol{p}$ due to a point vortex singularity at point $\boldsymbol{s}$ is:

$$\boldsymbol{u}_{vortex}(\boldsymbol{p},\boldsymbol{s}) = \Gamma\cdot\begin{pmatrix} \dfrac{\sin\theta}{2\cdot\pi\cdot|\boldsymbol{p}-\boldsymbol{s}|} \\ \dfrac{-\cos\theta}{2\cdot\pi\cdot|\boldsymbol{p}-\boldsymbol{s}|} \end{pmatrix} \tag{5.38}$$

where Γ is the vortex strength. To reduce the computational cost of the evaluation of Equation 5.37 and Equation 5.38, the trigonometric functions are computed using inner products and cross products: they can be more efficiently computed in a modern x86 or ARM processor than trigonometric functions. Imposing the boundary conditions, so the induced speed due to all the singularities is tangential to the last computed flow at the stator inlet and to the stator blades at the three-quarter-chord point of a blade, the problem becomes:

$$\boldsymbol{AIC}\cdot\begin{pmatrix}\Gamma_{origin}\\ \Gamma_{bl}\end{pmatrix} = -\begin{bmatrix}\boldsymbol{u}_{sink}\left(p_{st,in,bc},\boldsymbol{o}\right)\cdot\boldsymbol{n}_{st,in,bc}\\ \boldsymbol{u}_{sink}\left(p_{bl,bc},\boldsymbol{o}\right)\cdot\boldsymbol{n}_{bl,bc}\end{bmatrix} \tag{5.39}$$

where $\boldsymbol{AIC}$ is the matrix of aerodynamic influence coefficients, Γ_{bl} is the vortex strength of the stator blades, Γ_{origin} is the vortex strength of the origin, $\boldsymbol{p}_{bl,bc}$ is the three-quarter-chord point of one of the blades, $\boldsymbol{n}_{bl,bc}$ is the normal vector to the blade chord at that point, $\boldsymbol{o}$ is the point at the origin of the stator reference frame, $\boldsymbol{p}_{st,in,bc}$ is the point at the stator inlet where the flow speed angle at the last time-step is known and $\boldsymbol{n}_{st,in,bc}$ is the normal vector to that flow speed. $\boldsymbol{AIC}$ is computed as follows:

$$\begin{aligned}
\boldsymbol{AIC}_{1,1} &= \boldsymbol{u}_{vortex}\left(\boldsymbol{p}_{st,in,bc},\boldsymbol{o}\right)\cdot\boldsymbol{n}_{st,in,bc}\\
\boldsymbol{AIC}_{1,2} &= \sum\boldsymbol{u}_{vortex}\left(\boldsymbol{p}_{st,in,bc},\boldsymbol{p}_{bl,qc}\right)\cdot\boldsymbol{n}_{st,in,bc}\\
\boldsymbol{AIC}_{2,1} &= \boldsymbol{u}_{vortex}\left(\boldsymbol{p}_{bl,bc},\boldsymbol{o}\right)\cdot\boldsymbol{n}_{bl,bc}\\
\boldsymbol{AIC}_{2,2} &= \sum\boldsymbol{u}_{vortex}\left(\boldsymbol{p}_{bl,bc},\boldsymbol{p}_{bl,qc}\right)\cdot\boldsymbol{n}_{bl,bc}
\end{aligned} \tag{5.40}$$

where $\boldsymbol{p}_{bl,qc}$ is the blade quarter-chord point where the vortex is located. $\boldsymbol{AIC}_{1,1}$ and $\boldsymbol{AIC}_{2,1}$ are computing using a summatory for all the blades quarter-chord points. As seen in Equation 5.40, the second row of $\boldsymbol{AIC}$ has to be computed only if there is a change in the geometry of the stator (i.e., the blades are rotated)

and the first row only depends on the inlet flow angle for a given position of the blades, so memoisation techniques have been applied in order to minimise even more the computational cost of computing the stator outlet flow angle. After solving Equation 5.39 and obtaining the strength of the vortexes, the induced speed is computed at a point in the stator outlet: α_3 is taken as the angle of this induced speed. As the model produces small variations in the stator inlet and outlet flow angle in different azimuthal positions, both the inlet boundary condition and the outlet angle are integrated along a curve to get their mean value instead of computing them in just one point. As the problem presents periodic behaviour in azimuth, the integration paths are chosen between two blades.

Figure 5.4 shows the results obtained for a typical stator geometry with different discretisations. It is clear that the single panel approach lacks accuracy in this particular case, and that the asymptotic behaviour is reached with 4 panels. It is advisable to check the minimum amount of panels needed for a given geometry, but four appears to be a sensible value for straight vanes.

The set of equations for N_{panels} per blade becomes as in Equation 5.41:

$$\boldsymbol{AIC} \cdot \begin{pmatrix} \Gamma_{origin} \\ \Gamma_{bl_1} \\ \vdots \\ \Gamma_{bl_{N_{panels}}} \end{pmatrix} = - \begin{bmatrix} \boldsymbol{u}_{sink}\left(p_{st,in,bc}, \boldsymbol{o}\right) \cdot \boldsymbol{n}_{st,in,bc} \\ \boldsymbol{u}_{sink}\left(p_{bl,bc_1}, \boldsymbol{o}\right) \cdot \boldsymbol{n}_{bl,bc_1} \\ \vdots \\ \boldsymbol{u}_{sink}\left(p_{bl,bc_{N_{panels}}}, \boldsymbol{o}\right) \cdot \boldsymbol{n}_{bl,bc_{N_{panels}}} \end{bmatrix} \tag{5.41}$$

where Γ_{bl_j} is the vortex strength of the jth panel of the stator blade, $\boldsymbol{p}_{bl,bc_j}$ is the three-quarter-chord point of the jth panel of the reference blade and $\boldsymbol{n}_{bl,bc_j}$ is the unitary normal vector at that point. Again, the flow has been supposed periodic, so the vortex strength of the jth panel is the same for each blade, so the panel boundary conditions are that of only one of the blades. The new

aerodynamic influence coefficients can be computed as in Equation 5.42:

$$
\begin{aligned}
\boldsymbol{AIC}_{1,1} &= \boldsymbol{u}_{vortex}\left(\boldsymbol{p}_{st,in,bc}, \boldsymbol{o}\right) \cdot \boldsymbol{n}_{st,in,bc} \\
\boldsymbol{AIC}_{1,2} &= \sum \boldsymbol{u}_{vortex}\left(\boldsymbol{p}_{st,in,bc}, \boldsymbol{p}_{bl,qc_1}\right) \cdot \boldsymbol{n}_{st,in,bc} \\
&\vdots \\
\boldsymbol{AIC}_{1,N_{panels}} &= \sum \boldsymbol{u}_{vortex}\left(\boldsymbol{p}_{st,in,bc}, \boldsymbol{p}_{bl,qc_{N_{panels}}}\right) \cdot \boldsymbol{n}_{st,in,bc} \\
\boldsymbol{AIC}_{2,1} &= \boldsymbol{u}_{vortex}\left(\boldsymbol{p}_{bl,bc_1}, \boldsymbol{o}\right) \cdot \boldsymbol{n}_{bl,bc_1} \\
\boldsymbol{AIC}_{2,2} &= \sum \boldsymbol{u}_{vortex}\left(\boldsymbol{p}_{bl,bc_1}, \boldsymbol{p}_{bl,qc_1}\right) \cdot \boldsymbol{n}_{bl,bc_1} \\
&\vdots \\
\boldsymbol{AIC}_{2,N_{panels}+1} &= \boldsymbol{u}_{vortex}\left(\boldsymbol{p}_{bl,bc_1}, \boldsymbol{p}_{bl,qc_{N_{panels}}}\right) \cdot \boldsymbol{n}_{bl,bc_1} \\
&\vdots \\
\boldsymbol{AIC}_{N_{panels}+1,1} &= \boldsymbol{u}_{vortex}\left(\boldsymbol{p}_{bl,bc_{N_{panels}}}, \boldsymbol{o}\right) \cdot \boldsymbol{n}_{bl,bc_{N_{panels}}} \\
\boldsymbol{AIC}_{N_{panels}+1,2} &= \sum \boldsymbol{u}_{vortex}\left(\boldsymbol{p}_{bl,bc_{N_{panels}}}, \boldsymbol{p}_{bl,qc_1}\right) \cdot \boldsymbol{n}_{bl,bc_{N_{panels}}} \\
&\vdots \\
\boldsymbol{AIC}_{N_{panels}+1,N_{panels}+1} &= \sum \boldsymbol{u}_{vortex}\left(\boldsymbol{p}_{bl,bc_{N_{panels}}}, \boldsymbol{p}_{bl,qc_{N_{panels}}}\right) \cdot \boldsymbol{n}_{bl,bc_{N_{panels}}}
\end{aligned}
\tag{5.42}
$$

where $\boldsymbol{p}_{bl,qc_j}$ is the quarter-chord point of the jth panel of a blade. The summations are done across all the blades, using the quarter-chord point of each one. Again, only one reference blade is used for its panel boundary conditions.

The model can be further complicated if the flow is not assumed to be periodic: in that case, each blade should have its own panel vortex strengths and several potential vortexes should be put near the origin, as much as inlet boundary conditions are used. In that case, each stator channel might have its own outlet flow angle.

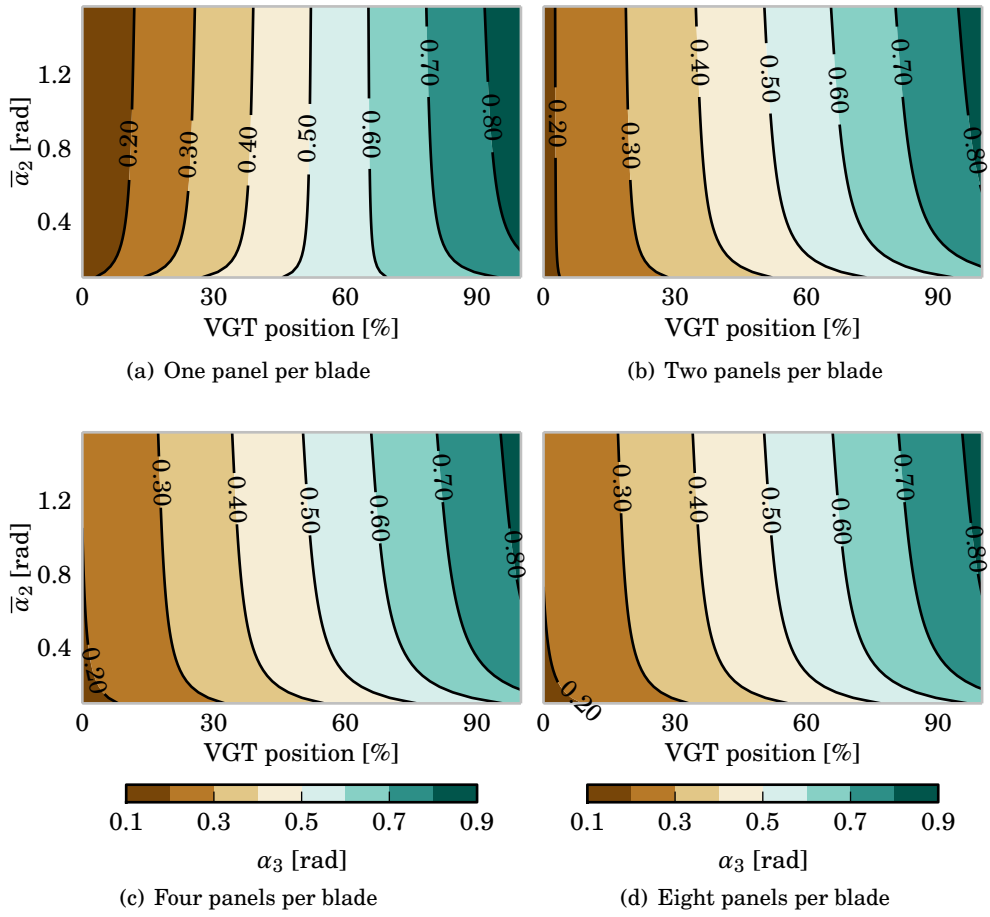

(a) One panel per blade

(b) Two panels per blade

(c) Four panels per blade

(d) Eight panels per blade

Figure 5.4: Stator outlet flow angle

5.5 Rotor

Rotor flow

The rotor outlet speed is computed assuming a constant rothalpy evolution. Some authors compute the rotor using rotating one-dimensional ducts with several source terms, such as in the work by Bellis et al. [87], but it has been demonstrated in the previous chapter that the turbine rotor can be safely assumed to behave in a quasi-steady manner. This way, the rotor outlet relative speed w_4 becomes:

$$T_{3t,rel} - \frac{\left(\omega \cdot r_{rt,in}\right)^2}{2 \cdot c_p} = T_4 - \frac{\left(\omega \cdot \bar{r}_{rt,out}\right)^2 - w_4^2}{2 \cdot c_p} \tag{5.43}$$

$$\begin{aligned} w_4 = \; & \left[2 \cdot c_p \cdot \left(T_{3t,rel} - T_4\right)\right. \\ & \left. -\omega^2 \cdot \left(r_{rt,in}^2 - \bar{r}_{rt,out}^2\right)\right]^{\frac{1}{2}} \end{aligned} \tag{5.44}$$

$$\frac{T_{3t,rel}}{T_4} = \left(\frac{p_{3,rel}}{p_4}\right)^{\frac{n_{rt}-1}{n_{rt}}} \tag{5.45}$$

$$\begin{aligned} w_4 = \; & \left\{2 \cdot \frac{\gamma}{\gamma - 1} \cdot R \cdot T_{3t,rel} \cdot \left[1 - \left(\frac{p_{3t,rel}}{p_4}\right)^{\frac{1-n_{rt}}{n_{rt}}}\right]\right. \\ & \left. -\omega^2 \cdot \left(r_{rt,in}^2 - \bar{r}_{rt,out}^2\right)\right\}^{\frac{1}{2}} \end{aligned} \tag{5.46}$$

where ω is the rotational speed of the rotor, $r_{rt,in}$ is the rotor inlet radius and $\bar{r}_{rt,out}$ is the rotor outlet mean radius. The relative pressure and temperature $p_{3t,rel}$ and $T_{3t,rel}$ are computed as follows:

$$T_{3t,rel} = T_3 + \frac{w_3^2}{2 \cdot c_p} \tag{5.47}$$

$$p_{3t,rel} = p_{3t} \cdot \left(\frac{T_{3t,rel}}{T_{3t}}\right)^{\frac{\gamma-1}{\gamma}} \tag{5.48}$$

The rotor inlet pressure and temperature are that of the stator cell and the outlet pressure is the pressure of the first cell of the turbine outlet.

The rotor inlet relative speed w_3 is computed as:

$$\begin{aligned} w_{3,r} &= u_{st} \cdot \sin \alpha_3 \\ w_{3,\theta} &= u_{st} \cdot \cos \alpha_3 - \omega \cdot r_{rt,in} \\ w_3 &= \sqrt{w_{3,r}^2 + w_{3,\theta}^2} \end{aligned} \tag{5.49}$$

where $w_{3,r}$ is the radial rotor inlet relative speed and $w_{3,\theta}$ is the tangential rotor inlet relative speed. A schematic drawing of the rotor inlet is shown in Figure 5.5, while the rotor outlet is shown in Figure 5.6.

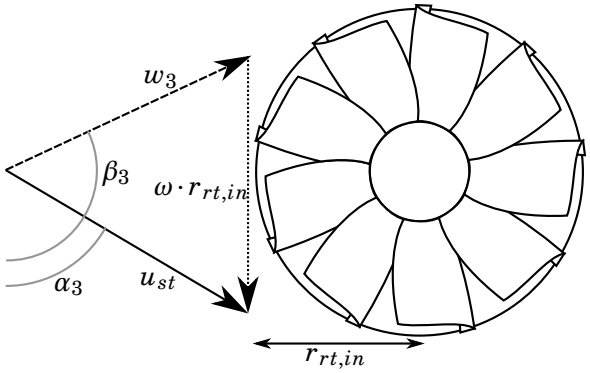

Figure 5.5: Rotor inlet velocity scheme.

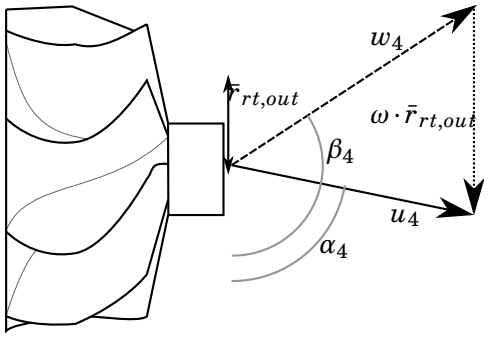

Figure 5.6: Rotor outlet velocity scheme.

To compute the rotor mass flow rate, the rotor outlet density is needed:

$$\begin{aligned}\rho_4 &= \frac{p_4}{R\cdot T_4} = \frac{p_4}{p_{3t,rel}}\cdot\frac{T_{3t,rel}}{T_4}\cdot\frac{p_{3t,rel}}{R\cdot T_{3t,rel}} \\ &= \frac{p_{3t,rel}}{R\cdot T_{3t,rel}}\cdot\left(\frac{p_{3t,rel}}{p_4}\right)^{-\frac{1}{n_{rt}}}\end{aligned} \tag{5.50}$$

Thus, the rotor outlet mass flow rate becomes:

$$\left.\frac{\mathrm{d}m}{\mathrm{d}t}\right|_{rt} = \frac{p_{3t,rel}}{R\cdot T_{3t,rel}}\cdot\left(\frac{p_{3t,rel}}{p_4}\right)^{-\frac{1}{n_{rt}}}\cdot A_4\cdot\sin\beta_4\cdot w_4 \tag{5.51}$$

The rotor outlet total temperature is:

$$\begin{aligned}T_{4t} = T_{3t,rel}\cdot\left(\frac{p_{3,rel}}{p_4}\right)^{\frac{n_{rt}-1}{n_{rt}}} &+ \frac{\left(w_4\cdot\sin\beta_4\right)^2}{2\cdot c_p} \\ &+ \frac{\left(w_4\cdot\cos\beta_4+\omega\cdot\bar{r}_{rt,out}\right)^2}{2\cdot c_p}\end{aligned} \tag{5.52}$$

and the turbine power output:

$$\dot{W} = \left.\frac{\mathrm{d}m}{\mathrm{d}t}\right|_{rt}\cdot c_p\cdot(T_{3t}-T_{4t}) \tag{5.53}$$

As in the case of the stator, the polytropic coefficient can be computed using losses models that dissipate stagnation pressure from the rotor inlet conditions to a virtual state after which a constant-entropy evolution is done:

$$n_{rt} = \frac{\ln\dfrac{p_{3t,rel}-\Delta p_{rt,loss}}{p_4}}{\dfrac{1-\gamma}{\gamma}\cdot\ln\dfrac{p_{3t,rel}}{p_4}+\ln\dfrac{p_{3t,rel}-\Delta p_{rt,loss}}{p_4}} \tag{5.54}$$

In this case, several losses model are used to compute $\Delta p_{rt,loss}$. The first implemented model is due to Futral et al. [69], and it is commonly known as the NASA model. This model can be implemented by a first virtual kinetic energy loss equivalent to the kinetic energy of the tangential component of the rotor

inlet flow followed by an isobaric process to recover the rotor inlet total relative temperature:

$$\frac{\Delta p_{rt,loss,NASA}}{p_{3t,rel}} = 1 - \left[\frac{T_{3t,rel} - \frac{w_3^2 \cdot \sin(\beta_{3,opt} - \beta_3)^2}{2 \cdot c_p}}{T_{3t,rel}} \right]^{\frac{\gamma}{\gamma - 1}} \tag{5.55}$$

where β_3 is the stator outlet flow angle in relative coordinates and $\beta_{3,opt}$ is the rotor inlet optimum angle. At the rotor inlet optimum angle the flow experiences no losses due to the NASA shock losses model.

The second losses model is due to Wasserbauer et al. [125], and it is computed as a stagnation pressure loss proportional to the dynamic pressure at the rotor outlet plus the component of the rotor inlet dynamic pressure that is normal to the optimum flow path:

$$\Delta p_{rt,loss,psg} = \frac{k_{rt,loss,psg}}{2} \cdot \left[\rho_3 \cdot w_3^2 \cdot \cos\left(\beta_{3,opt} - \beta_3\right) + \rho_4 \cdot w_4^2 \right] \tag{5.56}$$

where $k_{rt,loss,psg}$ is a fitting parameter. The last time-step rotor outlet relative velocity can be used to reduce computational costs. Thus, the total pressure loss becomes:

$$\Delta p_{rt,loss} = \Delta p_{rt,loss,NASA} + \Delta p_{rt,loss,psg} \tag{5.57}$$

Although tip clearance losses due to recirculation affect the rotor efficiency as can be seen in some recent works such as Huang's thesis [126], the U-RANS simulations used to calibrate the model lacked such effects, so no tip clearance losses model has been implemented.

Finally, if the rotor pressure ratio is high enough, the flow becomes sonic in the rotor throat. The rotor outlet pressure that produces critic conditions can be computed similarly to that of the stator, as seen in Equations (5.30) and (5.31).

$$p_{4,ch} = \left[\frac{2 \cdot c_p \cdot T_{3t,rel} - \omega^2 \left(r_{rt,in}^2 - \bar{r}_{rt,out}^2 \right)}{\left(1 + \frac{2}{\gamma - 1} \right) \cdot \gamma \cdot R \cdot T_{3t,rel}} \right]^{\frac{n_{rt}}{n_{rt} - 1}} \tag{5.58}$$

At each time-step, $p_{4,ch}$ is computed: if the rotor outlet pressure is less than it, the mass flow rate is computed as if $p_4 = p_{4,ch}$ and the final outlet speed is computed so the gas law is obeyed and the rotor outlet total temperature is equal to that of the rotor throat.

5.6 Mechanical losses model

In small automotive turbochargers, the bearing system usually consists in two different plain bearings: a radial journal bearing and a thrust bearing. As a first order approximation, the power drawn by the bearing system depends on the bearing and shaft geometry, the shaft rotational speed n and the dynamic viscosity μ. If the geometry remains stable, using the Buckingham π theorem leads to:

$$\dot{W}_{ml} \propto \mu \cdot \omega^2 \tag{5.59}$$

Using experimental data, it is usual to find results as in Figure 5.7.

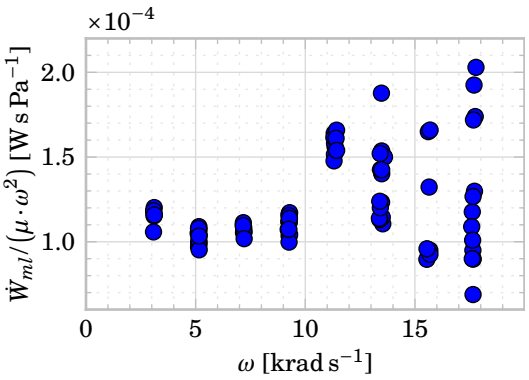

Figure 5.7: Buckingham π theorem applied to mechanical losses results.

As it can be seen, the mechanical losses power is not proportional to $\mu \cdot \omega^2$, what leads to think that the geometry is not constant and more work should be put into the development of a fast model that takes into account this geometry differences. While there are small variations for low shaft speeds, the results spread at higher speeds, with differences of the order of 100 % between different points.

The mechanical losses can be split into two different parts:

$$\dot{W}_{ml} = \dot{W}_{jb} + \dot{W}_{tb} \tag{5.60}$$

The first term, $\dot{W}_{jb}$, is due to the power losses in the radial bearing, where the bush can be fixed or unfixed. The second term, $\dot{W}_{tb}$, is due to the power losses in the thrust bearing. In both bearings, there is a tangential speed gradient in the oil film that creates viscous stresses, thus heating the oil and creating a loss in the power transmitted from the turbine to the compressor.

In order to obtain the power losses in the bearing system, the behaviour of the oil in an ideal journal and thrust bearing is studied. The equations

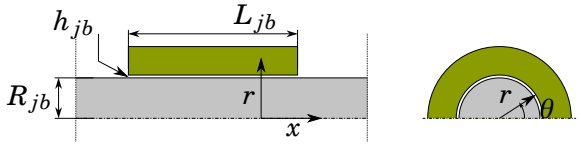

Figure 5.8: Schematic model of a journal bearing

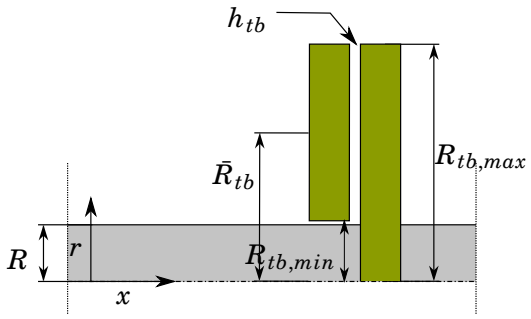

Figure 5.9: Schematic model of a thrust bearing

to compute the power losses in the ideal bearings (Figures 5.8 and 5.9), are developed performing the following assumptions:

1. Oil behaves as an incompressible fluid.
2. The flow through the bearings is steady.
3. The bearings are long enough to consider constant behaviour at each section.
4. The flow is circumferentially symmetric.
5. Body forces are negligible.
6. The Reynolds number $Re = \frac{\rho u_c h}{\mu}$ is expected to be small enough to make the viscous stresses comparable to the inertial forces of the fluid.
7. Film thickness in the bearing is smaller than any bearing geometry, i.e.

   a) $\frac{h_{jb}}{L_{jb}} \ll 1$, $\frac{h_{jb}}{R_{jb}} \ll 1$ and therefore $\frac{\rho u_c h_{jb}^2}{\mu L_{jb}} \ll 1$

   b) $\frac{h_{tb}}{R_{tb}} \ll 1 \Rightarrow \frac{\rho u_c h_{tb}^2}{\mu R_{tb}} \ll 1$

In the analysed turbochargers, points 6, 7a and 7b were true for the whole dataset, being the results of points 7a and 7b between 0.01 and 0.1. The circumferentially symmetric assumption, although is clearly invalid, is used as its consequences are consistent with what other authors have found. Indeed, Deligant et al. [98] found that the shaft eccentricity plays a negligible role in the global dissipated power inside the journal bearing, so the same results that are found for a symmetric case should apply to an eccentric bearing.

Journal bearing model

The power drawn by the ideal plain journal bearing is approximated by Equation 5.61.

$$\dot{W}_{jb} = \omega \cdot \int_{A_{jb}} R_{jb} \cdot \boldsymbol{\tau}' \cdot \mathrm{d}(\boldsymbol{n}A) \tag{5.61}$$

being ω the rotational speed of the journal, A_{jb} the surface of the journal bearing, R_{jb} the radius, $\boldsymbol{\tau}'$ the viscous stresses tensor and $\boldsymbol{n}$ the unitary normal vector to the surface. The integral can be approximated by the product of the surface of the journal bearing, $A_{jb} = 2\pi R_{jb} \cdot L_{jb}$, multiplied by the mean value of $\boldsymbol{\tau}' \cdot \boldsymbol{n}$, times the tangential speed $R_{jb} \cdot \omega$:

$$\begin{aligned} \dot{W}_{jb} &= A_{jb} \cdot \overline{(\boldsymbol{\tau}' \cdot \boldsymbol{n})} \cdot R_{jb} \cdot \omega \\ &= 2\pi R_{jb} \cdot L_{jb} \cdot \mu\left(\bar{T}_{oil}\right) \cdot \left.\frac{\partial u_\theta}{\partial r}\right|_{R_{jb}} \cdot R_{jb} \cdot \omega \end{aligned} \tag{5.62}$$

To obtain $\partial u_\theta / \partial r$, the continuity equation and the momentum conservation are used. First, solving the continuity equation for the simplified geometry of Figure 5.8:

$$\frac{\partial \rho}{\partial t} + \frac{1}{r}\left[\frac{\partial\left(\rho r u_r\right)}{\partial r} + \frac{\partial\left(\rho u_\theta\right)}{\partial \theta} + \frac{\partial\left(\rho r u_x\right)}{\partial x}\right] = 0 \tag{5.63}$$

Since the fluid is incompressible (assumption 1) and there is circumferential symmetry (assumption 4):

$$O\left(\frac{u_{r_c}}{h_{jb}}\right) + O\left(\frac{u_{x_c}}{L_{jb}}\right) = 0 \Rightarrow \frac{u_{r_c}}{u_{x_c}} \simeq \frac{h_{jb}}{L_{jb}} \ll 1 \tag{5.64}$$

where big O notation, for order of magnitude, is used.

This data may be used in order to get $\dfrac{\partial u_\theta}{\partial r}$ from the momentum conservation:

$$\rho\left(\frac{\partial \boldsymbol{u}}{\partial t} + \boldsymbol{u} \cdot \nabla \boldsymbol{u}\right) \cdot \boldsymbol{e}_\theta = \left(-\nabla p + \nabla \cdot \boldsymbol{\tau}' + \rho \boldsymbol{f}_m\right) \cdot \boldsymbol{e}_\theta \tag{5.65}$$

Taking into account that the flow is incompressible (assumption 1), circumferentially symmetric (assumption 4) and there are no body forces (assumption 5), Equation 5.65 can be simplified to:

$$u_r \frac{\partial u_\theta}{\partial r} + u_x \frac{\partial u_\theta}{\partial x} + \frac{u_r u_\theta}{r} = \nu \left[\frac{1}{r} \frac{\partial}{\partial r} \left(r \frac{\partial u_\theta}{\partial r} \right) + \frac{\partial^2 u_\theta}{\partial x^2} - \frac{u_\theta}{r^2} \right] \tag{5.66}$$

Taking the order of magnitude of the different terms of Equation 5.66 and skipping big O notation for ease of reading:

$$u_{r_c} \frac{u_{\theta_c}}{h_{jb}} + u_{x_c} \frac{u_{\theta_c}}{L_{jb}} + u_{r_c} \frac{u_{\theta_c}}{R_{jb}} = \nu \frac{u_{\theta_c}}{h_{jb}^2} + \nu \frac{u_{\theta_c}}{L_{jb}^2} + \nu \frac{u_{\theta_c}}{R_{jb}^2} \tag{5.67}$$

Dividing by the first term at the right hand side of the equation and using Equation 5.64:

$$\frac{\rho u_{x_c}}{\mu L_{jb}} h_{jb}^2 + \frac{\rho u_{x_c}}{\mu L_{jb}} h_{jb}^2 + \frac{\rho u_{x_c}}{\mu L_{jb}} h_{jb}^2 \frac{h_{jb}}{R_{jb}} = 1 + \left(\frac{h_{jb}}{L_{jb}} \right)^2 + \left(\frac{h_{jb}}{R_{jb}} \right)^2 \tag{5.68}$$

Thus, combining Equations (5.66) and (5.68), and taking into account assumptions 5 and 6, the most important part of the conservation of momentum for the θ component is:

$$\frac{1}{r} \frac{\partial}{\partial r} \left(r \frac{\partial u_\theta}{\partial r} \right) = 0 \Rightarrow \left. \frac{\partial u_\theta}{\partial r} \right|_{R_{jb}} \simeq \omega \cdot \frac{R_{jb}}{h_{jb}} \tag{5.69}$$

If the journal bearing is short as the one seen in Figure 5.10, the oil tangential speed gradient in the centre of the bearing (section B-B) is similar to the ideal, but it is almost zero near the edges (section A-A). In this case, a correction factor k_{jb} can be used.

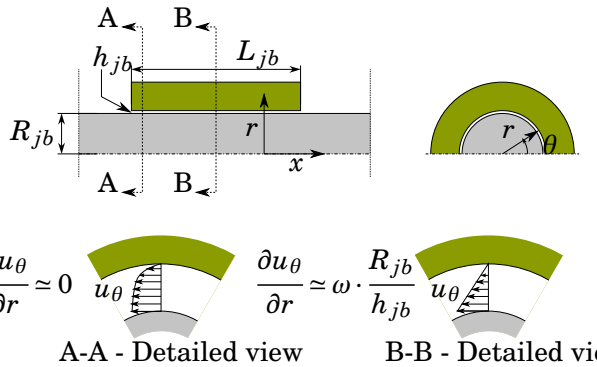

Figure 5.10: Simplified model of a short journal bearing

Hence, the mechanical power loss in the radial bearing is computed as:

$$\dot{W}_{jb} = 2\pi R_{jb}^3 k_{jb} \frac{L_{jb}}{h_{jb}} \mu\left(\bar{T}_{oil}\right) \omega^2 \tag{5.70}$$

The geometrical data may be directly measured or fitted experimentally within a simple constant parameter ($R_{jb}^3 k_{jb} L_{jb}/h_{jb}$) if mechanical power data are available.

Thrust bearing model

In the case of an ideal thrust bearing, the power losses can be computed as:

$$\dot{W}_{tb} = \omega \cdot \int_{A_{tb}} r \cdot \boldsymbol{\tau}' \cdot \mathrm{d}(\boldsymbol{n}A) \tag{5.71}$$

Again, the integral of Equation 5.71 can be approximated using mean values. Now, the surface of the thrust bearing is $A_{tb} = \pi\left(R_{tb,max}^2 - R_{tb,min}^2\right)$, the mean tangential speed is $\bar{R}_{tb} \cdot \omega$ and the mean viscous stress is $\mu\left(\bar{T}_{oil}\right) \cdot \partial u_\theta/\partial x$:

$$\begin{aligned} \dot{W}_{tb} &= A_{tb} \cdot \left(\overline{\boldsymbol{\tau}' \cdot \boldsymbol{n}}\right) \cdot \bar{R}_{tb} \cdot \omega \\ &= \pi\left(R_{tb,max}^2 - R_{tb,min}^2\right) \cdot \mu\left(\bar{T}_{oil}\right) \cdot \left.\frac{\partial u_\theta}{\partial x}\right|_{\bar{R}_{tb},h_{tb}} \cdot \bar{R}_{tb} \cdot \omega \end{aligned} \tag{5.72}$$

where $(\partial u_\theta/\partial x)|_{\bar{R}_{tb},h_{tb}}$ can be approximated using the continuity equation and the momentum conservation equations. The continuity equation gives similar results as in the ideal journal bearing case, thus allowing to simplify even more the momentum equation that will be used to compute the velocity gradient at the thrust bearing. Taking orders of magnitude in Equation 5.63 in the thrust bearing:

$$O\left(\frac{u_{r_c}}{R_{tb}}\right) + O\left(\frac{u_{x_c}}{h_{tb}}\right) = 0 \Rightarrow \frac{u_{x_c}}{u_{r_c}} \simeq \frac{h_{tb}}{R_{tb}} \ll 1 \tag{5.73}$$

With these results, and taking orders of magnitude in Equation 5.66 applied to the thrust bearing:

$$u_{r_c}\frac{u_{\theta_c}}{R_{tb}} + u_{x_c}\frac{u_{\theta_c}}{h_{tb}} + u_{r_c}\frac{u_{\theta_c}}{R_{tb}} = \nu u_{\theta_c}\left(\frac{1}{R_{tb}^2} + \frac{1}{h_{tb}^2} + \frac{1}{R_{tb}^2}\right) \tag{5.74}$$

Multiplying Equation 5.74 by $h_{tb}^2/\left(\nu \cdot u_{\theta_c}\right)$ and using Equation 5.73:

$$\frac{\rho u_{r_c}}{\mu R_{tb}} h_{tb}^2 + \frac{\rho u_{x_c}}{\mu R_{tb}} h_{tb}^2 + \frac{\rho u_{r_c}}{\mu R_{tb}} h_{tb}^2 = \left(\frac{h_{tb}}{R_{tb}}\right)^2 + 1 + \left(\frac{h_{tb}}{R_{tb}}\right)^2 \tag{5.75}$$

Every term in the momentum equation for θ is negligible but $\nu \cdot \frac{\partial^2 u_\theta}{\partial x^2}$. Thus, u_θ and its gradient can be obtained as:

$$\frac{\partial^2 u_\theta}{\partial x^2} = 0 \Rightarrow \left.\frac{\partial u_\theta}{\partial x}\right|_{\bar{R}_{tb}, h_{tb}} = \omega \cdot \frac{\bar{R}_{tb}}{h_{tb}} \tag{5.76}$$

In this case, the oil film thickness should not be considered constant. To compute it, the radial equation of momentum for steady, incompressible, circumferentially symmetric flow with no body forces is used:

$$\begin{gathered} u_r \frac{\partial u_r}{\partial r} + u_x \frac{\partial u_r}{\partial x} - \frac{u_\theta^2}{r} = \\ -\frac{\partial p}{\rho \partial r} + \frac{\nu}{r}\frac{\partial}{\partial r}\left(r \frac{\partial u_r}{\partial r}\right) + \nu \cdot \frac{\partial^2 u_r}{\partial x^2} - \nu \cdot \frac{u_r}{r^2} \end{gathered} \tag{5.77}$$

The orders of magnitude of the different terms are:

$$\begin{gathered} u_{r_c} \frac{u_{r_c}}{R_{tb}} + u_{x_c} \frac{u_{r_c}}{h_{tb}} + \frac{u_{\theta_c}^2}{R_{tb}} = \\ \frac{(\Delta p)_{R_{tb}}}{\rho_c R_{tb}} + \nu \frac{u_{r_c}}{R_{tb}^2} + \nu \frac{u_{r_c}}{h_{tb}^2} + \nu \frac{u_{r_c}}{R_{tb}^2} \end{gathered} \tag{5.78}$$

where $(\Delta p)_{R_{tb}}$ is the variation of the oil pressure through the radius of the thrust bearing. Dividing by the third term on the right hand side of Equation 5.78:

$$\begin{gathered} \frac{\rho_c u_{r_c}}{\mu R_{tb}} h_{tb}^2 + \frac{\rho_c u_{x_c}}{\mu R_{tb}} h_{tb}^2 + \frac{\rho_c u_{\theta_c}}{\mu R_{tb}} h_{tb}^2 \frac{u_{\theta_c}}{u_{r_c}} = \\ \frac{(\Delta p)_{R_{tb}}}{\mu R_{tb} u_{rc}} h_{tb}^2 + \left(\frac{h_{tb}}{R_{tb}}\right)^2 + 1 + \left(\frac{h_{tb}}{R_{tb}}\right)^2 \end{gathered} \tag{5.79}$$

All the terms are negligible but the first and the third at the right hand side of Equation 5.79 and hence Equation 5.77 is simplified to:

$$\frac{\partial p}{\partial r} = \mu \frac{\partial^2 u_r}{\partial x^2} \tag{5.80}$$

Assuming that the oil pressure is a constant at both sides of the thrust bearing plus a gradient at the working side and integrating twice:

$$\begin{aligned} F_{at} &= \int_{R_{tb,min}}^{R_{tb,max}} \left(\int_0^{R_{tb,i}} \frac{\partial p}{\partial r} \mathrm{d}r \right) \mathrm{d}R_{tb,i} \\ &= \int_{R_{tb,min}}^{R_{tb,max}} \left(\pi r \int_0^{R_{tb,i}} \mu \frac{\partial^2 u_r}{\partial x^2} \mathrm{d}r \right) \mathrm{d}R_{tb,i} \end{aligned} \tag{5.81}$$

u_r can be computed assuming a parabolic radial speed profile, similar to that of a Poiseuille planar flow:

$$u_r(x) = \frac{3}{2}\bar{u}_r \cdot \left[1 - \left(\frac{2x}{h_{tb}} - 1\right)^2\right] \tag{5.82}$$

The mean radial speed at a given radius is modelled as:

$$\bar{u}_r = \frac{\dot{m}_{oil,tb}}{2\pi r \rho h_{tb}} \tag{5.83}$$

The mass flow rate through the ideal thrust bearing can be computed as a constant fraction of the total mass flow rate in the full bearing system:

$$\dot{m}_{oil,tb} = k_m \dot{m}_{oil} \tag{5.84}$$

Using Equation 5.82, Equation 5.83 and Equation 5.84 together:

$$u_r(x) = \frac{3k_m \dot{m}_{oil}}{4\pi r \rho h_{tb}} \cdot \left[1 - \left(\frac{2x}{h_{tb}} - 1\right)^2\right] \tag{5.85}$$

Using Equation 5.85 in Equation 5.81 and solving for h_{tb}:

$$h_{tb} \simeq \sqrt[3]{\left|\frac{12k_m \dot{m}_{oil} \xi \mu}{F_{at}\rho}\right|} \tag{5.86}$$

and

$$\xi = R_{tb,max}^2/2 \cdot \left[\ln\left(R_{tb,max}\right) - 0.5\right] - R_{tb,min}^2/2 \cdot \left[\ln\left(R_{tb,min}\right) - 0.5\right] \tag{5.87}$$

The axial thrust can be computed using geometrical information and pressures at the compressor and turbine wheels. As the thrust bearing can be modelled symmetrically, only the absolute magnitude of the force is needed. Figure 5.11 shows an scheme of the proposed pressure distribution linearisation at turbine and compressor sides.

The pressure at the outlet of the compressor wheel ($p_{comp,rt,out}$) is supposed as slightly higher than the mean value between the pressure at the inlet ($p_{comp,in}$) and the pressure at the outlet ($p_{comp,out}$) of the compressor, as expected from the results from chapter 3. The pressure at the inlet of the turbine wheel p_3 can be calculated as seen in [31] or with the results from the model

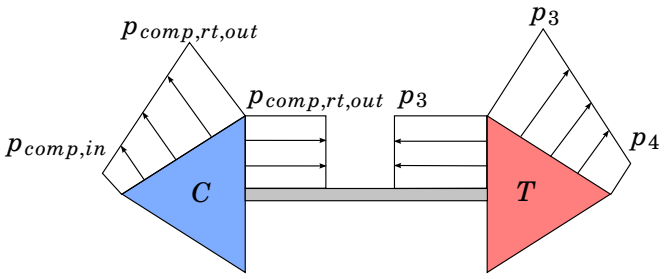

Figure 5.11: Schematic pressure distribution at the compressor and turbine wheels

described later. For more accurate results, the variation of the compressor rotor outlet pressure with the operating conditions should be used.

$$\begin{aligned} F_{comp} =& A'_{comp} \cdot \left[\frac{p_{comp,in} + 0.6 \cdot \left(p_{comp,out} - p_{comp,in}\right)}{2} \right. \\ & \left. -0.6 \cdot \left(p_{comp_o ut} - p_{comp,in}\right) \right] \\ =& A'_{comp} \cdot \frac{p_{comp,in} - 0.6 \cdot \left(p_{comp,out} - p_{comp,in}\right)}{2} \end{aligned} \tag{5.88}$$

$$F_{turb} = A'_{turb} \cdot \left(p_3 - \frac{p_3 + p_4}{2} \right) = A'_{turb} \cdot \left(\frac{p_3 - p_4}{2} \right) \tag{5.89}$$

$$\begin{aligned} F_{at} &= \left| F_{comp} + F_{turb} \right| \\ &= \left| A'_{comp} \cdot \frac{p_{comp,in} - 0.6 \cdot \left(p_{comp,out} - p_{comp,in}\right)}{2} + A'_{turb} \frac{p_3 - p_4}{2} \right| \end{aligned} \tag{5.90}$$

where A'_{comp} and A'_{turb} are the effective areas of the compressor and the turbine wheels. Each one is the projected area in the axial direction, multiplied by a constant that takes into account the non-linearities of the pressure distribution in the wheels:

$$A'_{comp} = k_{A_{comp}} \cdot A_{comp} \tag{5.91}$$

$$A'_{turb} = k_{A_{turb}} \cdot A_{turb} \tag{5.92}$$

The value of the tangential speed gradient in the thrust bearing is computed in Equation 5.93:

$$\left.\frac{\partial u_\theta}{\partial x}\right|_{\bar{R}_{tb},h_{tb}} = \omega \cdot \frac{\bar{R}_{tb}}{\sqrt[3]{\left|\frac{12 k_m \dot{m}_{oil} \xi \mu}{F_{at} \cdot \rho}\right|}} \tag{5.93}$$

where F_{at} is shown in Equation 5.90.

If the thrust bearing is short, which is usually the case, the tangential speed gradient should be corrected by a constant factor k_{tb} as in the case of the plain radial bearing. The factor k_{tb} can also take into account differences in the speed gradient due to other effects like grooves or gaps in the bearing. Figure 5.12 shows an scheme of short bearing effects on oil film velocity in the tangential direction.

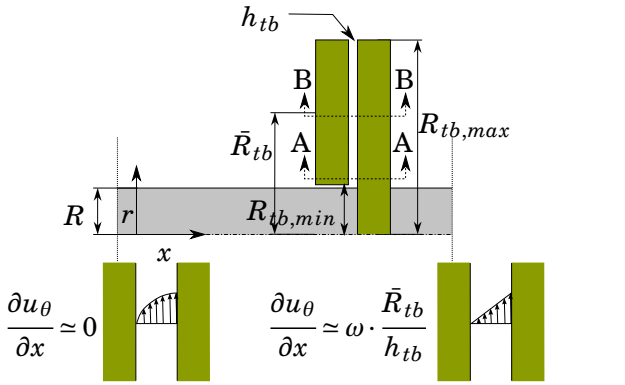

Figure 5.12: Simplified model of a short thrust bearing

Therefore, the final expression for the power loss in the thrust bearing is shown in Equation 5.94:

$$\dot{W}_{tb} = k_{tb} \pi \left(R_{tb,max}^2 - R_{tb,min}^2\right) \cdot \bar{R}_{tb}^2 \sqrt[3]{\left|\frac{F_{at} \rho}{12 k_m \dot{m}_{oil} \xi \mu}\right|} \mu \omega^2 \tag{5.94}$$

Pressure evolutions affect instantaneously compressor and turbine efficiencies and modify their mean value from steady tests, as can be seen in the work from Rajoo et al. [127], but they also affect the mechanical power losses and thus the mechanical efficiency, due to their effect in the term F_{at}.

An unintended side effect of the thrust bearing model is that it opens the door to future developments of shaft motion estimation, which may be useful to compute the tip clearance during unsteady simulations.

Full model

The full model couples the mechanical losses due to the radial and axial bearings. The oil that flows through them may pass through separate channels or may flow first through the radial bearing and then through the thrust bearing.

In both bearings (Equations (5.70) and (5.94)) it appears the oil viscosity, which varies considerably when increasing its temperature. The power losses computed assuming a constant temperature equal to the inlet temperature are overestimated, as shown in [98]. To compute the relationship between oil viscosity and temperature, Vogel's correlation has been used (see Equation 5.95), but other correlations may apply.

$$\mu = \mu(T) = k_1 \cdot \mathrm{e}^{\frac{k_2}{T - k_3}} \tag{5.95}$$

The values of the constants of Equation 5.95 may be obtained by experimental means using viscometers or using manufacturer-provided data sheets. Vogel's correlation is far less computationally efficient than a polynomial correlation with a similar number of terms, so it may be changed for faster evaluations. All the other terms in Equations (5.70) and (5.94) can be computed efficiently with little effort: the terms that go to the power of two can be computed multiplying them by themselves, and some libraries provide fast cubic root functions, such as `cbrt` in recent versions of the `GNU C Library` [128] (the respondent has tested version 2.19).

Separate oil feeding channels

In this case, there are different feeding channels for the radial and the axial bearings. The value of the mean viscosity of the flow ($\mu\left(\bar{T}_{oil}\right)$) can be obtained assuming that the power losses in the bearings are equal to the leap in enthalpy in the oil in adiabatic conditions.

$$\begin{aligned}
\dot{W}_{ml} &\simeq \dot{m}_{oil} c_{oil} \left(T_{oil,out} - T_{oil,in}\right) \\
&= \dot{W}_{jb} + \dot{W}_{tb} \\
&= k_{jb} 2\pi R_{jb}^3 \frac{L_{jb}}{h_{jb}} \mu\left(\bar{T}_{oil}\right) \omega^2 \\
&\quad + k_{tb} \pi \left(R_{tb,max}^2 - R_{tb,min}^2\right) \\
&\quad \cdot \bar{R}_{tb}^2 \sqrt[3]{\left| \frac{F_{at} \rho}{12 k_m \dot{m}_{oil} \xi \mu\left(\bar{T}_{oil}\right)} \right|} \cdot \mu\left(\bar{T}_{oil}\right) \omega^2
\end{aligned} \tag{5.96}$$

The weighted mean temperature of the oil is computed as:

$$\bar{T}_{oil} \simeq T_{oil,in} + k_T \left(T_{oil,out} - T_{oil,in} \right) \tag{5.97}$$

Using the relationship between $T_{oil,out}$, $\bar{T}_{oil}$ and $T_{oil,in}$ in the energy balance equation:

$$\begin{aligned} \bar{T}_{oil} =& T_{oil,in} + k_T k_{jb} 2\pi R_{jb}^3 \frac{L_{jb}}{h_{jb}} \mu\left(\bar{T}_{oil}\right) \frac{\omega^2}{\dot{m}_{oil} c_{oil}} \\ &+ k_T k_{tb} \pi \left(R_{tb,max}^2 - R_{tb,min}^2 \right) \\ &\cdot \bar{R}_{tb}^2 \sqrt[3]{\left| \frac{F_{at} \rho}{12 k_m \dot{m}_{oil} \xi \mu\left(\bar{T}_{oil}\right)} \right|} \cdot \mu\left(\bar{T}_{oil}\right) \frac{\omega^2}{\dot{m}_{oil} c_{oil}} \end{aligned} \tag{5.98}$$

which is an implicit equation that can be solved for $\bar{T}_{oil}$ using the correlation for $\mu(T)$ given in Equation 5.95. The respondent has used Brent's method to efficiently solve this implicit equation.

Using the value of $\mu\left(\bar{T}_{oil}\right)$ obtained by solving Equation 5.98, a non-isothermal approximation of the power losses in the bearing system is obtained.

The values of k_1, k_2, k_3, c and ρ may be obtained using experimental results or consulting the data sheet of the oil used, if it is not very old. If the density and the specific heat capacity of the oil is expected to change appreciably during the non-isothermal evolution, their behaviour should be modelled the same as the dynamic viscosity. The respondent found good results assuming k_T equal to 0.75. k_{jb} and k_{tb} can be obtained by experimental results. ξ is computed by Equation 5.87 and F_{at} is calculated as shown in Equation 5.90.

Common flow channel

In this case, the oil passes first through a radial bearing and, then, through a thrust bearing ($k_m = 1$). It can be modelled using two different mean temperatures:

$$\begin{aligned} \dot{W}_{ml} &\simeq \dot{m}_{oil} c_{oil} \left(T_{oil,out} - T_{oil,in} \right) \\ &= \dot{W}_{jb} + \dot{W}_{tb} \\ &= k_{jb} 2\pi R_{jb}^3 \frac{L_{jb}}{h_{jb}} \mu\left(\bar{T}_{oil,jb}\right) \omega^2 \\ &\quad + k_{tb} \pi \left(R_{tb,max}^2 - R_{tb,min}^2 \right) \\ &\quad \cdot \bar{R}_{tb}^2 \sqrt[3]{\left| \frac{F_{at} \rho}{12 k_m \dot{m}_{oil} \xi \mu\left(\bar{T}_{oil,tb}\right)} \right|} \cdot \mu\left(\bar{T}_{oil,tb}\right) \omega^2 \end{aligned} \tag{5.99}$$

where $\bar{T}_{oil,jb}$ is the mean temperature for the process inside the radial bearing and $\bar{T}_{oil,tb}$ is the mean oil temperature for the process inside the axial bearing. The weighted mean temperature of the oil in the first bearing is computed as:

$$\bar{T}_{oil,jb} \simeq T_{oil,in} + k_T \left(T_{oil,jb,out} - T_{oil,in} \right) \tag{5.100}$$

$$\bar{T}_{oil,jb} = T_{oil,in} + k_T k_{jb} 2\pi R_{jb}^3 \frac{L_{jb}}{h_{jb}} \mu \left(\bar{T}_{oil} \right) \frac{\omega^2}{\dot{m}_{oil} c_{oil}} \tag{5.101}$$

The radial bearing oil outlet temperature is trivially obtained after obtaining $\bar{T}_{oil,jb}$:

$$T_{oil,jb,out} = \frac{\bar{T}_{jb} - T_{oil,in}}{k_T} + T_{oil,in} \tag{5.102}$$

The weighted mean temperature of the oil in the second bearing is computed as:

$$\bar{T}_{oil,tb} \simeq T_{oil,jb,out} + k_T \left(T_{oil,out} - T_{oil,jb,out} \right) \tag{5.103}$$

$$\begin{aligned} \bar{T}_{oil,tb} =& k_T k_{tb} \pi \left(R_{tb,max}^2 - R_{tb,min}^2 \right) \\ & \cdot \bar{R}_{tb}^2 \sqrt[3]{\left| \frac{F_{at} \rho}{12 \dot{m}_{oil} \xi \mu \left(\bar{T}_{oil} \right)} \right|} \cdot \mu \left(\bar{T}_{oil,tb} \right) \frac{\omega^2}{\dot{m}_{oil} c_{oil}} \end{aligned} \tag{5.104}$$

The thrust bearing oil outlet temperature $T_{oil,out,tb}$ is obtained as:

$$T_{oil,out} = \frac{\bar{T}_{tb} - T_{oil,jb,out}}{k_T} + T_{oil,jb,out} \tag{5.105}$$

The resolution process is as follows: first, Equation 5.101 is solved to get the mean temperature at the radial bearing outlet; then, Equation 5.102 is solved to get its outlet temperature; this temperature is used in Equation 5.104 to get the average temperature at the axial bearing; Equation 5.105 is then used to get the oil outlet temperature. Using the outlet temperature, the mechanical losses power can be obtained by just computing the internal energy leap in the oil.

Heat flow addition

Heat flow can be added to the model before the oil enters the bearings and after it exits them, in the sump, to get the oil temperature at the oil outlet port. The bearings inlet temperature is computed as:

$$T_{oil,in} = T'_{oil,in} - \frac{\dot{Q}_{oil,in-housing}}{\dot{m}_{oil} \cdot c_{oil}} \tag{5.106}$$

where $T'_{oil,in}$ is the oil temperature at the inlet port, before entering the turbocharger, and $\dot{Q}_{oil,in-housing}$ is the heat flow from the oil inlet to the turbocharger housing. This heat flow is affecting the oil between the inlet port and the bearings. The oil temperature at the turbocharger outlet port is:

$$T'_{oil,out} = T'_{oil,in} + \frac{\dot{W}_{ml} - \dot{Q}_{oil,in-housing} - \dot{Q}_{oil,out-housing}}{\dot{m}_{oil} \cdot c_{oil}} \tag{5.107}$$

where $T'_{oil,out}$ is the temperature at the outlet port and $\dot{Q}_{oil,out,housing}$ is the heat flow from the oil to the housing after leaving the bearings.

5.7 Summary

In this chapter, several submodels to simulate part of automotive turbocharger performances have been presented, all of them able to be coupled with 1-dimensional engine simulation codes. The submodels compute the following aspects of a turbocharger operation:

- Adiabatic, steady-state performance and flow characteristics of a radial turbine stator.
- Adiabatic, steady-state performance of a radial turbine rotor.
- Adiabatic, unsteady operation of a radial turbine, including a novel approach to compute the volute with low computational cost.
- Power losses in the bearings subsystem.

From a turbine flow point-of-view, as the main accumulation and wave effects occur in the volute, an upgrade from the classic equivalent straight one-dimensional duct is needed to better compute the turbine response at very high frequencies. With classical equivalent one-dimensional volute models some of the accumulation and wave effects are captured, but their results are inherently less capable of capturing high frequency effects: at any given time, there could be important differences in the flow characteristics at different positions inside the volute that can not be computed. With a quasi-bidimensional volute, different stator channels may be subjected to different inlet conditions, while with the fully one-dimensional volute there is only one equivalent stator channel exposed to the duct outlet conditions. It is even possible to use different volute window areas for each cell in case that in the real turbine some channel blockage is expected due to mounting screws. The quasi-bidimensional model is also trivially adapted to twin-entry and waste-gate turbines.

A BEM model is used to compute the stator outlet angle for different operating conditions. This model should be able to reproduce this angle with different stator geometries, taking into account new developments such as blades with complex curvature laws. As this submodel uses the volute outlet flow angle to predict the stator outlet flow angle, it should give good results even during transient operation if quasi-steady assumptions are valid in the stator.

The stator and rotor main flows are computed similarly, using quasi-steady and adiabatic lumped elements: multiple total enthalpy conserving elements for the stator channels and a total rothalpy conserving element for the rotor. In view of the results presented in chapter 4, very simple total pressure losses submodels are used in order to reproduce their real behaviour.

Traditionally, mechanical losses in small turbochargers have been obtained as the product of a mechanical efficiency and the work performed by the turbine. This approach is possible since mechanical efficiency, in quasi-adiabatic conditions, has a rather linear relationship with turbocharger speed. So, at high speeds, it is possible to consider a constant value (close to unity) of this efficiency without affecting the results. But at low turbocharger speed this approach fails and the need of a mechanical losses model is mandatory, as well as during the warm-up phase of the oil, when its viscosity is far larger than that at highway operation and its variation as it heats up gives enormous differences in the dissipated power.

The mechanical losses model is based on the Navier Stokes equations applied to the two kinds of bearings (journal and thrust) normally used in small automotive turbochargers. Making some assumptions, a simplified model for the two bearings has been obtained. The model takes into account the working point (turbocharger speed, oil temperature and axial force) and the geometrical characteristics of the bearings. It has four calibration parameters that should be easily obtained by adjusting experimental data. A simple method to couple the mechanical losses model with a heat transfer lumped model is presented.

5.8 References

[31] J. R. Serrano, F. J. Arnau, V. Dolz, A. Tiseira, and C. Cervelló. “A model of turbocharger radial turbines appropriate to be used in zero- and one-dimensional gas dynamics codes for internal combustion engines modelling”. In: *Energy Conversion and Management* 49 (12 2008), pp. 3729–3745. DOI: 10.1016/j.enconman.2008.06.031 (cit. on pp. 17, 24, 161).

[32] A. W. Costall, R. M. McDavid, R. F. Martínez-Botas, and N. C. Baines. “Pulse performance modelling of a twin-entry turbocharger turbine under full unequal admission”. In: *Proceedings of ASME Turbo Expo 2009*. ASME, 2009. DOI: 10.1115/1.4000566 (cit. on pp. 17, 30, 31, 140, 202).

[34] M. Chiong, S. Rajoo, A. Romagnoli, A. Costall, and R. Martinez-Botas. "Integration of meanline and one-dimensional methods for prediction of pulsating performance of a turbocharger turbine". In: *Energy Conversion and Management* 81 (2014), pp. 270–281. ISSN: 0196-8904. DOI: 10.1016/j.enconman.2014.01.043 (cit. on pp. 17, 27, 31, 140).

[69] S. Futral, C. Wasserbauer, U. S. N. Aeronautics, and S. Administration. *Off-design performance prediction with experimental verification for a radial-inflow turbine: Samuel M.Futral Jr. and Charles A. Wasserbauer*. Tech. rep. NASA TN D-2621. NASA, 1965. URL: http://books.google.es/books?id=N1kzLAHfK-IC (cit. on pp. 26, 119, 153).

[76] J. Katz and A. Plotkin. *Low-Speed Aerodynamics*. 2nd. Cambridge University Press, 2001. ISBN: 978-0521665520 (cit. on pp. 28, 145).

[87] V. D. Bellis, S. Marelli, F. Bozza, and M. Capobianco. "1D Simulation and Experimental Analysis of a Turbocharger Turbine for Automotive Engines Under Steady and Unsteady Flow Conditions". In: *Energy Procedia* 45 (2014). {ATI} 2013 - 68th Conference of the Italian Thermal Machines Engineering Association, pp. 909–918. ISSN: 1876-6102. DOI: 10.1016/j.egypro.2014.01.096 (cit. on pp. 31, 151).

[98] M. Deligant, P. Podevin, and G. Descombes. "{CFD} model for turbocharger journal bearing performances". In: *Applied Thermal Engineering* 31.5 (2011). {MNF} 2009 Special Issue, pp. 811–819. ISSN: 1359-4311. DOI: 10.1016/j.applthermaleng.2010.10.030 (cit. on pp. 37, 157, 164).

[121] S. K. Godunov. "A Difference Scheme for Numerical Solution of Discontinuous Solution of Hydrodynamic Equations". In: *Matematicheskii Sbornik* 47 (1959), pp. 271–306 (cit. on p. 134).

[122] R. Courant, K. Friedrichs, and H. Lewy. "Über die partiellen Differenzengleichungen der mathematischen Physik". In: *Mathematische Annalen* 100.1 (Dec. 1, 1928), pp. 32–74. ISSN: 0025-5831. DOI: 10.1007/bf01448839 (cit. on p. 135).

[123] B. van Leer. "Towards the ultimate conservative difference scheme, V. A second order sequel to Godunov's method". In: *Journal of Computational Physics* 32 (1979), pp. 101–136 (cit. on p. 135).

[124] G. Guennebaud, B. Jacob, et al. *Eigen v3*. Last visited on 2014/10/30. 2010. URL: http://eigen.tuxfamily.org/ (cit. on p. 137).

[125] C. A. Wasserbauer and G. A. J. *FORTRAN program for predicting the off-design performance of radial inflow turbines*. Tech. rep. NASA TN-8063. NASA, 1975 (cit. on p. 154).

[126] A. Huang. *Loss Mechanisms in Turbine Tip Clearance Flows*. Master dissertation. 2011 (cit. on p. 154).

[127] S. Rajoo, A. Romagnoli, and R. F. Martinez-Botas. "Unsteady performance analysis of a twin-entry variable geometry turbocharger turbine". In: *Energy* 38.1 (2012), pp. 176–189. ISSN: 0360-5442. DOI: 10.1016/j.energy.2011.12.017 (cit. on p. 163).

[128] *The GNU C Library (glibc)*. Last visited on 2014/10/30. URL: http://www.gnu.org/software/libc/ (cit. on p. 164).

CHAPTER 6

Numerical model validation and results

Contents

Figures

Tables

6.1 Introduction

THE calibration and validation of the models are found in this chapter. The experimental calibration of each model is done using a random subset of the experimental data, while the validation is done using the whole datasets. The chapter is divided into two main parts: the first is devoted to the radial turbine model, while the second one contains the calibration and results concerning the mechanical losses model.

Three different campaigns are used for the turbine model: one of CFD data, other that has global turbine performance data and other with internal pressure data. The calibration process is done straight-forward using CFD data, as the internal variables are known, while it is more complicated using experimental data from the internal pressure campaign and has the most uncertainties using global characterisation data. The model is compared with simulations using a classic one-dimensional volute model consisting in an equivalent straight duct. Also, an overview of the performance of different numerical schemes is done, giving general recommendations.

The mechanical losses calibration and validation are done using data from three different turbocharger units, each one with different bearings arrangements, as well as different cooling subsystem characteristics. The results from the model are not only used under steady-state conditions, but also under pulsating flow, and the model is used to predict the power transmission losses for the three tested turbochargers with oil feeding conditions different from the ones that were measured, obtaining general tendencies that can be found during urban driving conditions.

6.2 Quasi-bidimensional turbine

The same sections as in chapter 4 and in Table 4.1 have been used during the validation of the quasi-bidimensional turbine model, as shown in Figure 6.1.

The simplified model has been validated against the U-RANS simulations that were described in chapter 4 and also against experimental results.

Calibration using CFD results

The model calibration using CFD data is straightforward. The 5 coefficients of the model ($C_{D_{st}}$, $k_{st,loss}$, $\beta_{3,opt}$, $k_{loss,psg}$ and $C_{D_{rt}}$) were selected as the time weighted averages during the steady-state CFD simulations for 181 krpm and an expansion ratio of 2.4. The averaging was done because, although steady-state boundary conditions were used, the simulation was carried out using an unsteady solver and the solution had a small pulsating behaviour due to the movement of the rotor. The model validation was performed with these

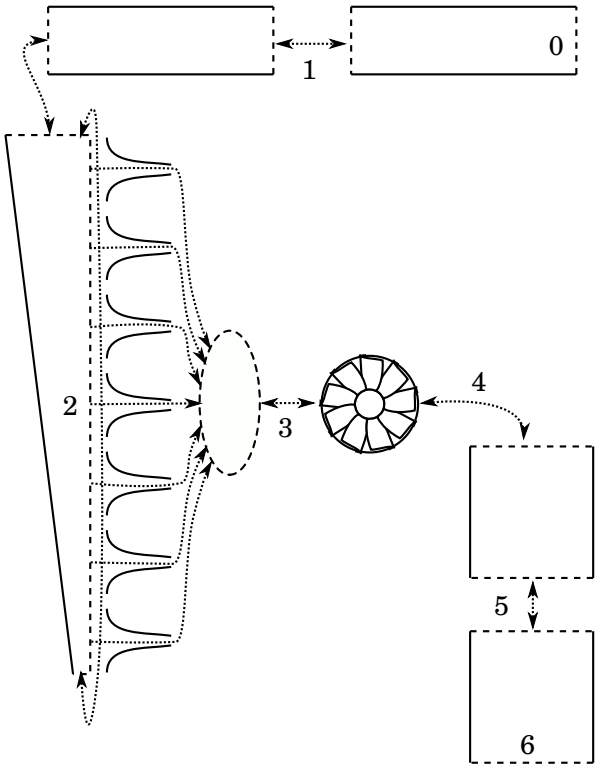

Figure 6.1: Quasi-bidimensional model scheme.

parameters, using pulsating boundary conditions as explained in the following section.

Validation using CFD results

The boundary conditions consisted of an isentropic pulsating total pressure and temperature inlet and a constant static pressure outlet. The total pressure at the inlet described a pure sinusoidal evolution. The rotor speed was maintained constant. The different cases are described in Table 6.1.

The data have been simulated also using a totally unidimensional equivalent volute. As there is no information about the stator inlet angle using this approach, the stator outlet angle has been set to the mean value obtained from the 3D simulations.

Figure 6.2 shows the turbine inlet corrected mass flow rate $\dot{m}_1^*$ versus the turbine total to static expansion ratio, p_{1t}/p_5. The turbine inlet corrected mass

Table 6.1: Simulated cases.

Case	Rotor speed	B.C. frequency	Inlet total pressure
1	90 krpm	50 Hz	101 to 221 kPa
2	90 krpm	130 Hz	101 to 221 kPa
3	181 krpm	50 Hz	151 to 331 kPa
4	181 krpm	90 Hz	151 to 331 kPa
5	181 krpm	130 Hz	151 to 331 kPa
6	750 krpm	130 Hz	151 to 331 kPa

flow rate is described as:

$$\dot{m}_1^* = \dot{m}_1 \cdot \sqrt{\frac{T_{1t}}{T_{ref}}} \cdot \frac{p_{ref}}{p_{1t}} \tag{6.1}$$

where the reference temperature is $T_{ref} = 288.15\,\mathrm{K}$ and the reference pressure $p_{ref} = 101325\,\mathrm{Pa}$. The figure shows good agreement between the CFD computation and the simplified model results. At the highest frequency, the amplitude of the oscillation is overestimated using the old volute model, while the quasi-bidimiensional approximation shows better behaviour.

The corrected mass flow rate for the stator $\dot{m}_{st}^*$ and the rotor $\dot{m}_{rt}^*$ are shown in Figure 6.3 and Figure 6.4. Their mass flow rates are corrected using the stator inlet total pressure and temperature and the rotor inlet total pressure and temperature, respectively. Again, the results are satisfactory in both cases. The rotor shows its biggest discrepancies at high speeds and low expansion ratios: this can be explained by the constant rotor outlet relative flow angle approach, and should be corrected in future works. In these cases, the amplitude of the mass flow rate oscillation is higher and better reproduced using the quasi-bidimensional volute. At the highest frequency, the stator results are problematic for both models, however.

Figure 6.5 shows the results for the stator outlet flow angle. The simplified model is not able to reproduce the biggest oscillations. However, this does not suppose big problems in the turbine power output nor its mass flow rate. The potential stator hypothesis can't stand against the fact that, when the biggest discrepancies appear, the expansion ratio and, thus, the flow speed is very low, easing the appearance of non-isentropic behaviour such as boundary layer and wake growth and flow detachment, as can be seen in Figure 6.6. In this figure, streamlines are plotted at two different times for case 2. At the lowest expansion ratio, the flow is almost tangential to the rotor and flow detachments appear. This kind of flow behaviour is not taken into account using potential flow theory and, thus, can not be computed properly without further refinements of the

model. Flow detachment appears at stator expansion ratios less than 1.15 and turbine expansion ratios around 1.5 in the turbine that the respondent studied, but further studies are needed to give a general rule for different turbines. At the highest frequency, the quasi steady-state assumption for the potential flow model is not valid, but it should not produce appreciable problems with real-world data as the amplitude associated to these high frequencies is drastically reduced.

Figure 6.7 shows the differences between the CFD and the simple model stator polytropic coefficient. The mean value and some of the variations are correctly taken into account, but the model underestimates the amplitude of the oscillation. The cases at 90 krpm were simulated with a very broad range of expansion ratios, even generating negative power output. At very low expansion ratios, the polytropic coefficient experiences large variations, presumably due to flow detachment. The differences in the streamlines are clearly visible in Figure 6.6, where the same case is plotted for a high expansion ratio and a low expansion ratio. At high expansion ratios, the flow is perfectly attached to the stator blade, while recirculation bubbles and full detachments appear in the very low expansion ratio case. While the stator head loss is approximately proportional to the dynamic pressure at its inlet in quasi-stationary or low frequency boundary conditions with attached flow, it begins to differ as accumulation effects and flow detachments rise.

Figure 6.8 shows the differences between the CFD and the simple model rotor polytropic coefficient. Again, large variations appear at very low expansion ratios. Albeit not perfectly, the general shape of the polytropic coefficient excursion is reproduced and, thus, the power output is satisfactorily computed: as can be seen in Table 6.2 and in Figure 6.9, the error committed while computing the power output is small. As in the stator case, the flow recirculates at very low expansion ratios, difficulting the polytropic coefficient estimation. A possible improvement in the accuracy could be achieved by means of two-zone modelling during recirculation events, using different models for attached and detached flow.

Figure 6.9 shows the turbine power output plotted against the turbine expansion ratio. The biggest errors appear at the highest expansion ratios, where the polytropic coefficient is underestimated, and at the lower expansion ratios, where it is overestimated. Further refinements of the losses modelling should correct these discrepancies. The amplitude of the power output evolution is better predicted using the quasi-bidimensional approach.

Figure 6.10 shows the volute outlet velocity distribution at four different times for the case at 181 krpm and 130 Hz. The volute outlet speed is plotted against an angular coordinate: this angular coordinate begins at the volute tongue, with positive angles measured in the normal flow direction. The model has been computed using an unusually large number of cells for the volute, 90.

The stator screws generate some blockage effect, so the volute outlet surface has been reduced in the presence of these fixing screws. The simple model is able to reproduce the dynamic behaviour across the volute, what it is expected to give it better high frequency prediction capabilities than more simple models, like using an straight duct for computing the volute. Figure 6.11 shows the volute total temperature at different angular positions. Again, the model is able to estimate this temperature distribution across the volute thanks to the quasi-bidimensional approach for volute modelling, giving results that can not be accomplished with a more simple equivalent one-dimensional duct.

Case	CFD	Proposed model	Error
1	2930.1 W	2975.9 W	1.6 %
2	2879.9 W	2883.5 W	0.1 %
3	9217.6 W	9138.7 W	0.9 %
4	9100.2 W	9070.8 W	0.3 %
5	8935.1 W	8895.4 W	0.4 %
6	9587.8 W	8576.0 W	10.5 %

Table 6.2: Turbine power output $\dot{W}$ error

It has been shown that, while the overall turbine power output error is small, there are some problems at high expansion ratios. This is expected to happen due to two different limitations of the current model: the rotor outlet flow angle is fixed for all operating conditions and the losses models underestimate the polytropic coefficient at high expansion ratios. As losses coefficients are adjusted for a fixed flow angle while in the CFD simulation vary, their values are not optimally selected. A more realistic rotor outlet flow angle model should enhance the model results. Also, at very low expansion ratios flow detachment and even inverse rotor and stator flow may appear, while the current model can not compute properly these situations. These effects limit the extrapolation capabilities of the presented model and will be taken into account in future works.

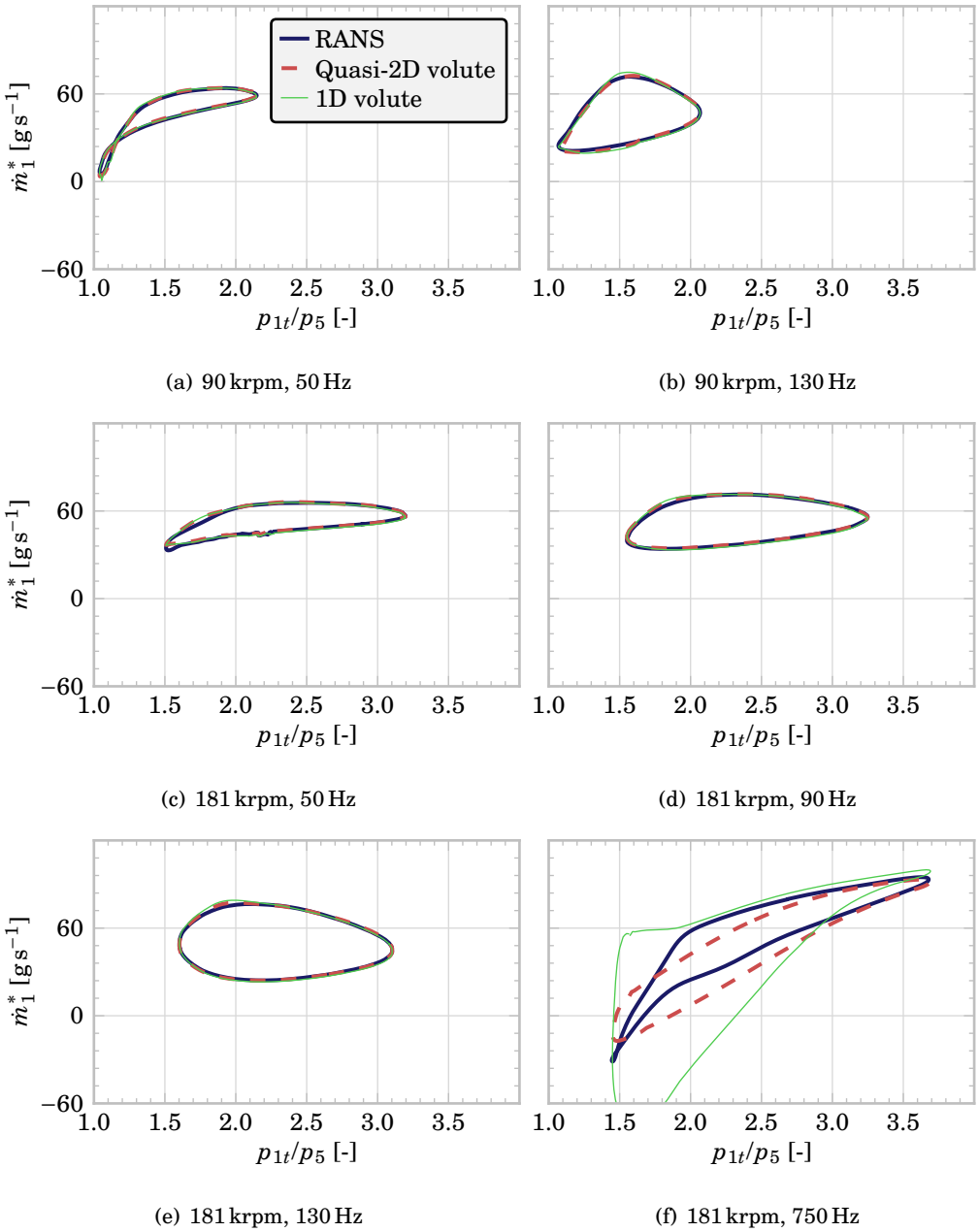

(a) 90 krpm, 50 Hz

(b) 90 krpm, 130 Hz

(c) 181 krpm, 50 Hz

(d) 181 krpm, 90 Hz

(e) 181 krpm, 130 Hz

(f) 181 krpm, 750 Hz

Figure 6.2: Turbine inlet corrected mass flow rate $\dot{m}_1^*$ vs. the turbine total to static expansion ratio p_{1t}/p_5

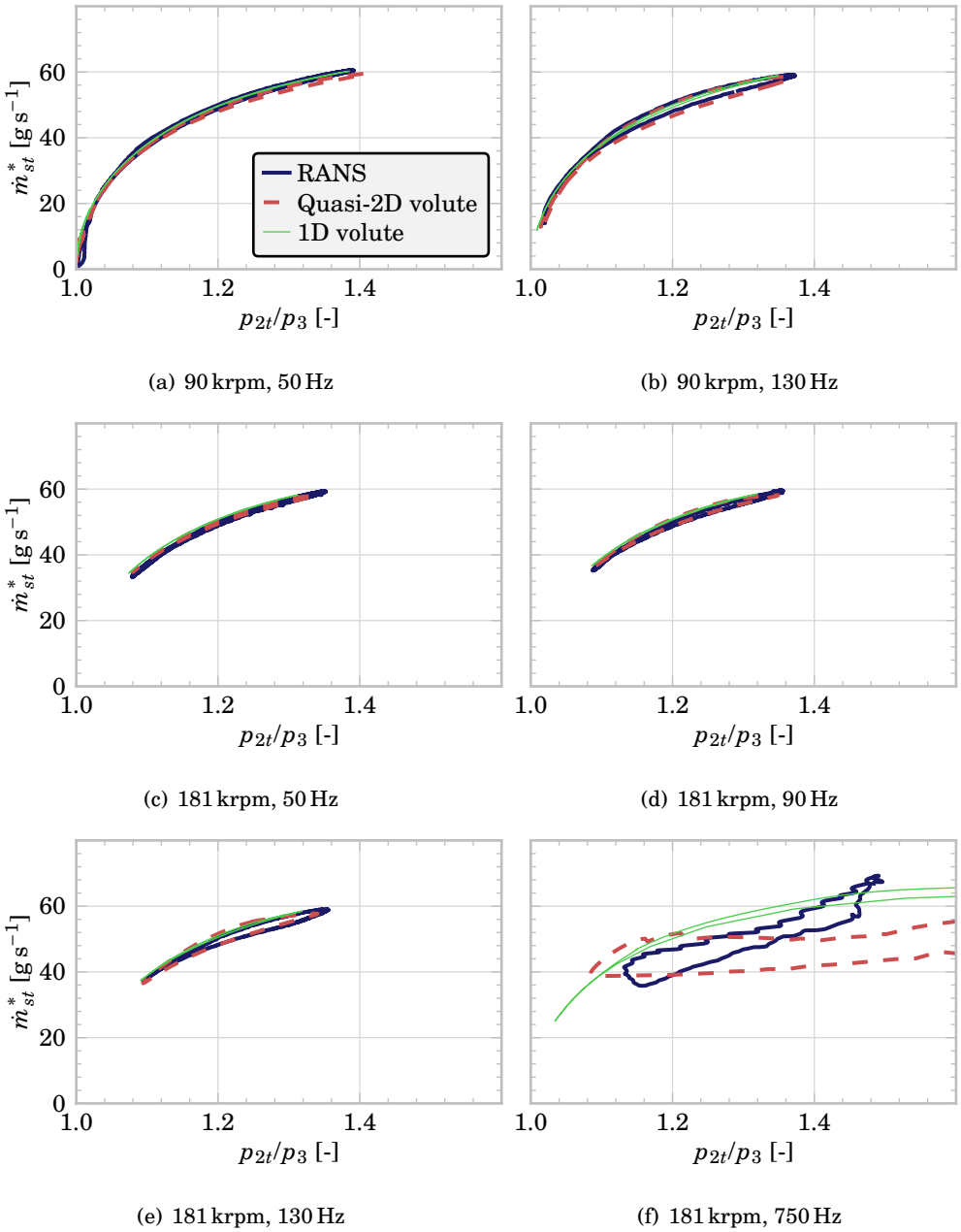

(a) 90 krpm, 50 Hz

(b) 90 krpm, 130 Hz

(c) 181 krpm, 50 Hz

(d) 181 krpm, 90 Hz

(e) 181 krpm, 130 Hz

(f) 181 krpm, 750 Hz

Figure 6.3: Stator corrected mass flow rate $\dot{m}^*_{st}$ vs. the stator total to static expansion ratio p_{2t}/p_3

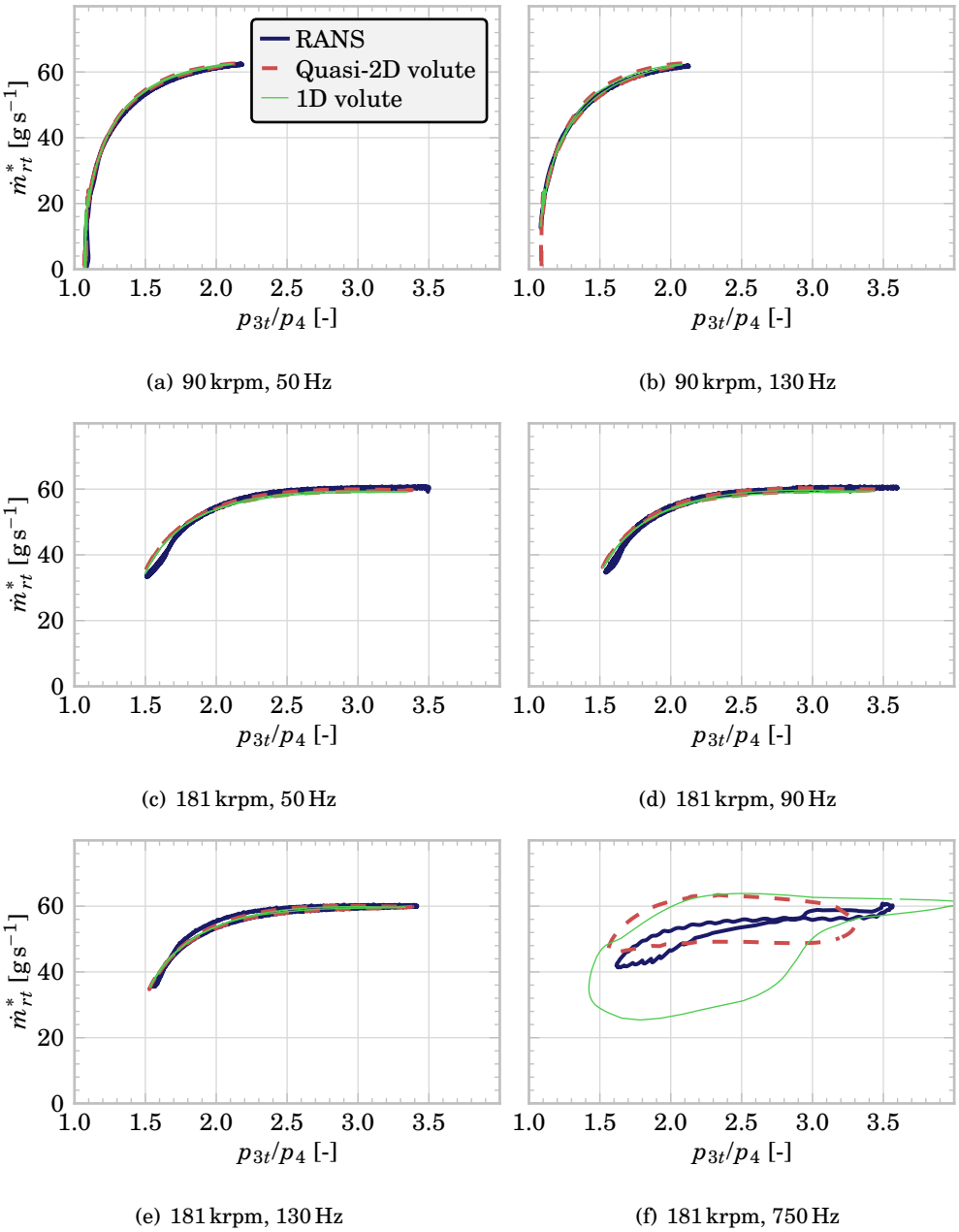

(a) 90 krpm, 50 Hz

(b) 90 krpm, 130 Hz

(c) 181 krpm, 50 Hz

(d) 181 krpm, 90 Hz

(e) 181 krpm, 130 Hz

(f) 181 krpm, 750 Hz

Figure 6.4: Rotor corrected mass flow rate $\dot{m}^*_{rt}$ vs. the rotor total to static expansion ratio p_{3t}/p_4

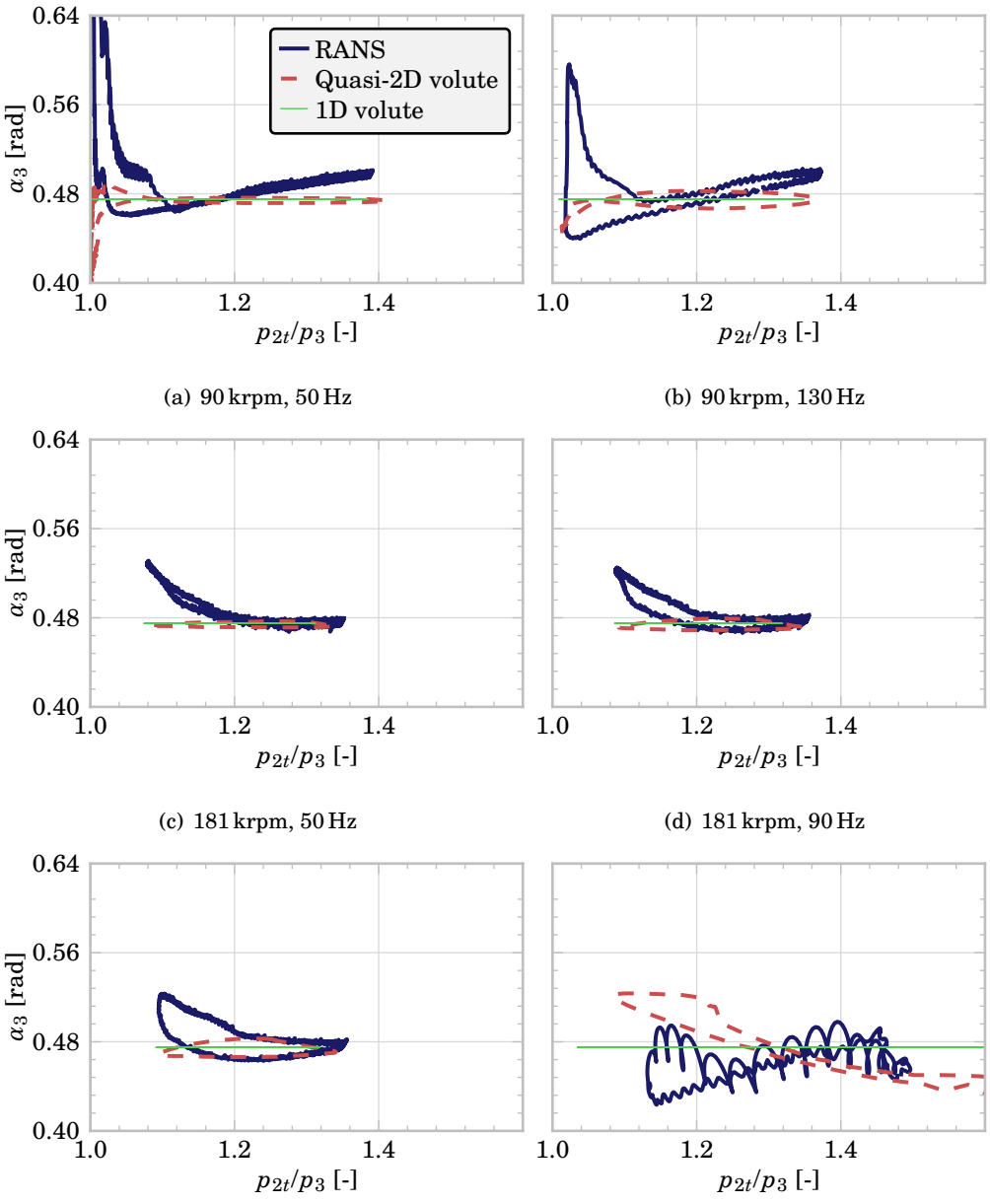

(a) 90 krpm, 50 Hz

(b) 90 krpm, 130 Hz

(c) 181 krpm, 50 Hz

(d) 181 krpm, 90 Hz

(e) 181 krpm, 130 Hz

(f) 181 krpm, 750 Hz

Figure 6.5: Stator outlet flow angle α_3 vs. the stator total to static expansion ratio p_{2t}/p_3

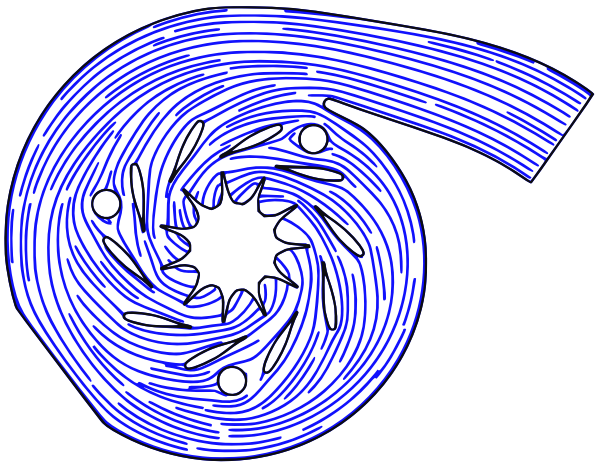

(a) 90 krpm, very high expansion ratio

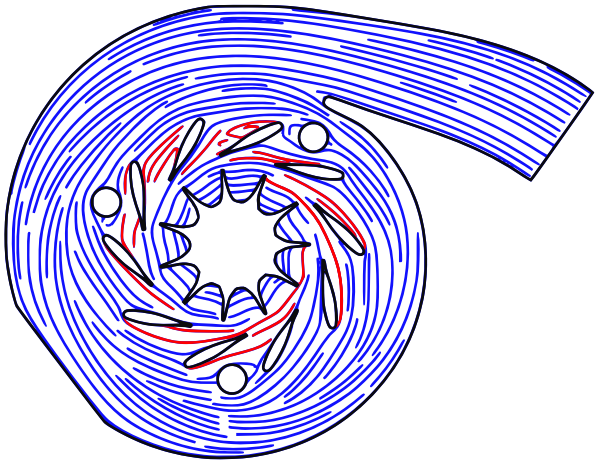

(b) 90 krpm, very low expansion ratio

Figure 6.6: Stator streamlines

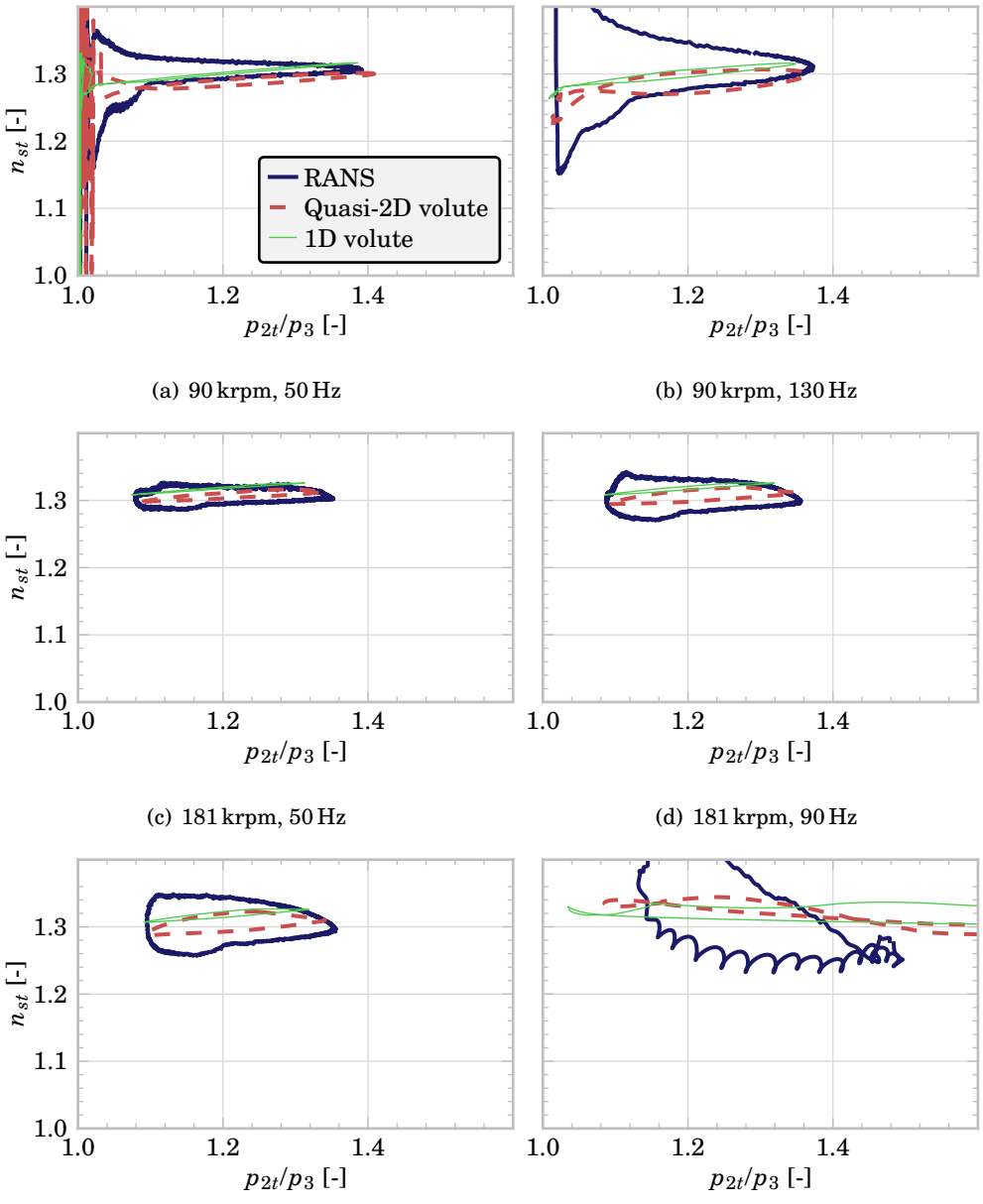

(a) 90 krpm, 50 Hz

(b) 90 krpm, 130 Hz

(c) 181 krpm, 50 Hz

(d) 181 krpm, 90 Hz

(e) 181 krpm, 130 Hz

(f) 181 krpm, 750 Hz

Figure 6.7: Stator polytropic coefficient n_{st} vs. the stator total to static expansion ratio p_{2t}/p_3

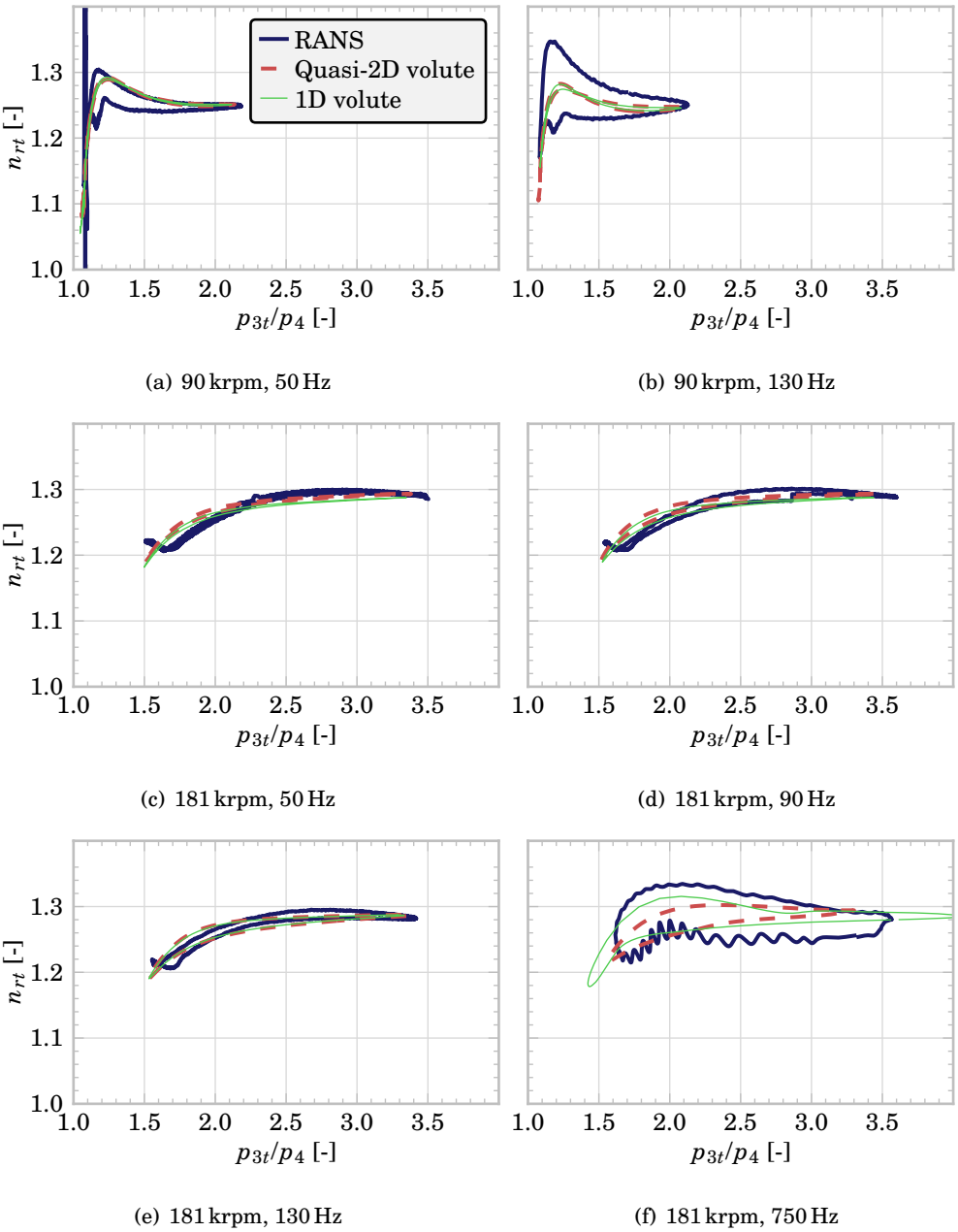

(a) 90 krpm, 50 Hz

(b) 90 krpm, 130 Hz

(c) 181 krpm, 50 Hz

(d) 181 krpm, 90 Hz

(e) 181 krpm, 130 Hz

(f) 181 krpm, 750 Hz

Figure 6.8: Rotor polytropic coefficient n_{rt} vs. the rotor total to static expansion ratio p_{3t}/p_4

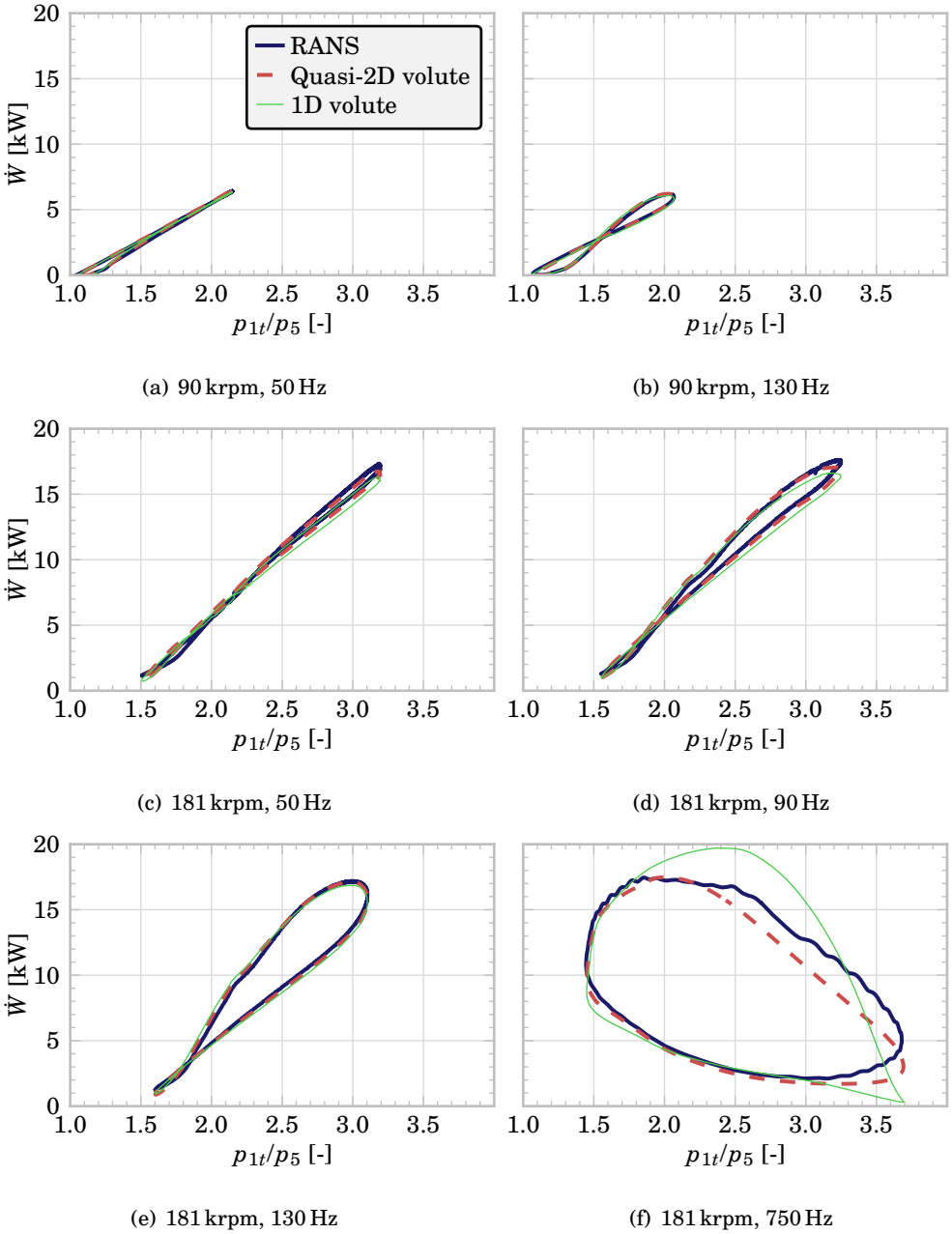

(a) 90 krpm, 50 Hz

(b) 90 krpm, 130 Hz

(c) 181 krpm, 50 Hz

(d) 181 krpm, 90 Hz

(e) 181 krpm, 130 Hz

(f) 181 krpm, 750 Hz

Figure 6.9: Turbine power output $\dot{W}$ vs. the turbine total to static expansion ratio p_{1t}/p_5

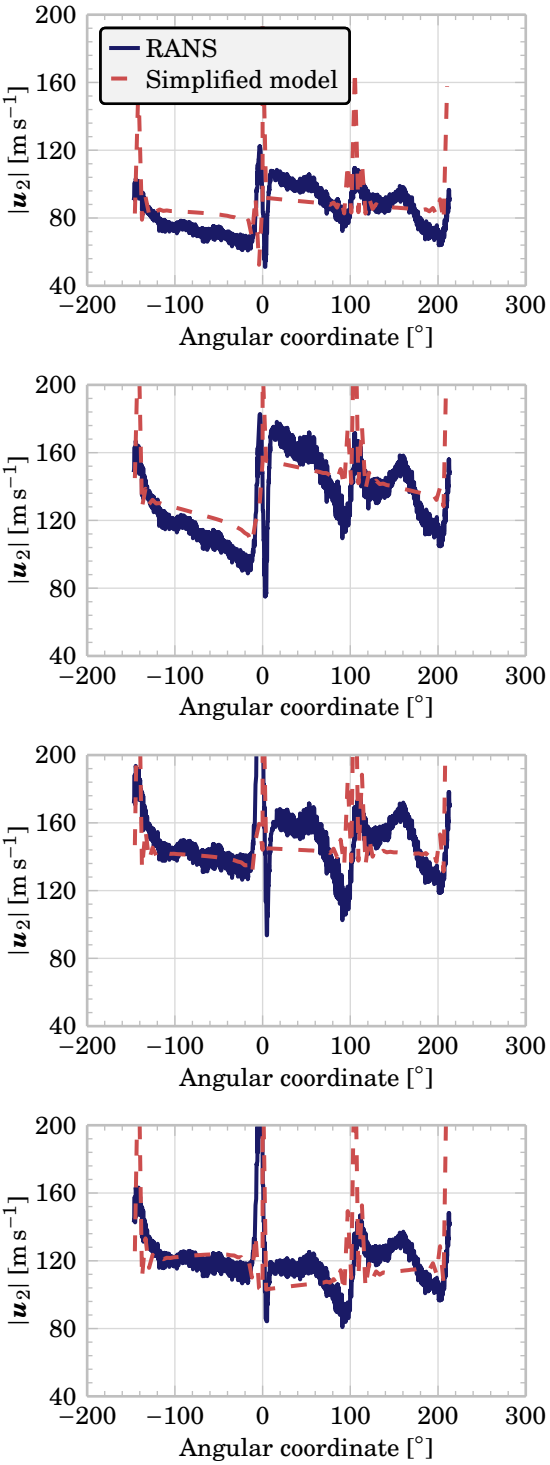

Figure 6.10: Volute outlet speed $\boldsymbol{u}_2$ for 181 krpm and 130 Hz

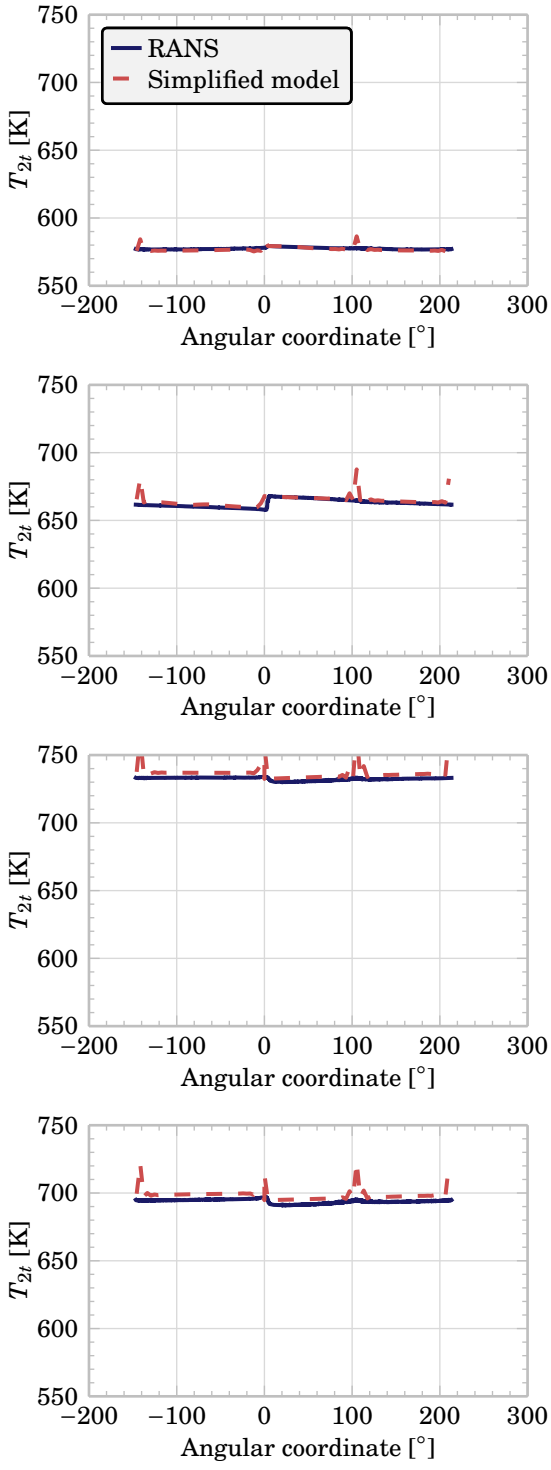

Figure 6.11: Volute total temperature T_{2t} for 181 krpm and 130 Hz

Experimental calibration and validation

The model has been calibrated and validated with experimental data from different turbines. In all the cases, and as will be done with the mechanical losses model, the calibration has been performed with a random limited subset of the experimental data, while the validation has been executed with the full datasets. This section contains the calibration, validation and results discussion for two different radial turbines that were measured using different experimental philosophies: in one case, the turbine behaviour was measured globally, obtaining pressures, temperatures and mass flow rates upstream and downstream of the turbine, and a pressure wave decomposition was performed; in the other case, the internal pressure of the turbine was also measured and the simulated values could thus be tested against these data, but no pressure wave decomposition was performed.

Calibration method

The model fitting is described in detail in this section, including the method used to get all the relevant geometrical data, which is measured from the turbine instead of being adjusted. The geometrical measurements have been done using a non-destructive method.

Turbine geometry The turbine geometry has been obtained by disassembling it and measuring its different parts. Of course, these geometrical data can be obtained from manufacturer's blueprints, but they were not available during the course of this work.

The volute itself has been used as a mould in which silicone has been injected in order to get its geometry. After the silicone had cured, it was extracted and measured. The mould for the internal pressure unit can be seen in Figure 6.12. The silicone mould of the volute can be cut at several volute sections to easily get an accurate description of its surface distribution as a function of the tangential coordinate without needing to cut the volute, so the unit can be used again if necessary with a careful reassembly.

After that, several photographs were taken and a vernier caliper was used to measure the rotor diameters and the rotor outlet angle, as can be seen in Figure 6.13. While the rotor diameters are easily measured using this technique, the rotor outlet angle varies from the root to the tip and it is difficult to measure without resorting to cutting it. The less destructive approach was used, however, so the rotor outlet metal angle was measured with a high degree of uncertainty. Another approach could be to get a tridimensional digitalisation of the rotor, but this is a time consuming technique that provides little benefits for the presented

model and it was seen as unnecessary and more interesting for tridimensional CFD analysis.

Finally, more photographs (Figure 6.14) were taken to measure the position of the stator vanes, their lengths and angles for different VGT displacements. The angle of each vane was individually measured and their mean value was used for each VGT displacement: a dispersion of about 1° was found between the different blades at each position, so the value for only one blade is not representative enough of the global position. The position of the vanes is measured with respect to the tangential circumference that passes through the rotation axis. There exists some uncertainty in the real position of the VGT vanes during the experiment as the positioning system presents some clearance. This clearance is reduced due to thermal expansion when the turbine is working at high temperatures and is presumed to exist to get into account this effect, but as the experiments were done under quasi-adiabatic conditions and the photographs of the VGT were taken at room temperature, this thermal expansion effect can't be exploited. At a fixed mechanism position, the vanes could be individually moved by hand a couple of degrees, so it is expected that aerodynamic forces are capable of moving the vanes during the experiments even when fixing the mechanism. This may explain some of the differences that will be seen later between the model and the measurements, but as they can be hardly taken into account, they will count as a weakness of this kind of modelling philosophy.

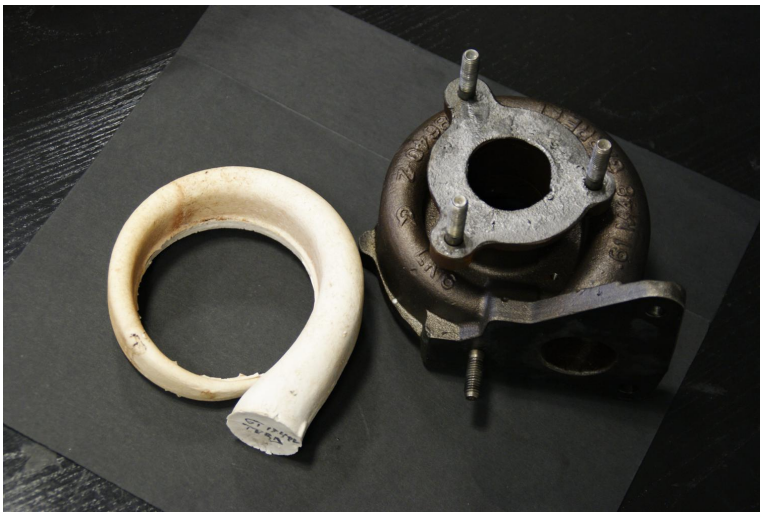

Figure 6.12: A silicone mould of the volute

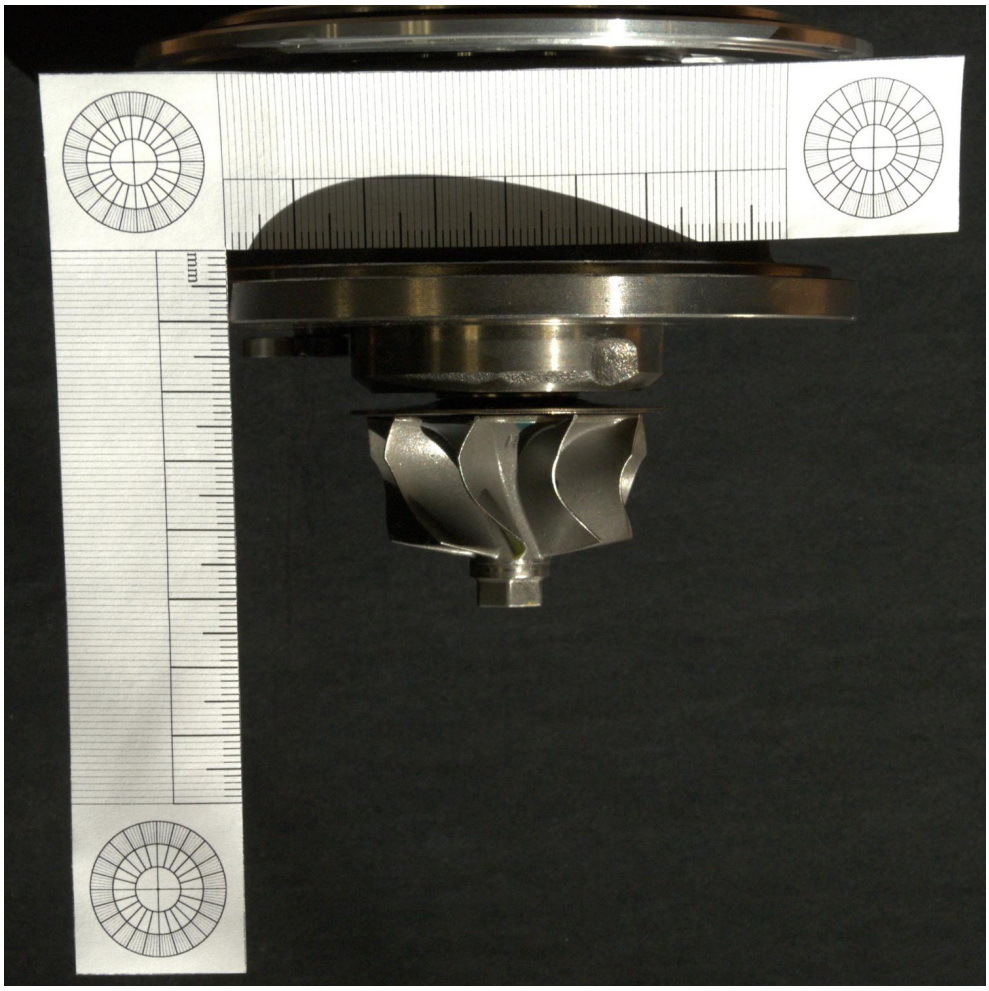

Figure 6.13: The turbine rotor wheel

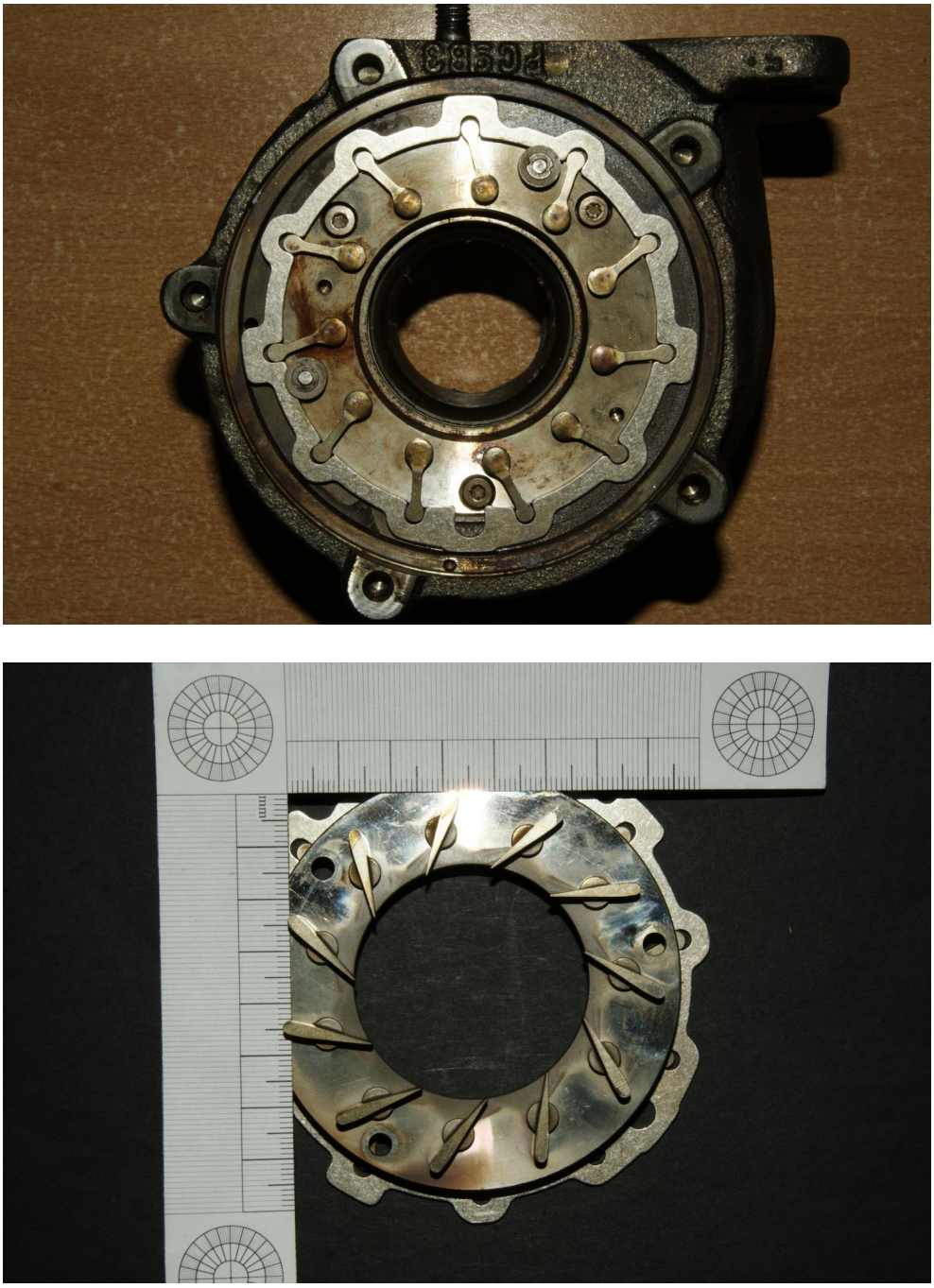

Figure 6.14: The turbine stator

Pressure decomposition campaign During this experimental campaign, no internal pressure was measured. The model fitting has to be done globally, using variables such as the global expansion ratio of the turbine, its mass flow rate or the rotor speed.

Stator and rotor parameters The calibration process has been done using a random subset of the experimental data, covering all the VGT positions. It has been done as follows:

- First, an initial set of parameters is chosen.
- An optimisation procedure is used to minimise the root mean square error ($RMSE$) of the mass flow rate and the turbine power output, using the parameters of the model as the variables of the nonlinear programming algorithm.
  - One by one, an experimental steady-state data point is selected, until all points are exhausted. For that point:
    - The VGT position and the rotational speed are set.
    - The inlet total pressure and temperature and an initial almost null speed are imposed in the volute.
    - An initial stator outlet pressure is set.
    - The following loop is repeated until convergence using Brent's method using the stator outlet pressure as the objective function variable:
      - The stator outlet speed and flow angle are computed.
      - The rotor inlet relative pressure and temperature are computed.
      - The rotor mass flow rate is obtained using the variables computed during this loop.
      - The difference between the mass flow rate of the stator and the mass flow rate of the rotor is returned.
    - The error between the simulated and the measured mass flow rate is recorded, as well as the error between the simulated turbine power output and the actually measured power output.
  - The $RMSE$ of both the mass flow rate and the turbine power output are computed and summed.

The mass flow rate $RMSE$ can be obtained as:

$$RMSE_{\dot{m}_{turb}} = \sqrt{\frac{\sum_i^{N_{exp}} \left(\dot{m}_{model,i} - \dot{m}_{exp,i}\right)^2}{N_{exp}}} \tag{6.2}$$

where N_{exp} is the number of experimental points, $\dot{m}_{model,i}$ is the mass flow rate obtained with the model for the experimental point number i and $\dot{m}_{exp,i}$ is the experimental mass flow rate measured in the experimental point number i.

The turbine power output $RMSE$ is:

$$RMSE_{\dot{W}_{turb}} = \sqrt{\frac{\sum_i^{N_{exp}} \left(\dot{W}_{turb,model,i} - \dot{W}_{turb,exp,i}\right)^2}{N_{exp}}} \tag{6.3}$$

where $\dot{W}_{turb,model,i}$ is the turbine power output obtained with the model for the experimental point number i and $\dot{W}_{turb,exp,i}$ is the experimental turbine power output for the same point.

The objective function f computes the sum of both the mass flow rate and the turbine power output $RMSE$:

$$f\left(C_{D_{st}}, k_{st,loss}, \beta_{3,opt}, k_{rt,loss,psg}, \beta_4, C_{D_{rt}}\right) = RMSE_{\dot{m}_{turb}} + RMSE_{\dot{W}_{turb}} \tag{6.4}$$

The optimisation algorithm is formally described as:

$$\begin{aligned}
&\underset{C_{D_{st}}, k_{st,loss}, \beta_{3,opt}, k_{rt,loss,psg}, \beta_4, C_{D_{rt}}}{\text{minimise}} && f\left(C_{D_{st}}, k_{st,loss}, \beta_{3,opt}, k_{rt,loss,psg}, \beta_4, C_{D_{rt}}\right) \\
&\text{subject to} && C_{D_{st}}\big|_{min} \leq C_{D_{st}} \leq C_{D_{st}}\big|_{max} \\
& && k_{st,loss}\big|_{min} \leq k_{st,loss} \leq k_{st,loss}\big|_{max} \\
& && \beta_{3,opt}\big|_{min} \leq \beta_{3,opt} \leq \beta_{3,opt}\big|_{max} \\
& && k_{rt,loss,psg}\big|_{min} \leq k_{rt,loss,psg} \leq k_{rt,loss,psg}\big|_{max} \\
& && \beta_4\big|_{min} \leq \beta_4 \leq \beta_4\big|_{max} \\
& && C_{D_{rt}}\big|_{min} \leq C_{D_{rt}} \leq C_{D_{rt}}\big|_{max}
\end{aligned} \tag{6.5}$$

The optimisation process has been carried out using a sequential quadratic programming (SQP) algorithm for its robustness and fast operation against other methods such as genetic algorithms. The initial set of parameters is chosen as follows: $C_{D_{st}} = 0.97$, $k_{st,loss} = 0.5$, $\beta_{3,opt} = \pi/2$, $k_{rt,loss,psg} = 0.5$, $\beta_4 = \beta_{4,metal}$ and $C_{D_{rt}} = 0.99$.

Internal pressure campaign The data from the internal pressure campaign have been used to calibrate the quasi-bidimensional turbine model. The method to get the geometrical parameters is shared with that of the pressure decomposition campaign, while the model coefficients are adjusted in a slightly different way due to the availability of stator outlet pressure measurements.

Stator parameters In order to obtain the stator passage losses parameter and discharge coefficient, turbine mass flow rate, inlet total conditions and stator static pressure during steady tests have been used. The method is as follows:

- A pair of stator passage losses parameter and discharge coefficient is selected.
- For each experimental point, the total conditions are imposed at the turbine inlet.
- For each experimental point, the stator geometry and static pressure are imposed.
- For each experimental point, the volute and stator set is simulated until convergence.
- The root mean square error ($RMSE$) of the mass flow rate is obtained, see Equation 6.2 and Equation 6.3.
- The pair of stator passage losses parameter and discharge coefficient is changed and another iteration begins using an optimisation algorithm in order to minimise the aforementioned mass flow rate $RMSE$.

In this case, the non-linear programming problem is reduced to:

$$f\left(C_{D_{st}}, k_{st,loss}\right) = RMSE_{\dot{m}_{turb}} \tag{6.6}$$

$$\begin{aligned} \underset{C_{D_{st}}, k_{st,loss}}{\text{minimise}} \quad & f\left(C_{D_{st}}, k_{st,loss}\right) \\ \text{subject to} \quad & C_{D_{st}}\big|_{min} \leq C_{D_{st}} \leq C_{D_{st}}\big|_{max} \\ & k_{st,loss}\big|_{min} \leq k_{st,loss} \leq k_{st,loss}\big|_{max} \end{aligned} \tag{6.7}$$

which is a problem much simpler to optimise, having only two variables.

Rotor parameters The rotor passage losses coefficient and outlet flow angle deviation were obtained similarly to the stator parameters. Rotor outlet static pressure was also used. The method is as follows:

- A pair of rotor passage losses parameter and outlet flow angle is selected.
- For each experimental point, the stator static pressure, static temperature, flow speed and angle are imposed. The flow speed and angle were obtained during the stator calibration.
- For each experimental point, the rotor outlet pressure is imposed.

- The rotor mass flow rate is computed.
- The root mean square error ($RMSE$) of the mass flow rate and the turbine power output is obtained, see Equation 6.2
- The pair of rotor passage losses coefficient and outlet flow angle is changed and another iteration begins using an optimisation algorithm in order to minimise the aforementioned mass flow rate $RMSE$.

The non-linear programming problem is again simpler than in the global case:

$$f\left(\beta_{3,opt}, k_{rt,loss}\beta_4, C_{D_{rt}}\right) = RMSE_{\dot{m}_{turb}} + RMSE_{\dot{W}_{turb}} \tag{6.8}$$

$$\begin{aligned} \underset{\beta_{3,opt},k_{rt,loss,psg},\beta_4,C_{D_{rt}}}{\text{minimise}} \quad & f\left(\beta_{3,opt}, k_{rt,loss,psg}, \beta_4, C_{D_{rt}}\right) \\ \text{subject to} \quad & \beta_{3,opt}\big|_{min} \leq \beta_{3,opt} \leq \beta_{3,opt}\big|_{max} \\ & k_{rt,loss,psg}\big|_{min} \leq k_{rt,loss,psg} \leq k_{rt,loss,psg}\big|_{max} \\ & \beta_4\big|_{min} \leq \beta_4 \leq \beta_4\big|_{max} \\ & C_{D_{rt}}\big|_{min} \leq C_{D_{rt}} \leq C_{D_{rt}}\big|_{max} \end{aligned} \tag{6.9}$$

Model validation with experimental data

Pressure decomposition campaign The results for the turbine map can be seen in Figure 6.15. The model has been fitted using the procedure described in section 6.2 using a random subset of one third of the measured points. The turbine corrected mass flow rate $\dot{m}^*_{turb}$ and power output $\dot{W}_{turb}$ are plotted against the turbine total to static expansion ratio $\pi_{0t,6}$. The turbine corrected mass flow rate is defined as:

$$\dot{m}^*_{turb} = \dot{m}_{turb} \cdot \frac{p_{ref}}{p_{0t}} \cdot \sqrt{\frac{T_{0t}}{T_{ref}}} \tag{6.10}$$

where a reference pressure p_{ref} and temperature T_{ref} are 101325 Pa and 288.15 K, respectively.

The model performs better for higher VGT positions. The passage losses parameters were kept constant for all the points at each rack position, and better results should be achievable if correlations are used instead, being the parameters a function of some flow characteristic such as its Reynolds number.

After fitting the parameters with steady-state data, the instantaneous results were obtained. In this case, the instantaneous simulations were carried out imposing the corresponding pressure wave at each end of the gas stand ducts: the incident pressure $p_{0,right}$ at the turbine inlet duct and the second reflection $p_{6,left}$ at the turbine outlet duct. The entropy level was set to a constant during the simulations, and equal to the average value obtained during each test at each position. Of course, the last assumption is more valid at the turbine inlet than at the turbine outlet. Figure 6.16 shows the reflected pressure wave results and Figure 6.17 shows the transmitted pressure wave, both in time domain. Figure 6.18 and Figure 6.19 show the same results but in frequency domain, referenced to a pressure level of 20 µPa. They have been obtained estimating the power spectral density using Welch's average periodogram method [119], windowing the data with a Hanning window [120]. The simulations are carried out using the Minmod limiter, a second order time-integrator and the KT central scheme.

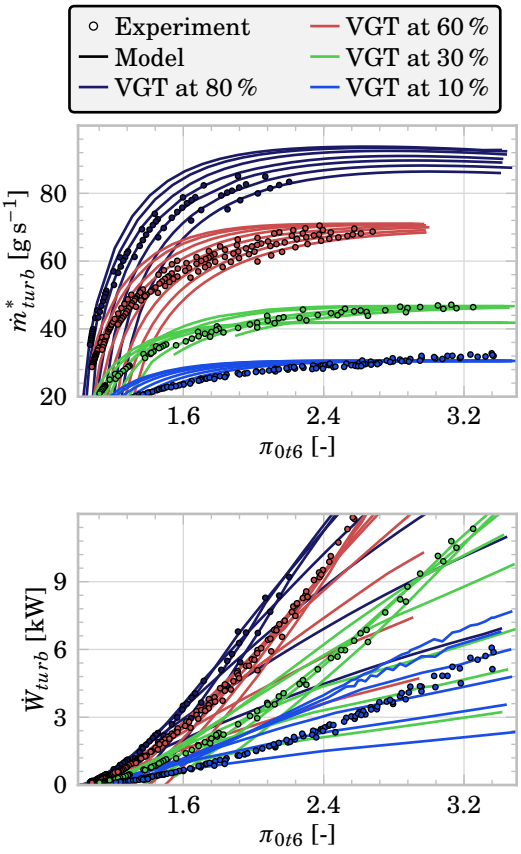

Figure 6.15: Fourth turbocharger, turbine map - measured vs. model

The quasi-bidimensional volute model is compared with a fully one-dimensional equivalent duct model of the volute. The one-dimensional model can be found in [32] and in [18]. Figure 6.16 and Figure 6.17 show differences that are only visible after careful examination. In the frequency domain, however, the differences are more clear and are found at the highest frequencies. Figure 6.18 shows the results for the reflected wave in the frequency domain. Although both models present differences with the experimental data, the quasi-bidimensional volute shows the highest level of correlation at high frequencies. The volute produces an averaging effect in the pressure pulse at high frequencies, as described in [3], that reduces the amplitude of the signal at high frequencies and can't be reproduced using a one-dimensional duct. The results for the

transmitted wave are worse-predicted, but the quasi-bidimensional code still produces a more realistic spectrum. The flow at the turbine outlet has an important 3-dimensional nature and, although the volume of this plenum is imposed in the model, it is computed as a small one-dimensional duct, what explains the worsening of the results compared to the reflected wave.

Figure 6.20 and Figure 6.21 show the mass flow rate upstream and downstream of the turbine. The amplitude of the pulsation at the turbine inlet is only slightly better reproduced with the quasi-bidimensional volute model, as its main differences with the classical one-dimensional volute are at high frequencies. The higher error in the high frequency components of the classical volute code is more visible in these graphics.

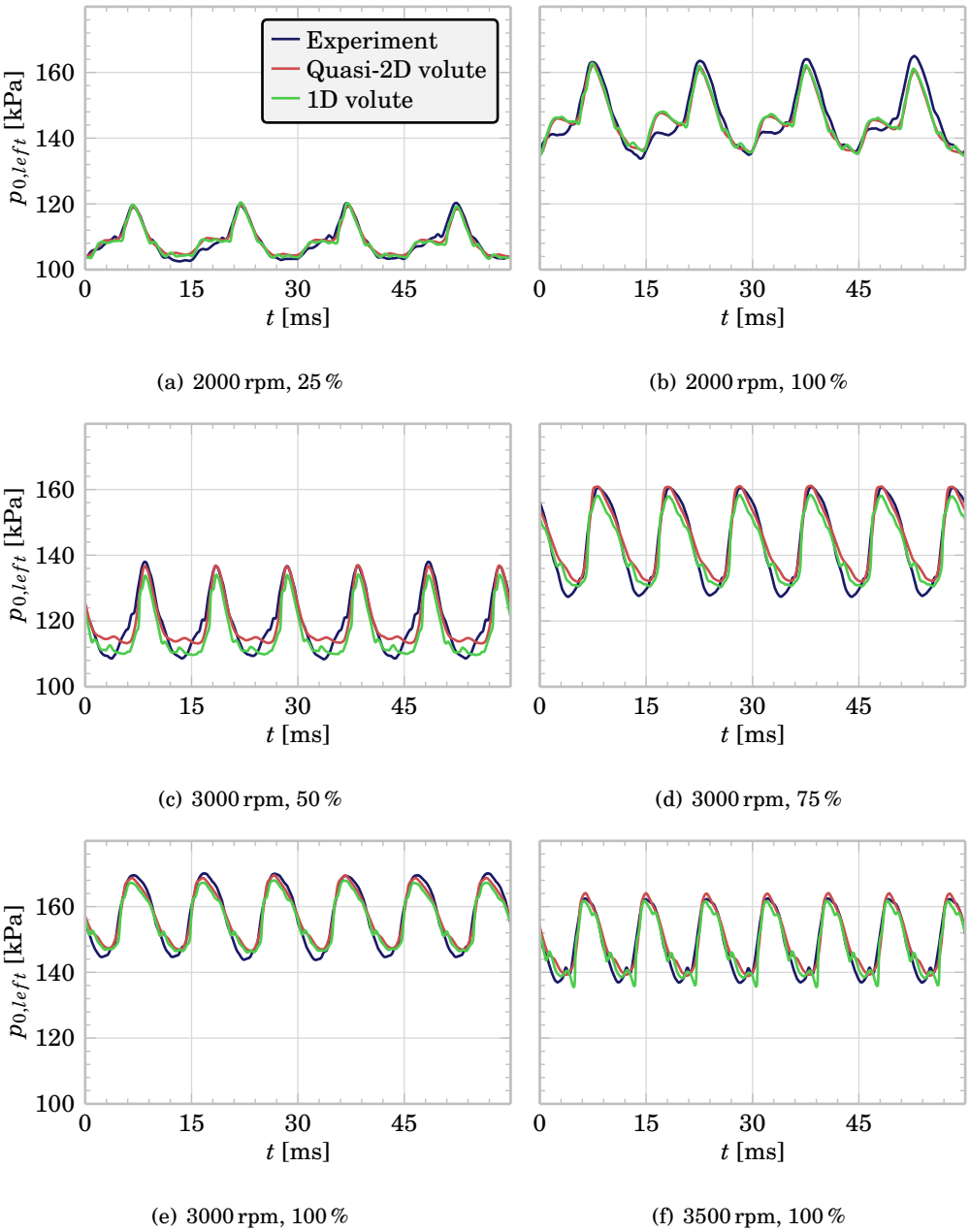

(a) 2000 rpm, 25 %

(b) 2000 rpm, 100 %

(c) 3000 rpm, 50 %

(d) 3000 rpm, 75 %

(e) 3000 rpm, 100 %

(f) 3500 rpm, 100 %

Figure 6.16: First turbocharger instantaneous results, reflected wave

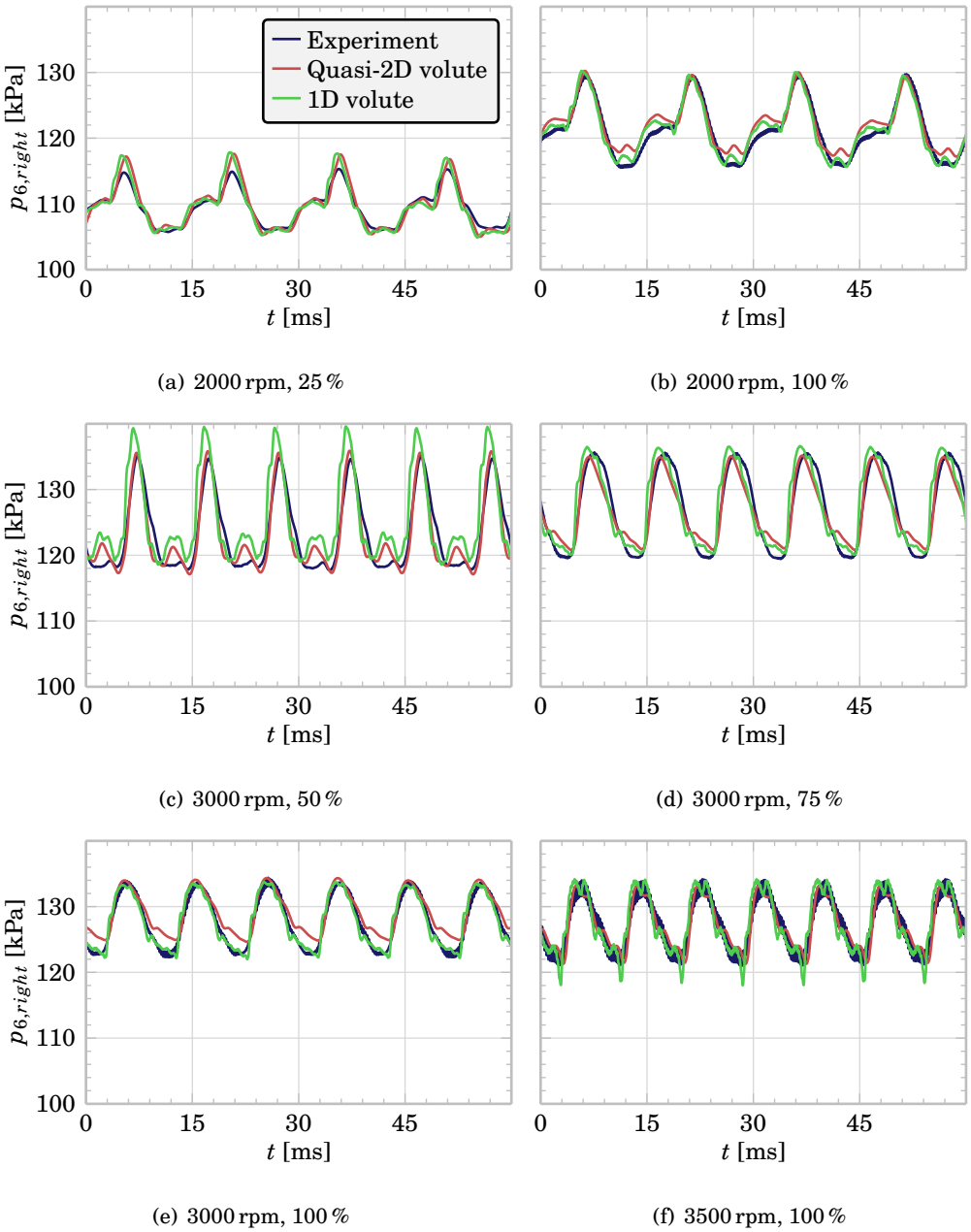

(a) 2000 rpm, 25 %

(b) 2000 rpm, 100 %

(c) 3000 rpm, 50 %

(d) 3000 rpm, 75 %

(e) 3000 rpm, 100 %

(f) 3500 rpm, 100 %

Figure 6.17: First turbocharger instantaneous results, transmitted wave

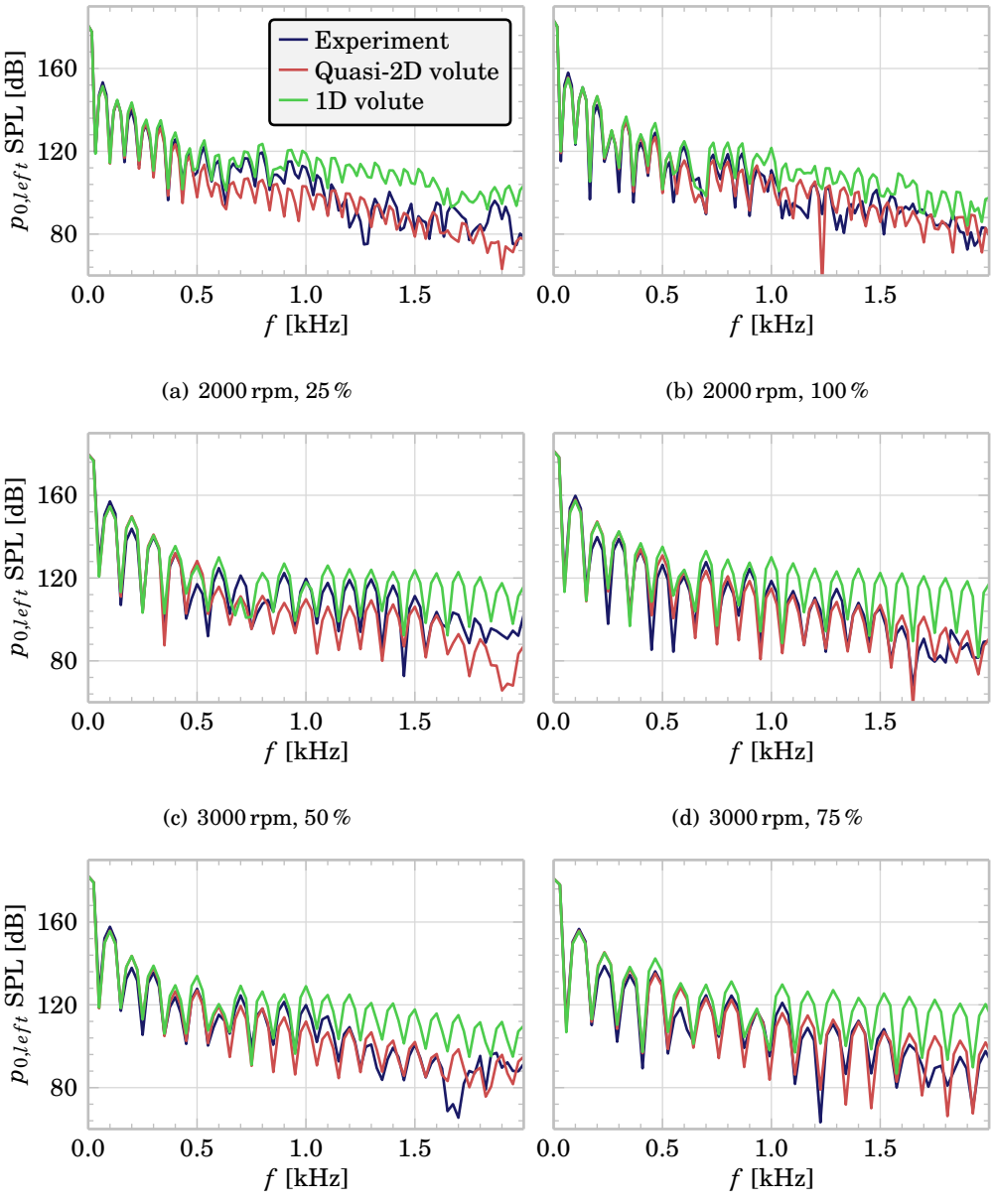

(a) 2000 rpm, 25 %

(b) 2000 rpm, 100 %

(c) 3000 rpm, 50 %

(d) 3000 rpm, 75 %

(e) 3000 rpm, 100 %

(f) 3500 rpm, 100 %

Figure 6.18: First turbocharger instantaneous results, sound pressure level of the simulated reflected wave

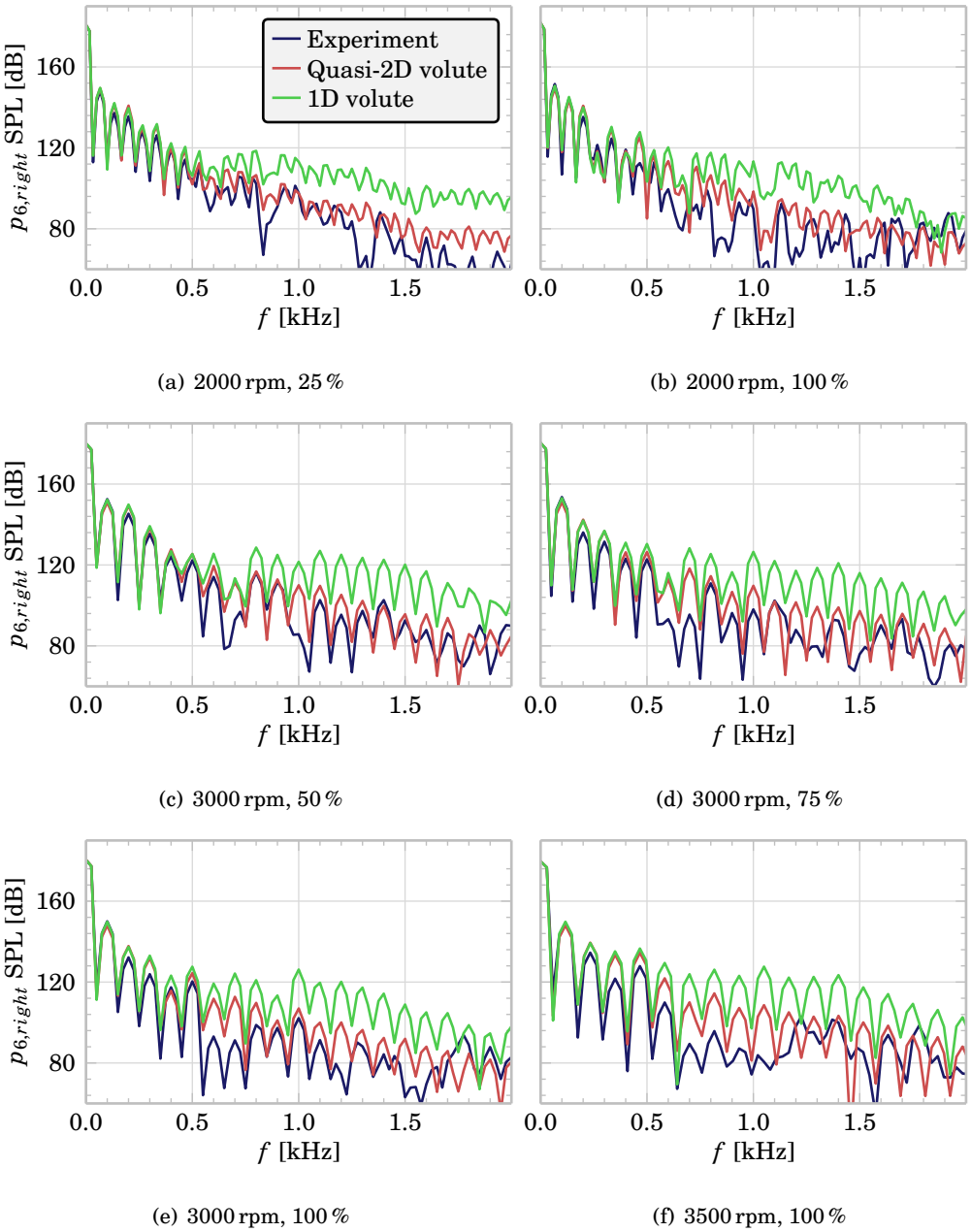

(a) 2000 rpm, 25 %

(b) 2000 rpm, 100 %

(c) 3000 rpm, 50 %

(d) 3000 rpm, 75 %

(e) 3000 rpm, 100 %

(f) 3500 rpm, 100 %

Figure 6.19: First turbocharger instantaneous results, sound pressure level of the simulated transmitted wave

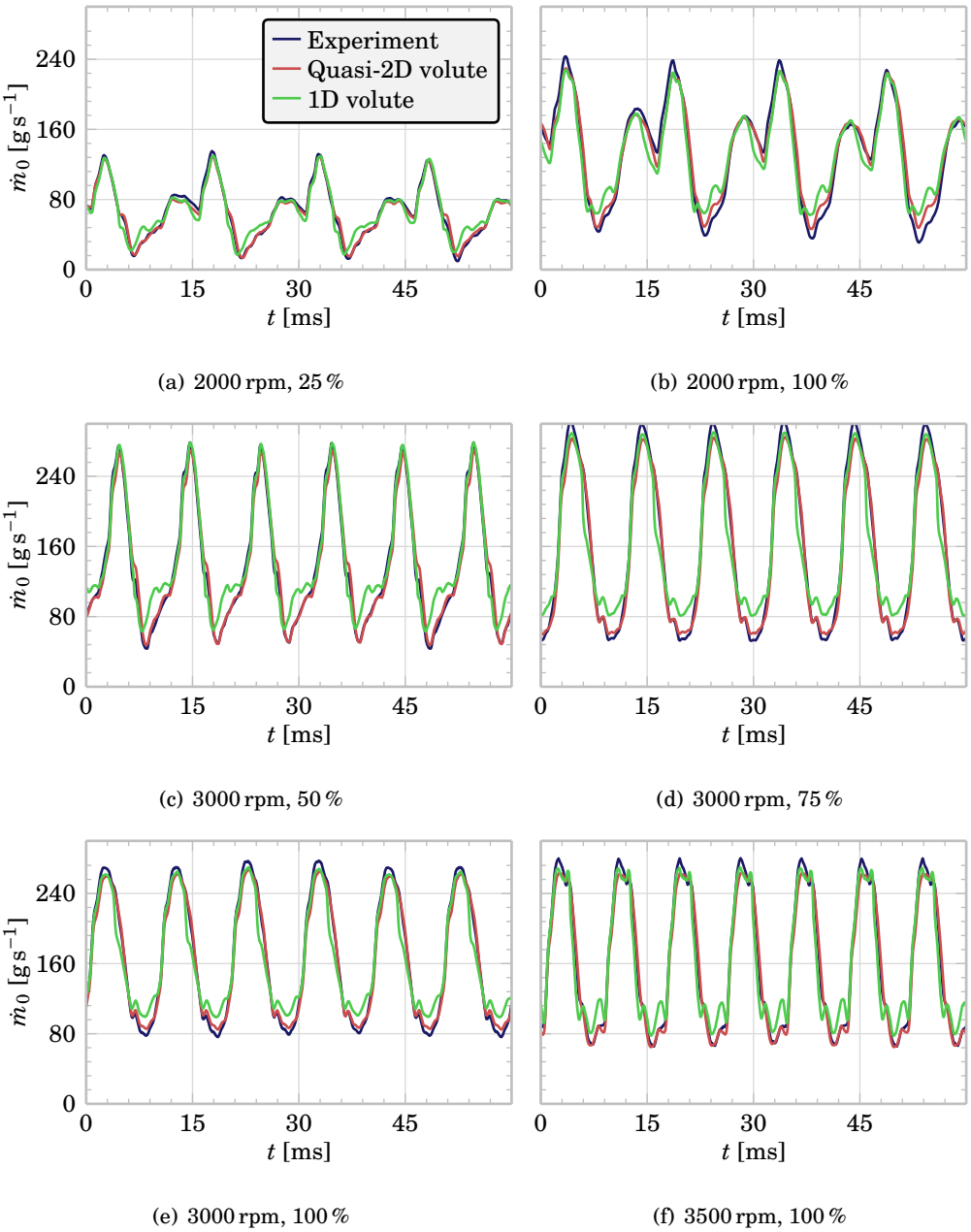

(a) 2000 rpm, 25 %

(b) 2000 rpm, 100 %

(c) 3000 rpm, 50 %

(d) 3000 rpm, 75 %

(e) 3000 rpm, 100 %

(f) 3500 rpm, 100 %

Figure 6.20: First turbocharger instantaneous results, inlet mass flow rate

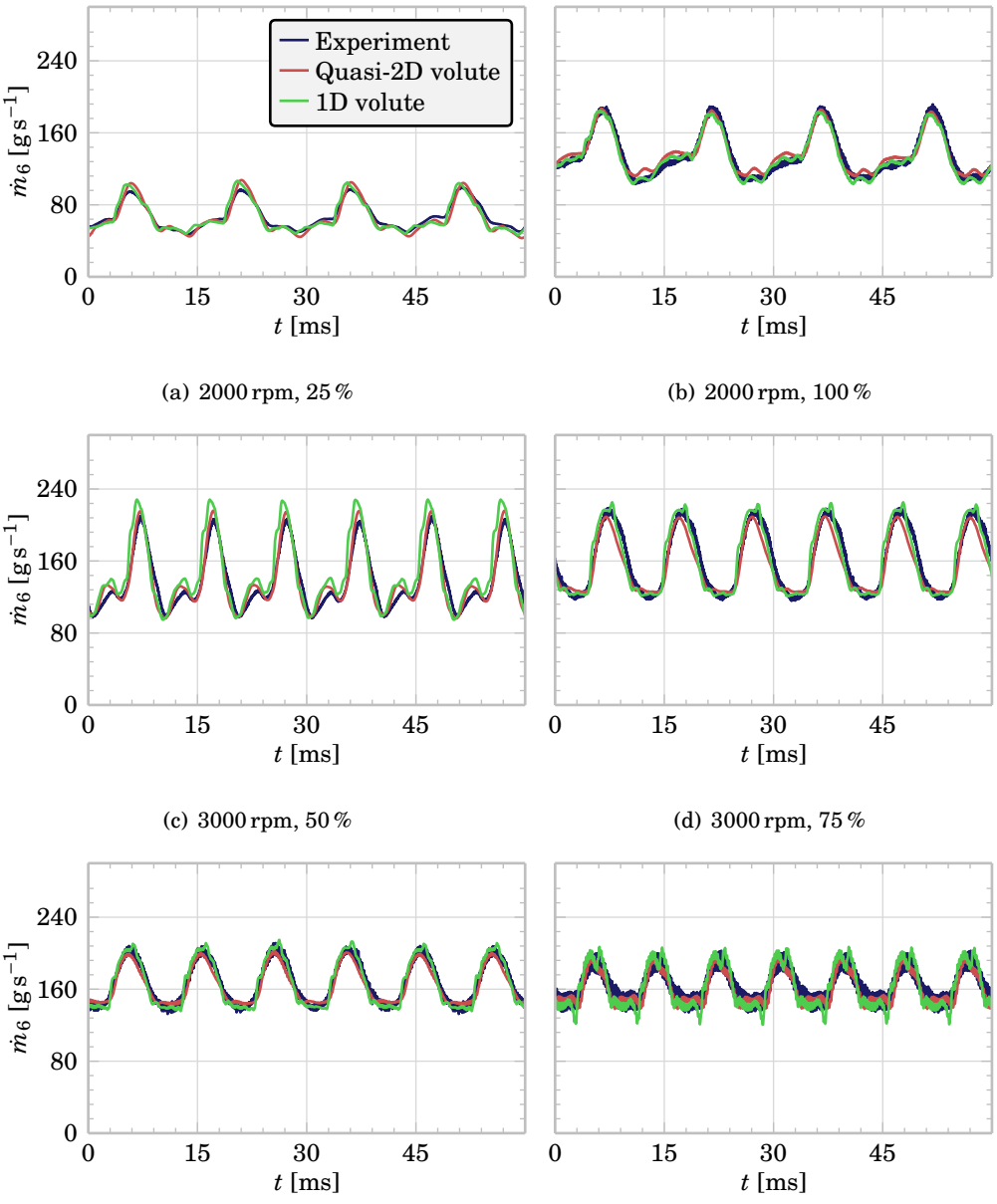

(a) 2000 rpm, 25 %

(b) 2000 rpm, 100 %

(c) 3000 rpm, 50 %

(d) 3000 rpm, 75 %

(e) 3000 rpm, 100 %

(f) 3500 rpm, 100 %

Figure 6.21: First turbocharger instantaneous results, outlet mass flow rate

Internal pressure campaign The results for the turbine map can be seen in Figure 6.22. The model has been fitted using the procedure described in section 6.2 using a random subset of one third of the measured points. The turbine corrected mass flow rate $\dot{m}^*$ and power output $\dot{W}$ are plotted against the turbine total to static expansion ratio $\pi_{0t,6}$. The turbine corrected mass flow rate is defined as:

$$\dot{m}^* = \dot{m} \cdot \frac{p_{ref}}{p_{0t}} \cdot \sqrt{\frac{T_{0t}}{T_{ref}}} \tag{6.11}$$

where a reference pressure p_{ref} and temperature T_{ref} are 101 325 Pa and 288.15 K, respectively.

The level of correlation between the model results and the experimental data decreases with the most closed positions, as some effects are not being properly modelled: the stator discharge coefficient is kept constant, while it should vary with different mass flow rates, and its outlet angle prediction losses accuracy as more entropy is generated. The model also appears to overestimate the mass flow rate at very low expansion ratios, probably due to the constant discharge coefficient. The stator pressure is accurately predicted, as it has been used during the calibration. The model naturally predicts choked flow, although there is not experimental data available to asses the validity of these results. The maximum computed expansion ratio is 3, as no measured speed line appears to choke at higher expansion ratio. The model also predicts negative power results at very low expansion ratios, in points where the mass flow rate is still bigger than zero (i.e., the flow is not

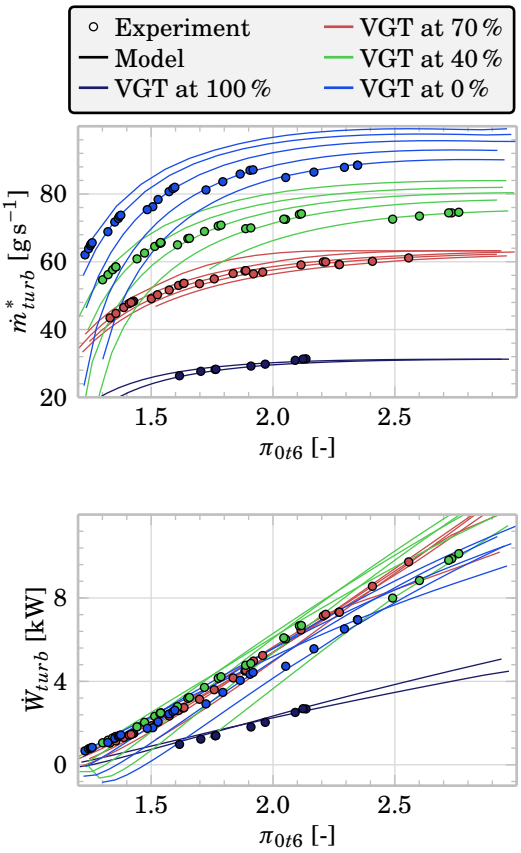

Figure 6.22: Fourth turbocharger, turbine map - measured vs. model

totally reversed) but the losses inside the rotor are so big that the air steals energy from it, instead of giving power. At these very low expansion ratios, however, some flow reversal is expected and the results should be taken as main tendencies, unless they are proven right with further experimental research. The model doesn't compute flow reversal, as the stator and rotor submodels only compute straight flow.

The instantaneous simulations were carried out imposing total pressure and temperature boundary conditions in the inlet pipe and static pressure in the outlet pipe. As the instantaneous temperature variation is not known, the total temperature is supposed to remain constant at the inlet boundary condition. The Minmod limiter was used, as well as the Heun's second order time integrator and the KT central scheme.

The sound pressure level is approximated using power spectral density obtained by using Welch's average periodogram method [119] using a Hann window [120] with a 50 % overlap for a 1 s signal. The results are plotted for frequencies up to 1000 Hz, as the signal-to-noise ratio during the experiments was slightly less than 80 dB. At these frequencies, there are only small differences between the totally one-dimensional volute and the quasi-bidimensional volute. The results are not plotted for the smaller VGT aperture as they were not satisfactory.

The volute SPL results are shown in Figure 6.23 and Figure 6.24, whereas the stator results are plotted in Figure 6.25. Both models give similar results, but the validation is somewhat masked due to the high experimental noise. The differences between both models are better shown in the time domain, in Figure 6.26, Figure 6.27 and Figure 6.28: the quasi-bidimensional model produces better phase accuracy even when the amplitude is similar for both models, probably due to its "averaging" effect as the flow exits through its lateral window.

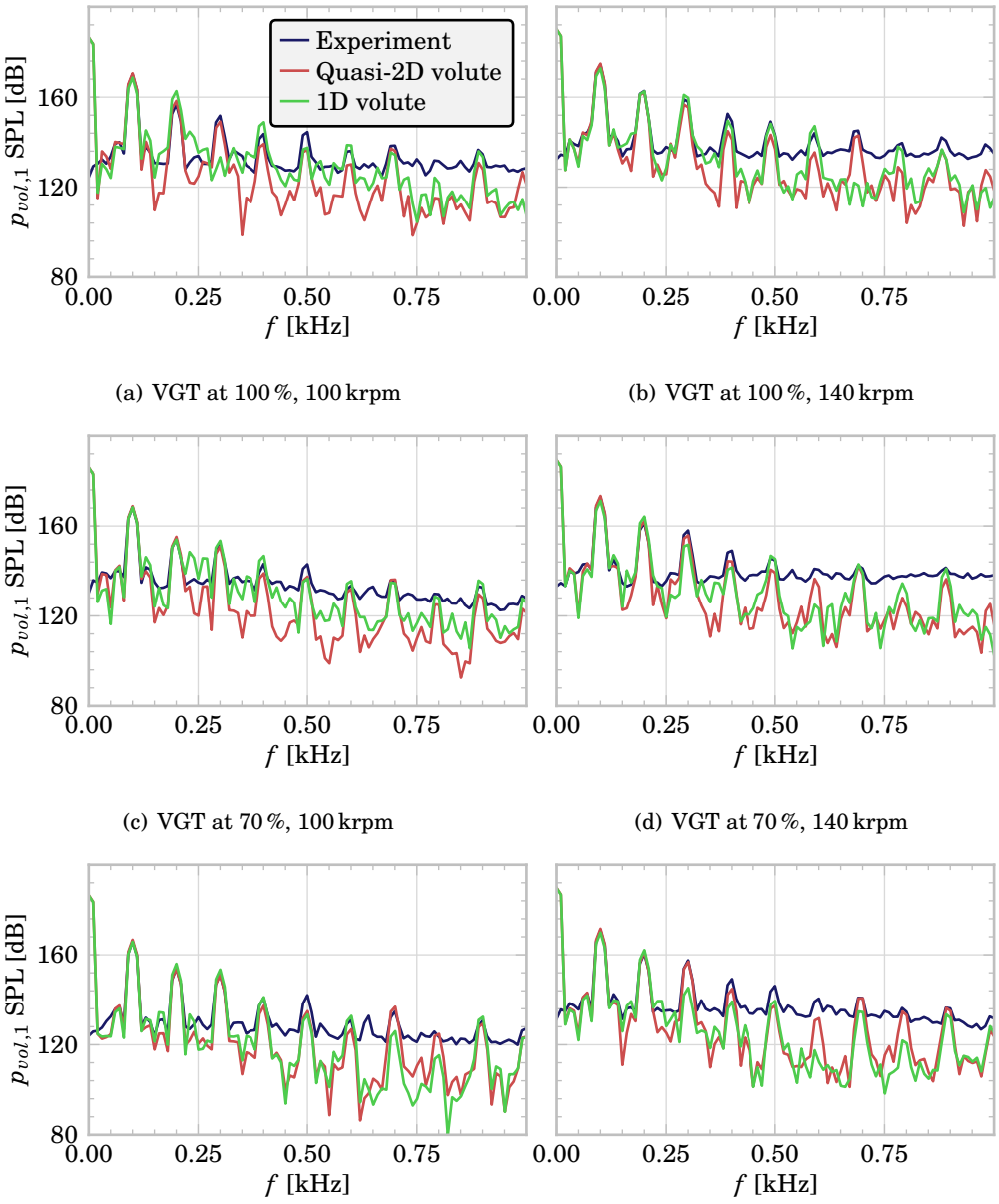

(a) VGT at 100 %, 100 krpm

(b) VGT at 100 %, 140 krpm

(c) VGT at 70 %, 100 krpm

(d) VGT at 70 %, 140 krpm

(e) VGT at 40 %, 100 krpm

(f) VGT at 40 %, 140 krpm

Figure 6.23: Fourth turbocharger instantaneous results, volute inlet pressure sound pressure level

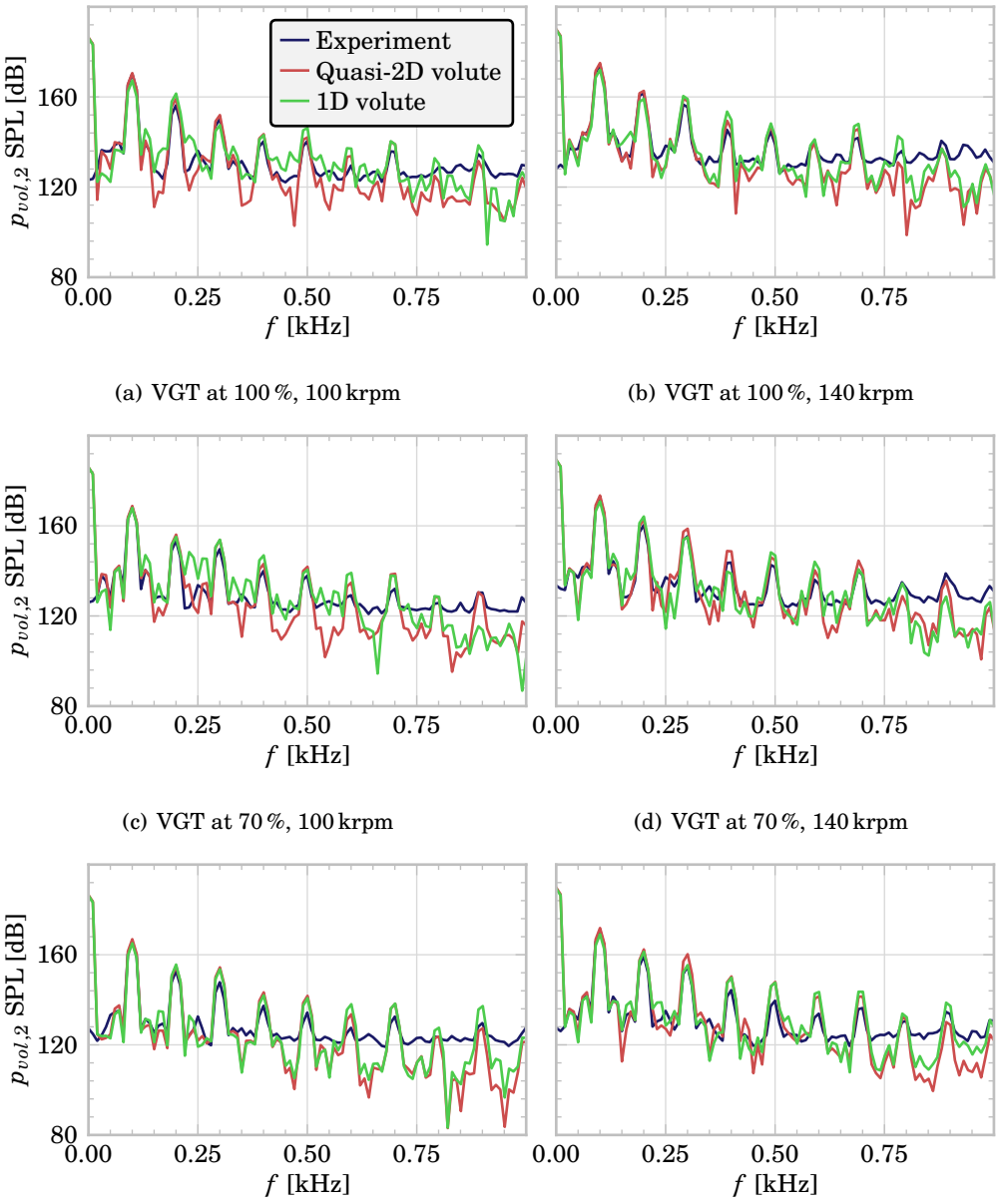

(a) VGT at 100 %, 100 krpm

(b) VGT at 100 %, 140 krpm

(c) VGT at 70 %, 100 krpm

(d) VGT at 70 %, 140 krpm

(e) VGT at 40 %, 100 krpm

(f) VGT at 40 %, 140 krpm

Figure 6.24: Fourth turbocharger instantaneous results, volute centre pressure sound pressure level

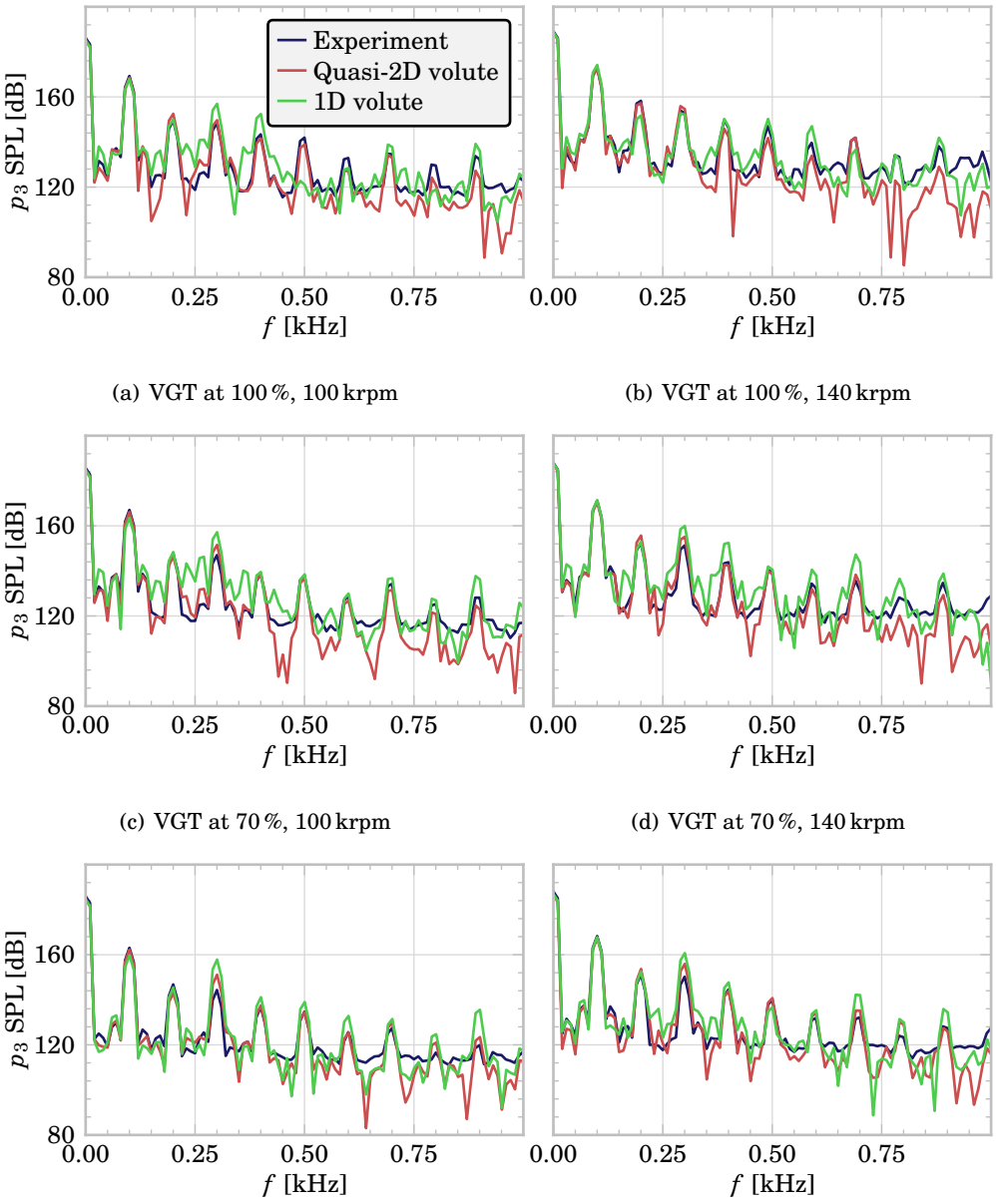

(a) VGT at 100 %, 100 krpm

(b) VGT at 100 %, 140 krpm

(c) VGT at 70 %, 100 krpm

(d) VGT at 70 %, 140 krpm

(e) VGT at 40 %, 100 krpm

(f) VGT at 40 %, 140 krpm

Figure 6.25: Fourth turbocharger instantaneous results, stator outlet pressure sound pressure level

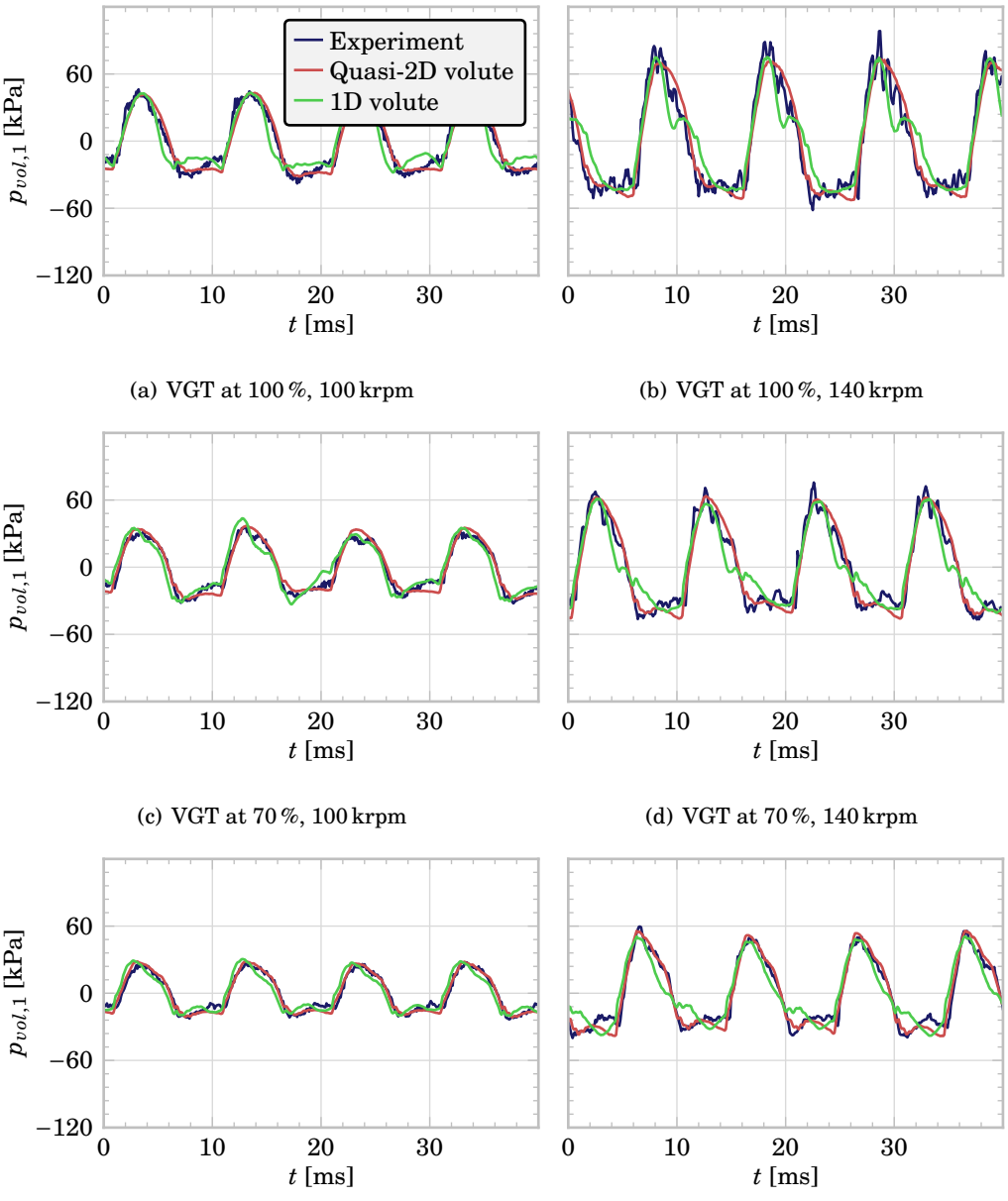

(a) VGT at 100 %, 100 krpm

(b) VGT at 100 %, 140 krpm

(c) VGT at 70 %, 100 krpm

(d) VGT at 70 %, 140 krpm

(e) VGT at 40 %, 100 krpm

(f) VGT at 40 %, 140 krpm

Figure 6.26: Fourth turbocharger instantaneous results, volute inlet pressure

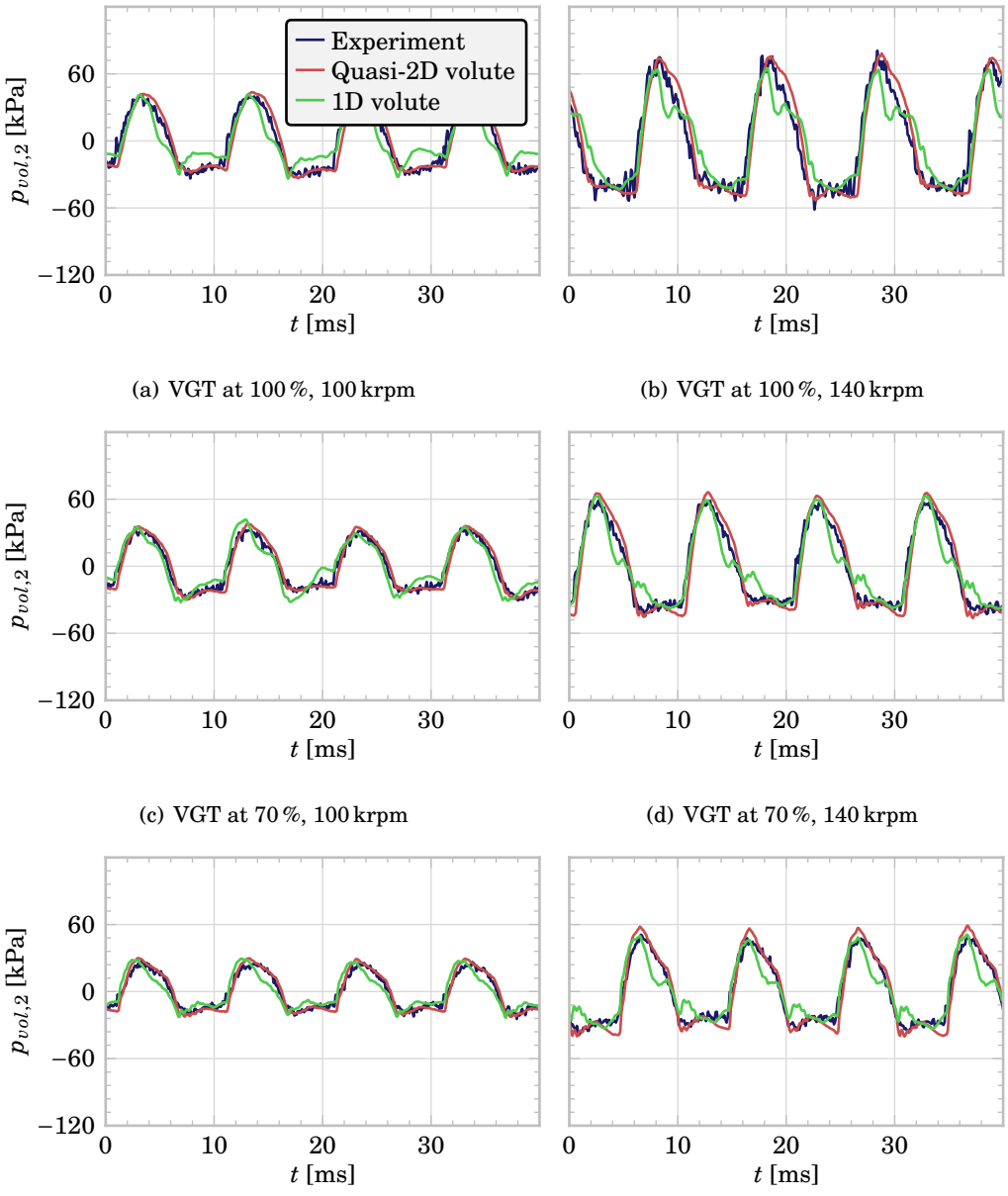

(a) VGT at 100 %, 100 krpm

(b) VGT at 100 %, 140 krpm

(c) VGT at 70 %, 100 krpm

(d) VGT at 70 %, 140 krpm

(e) VGT at 40 %, 100 krpm

(f) VGT at 40 %, 140 krpm

Figure 6.27: Fourth turbocharger instantaneous results, volute centre pressure

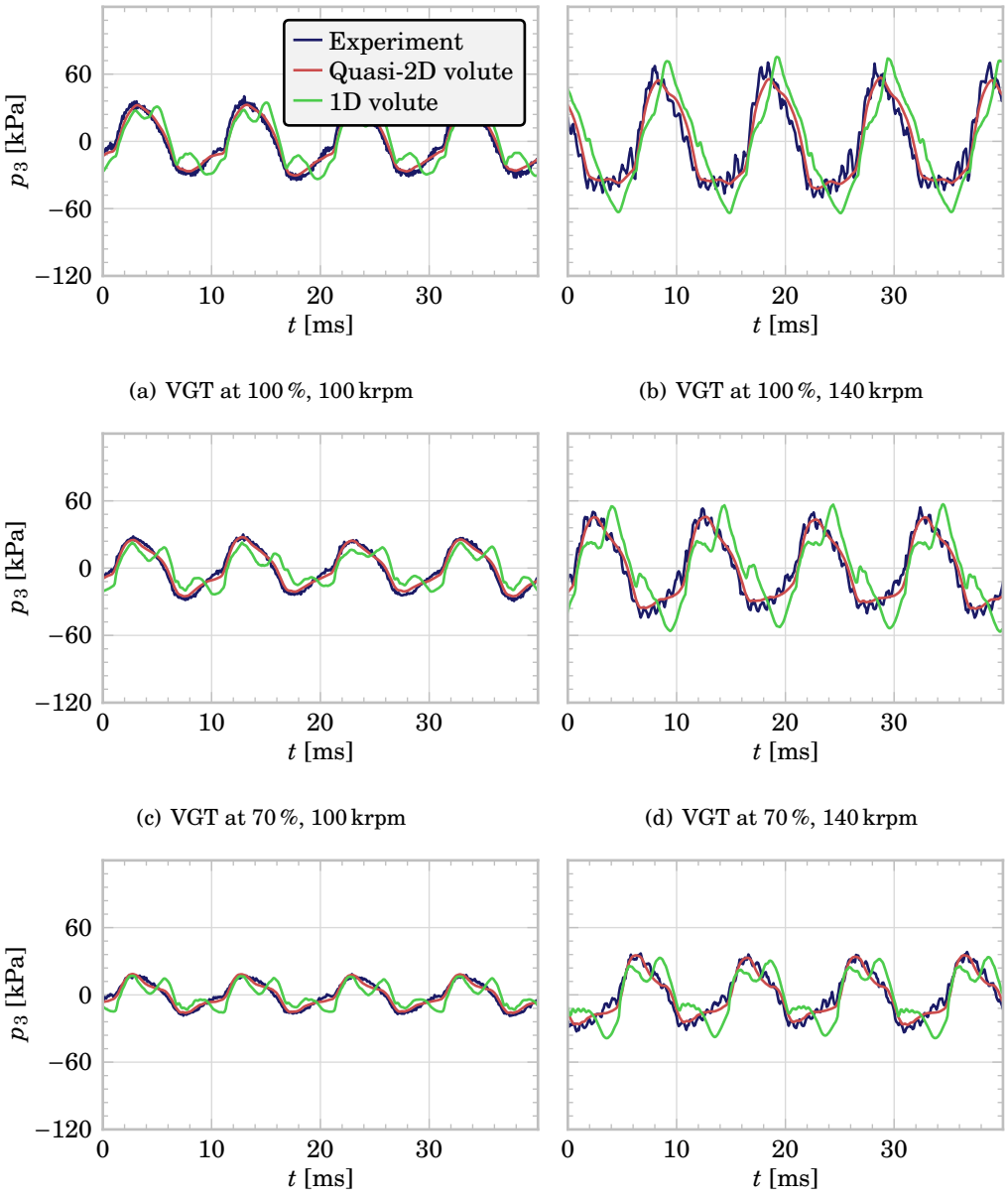

(a) VGT at 100 %, 100 krpm

(b) VGT at 100 %, 140 krpm

(c) VGT at 70 %, 100 krpm

(d) VGT at 70 %, 140 krpm

(e) VGT at 40 %, 100 krpm

(f) VGT at 40 %, 140 krpm

Figure 6.28: Fourth turbocharger instantaneous results, stator outlet pressure

Numerical scheme selection

State of the art one-dimensional engine simulation codes are becoming fast enough to attain speeds between 1 % and 5 % of real-time for realistic engines and running in commodity hardware, so they seem a viable alternative for HIL experiments in a not so distant future. Algorithm improvements should speed up current codes, and upgrades in SIMD operations as the rise from 4 double precision to 8 double precision floating point operations (FLOP) per cycle seen in the last generations of x86 processors, will provide means to reduce the time needed to achieve the goal of HIL simulation of a full engine with wave-action effects. The optimum selection of numerical schemes for one-dimensional modelling should provide means of more complex real-time simulations. Also, high frequency results can be affected by the selected scheme, as some of them are somewhat more diffusive than others and some limiters are more aggressive at fitting inside the second order TVD region, so a study of this influence is also necessary to minimise simulation errors, providing the optimum combination of schemes for a typical simulated turbine.

As previously noted, several time-integration schemes have been tested:

1 Explicit Euler scheme (first-order accurate).

2 Explicit Heun's method (second-order accurate, two steps).

3 Explicit fourth order Runge-Kutta method (fourth-order accurate, four steps).

Also, several limiter functions have been tested:

A Koren.

B Minmod.

C MC.

D Ospre.

E Superbee.

F UMIST

G Van-Albada.

H Van-Leer.

Finally, four different schemes have been used to compute the flux between cells:

- Harten-Lax-Van Leer solver, using a 2 wave approximation of the Riemann fan, see [129].
- Harten-Lax-Van Leer-Contact solver, using a 3 wave approximation of the Riemann fan, see [130].
- Kurganov and Tadmor central scheme, a Riemann-solver free method, see [131].
- Advection Upstream Splitting Method, which divides the flux into two different parts: a convective flux and a pressure flux; see [132].

All the implemented limiters maintain second-order TVD properties, giving second-order spatial accuracy where the state vector is smooth enough and resorting to first-order accuracy in the presence of abrupt gradients and shocks.

The different methods are tested with two different boundary conditions: 130 Hz and 750 Hz. The Courant number is always set at the maximum value that ensures the numerical convergence of the simulation.

All the methods are implemented trying to optimise the locality of the data in order to avoid as much cache misses as possible. Also, all the operations are vectorised, with all the vectors aligned to 128 bit bounds in order to exploit single instruction, multiple data (SIMD) operations of the processor where the simulations are done (in particular, SSSE3 instructions). This way, the differences between the different methods are not only due to the complexity of the mathematical algorithms, but also due to data locality and SIMD exploitability. Whenever a SIMD instruction is executed, two members of a vector can be computed at the same time, as the code uses double precision (64 bit per floating point element). Memoisation has also been used in order to reduce the amount of needed operations at a cost of slightly higher memory consumption. Heap allocations are also avoided whenever possible in favour of stack usage to reduce the overall computational costs. The data is passed as const references between the different functions to avoid copy overheads.

The different schemes are tested for errors in the mass flow rate and power output amplitudes. Amplitude errors are defined as:

$$\varepsilon_{\Delta\dot{m}_1} = \frac{\left(\dot{m}_{1,model,max} - \dot{m}_{1,model,min}\right) - \left(\dot{m}_{1,RANS,max} - \dot{m}_{1,RANS,min}\right)}{\dot{m}_{1,RANS,max} - \dot{m}_{1,RANS,min}} \tag{6.12}$$

$$\varepsilon_{\Delta\dot{m}_1} = \frac{\left(\dot{W}_{turb,model,max} - \dot{W}_{turb,model,min}\right) - \left(\dot{W}_{turb,RANS,max} - \dot{W}_{turb,RANS,min}\right)}{\dot{W}_{turb,RANS,max} - \dot{W}_{turb,RANS,min}} \tag{6.13}$$

The subscript $RANS$ is for the results of the three-dimensional simulation, while $model$ is for the results of the simplified model.

The relative speed is defined against the maximum speed obtained for each case.

The differences in accuracy between the different methods are almost negligible at the lowest frequency, and the level of error in indeed almost null with all the tested combinations. At low frequencies, the accuracy of the method is not bounded by the time-integration error, as the CFL condition renders the problem so stiff for explicit schemes that the time-step is low enough even for first-order accurate solvers. At 750 Hz, however, the error of the power amplitude prediction is clearly reduced using a second order scheme, while a fourth order one doesn't produce noticeable improvements and almost doubles the computational time. To get the same level of accuracy at 750 Hz with the first order time-integration scheme, the time-step has to be reduced to levels that induce higher computational costs than that of Heun's method.

The fastest simulation times are obtained using the Minmod limiter or with the VanLeer limiter. The differences in computational time between the different implemented limiters are only of around a couple percent points. The most accurate limiter for mass flow rate estimation appears to be the Minmod limiter, although it is the most conservative in terms of its TVD compliance, but only when used with the HLLC approximate Riemann solver: coupled with the AUSM solver, which is more diffusive than the HLLC solver, it underestimates the amplitude of the mass flow rate evolution. As with the power output amplitude, however, it is always overestimated and the error is minimised with the AUSM solver. A Pareto optimality is obtained with the KT scheme and the Minmod limiter using Heun's method, which is also the fastest combination for second order in time.

As a general recommendation, the scheme by Kurganov and Tadmor combined with the Minmod limiter and Heun's time integration scheme should be used to obtain the best results at the highest frequencies. The HLL approximate Riemann solver gives similar results to KT in the tested cases, but with a 3 % overhead in computational costs. The selected combination of schemes is 10 % faster than the worst-case selection using Heun's method. If the highest accuracy at high frequencies is not needed, a combination of first order forward Euler method with KT and Minmod should give 80 % extra speed over Heun's method. The fourth-order, four-steps Runge-Kutta method shows no clear advantage over Heun's method, so it may be safely discarded.

Figure 6.30 shows the time-domain results of three different time-integration schemes for the turbine power output for 130 Hz and 750 Hz, using the Minmod limiter function and three different inter-cell fluxes approximations. Although the differences remain small, they are visible in the right-hand-side plot. Due to the stiffness of the equations of the system, explicit schemes must use a small

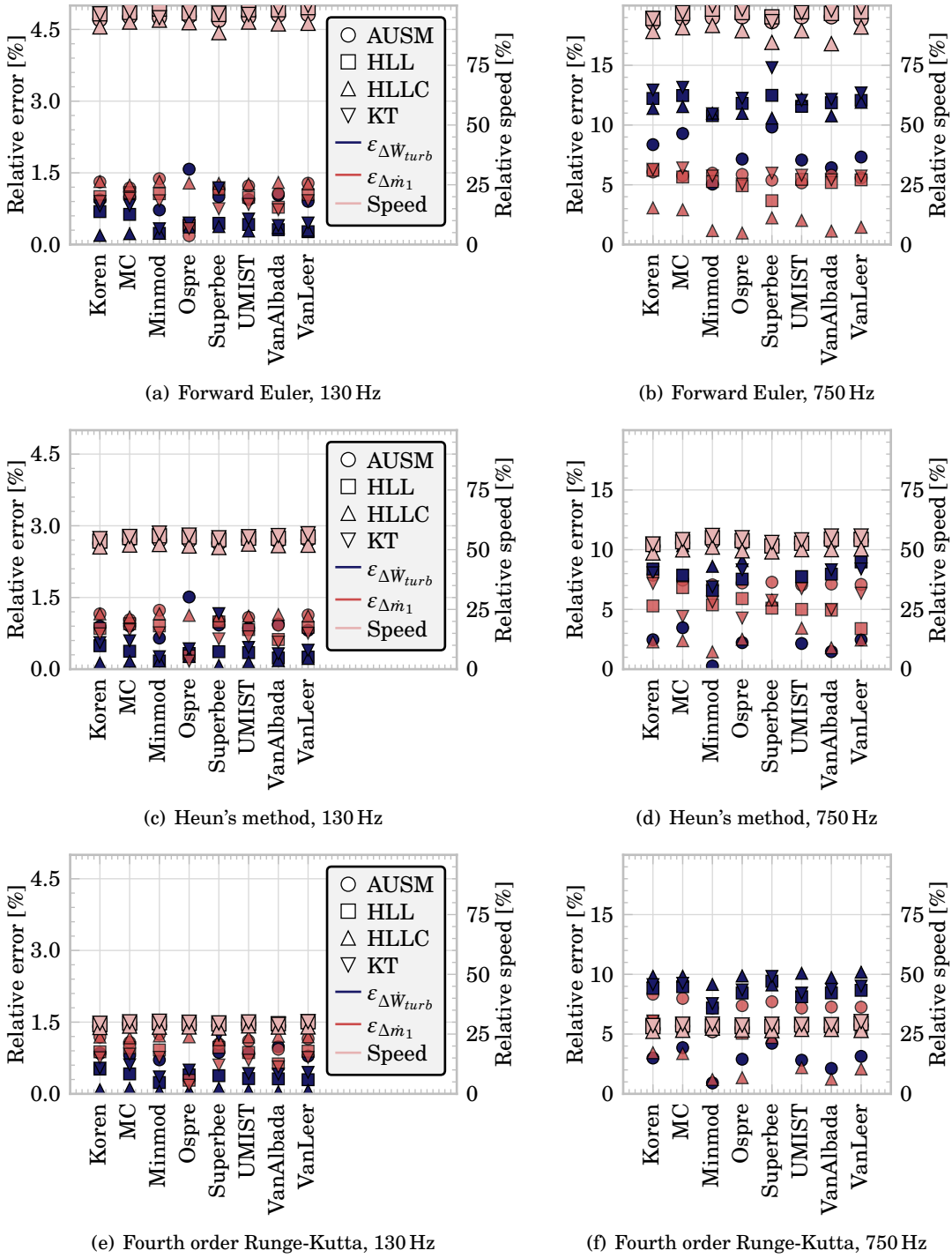

(a) Forward Euler, 130 Hz

(b) Forward Euler, 750 Hz

(c) Heun's method, 130 Hz

(d) Heun's method, 750 Hz

(e) Fourth order Runge-Kutta, 130 Hz

(f) Fourth order Runge-Kutta, 750 Hz

Figure 6.29: Solver test results

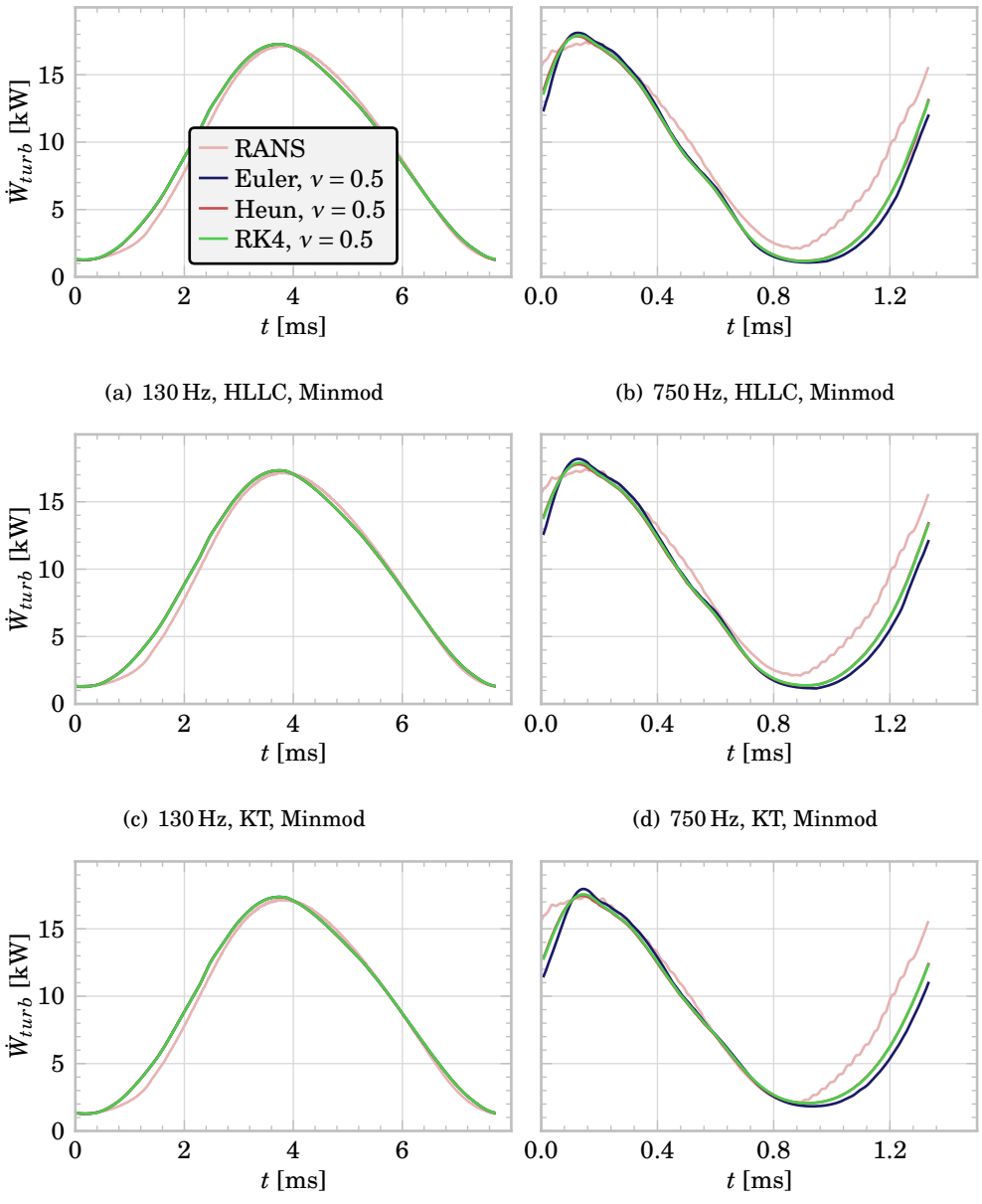

(a) 130 Hz, HLLC, Minmod

(b) 750 Hz, HLLC, Minmod

(c) 130 Hz, KT, Minmod

(d) 750 Hz, KT, Minmod

(e) 130 Hz, AUSM, Minmod

(f) 750 Hz, AUSM, Minmod

Figure 6.30: $\dot{W}_{turb}$, time-integration scheme comparison

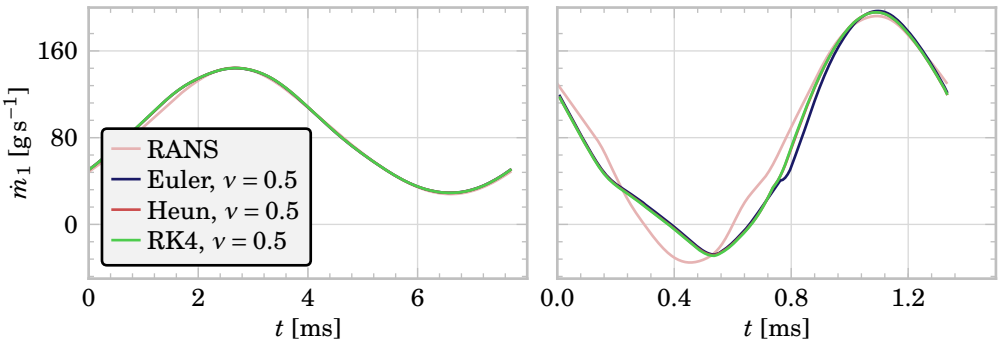

(a) 130 Hz, HLLC, Minmod

(b) 750 Hz, HLLC, Minmod

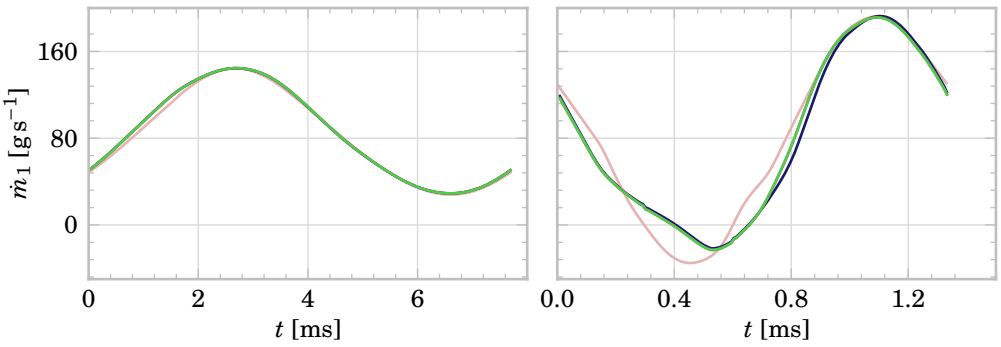

(c) 130 Hz, KT, Minmod

(d) 750 Hz, KT, Minmod

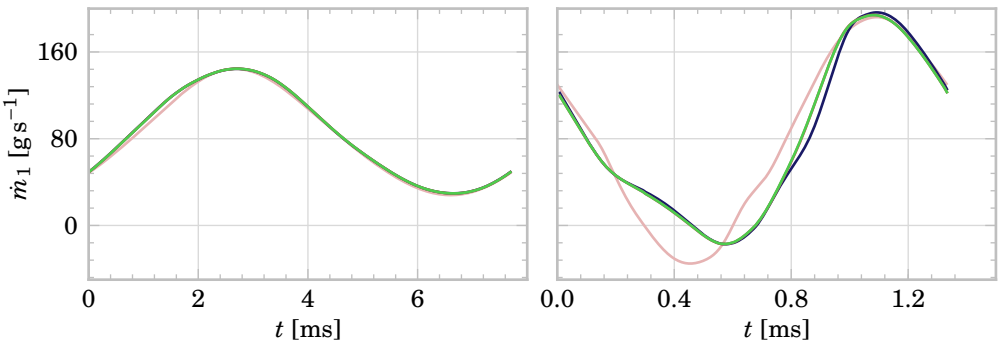

(e) 130 Hz, AUSM, Minmod

(f) 750 Hz, AUSM, Minmod

Figure 6.31: $\dot{m}_1$, time-integration scheme comparison

time-step to avoid unstabilities, getting enough accuracy for all the cases except for the highest frequencies. The implemented fourth order Runge-Kutta method incurs in a computational cost penalty too high for its small improvements over the Heun's method, so the latter one is recommended in cases where very high frequency, extremely high amplitude boundary conditions are expected. If the amplitude for the highest harmonics is low enough, a first order method such as the forward Euler method may be accurate enough. The turbine power output is better reproduced using the AUSM method, while in the case of the mass flow rate (Figure 6.31) the best amplitude prediction is obtained by the HLLC approximate Riemann solver.

6.3 Mechanical losses

In this section, the mechanical losses model is calibrated using a random subset of the available experimental for three different turbochargers. Then, it is validated against the full steady-state dataset, and the instantaneous prediction for three different pulsating flow cases is shown. Finally, the effects of oil mass flow rate and inlet temperature are studied using the model, showing tendencies that are compatible with the results provided by other authors.

Calibration

The model developed in section section 5.6 needs the adjustment of different parameters. The following procedure has been employed:

- First, a random subset of only one tenth of the whole experimental dataset of each turbocharger was selected.
- Then, the model parameters were adjusted in order to predict mechanical efficiency that fits the subset of experimental data.
- Finally, the model is applied to the whole experimental dataset.

The fitting procedure has been made minimising the root mean square error of the mechanical losses power ($RMSE_{ml}$, Equation 6.14).

$$RMSE_{ml}\left(k_{jb}, k_{tb}, k_{A_{comp}}, k_{A_{turb}}\right) = \sqrt{\frac{1}{N_{exp}} \cdot \sum_{i}^{N_{exp}} \left(\frac{\dot{W}_{ml,model_i} - \dot{W}_{ml,meas_i}}{\dot{W}_{ml,meas_i}} \right)^2} \tag{6.14}$$

by means of the SLSQP algorithm developed by Kraft [133] using `SciPy` [134]. The minimisation problem is described formally as:

$$\begin{aligned} \underset{k_{jb},k_{tb},k_{A_{comp}},k_{A_{turb}}}{\text{minimise}} \quad & RMSE_{ml}\left(k_{jb},k_{tb},k_{A_{comp}},k_{A_{turb}}\right) \\ \text{subject to} \quad & 0 \leq k_{jb} \leq 1 \\ & 0 \leq k_{tb} \leq 1 \\ & 0.5 \leq k_{A_{comp}} \leq 1.5 \\ & 0.5 \leq k_{A_{turb}} \leq 1.5 \end{aligned} \tag{6.15}$$

There seems to exist a tendency between the values of $2\pi \cdot k_{jb} \cdot L_{jb} \cdot R_{jb}^3/h_{jb}$ and $k_{tb} \cdot \pi \cdot \left(R_{tb,max}^2 - R_{tb,min}^2\right)\bar{R}_{tb}^2/\xi^{1/3}$ and the compressor frontal area, A_c. A larger turbocharger database is needed, however, to validate these tendencies.

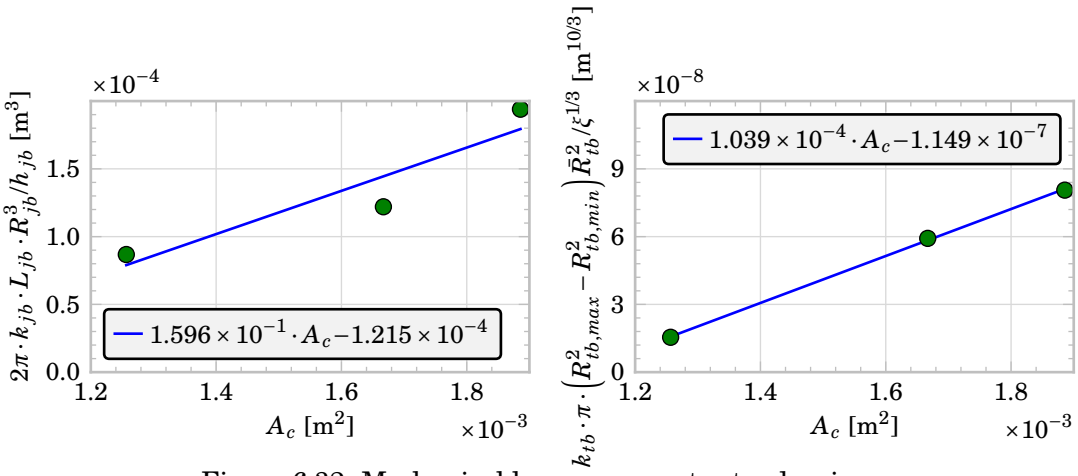

Figure 6.32: Mechanical losses parameter tendencies

Validation

In order to asses the robustness of the model adjustment method, the parameters obtained by fitting only a random subset of the experimental data are compared with those obtained after fitting the whole dataset.

The full model gives good results with very low computational cost. Also, the results obtained by fitting a random partial dataset (Figure 6.33 and Figure 6.34) are almost identical to those of Figure 6.35 and Figure 6.36, where the parameters were fitted to the whole experimental database, showing model robustness. The solid lines represent perfect fit, the dashed lines represent a 25 W or 5 % of efficiency deviation and the dash-dotted lines represent a 50 W or 10 % of efficiency deviation. There are, however, discrepancies at high rotational

speeds. The experiments were done with high oil inlet temperatures at high rotational speeds in order to minimise the heat fluxes, and the lubrication film may have broken during these phases. Figure 6.37 shows a damaged thrust bearing of one of the tested turbochargers. There are scratches over its surface that are compatible with partial oil film loss due to extremely low viscosities. Partially-dry contact between the bearing washers is not taken into account in the model and may explain part of the discrepancies, so further research is needed to improve it.

In order to confirm the need of computing both the journal and the thrust bearings and not only one of them, the model was fitted two more times, first forcing k_{tb} to be equal to 0 and then forcing k_{jb} to be equal to 0. The results of these additional fitting procedures were unsatisfactory, showing that a full model is needed in order to compute properly the behaviour of the bearing system.

The full steady experimental campaign has been simulated using the standard `OpenWAM` [135] turbocharger model with three different configuration for the mechanical losses submodel: first, the model proposed in this thesis; second, no mechanical losses; third, a constant mechanical efficiency of 90 %. From the results shown in Figure 6.38 it is clear that, although some errors in the turbocharger rotational speed are present with the proposed model, it produces better results than using a constant mechanical efficiency value, thus providing better boost pressure predictions. The improvement from a constant efficiency approach during simulations of the warm-up phase of urban driving cycles is clear, as the oil temperature and viscosity dramatically changes.

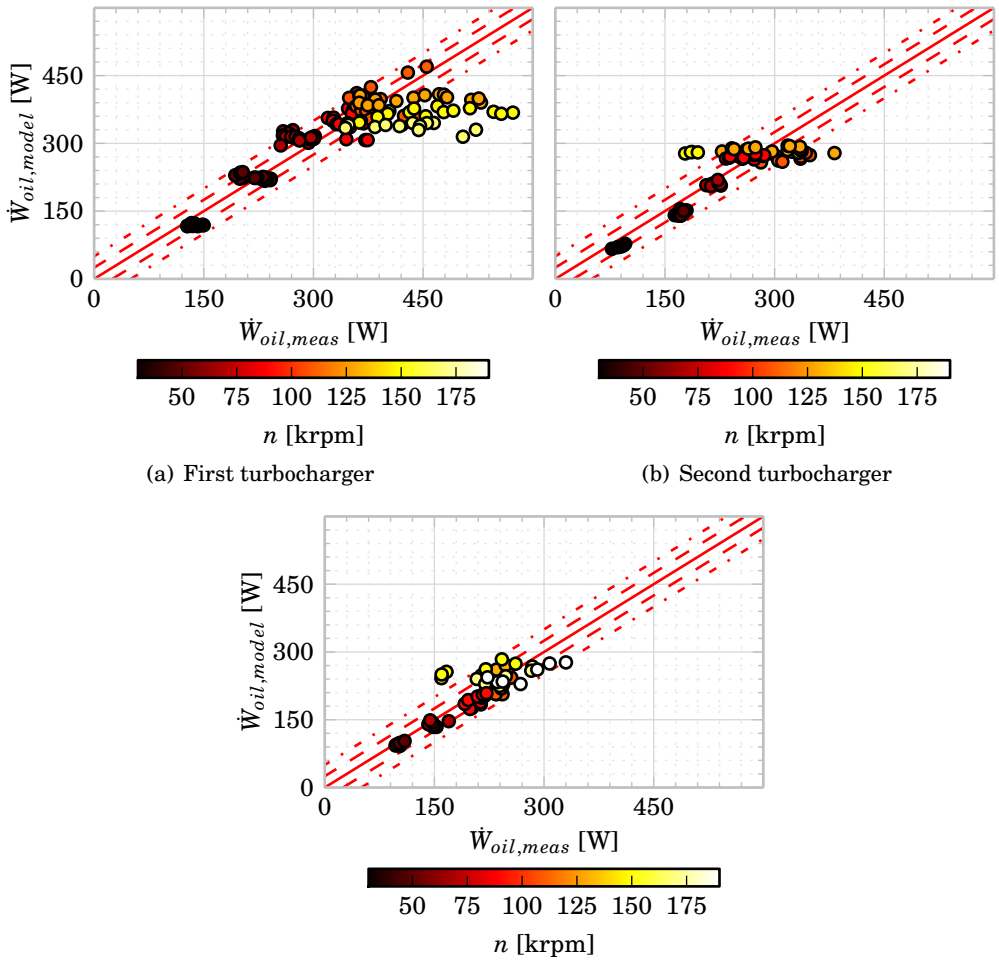

(a) First turbocharger

(b) Second turbocharger

(c) Third turbocharger

Figure 6.33: Mechanical losses power, measured vs. model., calibrated with a partial dataset

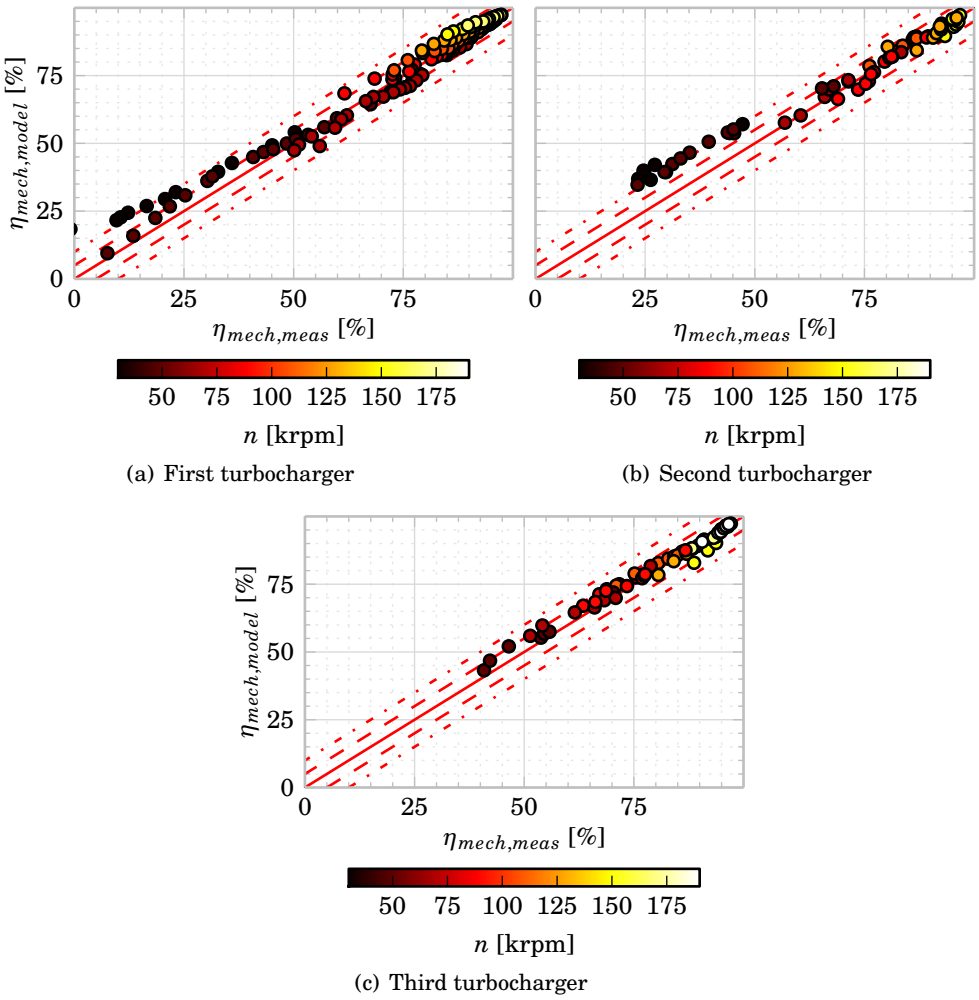

(a) First turbocharger

(b) Second turbocharger

(c) Third turbocharger

Figure 6.34: Mechanical efficiency, measured vs. model., calibrated with a partial dataset

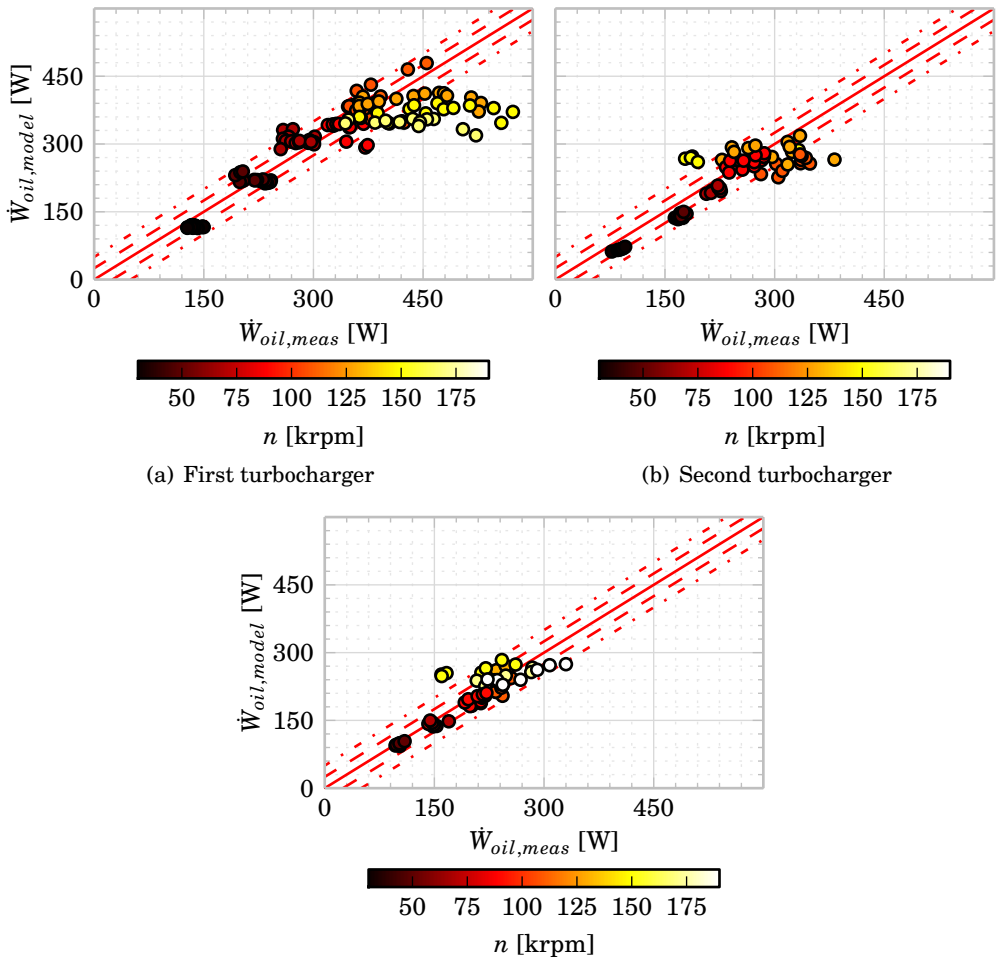

(a) First turbocharger

(b) Second turbocharger

(c) Third turbocharger

Figure 6.35: Mechanical losses power, measured vs. model., calibrated with full dataset

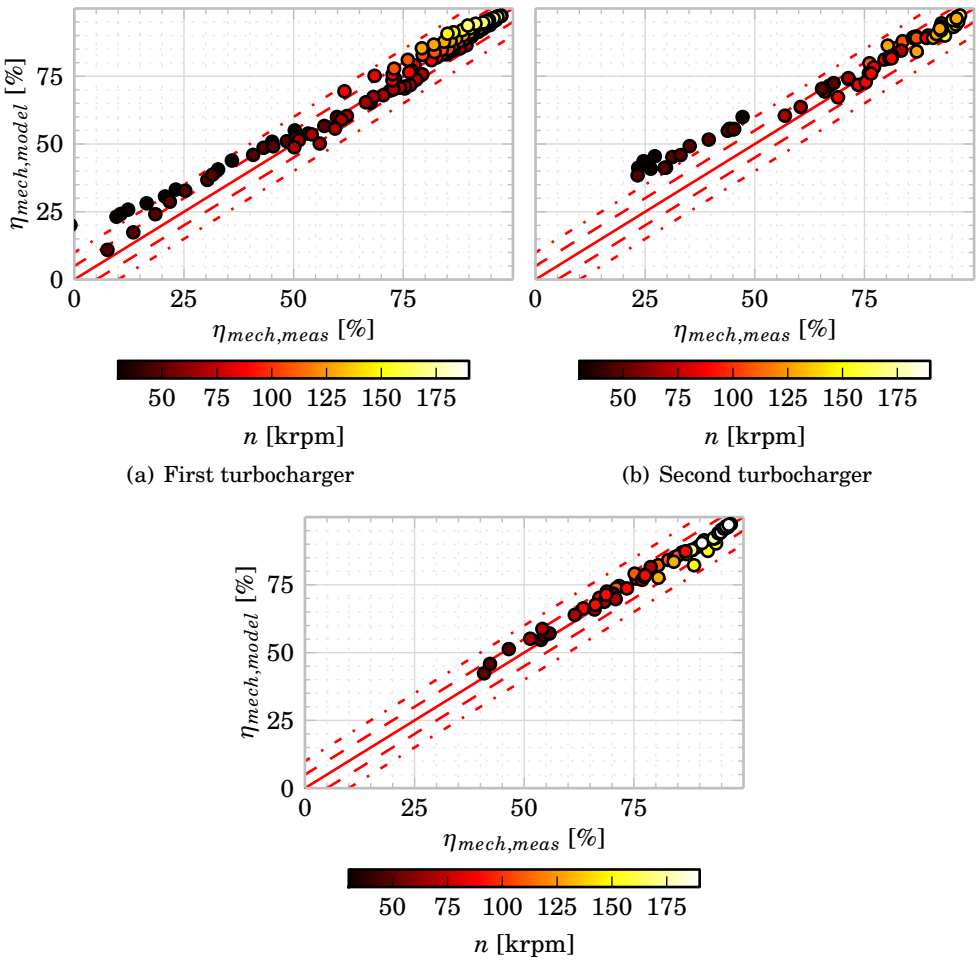

(a) First turbocharger

(b) Second turbocharger

(c) Third turbocharger

Figure 6.36: Mechanical efficiency, measured vs. model., calibrated with whole dataset

Figure 6.37: Damaged thrust bearing washers after high oil temperature experiments

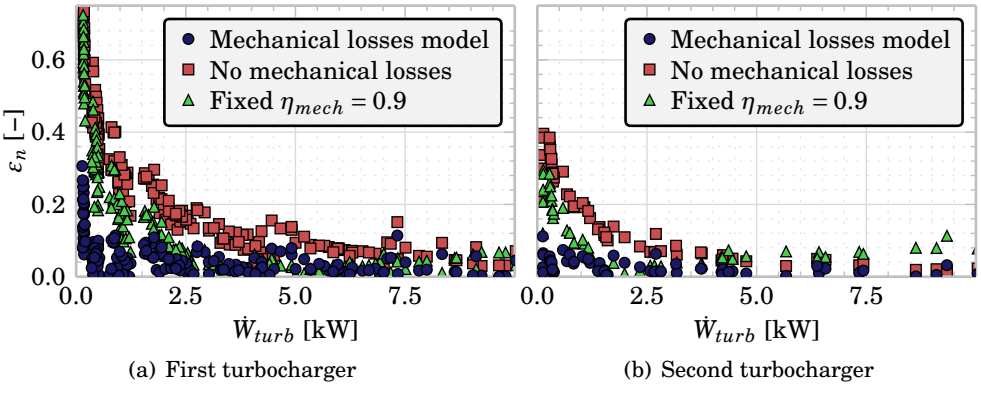

(a) First turbocharger

(b) Second turbocharger

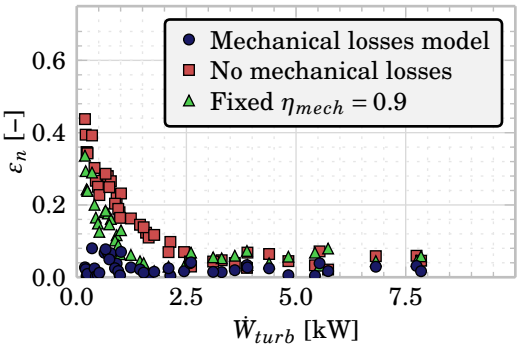

(c) Third turbocharger

Figure 6.38: Mechanical losses model speed error - steady tests.

Pulsating flow results

Table 6.3: Mechanical losses model error during pulsating simulations.

Engine speed [rpm]	BMEP [kPa]	ε_n [%]	$\varepsilon_{\dot{m}_{turb}}$ [%]	$\varepsilon_{\dot{m}_{comp}}$ [%]	$\varepsilon_{\pi_{turb}}$ [%]	$\varepsilon_{\pi_{comp}}$ [%]
2000	260	1.7	0.5	1.9	0.1	0.1
2000	630	4.5	0.9	4.8	0.1	2.1
2000	760	0.1	3.4	0.0	0.9	1.7

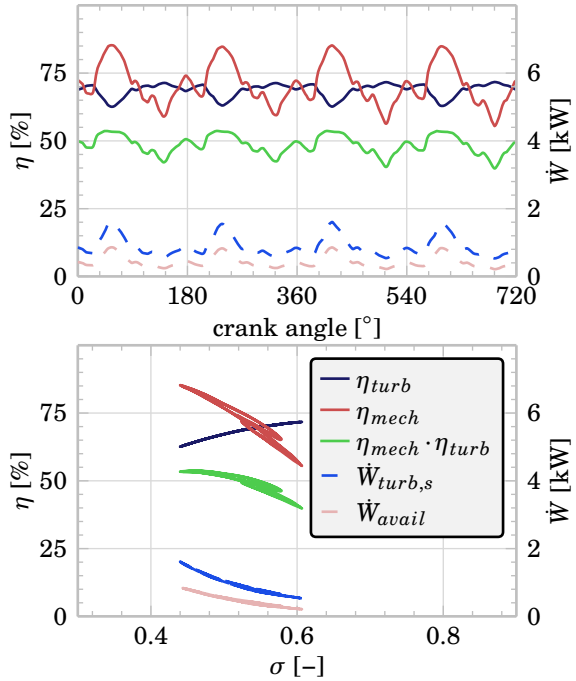

Figure 6.39: First turbocharger, engine at 2000 rpm and 260 kPa

In Figure 6.39, results for pulsating flow at an engine speed of 2000 rpm and an engine BMEP of 260 kPa are presented for the first turbocharger. The upper graph of Figure 6.39 shows in blue solid line the isentropic efficiency of the turbine, calculated with the model described in the work from Payri et al. [136]; in red solid line the mechanical efficiency; and in green solid line the product of both, plotted against the crank angle. As it can be seen, both mechanical and isentropic efficiency are unphased. It is clearer in the lower graphic, where the efficiencies are plotted against the blade tip speed ratio: when the isentropic efficiency rises, the mechanical efficiency drops. The available power is the

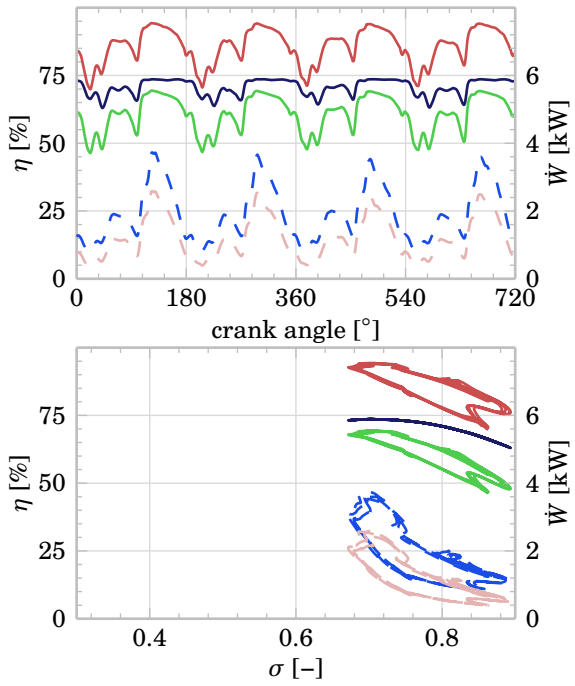

Figure 6.40: Second turbocharger, engine at 2000 rpm and 630 kPa

isentropic turbine power times the isentropic efficiency times the mechanical efficiency.

In Figure 6.40, results are plotted for an engine speed of 2000 rpm and an engine BMEP of 630 kPa for the second turbocharger. Again, both mechanical and isentropic efficiencies are unphased. Nevertheless, in this case the product of both efficiencies is working near its maximum value during longer periods of time. As the minimum efficiencies happen at high blade tip to air speed ratio, its effect is minimised.

In Figure 6.41, results are shown for an engine speed of 2000 rpm and an engine BMEP of 760 kPa for the third turbocharger. This time, both mechanical and isentropic efficiency appear to be almost in phase, so the maximum of the product is near the maximum of the turbine maximum isentropic efficiency, which can be translated into maximum available power at the compressor side. The available power is a scaled-down and deformed version of the turbine isentropic power.

During pulsating flow, the mechanical efficiency of the turbocharger can instantaneously change between very high and very low values, due to variations in both power transmission losses and turbine power output. The model of power transmission loss can change instantaneously due to crank angle variations of

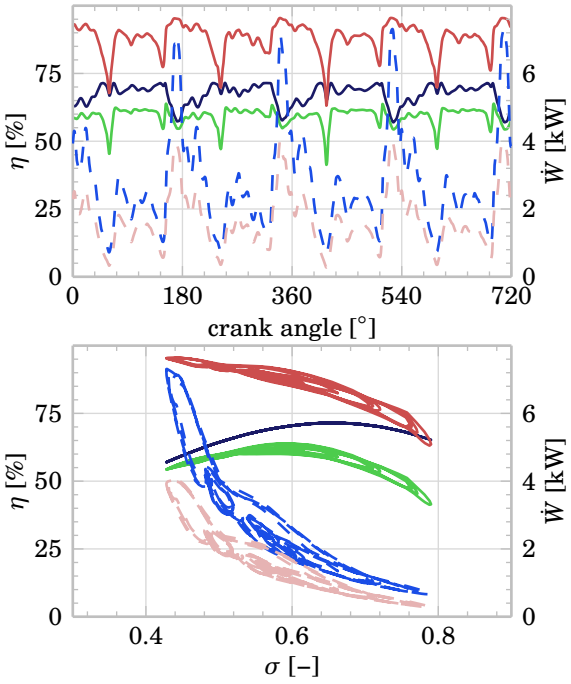

Figure 6.41: Third turbocharger, engine at 2000 rpm and 760 kPa

axial loading, affecting axial thrust bearing power losses.

If a constant mechanical efficiency is used to model the turbocharger behaviour, there will be bigger errors than when modelling its instantaneous variations. The mechanical efficiency times the isentropic turbine efficiency can change notably even when the turbine isentropic efficiency is almost constant due to changes in mechanical efficiency. The model also shows that the mechanical efficiency can have its minimum value at points of high or low isentropic turbine efficiency, depending on the operating conditions.

Effect of the oil conditions

The presented model can be used to test the effects of the oil conditions in the mechanical losses of the turbocharger. The simulations have been done with the following characteristics:

- The three turbochargers for which experimental data are available have been computed.
- The compressor and turbine pressures have been maintained the same as in the quasi-adiabatic experimental campaign.
- The same oil as in the experimental campaign is used.
- Three oil inlet temperatures are used: 310 K, 340 K and 370 K.
- Two different oil mass flow rates are used: $2\,g\,s^{-1}$ and $15\,g\,s^{-1}$.

The results are plotted in Figures 6.42 to 6.44 for the power losses and in Figures 6.45 to 6.47 for the mechanical efficiency. The simulated mechanical efficiency is computed as follows:

$$\eta_{mech} = \frac{\dot{W}_{turb,meas} - \dot{W}_{ml,meas}}{\dot{W}_{turb,meas} - \dot{W}_{ml,meas} + \dot{W}_{ml,sim}} \tag{6.16}$$

The results from these simulations are similar for all the turbochargers. The results for 370 K and $15\,g\,s^{-1}$ will be used as reference values.

During urban driving cycles, where both the oil inlet temperature and mass flow rate are low and values of 310 K and $2\,g\,s^{-1}$ are typical, the mechanical losses power is similar to the reference value. At that low temperatures, if the oil pressure rises, providing a higher oil mass flow rate, the mechanical losses power can be doubled.

Some time after the engine start, when the oil temperature is still rising but is high enough to generate low oil viscosities, the differences between a very low and a high mass flow rate are also very important.

Finally, at high oil temperatures and very low oil pressures and, thus, low mass flow rates, the mechanical losses are minimum.

The oil mass flow rate has two different effects: first, it modifies the thickness of the lubrication film in the axial bearing; second, it modifies the oil mean temperature during the process. Higher mass flow rates produce thicker lubrication films in the axial bearing, reducing its losses, but also reduce the mean oil temperature during the process for a given dissipated power, rising the mean oil viscosity. Of the two effects, the most important seams to be the oil viscosity increase, drastically rising the dissipated mechanical power. Similar results were obtained by Deligant et al. [93] using a torquemeter to measure

mechanical losses, with increasing power dissipation for higher oil pressures and mass flow rates.

Minimising oil pressure may lead to higher turbocharger mechanical efficiencies, with the highest effects during the engine warm-up phase, what results in lower turbine expansion ratio requirements and lower exhaust back-pressures. Lowering the oil viscosity by rising its temperature will further reduce the mechanical losses. Lower mass flow rates and viscosities, however, also affect other aspects of the turbocharger operation:

- High oil temperatures reduce the cooling effect of the lubrication.
- Low oil viscosities rise the risk of metal-to-metal contact in the bearings, reducing the expected life of the the turbocharger.
- Low mass flow rates also rise the risk of metal-to-metal contact and reduce the cooling effect of the lubrication.

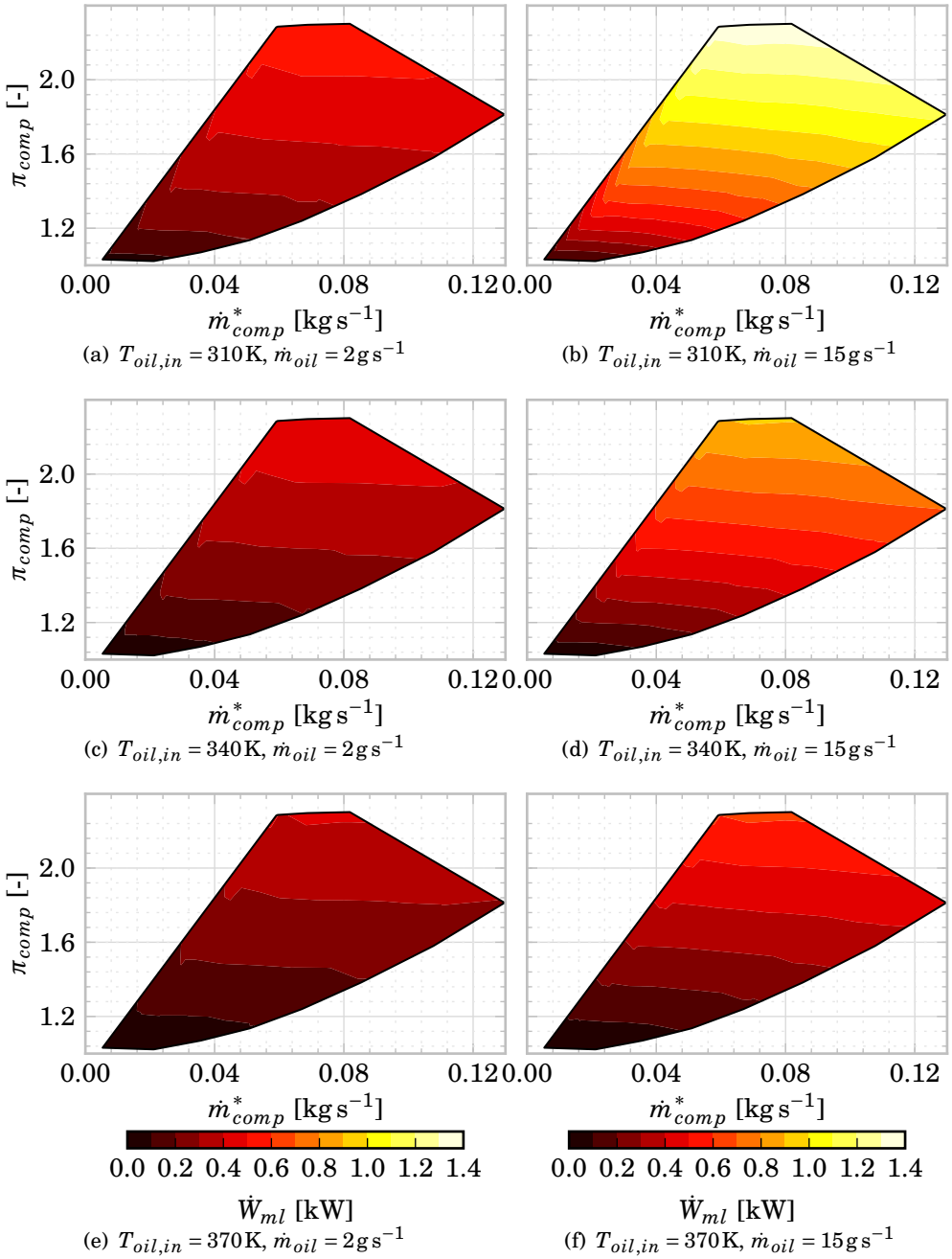

(a) $T_{oil,in} = 310\,\mathrm{K}$, $\dot{m}_{oil} = 2\,\mathrm{g\,s^{-1}}$ (b) $T_{oil,in} = 310\,\mathrm{K}$, $\dot{m}_{oil} = 15\,\mathrm{g\,s^{-1}}$

(c) $T_{oil,in} = 340\,\mathrm{K}$, $\dot{m}_{oil} = 2\,\mathrm{g\,s^{-1}}$ (d) $T_{oil,in} = 340\,\mathrm{K}$, $\dot{m}_{oil} = 15\,\mathrm{g\,s^{-1}}$

(e) $T_{oil,in} = 370\,\mathrm{K}$, $\dot{m}_{oil} = 2\,\mathrm{g\,s^{-1}}$ (f) $T_{oil,in} = 370\,\mathrm{K}$, $\dot{m}_{oil} = 15\,\mathrm{g\,s^{-1}}$

Figure 6.42: Mechanical losses - oil temperature and mass flow rate effect. First turbocharger.

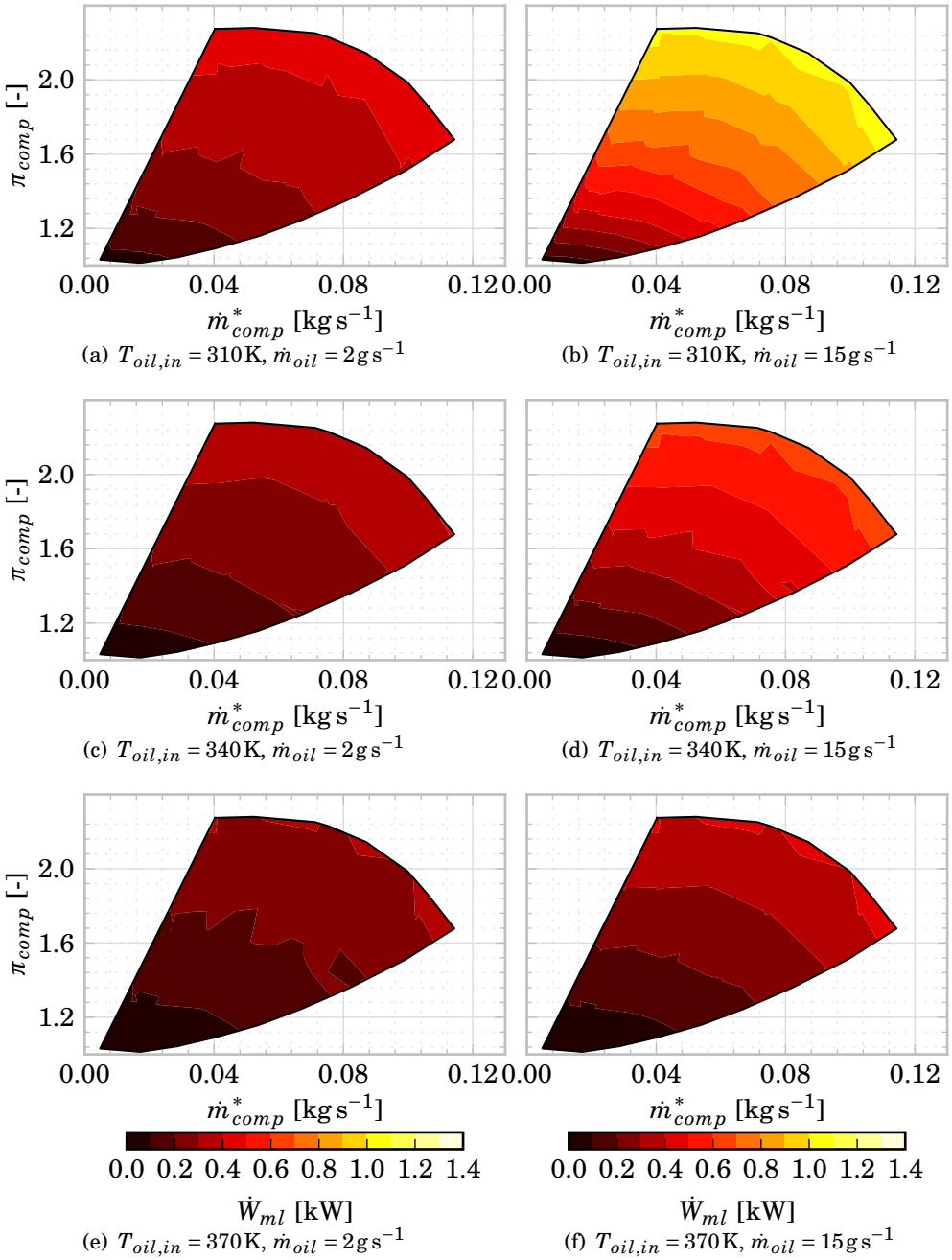

(a) $T_{oil,in} = 310\,\mathrm{K}$, $\dot{m}_{oil} = 2\,\mathrm{g\,s^{-1}}$

(b) $T_{oil,in} = 310\,\mathrm{K}$, $\dot{m}_{oil} = 15\,\mathrm{g\,s^{-1}}$

(c) $T_{oil,in} = 340\,\mathrm{K}$, $\dot{m}_{oil} = 2\,\mathrm{g\,s^{-1}}$

(d) $T_{oil,in} = 340\,\mathrm{K}$, $\dot{m}_{oil} = 15\,\mathrm{g\,s^{-1}}$

(e) $T_{oil,in} = 370\,\mathrm{K}$, $\dot{m}_{oil} = 2\,\mathrm{g\,s^{-1}}$

(f) $T_{oil,in} = 370\,\mathrm{K}$, $\dot{m}_{oil} = 15\,\mathrm{g\,s^{-1}}$

Figure 6.43: Mechanical losses - oil temperature and mass flow rate effect. Second turbocharger.

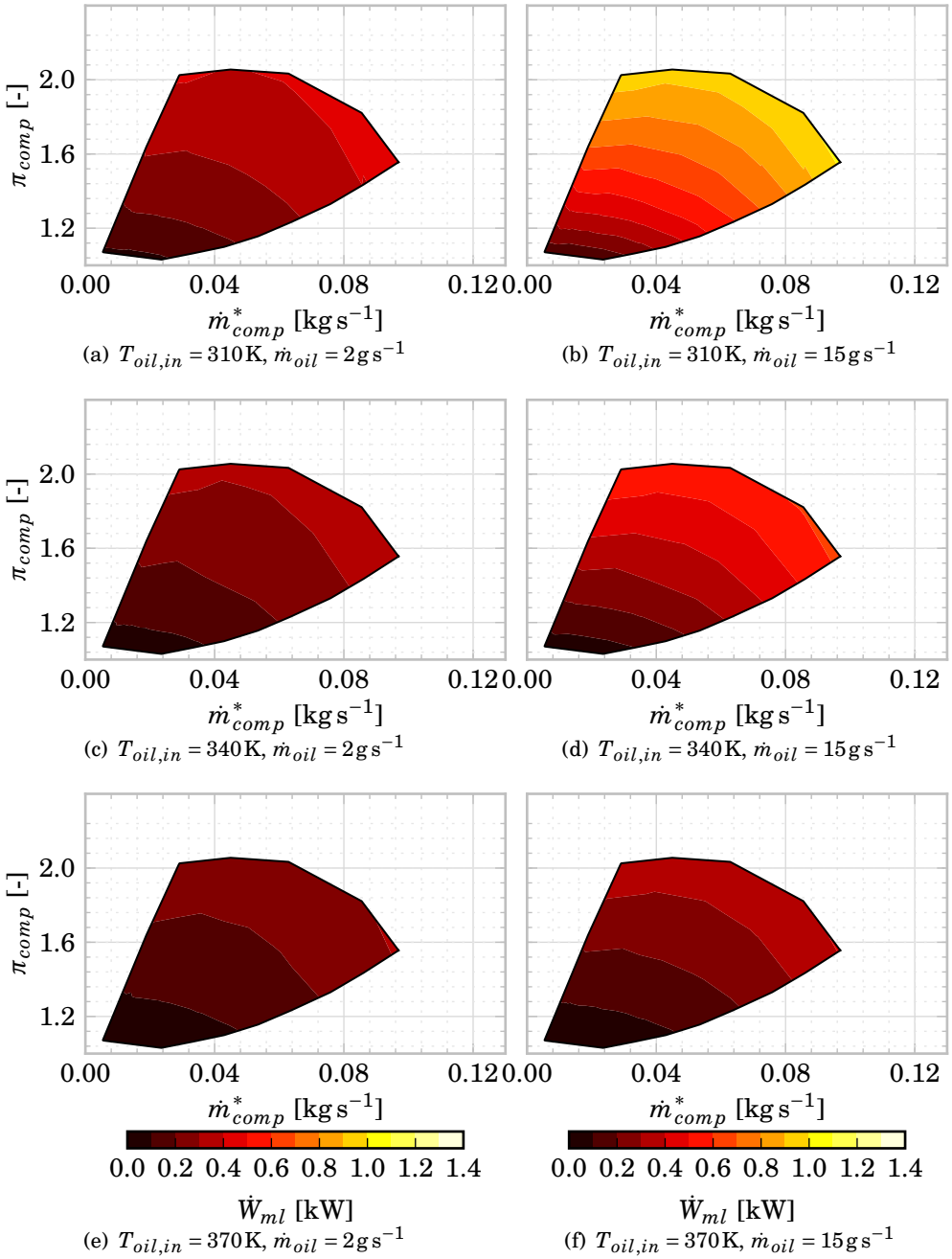

(a) $T_{oil,in} = 310\,\mathrm{K}$, $\dot{m}_{oil} = 2\,\mathrm{g\,s^{-1}}$ (b) $T_{oil,in} = 310\,\mathrm{K}$, $\dot{m}_{oil} = 15\,\mathrm{g\,s^{-1}}$

(c) $T_{oil,in} = 340\,\mathrm{K}$, $\dot{m}_{oil} = 2\,\mathrm{g\,s^{-1}}$ (d) $T_{oil,in} = 340\,\mathrm{K}$, $\dot{m}_{oil} = 15\,\mathrm{g\,s^{-1}}$

(e) $T_{oil,in} = 370\,\mathrm{K}$, $\dot{m}_{oil} = 2\,\mathrm{g\,s^{-1}}$ (f) $T_{oil,in} = 370\,\mathrm{K}$, $\dot{m}_{oil} = 15\,\mathrm{g\,s^{-1}}$

Figure 6.44: Mechanical losses - oil temperature and mass flow rate effect. Third turbocharger.

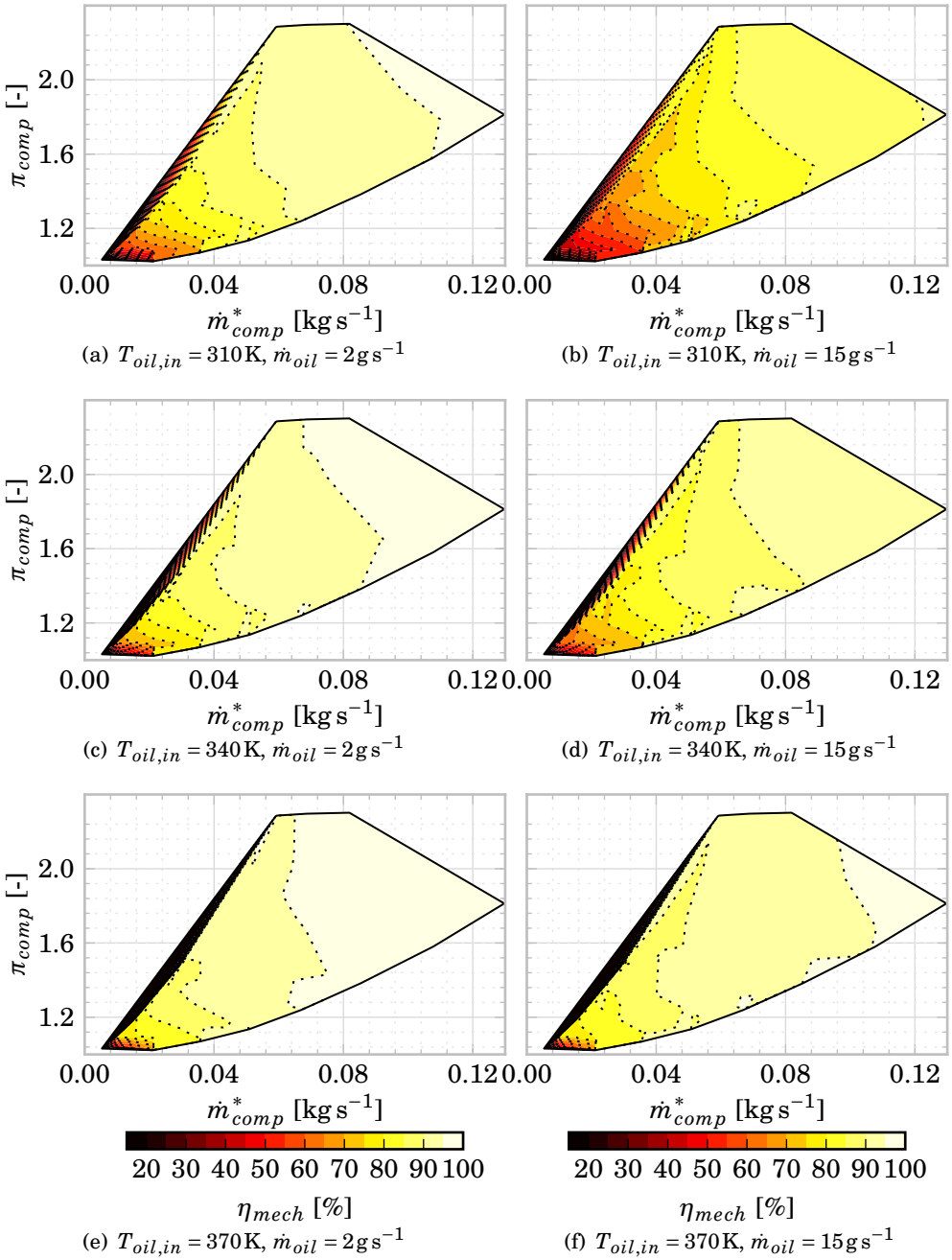

(a) $T_{oil,in} = 310\,\mathrm{K}$, $\dot{m}_{oil} = 2\,\mathrm{g\,s^{-1}}$

(b) $T_{oil,in} = 310\,\mathrm{K}$, $\dot{m}_{oil} = 15\,\mathrm{g\,s^{-1}}$

(c) $T_{oil,in} = 340\,\mathrm{K}$, $\dot{m}_{oil} = 2\,\mathrm{g\,s^{-1}}$

(d) $T_{oil,in} = 340\,\mathrm{K}$, $\dot{m}_{oil} = 15\,\mathrm{g\,s^{-1}}$

(e) $T_{oil,in} = 370\,\mathrm{K}$, $\dot{m}_{oil} = 2\,\mathrm{g\,s^{-1}}$

(f) $T_{oil,in} = 370\,\mathrm{K}$, $\dot{m}_{oil} = 15\,\mathrm{g\,s^{-1}}$

Figure 6.45: Mechanical efficiency - oil temperature and mass flow rate effect. First turbocharger.

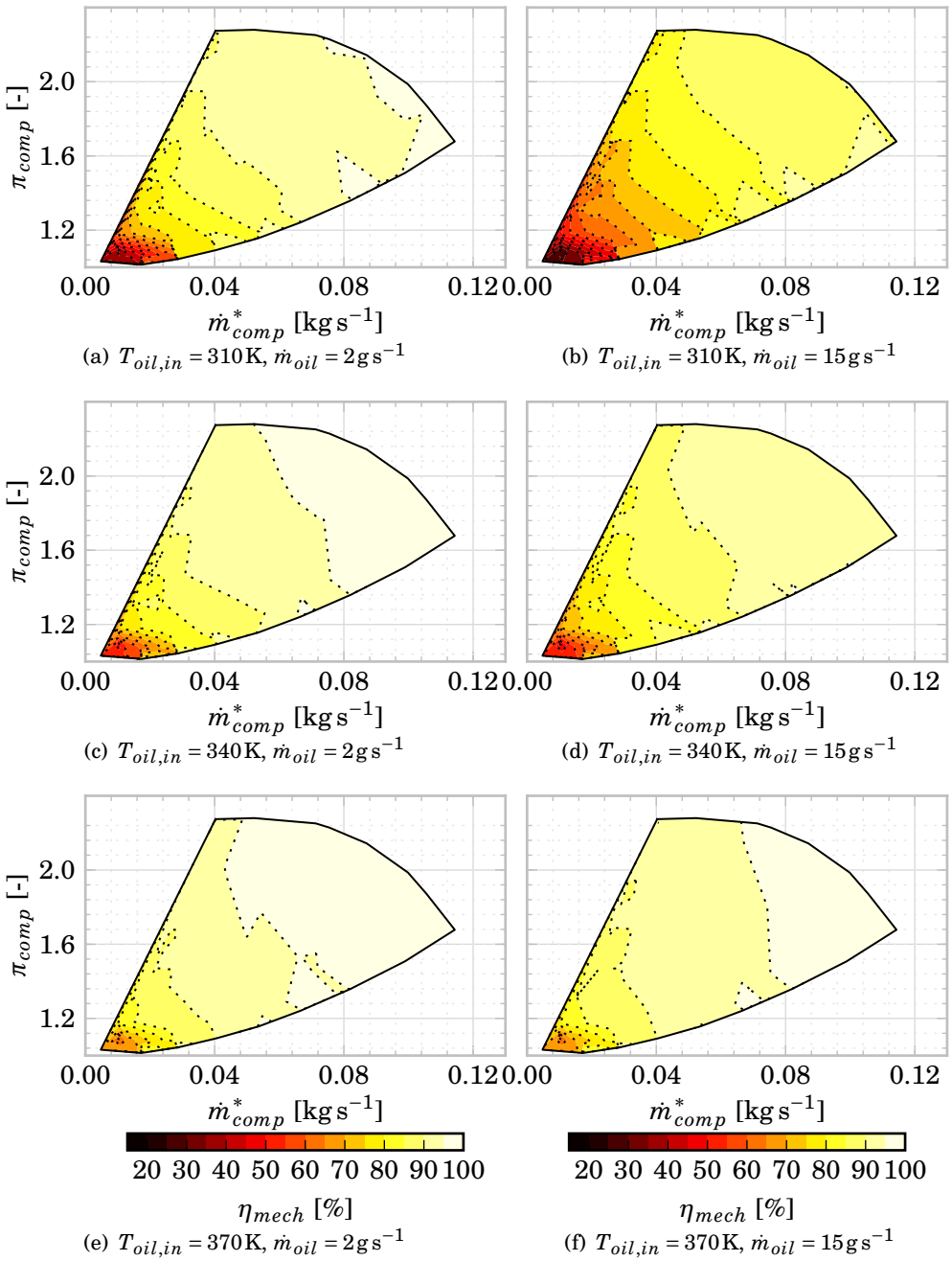

(a) $T_{oil,in} = 310\,\mathrm{K}$, $\dot{m}_{oil} = 2\,\mathrm{g\,s^{-1}}$

(b) $T_{oil,in} = 310\,\mathrm{K}$, $\dot{m}_{oil} = 15\,\mathrm{g\,s^{-1}}$

(c) $T_{oil,in} = 340\,\mathrm{K}$, $\dot{m}_{oil} = 2\,\mathrm{g\,s^{-1}}$

(d) $T_{oil,in} = 340\,\mathrm{K}$, $\dot{m}_{oil} = 15\,\mathrm{g\,s^{-1}}$

(e) $T_{oil,in} = 370\,\mathrm{K}$, $\dot{m}_{oil} = 2\,\mathrm{g\,s^{-1}}$

(f) $T_{oil,in} = 370\,\mathrm{K}$, $\dot{m}_{oil} = 15\,\mathrm{g\,s^{-1}}$

Figure 6.46: Mechanical efficiency - oil temperature and mass flow rate effect. Second turbocharger.

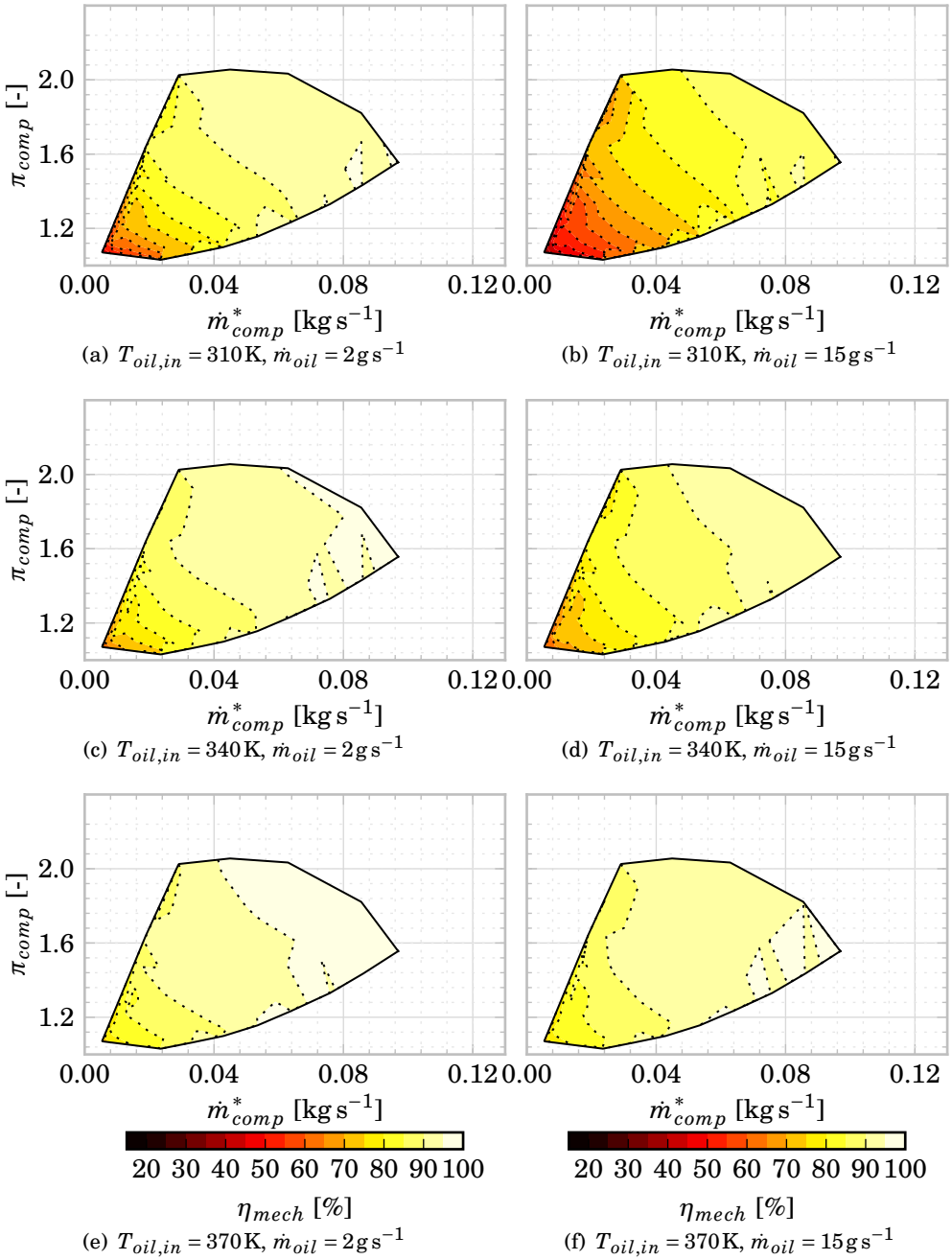

(a) $T_{oil,in} = 310\,\mathrm{K}$, $\dot{m}_{oil} = 2\,\mathrm{g\,s^{-1}}$

(b) $T_{oil,in} = 310\,\mathrm{K}$, $\dot{m}_{oil} = 15\,\mathrm{g\,s^{-1}}$

(c) $T_{oil,in} = 340\,\mathrm{K}$, $\dot{m}_{oil} = 2\,\mathrm{g\,s^{-1}}$

(d) $T_{oil,in} = 340\,\mathrm{K}$, $\dot{m}_{oil} = 15\,\mathrm{g\,s^{-1}}$

(e) $T_{oil,in} = 370\,\mathrm{K}$, $\dot{m}_{oil} = 2\,\mathrm{g\,s^{-1}}$

(f) $T_{oil,in} = 370\,\mathrm{K}$, $\dot{m}_{oil} = 15\,\mathrm{g\,s^{-1}}$

Figure 6.47: Mechanical efficiency - oil temperature and mass flow rate effect. Third turbocharger.

6.4 Summary

In this chapter, the models developed during the production of the present thesis have been calibrated and validated against experimental and CFD data, showing good agreement in their results.

For the quasi-bidimensional turbine model, a validation has been performed using CFD data and experimental data. Considering the CFD data, the model shows promising results while computing the characteristics of the flow across the volute. It presents better agreement with the CFD data than when using an equivalent one-dimensional duct model volute, with growing differences as the frequency of the boundary conditions rises.

Also, it has been demonstrated that a BEM model is able to compute the stator outlet flow angle with good precision even for transient pulsating flow applications only by imposing basic geometric information. This is specially important in order to compute the turbine behaviour at stator angles not represented in the turbine map: the angle does not need to be interpolated but can be directly computed. With more complex vane geometries it should be possible to get good results by rising the number of panels used to approximate the blades. The BEM model starts to fail with low expansion ratios due to the flow being too distant from homentropic conditions but behaves well at high Mach number. In order to improve the predictions with wide wakes and flow detachments while maintaining low computational costs, general correlations coupled with the current model should be developed.

The small hysteretic behaviour of the stator and the rotor is also approximated, although it has low influence in the global behaviour of the turbine at low and medium frequencies. At very high frequencies, however, it is expected that this hysteretic effects will grow.

A study of the influence of the numerical schemes used in the computations is presented for different excitation frequencies. The optimum selection of these numerical schemes for radial turbine simulation has been proposed.

Using experimental data, the proposed volute model has shown measurable improvements versus the equivalent one-dimensional duct volute in pressure and mass flow rate estimation at frequencies higher than 1000 Hz. The pressure evolution is also better reproduced with the proposed model, even at lower frequencies, as the phase of the waves is better simulated thanks to the gradual flow exit through the volute lateral window.

For the mechanical losses model, four parameters (one for the radial bearing and three for the axial bearing) have been adjusted by using quasi-adiabatic tests performed on three different turbochargers, showing the need of modelling the two bearings in order to get the best results:

- Journal bearing model gives good results without the need of an axial

bearing model at low pressure ratios, but fails as the axial load rises at higher turbocharger speeds.

- The axial bearing model by itself is not able to reproduce at all the experimental behaviour.

Simple trends have been obtained between fitting coefficients of the model and basic geometrical parameters of the turbocharger. Nevertheless, these simple trends must be confirmed with further experiments in a larger number of different turbocharger models.

Although typically high during highway driving conditions, mechanical efficiency of turbochargers becomes small during urban driving cycles, when oil temperature is relatively low. With current downsizing trends, turbines tend to work under high amplitude pulsating flow, rendering its power output and mechanical losses far from constant even at steady engine operation. Non-linear effects make even more difficult to properly achieve good results during 0d-1d simulations of engines, so it is important to take into account the instantaneous variation of both turbine power output and mechanical losses to get better results. The mechanical losses model presented in this thesis gives some insight about the instantaneous evolution of mechanical efficiency during pulsating flow conditions, showing that, at low to medium engine operating points, it can vary greatly during an engine cycle. When simulating highly variable turbocharger conditions the constant mechanical efficiency computations show weakness, underestimating the available power at the compressor side at high rotational speeds or overestimating it at low rotational speeds. If only very high turbine powers will be simulated, a constant mechanical efficiency should give accurate results.

A simple evaluation of the effects in the predicted dissipated power produced by different oil feeding mass flow rate and temperature has been performed, and the big effects that they have in the final results have been highlighted.

6.5 References

[3] J. Galindo, P. Fajardo, R. Navarro, and L. M. García-Cuevas. "Characterization of a radial turbocharger turbine in pulsating flow by means of CFD and its application to engine modeling". In: *Applied Energy* 103 (2013), pp. 116–127. ISSN: 0306-2619. DOI: 10.1016/j.apenergy.2012.09.013 (cit. on pp. vii, 17, 19, 21, 29, 117, 202).

[18] M. Á. Reyes-Belmonte. "Contribution to the Experimental Characterization and 1-D Modelling of Turbochargers for IC Engines". PhD thesis. Universitat Politècnica de València, Dec. 2013 (cit. on pp. 5, 24, 202).

[32] A. W. Costall, R. M. McDavid, R. F. Martínez-Botas, and N. C. Baines. "Pulse performance modelling of a twin-entry turbocharger turbine under full unequal admission". In: *Proceedings of ASME Turbo Expo 2009*. ASME, 2009. DOI: 10.1115/1.4000566 (cit. on pp. 17, 30, 31, 140, 202).

[93] M. Deligant, P. Podevin, and G. Descombes. "Experimental identification of turbocharger mechanical friction losses". English. In: *Energy* 39.1 (Mar. 2012), 388–394. ISSN: 0360-5442. DOI: 10.1016/j.energy.2011.12.049 (cit. on pp. 34, 81, 235).

[119] P. Welch. "The Use of Fast Fourier Transform for the Estimation of Power Spectra: A Method Based on Time Averaging Over Short, Modified Periodograms". In: *IEEE Transactions on Audio Electroacoustics* 15 (2 June 1967), pp. 70–73. ISSN: 0018-9278. DOI: 10.1109/TAU.1967.1161901 (cit. on pp. 91, 202, 211).

[120] F. Harris. "On the use of windows for harmonic analysis with the discrete Fourier transform". In: *Proceedings of the IEEE*. Vol. 66. IEEE, Jan. 1978, pp. 51–83. DOI: 10.1109/PROC.1978.10837 (cit. on pp. 91, 202, 211).

[129] B. Einfeld. "On Godunov-type methods for gas dynamics". In: *SIAM J. Numer. Anal.* 25.2 (Apr. 1988), pp. 294–318. ISSN: 0036-1429. URL: 10.1137/0725021 (cit. on p. 219).

[130] E. Toro, M. Spruce, and W. Speares. "Restoration of the contact surface in the HLL-Riemann solver". English. In: *Shock Waves* 4.1 (1994), pp. 25–34. ISSN: 0938-1287. DOI: 10.1007/BF01414629 (cit. on p. 219).

[131] A. Kurganov and E. Tadmor. "New High-Resolution Central Schemes for Nonlinear Conservation Laws and Convection-Diffusion Equations". In: *J. Comput. Phys* 160.1 (2000), pp. 241–282. DOI: 10.1006/jcph.2000.6459 (cit. on p. 219).

[132] M.-S. Liou and C. J. Steffen Jr. "A New Flux Splitting Scheme ". In: *Journal of Computational Physics* 107.1 (1993), pp. 23–39. ISSN: 0021-9991. DOI: 10.1006/jcph.1993.1122 (cit. on p. 219).

[133] D. Kraft and Deutsche Forschungs- Versuchsanstalt Luft- Raumfahrt und für und Köln. *A software package for sequential quadratic programming*. Forschungsbericht / Deutsche Forschungs- und Versuchsanstalt für Luft- und Raumfahrt. Dt. Forschungs- u. Versuchsanst. für Luft- u. Raumfahrt (DFVLR), 1988. URL: http://books.google.es/books?id=1Di-ZwEACAAJ (cit. on p. 225).

[134] E. Jones, T. Oliphant, P. Peterson, et al. *SciPy: Open source scientific tools for Python*. Last visited on 2014/10/30. 2001–. URL: http://www.scipy.org/ (cit. on p. 225).

[135] CMT - Motores Térmicos, Universitat Politècnica de València. *OpenWAM*. Last visited on 2014/10/30. URL: http://www.openwam.org/ (cit. on pp. 226, 248).

[136] F. Payri, J. R. Serrano, P. Fajardo, M. Á. Reyes-Belmonte, and R. Gozalbo-Belles. "A physically based methodology to extrapolate performance maps of radial turbines ". In: *Energy Conversion and Management* 55 (2012), pp. 149–163. ISSN: 0196-8904. DOI: 10.1016/j.enconman.2011.11.003 (cit. on p. 232).

CHAPTER 7

Conclusions and future works

Contents

7.1 Introduction

DURING the present work, a mechanical losses and a radial turbine model have been developed and tested, with the aim to be able to connect them to existing one-dimensional engine simulation codes.

In order to develop the models, the results from an extensive testing campaign have been used, as well as CFD results.

The developed models assume adiabatic conditions, and thus should be corrected using heat transfer models such as the ones described by Olmeda et al. [111]. The heat transfer results can be used straightforwardly with both the mechanical losses and the turbine models, and further refinements can be easily implemented in the turbine model using source terms in the finite-volumes code.

7.2 Main contributions

The main contributions of this thesis are the development and validation of a mechanical losses and a turbine model, the latter accounting for acoustic non-linear effects at up to 2000 Hz, improving the last developments made in this area by the respondent's research team.

The developed models use relatively easily measurable geometric data, as well as experimental data to fit their parameters. Although part of the experimental data is provided by turbocharger manufacturers in the form of turbine maps, other is only obtained after specific testing campaigns, such as the oil inlet temperature or mass flow rate. Nevertheless, once fitted, the models can be used coupled with a heat transfer model to compute the turbine performance and the power available at the compressor side regardless of the operating conditions, whether there are highly pulsating flow, different temperatures than in the maps characterisation or different oil flow characteristics are used. They are a powerful tool for today's engine development needs, as manufacturers are facing more stringent emission regulations and rising oil prices lead to more pressure for higher efficiencies. Highly downsized and efficiently turbocharged engines are an obvious way to achieve their objectives, which means higher levels of pulsation at the turbine inlet, so very good predictions of pulsating flow performance are needed. Also, as more work is needed to reduce fuel consumption and emissions during engine driving conditions, accurate mechanical losses estimation becomes a key feature for today's engine one-dimensional simulation codes.

The models developed for this thesis have been implemented in `OpenWAM` [135], an engine simulation code developed at CMT - Motores Térmicos, Universitat Politècnica de València, and they have been successfully used in real-world simulations in several research projects.

Quasi-bidimensional turbine model

The use of a bidimensional potential model to predict the stator outlet flow angle should reduce the amount of fitting parameters needed to model the turbine performance. It is not fully validated, however, as no experimental measurements of the flow angle have been performed and only one stator has been simulated in CFD.

The quasi-bidimensional volute has proven to be a robust method to improve current equivalent one-dimensional duct approaches at high frequencies with a very low penalty in computational costs. An experimental campaign was performed using cold pulsating flow in a turbocharger gas stand, using beamforming arrays to decompose the measured pressures into incident and reflected waves at the turbine inlet and into transmitted and second reflection waves at the turbine outlet. The classic volute model produced good predictions at up to 800 Hz or 1000 Hz, while the new model improved these results and obtained better predictions at up to 2000 Hz. Higher frequencies, however, are affected by flow phenomena that is neither simulated nor modelled, so it can't be properly reproduced without further developments of the model. It has also been tested against CFD data at different boundary condition frequencies. Good results were obtained with the classic volute at up to 130 Hz, although slightly worse than with a quasi-bidimensional volute; at 750 Hz and a very large amplitude, the differences between both models became more evident, with clearly better results for the quasi-bidimensional volute. The amplitude of the pulse was kept constant at 50 Hz, 90 Hz, 130 Hz and 750 Hz to get similar pressure ratio ranges in all the cases and, although is not a realistic amplitude for the latter case, it made the differences between both models more evident.

Mechanical losses model

A fast mechanical losses lumped model has been developed and tested for the present thesis. It models the power dissipated at both the journal and thrust bearings of small automotive turbochargers. The model computes the effects of both types of bearings as simple dimensional analysis using experimental data proved that the dissipated power can't be completely modelled considering only the journal bearing. Also, the use of a heat transfer model to correct for heat flow effects is needed when trying to use indirect mechanical losses measurements to fit and validate the model, with varying levels of importance depending on the characteristics of each turbocharger. The experimental data needed to calibrate the model are easily obtained during turbocharger characterisations, while the geometrical data can be measured after disassembling a turbocharger unit or by using manufacturer's data. No manufacturer's geometrical data were available during the redaction of this work, however, so the internal geometry was directly

measured.

Both sub-models are developed assuming harsh simplifications for the flow behaviour and using a very simple geometric idealisation, but have shown accurate predictions in a very broad range of operating conditions, failing just at very high oil temperatures, where metal-to-metal contact is produced and where turbochargers don't work in real-life applications. They are developed from first-principles, simplifying the Navier-Stokes equations until a simple algebraic relationship between some operational and geometric parameters, such as the shaft radius or its rotational speed, and the final power dissipated at each of the bearings is obtained. Although they assume adiabatic conditions, an easy method to couple them with a heat transfer model is presented and used during the validation phase. Also, both bearing submodels are coupled in two different cases, one where there is an independent oil inlet for each of the bearings and other where the flow first passes through the journal bearing and then enters the thrust bearing. The journal bearing model is valid for both semi-floating and floating ring bearings, without further modifications.

The model is fitted using a reduced random subset of 10 % of the steady-state experimental data, correcting it using a heat transfer model. The fit has proven to be robust, as almost the same results were obtained after several fitting processes, as well as after using the whole steady-state dataset. The use of extended maps, obtained using a closed-loop in the compressor side, has provided means to test a broad range of axial thrusts, necessary as its value during quasi-adiabatic tests is inherently different to that that is obtained during highway driving, which should be also different from the values typical of urban driving cycles. After fitting the model, it is used to compute the whole dataset, including some pulsating flow points resembling urban driving conditions. The majority of the computed points had less than 5 % error in turbocharger rotational speed prediction, while when using just a constant mechanical efficiency of 90 %, as it is commonly used, the errors ranged between 10 % and 30 %. Pulsating flow simulations computed instantaneous variations in mechanical efficiency between 60 % and 85 % during urban driving conditions, highlighting the importance of computing the dissipated power with the model instead of correlating the mechanical efficiency from steady-state data.

The model has been also used to test the effects of varying oil mass flow rates and inlet temperatures, and can be used with different oils just changing the density and viscosity correlations.

7.3 Limitations

Although the main objectives stated in chapter 1 have been accomplished, the models developed present some limitations that should be addressed.

First, no general correlations for the fitting parameters were obtained. These correlations should reduce the burden of model calibration, allowing to get good approximations of the turbocharger behaviour using less data than is currently used. Good correlations of the model parameters should be a function of the turbocharger geometry and the operating conditions, reducing the number of fitting constants to their minimum. Although the turbine map is easily obtained, no mechanical losses data is provided by turbocharger manufacturers, so nowadays they have to be measured for each unit, and they have to be disassembled as no internal blueprints are provided: a method to approximate the parameters as a function of some easily obtained data (i.e., the turbine and compressor wheel diameters or the maximum rotational speed) will allow the usage of the mechanical losses model even when no real turbocharger unit is available.

The mechanical losses model is not currently designed to predict metal-to-metal contact effects, so its predictions become more and more invalid as the lubrication film is broken by higher axial thrusts and lower oil viscosities. Very simple axial-only shaft motion is computed, so more cases of metal-to-metal contact are not accounted for without further modifications of the model, such as journal bearing metal contact.

The potential flow stator model can't reproduce the flow angle at very low expansion ratios, where the non-isentropic effects are of higher importance. A potential model will never be able to give full-range accurate predictions without coupling it with some correcting correlation. The turbine should only work at extremely low expansion ratios during limited amounts of time, however, what limits the scope of the problems associated to a potential flow model. The validation of this model is also limited, as only one stator at a single position has been simulated and no direct experimental measurements of the stator outlet flow angle were performed.

From the turbine rotor point-of-view, its losses sub-models are quite limited. The models have been introduced using CFD data that lacks some effects, such as tip clearance losses or backplate friction losses. Tip clearance losses CFD results are very valuable to assess the validity or even improve the tip clearance losses models found in the literature, and may be used as part of a multi-zone rotor model that computes flow recirculation. Backplate friction losses should not affect the total pressure loss at the rotor, so they should have no effects in the rotor mass flow rate results, but they reduce the turbine power output and can be seen as an extra source of mechanical losses.

7.4 Future works

Further research is needed in order to correlate the turbine meanline model parameters with operating conditions such as the Reynolds number and geometric data such as the number of blades or the channel lengths. In its current state, the parameters are adjusted using experimental data and a simple interpolation is done between VGT rack positions to get their new values. More CFD studies should be used to better understand their global tendencies, using different stator and rotor geometries. A database of several turbine maps characterised at a broad range of expansion ratios, rotational speeds and stator positions should be obtained under steady-state conditions. The rotor and stator discretisation should also consider different clearances. The bi-dimensional potential flow approach for computing the stator outlet flow angle should be validated at different rack positions and different stator geometries, which can be done not only using CFD simulations, but also using a special test rig using scaled up radial stators. A scaled up stator mock-up is currently being built by the respondent's research team, and the flow angle will be measured using miniature impact probes or even some laser anemometry technique might be applied.

The current turbine model can't reproduce some high frequency phenomena like blade-passing and turbulent flow noise. These effects can't be directly simulated using a simple meanline model coupled with a one-dimensional Euler solver, but may be taken into account using noise generation models. Flow noise may be modelled using random and broadband pressure source terms, with an amplitude correlated to the mass flow rate. Blade passing noise can be easily modelled as a pressure source term at the rotor inlet and outlet with main frequencies equal to the rotational frequency and the blade passing frequency, using an amplitude that can be correlated to the mass flow rate.

A simple meanline model of the compressor rotor should also be developed. CFD simulations made by Navarro [20] have shown very interesting results about flow recirculation inside the compressor rotor, and they can be used to develop a two-zone meanline model that considers flow recirculation evolution as a function of the rotational speed and pressure ratio.

The quasi-bidimensional volute model should be easily used within a compressor model. Using two rows of cells, one for the diffuser and other one for the volute duct, it may allow to improve the behaviour of the compressor model at high frequencies and may also ease the implementation of more complex compressor surge computations: during surge episodes, flow reversal may affect only part of the diffuser, leading to asymmetries that should be computable using this approach. This way, models such as the one by Tiseira Izaguirre [14] can be extended to compute partial flow detachment. It has to be tested also with twin-entry and waste-gate turbines: the twin-entry case should be easily computed connecting the stator nozzles to both volutes, and the waste-gate

turbine case can be computed using a source term connecting part of the volute cells to the turbine outlet duct, maybe using a nozzle-like approach as in the turbine stator.

The mechanical losses model presents a basic computation of axial shaft motion that might be coupled with rotor clearance losses models, leading to more accurate performance predictions. The kind of information needed to develop such a model is obtainable by means of CFD, and the results can be tested against experimental data in a standard gas stand by pressurising the compressor air loop and, thus, modifying the axial thrust. Non-invasive experimental optical techniques such as the ones described in the work by Pastor et al. [137], with small modifications, can be used to obtain the physical displacement of the shaft with little modifications of the turbocharger unit. Further developments should also consider possible metal-to-metal contact, not only to more realistically compute the mechanical power dissipation under extreme axial thrust or oil temperature, but also as a means to predict possible physical damage in the bearings. A larger experimental database will be needed to get general correlations for the fitting parameters of the model.

7.5 References

[14] A. O. Tiseira Izaguirre. “Caracterización experimental y modelado de bombeo en compresores centrífugos de sobrealimentación”. PhD thesis. Universitat Politècnica de València, 2008 (cit. on pp. 5, 18, 252).

[20] R. Navarro. “A numerical approach for predicting flow-induced acoustics at near-stall conditions in an automotive turbocharger compressor”. PhD thesis. Universitat Politècnica de València, 2014 (cit. on pp. 5, 21, 252).

[111] P. Olmeda, V. Dolz, F. J. Arnau, and M. Á. Reyes-Belmonte. “Determination of heat flows inside turbochargers by means of a one dimensional lumped model”. In: *Mathematical and Computer Modelling* 57.7–8 (2013), pp. 1847–1852. ISSN: 0895-7177. DOI: 10.1016/j.mcm.2011.11.078 (cit. on pp. 41, 71, 105, 248).

[135] CMT - Motores Térmicos, Universitat Politècnica de València. *OpenWAM*. Last visited on 2014/10/30. URL: http://www.openwam.org/ (cit. on pp. 226, 248).

[137] J. V. Pastor, J. R. Serrano, V. Dolz, M. A. López, and F. Bouffaud. “Study of a turbocharger shaft motion by means of non-invasive optical techniques: Application to the behaviour analysis in turbocharger lubrication failures”. In: *Mechanical Systems and Signal Processing* 32 (2012), pp. 292–305. DOI: 10.1016/j.ymssp.2012.04.020 (cit. on p. 253).

Bibliography

[30] **Abidat, M., Hachemi, M., Hamidou, M. K., and Baines, N.**
"Prediction of the steady and non-steady flow performance of a highly loaded mixed flow turbine"
in: *Proceedings of the Institution of Mechanical Engineers*. Vol. 212 1998, pp. 173–184. DOI: 10.1243/0957650981536844 (cit. on pp. 17, 30)

[29] **Aymanns, R., Scharf, J., Uhlmann, T., and Lückmann, D.**
"A revision of Quasi Steady Modelling of Turbocharger Turbines in the Simulation of Pulse Charged Engines"
in: *16th Supercharging Conference* 2011 (cit. on pp. 17, 19)

[79] **Baines, N., Halijouy-Benisi, A., and Yeo, J. H.**
"The pulse flow performance and modelling of radial inflow turbines"
in: *Proceedings of the Institution of Mechanical Engineers, 5th International Conference on Turbocharging and Turbochargers* 1994, pp. 209–220 (cit. on p. 29)

[109] **Baines, N., Wygant, K. D., and Dris, A.**
"The Analysis of Heat Transfer in Automotive Turbochargers"
English. In: *Journal of Engineering for Gas Turbineas and Power - Transactions of the ASME* 132.4 (Apr. 2010). ISSN: 0742-4795. DOI: 10.1115/1.3204586 (cit. on pp. 40, 68)

[114] **Baroudi, D. and Thibert, E.**
"An instrumented structure to measure avalanche impact pressure: Error analysis from Monte Carlo simulations"
in: *Cold Regions Science and Technology* 59.2-3 (2009). International Snow Science Workshop (ISSW) 2008, pp. 242–250. ISSN: 0165-232X. DOI: 10.1016/j.coldregions.2009.05.010 (cit. on p. 66)

[87] **Bellis, V. D., Marelli, S., Bozza, F., and Capobianco, M.**
"1D Simulation and Experimental Analysis of a Turbocharger Turbine for Automotive Engines Under Steady and Unsteady Flow Conditions"
in: *Energy Procedia* 45 (2014). {ATI} 2013 - 68th Conference of the Italian

Thermal Machines Engineering Association, pp. 909–918. ISSN: 1876-6102. DOI: 10.1016/j.egypro.2014.01.096 (cit. on pp. 31, 151)

[74] **Benner, M., Sjolander, S., and Moustapha, S.**
"An empirical prediction method for secondary losses in turbines - Part I: A new loss breakdown scheme and penetration depth correlation"
in: *Journal of Turbomachinery* 128.2 (2006). cited By (since 1996)23, pp. 273–280. ISSN: 0889504X. DOI: 10.1115/1.2162593
(cit. on p. 28)

[75] **Benner, M., Sjolander, S., and Moustapha, S.**
"An empirical prediction method for secondary losses in turbines - Part II: A new secondary loss correlation"
in: *Journal of Turbomachinery* 128.2 (2006). cited By (since 1996)25, pp. 281–291. ISSN: 0889504X. DOI: 10.1115/1.2162594
(cit. on p. 28)

[99] **Bouard, L., Fillon, M., and Frêne, J.**
"Comparison between three turbulent models — application to thermo-hydrodynamic performances of tilting-pad journal bearings"
in: *Tribology International* 29.1 (1996). {AUSTRIB} '94, pp. 11–18. ISSN: 0301-679X. DOI: 10.1016/0301-679X(95)00028-3 (cit. on p. 37)

[53] **Broatch, A., Galindo Lucas, J., Navarro, R., and García-Tíscar, J.**
"Numerical and experimental analysis of automotive turbocharger compressor aeroacoustics at different operating conditions"
in: *International Journal of Heat and Fluid Flow* (2014) (cit. on p. 21)

[64] **Canova, M.**
"Development and validation of a control-oriented library for the simulation of automotive engines"
in: *International Journal of Engine Research* 5.3 (2004), pp. 219–228. ISSN: 1468-0874. DOI: 10.1243/1468087041549625 (cit. on p. 24)

[65] **Canova, M., Midlam-Mohler, S., Guezennec, Y., and Rizzoni, G.**
"Mean value modeling and analysis of HCCI diesel engines with external mixture formation"
in: *Journal of Dynamic Systems, Measurement and Control* 131.1 (2008). DOI: 10.1115/1.2977465 (cit. on p. 24)

[116] **Casey, M. V. and Schlegel, M.**
"Estimation of the performance of turbocharger compressors at extremely low pressure ratios"
English. In: *Proceedings of the Institution of Mechanical Engineers Part A - Journal of Power and Energy* 224.A2 (2010), 239–250. ISSN: 0957-6509. DOI: {10.1243/09576509JPE810} (cit. on p. 69)

[13] **Cervelló, C.**
"Contribución a la caracterización experimental y al modelado de turbinas de geometría variable en grupos de sobrealimentación"
PhD thesis. Universitat Politècnica de València 2005 (cit. on p. 5)

[83] **Chen, H. and Winterbone, D.**
"A method to predict performance of vaneless radial turbine under steady and unsteady flow conditions"
in: *Turbocharging and Turbochargers*. Institution of Mechanical Engineers 1990, pp. 13–22 (cit. on pp. 29–31)

[89] **Chen, W. J.**
"Rotordynamics and bearing design of turbochargers"
English. In: *Mechanical Systems and Signal Processing* 29.SI (May 2012), pp. 77–89. ISSN: 0888-3270. DOI: 10.1016/j.ymssp.2011.07.025 (cit. on p. 32)

[68] **Chiong, M. S., Rajoo, S., Romagnoli, A., and Martínez-Botas, R. F.**
"Single Entry Mixed Flow Turbine Performance Prediction With 1-D Gas Dynamic Code Coupled With Mean Line Model"
in: *International Journal of Gas Turbine, Propulsion and Power Systems* 4.2 (June 2012), pp. 8–16. ISSN: 1882-5079 (cit. on pp. 26, 31)

[84] **Chiong, M. S., Rajoo, S., Romagnoli, A., and Martínez-Botas, R.**
"Unsteady performance prediction of a single entry mixed flow turbine using 1-D gas dynamic code extended with meanline model"
in: *Proceedings of the ASME Turbo Expo*. Vol. 5. ASME 2012, pp. 781–795. DOI: 10.1115/GT2012-69176 (cit. on p. 30)

[34] **Chiong, M., Rajoo, S., Romagnoli, A., Costall, A., and Martinez-Botas, R.**
"Integration of meanline and one-dimensional methods for prediction of pulsating performance of a turbocharger turbine"
in: *Energy Conversion and Management* 81 (2014), pp. 270–281. ISSN: 0196-8904. DOI: 10.1016/j.enconman.2014.01.043 (cit. on pp. 17, 27, 31, 140)

[135] **CMT - Motores Térmicos, Universitat Politècnica de València**
OpenWAM
Last visited on 2014/10/30. URL: http://www.openwam.org/ (cit. on pp. 226, 248)

[32] **Costall, A. W., McDavid, R. M., Martínez-Botas, R. F., and Baines, N. C.**
"Pulse performance modelling of a twin-entry turbocharger turbine under full unequal admission"

in: *Proceedings of ASME Turbo Expo 2009*. ASME 2009. DOI: 10.1115/1.4000566 (cit. on pp. 17, 30, 31, 140, 202)

[122] **Courant, R., Friedrichs, K., and Lewy, H.**
"Über die partiellen Differenzengleichungen der mathematischen Physik"
in: *Mathematische Annalen* 100.1 (Dec. 1, 1928), pp. 32–74. ISSN: 0025-5831. DOI: 10.1007/bf01448839 (cit. on p. 135)

[133] **D. Kraft and Deutsche Forschungs- Versuchsanstalt Luft- Raumfahrt und für und Köln**
A software package for sequential quadratic programming
Forschungsbericht / Deutsche Forschungs- und Versuchsanstalt für Luft- und Raumfahrt. Dt. Forschungs- u. Versuchsanst. für Luft- u. Raumfahrt (DFVLR) 1988. URL: http://books.google.es/books?id=1Di-ZwEACAAJ (cit. on p. 225)

[73] **Dahlquist, A. N.**
Investigation of Losses Prediction Methods in 1D for Axial Gas Turbines
2008 (cit. on p. 28)

[93] **Deligant, M., Podevin, P., and Descombes, G.**
"Experimental identification of turbocharger mechanical friction losses"
English. In: *Energy* 39.1 (Mar. 2012), 388–394. ISSN: 0360-5442. DOI: 10.1016/j.energy.2011.12.049 (cit. on pp. 34, 81, 235)

[98] **Deligant, M., Podevin, P., and Descombes, G.**
"{CFD} model for turbocharger journal bearing performances"
in: *Applied Thermal Engineering* 31.5 (2011). {MNF} 2009 Special Issue, pp. 811–819. ISSN: 1359-4311. DOI: 10.1016/j.applthermaleng.2010.10.030 (cit. on pp. 37, 157, 164)

[92] **Deligant, M., Podevin, P., Descombes, G., Lamquin, T., Vidal, F., and Marchal, A.**
"Effect of axial load on turbocharger friction losses"
in: *Proceedings of the 13th EAEC European Congress*. Valencia, Spain 2011 (cit. on p. 34)

[105] **Deligant, M., Podevin, P., Vidal, F., Tyminski, W., Guilain, S., and Lahjaily, H.**
"3D thermal steady-state CFD analysis of power friction losses in a turbocharger's journal bearing and comparison with finite difference method and experimentation"
in: *12th European Automotive Congress: EAEC 2009, Bratislava* 2009 (cit. on p. 40)

[90] **Deligant, M., Podevin, P., Descombes, G., Thierry, L., Fabrice, V., and Marche, A.**
"Experimental Study of Turbocharger's Performances at Low Speeds"
English. In: *Proceedings of the ASME Internal Combustion Engine Division Fall Technical Conference*. ASME, Internal Combust Engine Div. Three Park Avenue, New York, NY 10016-5990 USA: AMER SOC MECHANICAL ENGINEERS 2010, 911–918. ISBN: 978-0-7918-4944-6. DOI: 10.1115/ICEF2010-35071 (cit. on p. 33)

[88] **Diango, A., Perilhon, C., Descombes, G., and Danho, E.**
"Application of exergy balances for the optimization of non-adiabatic small turbomachines operation"
English. In: *Energy* 36.5 (May 2011), 2924–2936. ISSN: 0360-5442. DOI: 10.1016/j.energy.2011.02.035 (cit. on p. 32)

[129] **Einfeld, B.**
"On Godunov-type methods for gas dynamics"
in: *SIAM J. Numer. Anal.* 25.2 (Apr. 1988), pp. 294–318. ISSN: 0036-1429. URL: 10.1137/0725021 (cit. on p. 219)

[57] **Eriksson, L.**
"Modeling and Control of Turbocharged SI and DI Engines"
in: *Oil & Gas Science and Technology - Rev. IFP* 62.4 (2007), pp. 523–538. DOI: 10.2516/ogst:2007042 (cit. on p. 22)

[56] **Eriksson, L., Nielsen, L., Brugård, J., Bergström, J., Pettersson, F., and Andersson, P.**
"Modeling of a turbocharged {SI} engine"
in: *Annual Reviews in Control* 26.1 (2002), pp. 129–137. ISSN: 1367-5788. DOI: 10.1016/S1367-5788(02)80022-0 (cit. on p. 21)

[9] **European Parliament, Council of the European Union**
"Regulation (EC) No 715/2007 of the European Parliament and of the Council of 20 June 2007 on type approval of motor vehicles with respect to emissions from light passenger and commercial vehicles (Euro 5 and Euro 6) and on access to vehicle repair and maintenance information (Text with EEA relevance) "
in: *Official Journal of the European Union* 50 (June 2007), pp. 1–16. ISSN: 1725-2555. URL: http://eur-lex.europa.eu/legal-content/EN/TXT/?uri=OJ:L:2007:171:TOC (cit. on pp. 3, 15, 73)

[10] **European Parliament, Council of the European Union**
"Regulation (EC) No 595/2009 of the European Parliament and of the Council of 18 June 2009 on type-approval of motor vehicles and engines with respect to emissions from heavy duty vehicles (Euro VI) and on access to vehicle repair and maintenance information and amending

Regulation (EC) No 715/2007 and Directive 2007/46/EC and repealing Directives 80/1269/EEC, 2005/55/EC and 2005/78/EC (Text with EEA relevance) ”
in: *Official Journal of the European Union* 52 (July 2009), pp. 1–13. DOI: 10.3000/17252555.L_2009.188.eng (cit. on pp. 3, 15, 73)

[8] **European Parliament, Council of the European Union**
“Regulation (EU) No 510/2011 of the European Parliament and of the Council of 11 May 2011 setting emission performance standards for new light commercial vehicles as part of the Union’s integrated approach to reduce CO 2 emissions from light-duty vehicles (Text with EEA relevance)”
in: *Official Journal of the European Union* 54 (May 2011), pp. 1–15. DOI: 10.3000/17252555.L_2011.145.eng (cit. on p. 3)

[113] *Evaluation of measurement data – Guide to the expression of uncertainty in measurement*
100:2008. JCGM Sept. 2008. URL: http://www.bipm.org/utils/common/documents/jcgm/JCGM_100_2008_E.pdf (cit. on p. 66)

[17] **Fajardo Peña, P.**
“Methodology for the Numerical Characterization of a Radial Turbine under Steady and Pulsating Flow”
PhD thesis. Universitat Politècnica de València July 2012
(cit. on pp. 5, 114, 117)

[54] **Fang, X., Dai, Q., Yin, Y., and Xu, Y.**
“A compact and accurate empirical model for turbine mass flow characteristics”
in: *Energy* 35.12 (2010), pp. 4819–4823. ISSN: 0360-5442. DOI: 10.1016/j.energy.2010.09.006 (cit. on pp. 21, 22)

[55] **Fang, X. and Xu, Y.**
“Development of an empirical model of turbine efficiency using the Taylor expansion and regression analysis”
English. In: *Energy* 36.5 (May 2011), 2937–2942. ISSN: 0360-5442. DOI: 10.1016/j.energy.2011.02.036 (cit. on pp. 21, 22)

[69] **Futral, S., Wasserbauer, C., Aeronautics, U. S. N., and Administration, S.**
Off-design performance prediction with experimental verification for a radial-inflow turbine: Samuel M.Futral Jr. and Charles A. Wasserbauer
tech. rep. NASA TN D-2621. NASA 1965. URL: http://books.google.es/books?id=N1kzLAHfK-IC (cit. on pp. 26, 119, 153)

[4] **Galindo Lucas, J., Tiseira Izaguirre, A., Fajardo Peña, P., and García-Cuevas, L. M.**
"Development and validation of a radial variable geometry turbine model for transient pulsating flow applications"
in: *Energy Conversion and Management* 85 (2014), pp. 190–203. ISSN: 0196-8904. DOI: 10.1016/j.enconman.2014.05.072 (cit. on p. vii)

[5] **Galindo, J., Climent, H., Tiseira, A., and García-Cuevas, L. M.**
"Effect of the numerical scheme resolution on quasi-2D simulation of an automotive radial turbine under highly pulsating flow"
in: *Journal of Computational and Applied Mathematics* ()
(cit. on p. vii)

[3] **Galindo, J., Fajardo, P., Navarro, R., and García-Cuevas, L. M.**
"Characterization of a radial turbocharger turbine in pulsating flow by means of CFD and its application to engine modeling"
in: *Applied Energy* 103 (2013), pp. 116–127. ISSN: 0306-2619. DOI: 10.1016/j.apenergy.2012.09.013
(cit. on pp. vii, 17, 19, 21, 29, 117, 202)

[47] **Galindo, J., Hoyas, S., Fajardo, P., and Navarro, R.**
"Set-up analysis and optimization of CFD simulations for radial turbines"
in: *Engineering Applications of Computational Fluid Mechanics* 7.4 (2013), pp. 441–460 (cit. on pp. 20, 114)

[95] **Gjika, K. and Larue, G. D.**
"Axial Load Control on High-Speed Turbochargers: Test and Prediction"
in: *Proceedings of the ASME Turbo Expo 2008: Power for Land, Sea and Air*. Berlin, Germany June 2008, pp. 705–712. ISBN: 978-0-7918-4311-6. DOI: 10.1115/GT2008-50756 (cit. on p. 34)

[121] **Godunov, S. K.**
"A Difference Scheme for Numerical Solution of Discontinuous Solution of Hydrodynamic Equations"
in: *Matematicheskii Sbornik* 47 (1959), pp. 271–306 (cit. on p. 134)

[124] **Guennebaud, G., Jacob, B., et al.**
Eigen v3
Last visited on 2014/10/30 2010. URL: http://eigen.tuxfamily.org/
(cit. on p. 137)

[120] **Harris, F.**
"On the use of windows for harmonic analysis with the discrete Fourier transform"
in: *Proceedings of the IEEE*. Vol. 66. IEEE Jan. 1978, pp. 51–83. DOI: 10.1109/PROC.1978.10837 (cit. on pp. 91, 202, 211)

[46] **Hellström, F.**
"Numerical computations of the unsteady flow in turbochargers"
PhD thesis. Royal Institute of Technology KTH Mechanics 2010
(cit. on p. 20)

[45] **Hillewaert, K. and Van den Braembussche, R.**
"Numerical simulation of impeller-volute interaction in centrifugal compressors"
in: *Journal of Turbomachinery* 121 (1999), pp. 603–608. DOI: 10.1115/1.2841358 (cit. on p. 20)

[103] **Hu, L., Yang, C., Sun, H., Krivizky, E., Larosiliere, L., Zhang, J., and Lai, M.**
Experimental and Computational Analysis of Impact of Self Recirculation Casing Treatment on Turbocharger Compressor
tech. rep. 2001-01-0272. SAE International 2010. DOI: 10.4271/2010-01-1224 (cit. on pp. 38, 39)

[85] **Hu, X.**
"An advanced turbocharger model for the internal combustion engine"
PhD thesis. Purdue University 2000 (cit. on p. 30)

[126] **Huang, A.**
Loss Mechanisms in Turbine Tip Clearance Flows
Master dissertation 2011 (cit. on p. 154)

[101] **Huiping, L., Hua, X., Peter, J. E., and Zhongmin, J.**
"Application of computational fluid dynamics and fluid-structure interaction method to the lubrication study of a rotor-bearing system"
in: *Tribology Letters* 28 (2010), pp. 325–336. DOI: 10.1007/s11249-010-9612-6 (cit. on p. 37)

[25] **Iwasaki, M., Ikeya, N., Marutani, Y., and Kitazawa, T.**
Comparison of Turbocharger Performance Between Steady Flow and Pulsating Flow on Engines
tech. rep. 940839. SAE International 1994. DOI: 10.4271/940839 (cit. on p. 17)

[67] **Japikse, D. and Baines, N. C.**
Introduction to turbomachinery
Concepts ETI 1997. ISBN: 978-0933283107 (cit. on p. 26)

[63] **Jensen, J., Kristensen, A., Sorenson, S., Houbak, N., and Hendricks, E.**
Mean value modeling of a small turbocharged diesel engine
tech. rep. 910070. SAE International 1991. DOI: 10.4271/910070 (cit. on p. 23)

[134] **Jones, E., Oliphant, T., Peterson, P., et al.**
SciPy: Open source scientific tools for Python
Last visited on 2014/10/30 2001–. URL: http://www.scipy.org/
(cit. on p. 225)

[76] **Katz, J. and Plotkin, A.**
Low-Speed Aerodynamics
2nd. Cambridge University Press 2001. ISBN: 978-0521665520
(cit. on pp. 28, 145)

[86] **King, A.**
"A turbocharger unsteady performance model for the GT-Power internal combustion engine simulation"
PhD thesis. Purdue University 2002 (cit. on p. 30)

[131] **Kurganov, A. and Tadmor, E.**
"New High-Resolution Central Schemes for Nonlinear Conservation Laws and Convection-Diffusion Equations"
in: *J. Comput. Phys* 160.1 (2000), pp. 241–282. DOI: 10.1006/jcph.2000.6459 (cit. on p. 219)

[28] **Lam, J., Roberts, Q., and McDonell, G.**
"Flow modelling of a turbocharger turbine under pulsating flow"
in: *Seventh International Conference Turbochargers and Turbocharging* 2002 (cit. on pp. 17, 19)

[15] **Lang, R.**
"Contribución a la mejora del margen de bombeo en compresores centrífugos de sobrealimentación"
PhD thesis. Universitat Politècnica de València 2011 (cit. on p. 5)

[81] **Larsson, S. and Thomée, V.**
Partial Differential Equations with Numerical Methods
vol. 45. Texts in Applied Mathematics. Springer 2003. ISBN: 10.1007/978-3-540-88706-5. DOI: 10.1007/978-3-540-88706-5 (cit. on p. 29)

[123] **Leer, B. van**
"Towards the ultimate conservative difference scheme, V. A second order sequel to Godunov's method"
in: *Journal of Computational Physics* 32 (1979), pp. 101–136
(cit. on p. 135)

[82] **LeVeque, R. J.**
Finite Volume Methods for Hyperbolic Problems
Cambridge Texts in Applied Mathematics. Cambridge University Press 2002. ISBN: ISBN 0-521-81087-6. (Cit. on p. 29)

[102] **Lihua, L., Hao, S., Yingchun, L., and Qiang, Z.**
"Research on Static Stiffness of Hydrostatic Bearing using Fluid-Structure Interaction Analysis"
in: *Procedia Engineering* 29 (2012). 2012 International Workshop on Information and Electronics Engineering, pp. 1304–1308. ISSN: 1877-7058. DOI: 10.1016/j.proeng.2012.01.131 (cit. on p. 38)

[132] **Liou, M.-S. and Steffen Jr., C. J.**
"A New Flux Splitting Scheme "
in: *Journal of Computational Physics* 107.1 (1993), pp. 23–39. ISSN: 0021-9991. DOI: 10.1006/jcph.1993.1122 (cit. on p. 219)

[44] **Liu, Z. and Hill, D.**
"Issues surrounding multiple frames of reference models for turbo compressor applications"
in: *Fifteenth International Compressor Engineering Conference*. Purdue University 2000 (cit. on p. 19)

[19] **López Hidalgo, M. A.**
"Estudio teórico-experimental de la dinámica rotacional de un turbocompresor de MCIA. Aplicación al diagnóstico de fallos"
PhD thesis. Universitat Politècnica de València 2014 (cit. on p. 5)

[35] **Luján, J. M., Bermúdez, V., Serrano, J. R., and Cervelló, C.**
Test Bench for Turbocharger Groups Characterization
SAE Technical Paper 2002-01-0163. SAE International Mar. 2002. DOI: 10.4271/2002-01-0163 (cit. on p. 18)

[26] **Luján, J. M., Galindo Lucas, J., and Serrano, J. R.**
Efficiency Characterization of Centripetal Turbines under Pulsating Flow Conditions
tech. rep. 2001-01-0272. SAE International 2001. DOI: 10.4271/2001-01-0272 (cit. on pp. 17, 29)

[100] **Maneshian, B. and Gandjalikhan Nassab, S.**
"Thermohydrodynamic Characteristics of Journal Bearings Running Under Turbulent Condition"
in: *IJE Transactions A: Basics* 22 (2009), pp. 181–194 (cit. on p. 37)

[115] **Marelli, S. and Capobianco, M.**
"Steady and pulsating flow efficiency of a waste-gated turbocharger radial flow turbine for automotive application"
in: *Energy* 36.1 (2011), pp. 459–465. ISSN: 0360-5442. DOI: 10.1016/j.energy.2010.10.019 (cit. on pp. 68, 117)

[72] **Meitner, P. L. and Glassman, A. J.**
Computer code for off-design performance analysis of radial-inflow turbines with rotor blade sweep
tech. rep. 2199. NASA 1983 (cit. on p. 27)

[52] **Mendonça, F., Baris, O., and Capon, G.**
"Simulation of Radial Compressor Aeroacoustics using CFD"
in: *Proceedings of ASME Turbo Expo* 2012, pp. 1823–1832. DOI: 10.1115/GT2012-70028 (cit. on p. 21)

[49] **Menter, F. R.**
"Two-equation eddy-viscosity turbulence models for engineering applications"
in: *AIAA journal* 32.8 (1994), pp. 1598–1605. DOI: 10.2514/3.12149 (cit. on p. 20)

[50] **Menter, F. R., Kuntz, M., and Langtry, R.**
"Ten years of industrial experience with the SST turbulence model"
in: *Turbulence, heat and mass transfer* 4 (2003), pp. 625–632 (cit. on p. 20)

[51] **Menter, F. R., Langtry, R., and Hansen, T.**
"CFD simulation of turbomachinery flows - verification, validation and modelling"
in: *European Congress on Computational Methods in Applied Sciences and Engineering* 2004 (cit. on p. 20)

[70] **Mizumachi, N., Yoshiki, D., and Endoh, T. A.**
"A study on performance of radial turbine under unsteady flow conditions"
in: *Report of the Institute of Industrial Science* 28 (1979), pp. 122–130 (cit. on p. 27)

[36] **Naundorf, D., Bolz, H., and Mandel, M.**
Design and Implementation of a New Generation of Turbo Charger Test Benches Using Hot Gas Technology
tech. rep. 2001-01-0279. SAE International 2001. DOI: 10.4271/2001-01-0279 (cit. on p. 18)

[20] **Navarro, R.**
"A numerical approach for predicting flow-induced acoustics at near-stall conditions in an automotive turbocharger compressor"
PhD thesis. Universitat Politècnica de València 2014 (cit. on pp. 5, 21, 252)

[112] **Olmeda, P., Dolz, V., Arnau, F., and Reyes-Belmonte, M.**
"Determination of heat flows inside turbochargers by means of a one dimensional lumped model"
in: *Mathematical and Computer Modelling* 57 (2013), pp. 1847–1852. ISSN: 0895-7177. DOI: 10.1016/j.mcm.2011.11.078

[111] **Olmeda, P., Dolz, V., Arnau, F. J., and Reyes-Belmonte, M. Á.**
"Determination of heat flows inside turbochargers by means of a one dimensional lumped model"
in: *Mathematical and Computer Modelling* 57.7–8 (2013), pp. 1847–1852. ISSN: 0895-7177. DOI: 10.1016/j.mcm.2011.11.078
(cit. on pp. 41, 71, 105, 248)

[7] **Olmeda, P., Tiseira, A., Dolz, V., and García-Cuevas, L. M.**
"Uncertainties in power computations in a turbocharger test bench"
in: *Measurement* 59 (2015), pp. 363–371. ISSN: 0263-2241. DOI: 10.1016/j.measurement.2014.09.055 (cit. on p. viii)

[59] **Orkisz, M. and Stawarz, S.**
"Modeling of turbine engine axial-flow compressor and turbine characteristics"
in: *Journal of Propulsion and Power* 16 (2000), pp. 336–339. ISSN: 0748-4658. DOI: 10.2514/2.5574 (cit. on p. 22)

[43] **Palfreyman, D. and Martinez-Botas, R.**
"The pulsating flow field in a mixed flow turbocharger turbine: An experimental and computational study"
in: *Journal of turbomachinery* 127 (1 2005), pp. 144–155. DOI: 10.1115/1.1812322 (cit. on p. 19)

[137] **Pastor, J. V., Serrano, J. R., Dolz, V., López, M. A., and Bouffaud, F.**
"Study of a turbocharger shaft motion by means of non-invasive optical techniques: Application to the behaviour analysis in turbocharger lubrication failures"
in: *Mechanical Systems and Signal Processing* 32 (2012), pp. 292–305. DOI: 10.1016/j.ymssp.2012.04.020 (cit. on p. 253)

[11] **Payri, F.**
"Predicción de las actuaciones de los grupos de sobrealimentación para motores diesel de automoción"
PhD thesis. Universidad Politécnica de Madrid 1973 (cit. on p. 5)

[77] **Payri, F., Benajes, J., Galindo, J., and Serrano, J. R.**
"Modelling of turbocharged diesel engines in transient operation. Part 2: Wave action models for calculating the transient operation in a high

speed direct injection engine"
in: *Proceedings of the Institution of Mechanical Engineers, Part D: Journal of Automobile Engineering* 216.6 (2002), pp. 479–493. DOI: 10.1243/09544070260137507 (cit. on p. 29)

[61] **Payri, F., Benajes, J., Jullien, J., and Duan, Q.**
"Non-steady flow behaviour of a supercharger turbine"
in: *Proceedings of the Third EAEC International Conference*. Strasssbourg 1991 (cit. on p. 23)

[62] **Payri, F., Benajes, J., and Reyes, M.**
"Modelling of supercharger turbines in internal-combustion engines"
in: *Journal of Mechanical Science* 38 (8-9 1996), pp. 835–869. DOI: 10.1016/0020-7403(95)00105-0 (cit. on pp. 23, 29)

[110] **Payri, F., Olmeda, P., Arnau, F. J., Dombovsky, A., and Smith, L.**
"External heat losses in small turbochargers: Model and experiments"
in: *Energy* 71 (2014), pp. 534–546. DOI: 10.1016/j.energy.2014.04.096 (cit. on p. 41)

[136] **Payri, F., Serrano, J. R., Fajardo, P., Reyes-Belmonte, M. Á., and Gozalbo-Belles, R.**
"A physically based methodology to extrapolate performance maps of radial turbines "
in: *Energy Conversion and Management* 55 (2012), pp. 149–163. ISSN: 0196-8904. DOI: 10.1016/j.enconman.2011.11.003 (cit. on p. 232)

[38] **Payri, F., Serrano, J. R., Olmeda, P., Páez, A., and Vidal, F.**
"Experimental Methodology to Characterize Mechanical Losses in Small Turbochargers"
English. In: *Proceedings of the ASME Turbo Expo 2010*. Vol. 2010. 44007. Int Gas Turbine Inst. Glasgow, Scotland: ASME June 2010, pp. 413–423. ISBN: 978-0-7918-4400-7. DOI: 10.1115/GT2010-22815 (cit. on pp. 18, 36, 38, 71)

[39] **Piñero, G., Vergara, L., Desantes, J. M., and Broatch, A.**
"Estimation of velocity fluctuation in internal combustion engine exhaust systems through beamforming techniques"
in: *Measurement Science and Technology* 11.11 (2000), p. 1585. DOI: 10.1088/0957-0233/11/11/307 (cit. on pp. 18, 89)

[108] **Podevin, P., Toussaint, M., Richarg, G., and Farinole, G.**
"Performances of turbocharger at low speed"
in: *Proceedings of the SYMKOM02 congress*. Lodz, Pologne 2002 (cit. on p. 40)

[91] **Podevin, P., Clenci, A., and Descombes, G.**
"Influence of the lubricating oil pressure and temperature on the performance at low speeds of a centrifugal compressor for an automotive engine"
English. In: *Applied Thermal Engineering* 31.2-3 (Feb. 2011), pp. 194–201. ISSN: 1359-4311. DOI: 10.1016/j.applthermaleng.2010.08.033 (cit. on p. 33)

[127] **Rajoo, S., Romagnoli, A., and Martinez-Botas, R. F.**
"Unsteady performance analysis of a twin-entry variable geometry turbocharger turbine"
in: *Energy* 38.1 (2012), pp. 176–189. ISSN: 0360-5442. DOI: 10.1016/j.energy.2011.12.017 (cit. on p. 163)

[37] **Reuter, S., Koch, A., and Kaufmann, A.**
"Extension of performance maps of radial turbocharger turbines using pulsating hot gas flow"
in: *9th International Conference on Turbochargers and Turbocharging*. IMechE 2010 (cit. on p. 18)

[18] **Reyes-Belmonte, M. Á.**
"Contribution to the Experimental Characterization and 1-D Modelling of Turbochargers for IC Engines"
PhD thesis. Universitat Politècnica de València Dec. 2013 (cit. on pp. 5, 24, 202)

[104] **Reynolds, O.**
"On the Theory of Lubrication and Its Application to Mr. Beauchamp Tower's Experiments, Including an Experimental Determination of the Viscosity of Olive Oil"
in: *Philosophy Transactions of the Royal Society of London* 177 (1886), pp. 157–234 (cit. on p. 39)

[71] **Romagnoli, A.**
"Aerodynamic and thermal characterization of turbocharger turbines: experimental and computational evaluation"
PhD thesis. Imperial College, University of London June 2010 (cit. on p. 27)

[33] **Romagnoli, A. and Martinez-Botas, R.**
"Performance prediction of a nozzled and nozzleless mixed-flow turbine in steady conditions "
in: *International Journal of Mechanical Sciences* 53.8 (2011), pp. 557–574. ISSN: 0020-7403. DOI: 10.1016/j.ijmecsci.2011.05.003 (cit. on pp. 17, 27, 28)

[23] **SAE**
Supercharger Testing Standard
SAE J1723. Society of Automotive Engineers Aug. 1995
(cit. on pp. 10, 18, 59, 77)

[24] **SAE**
Turbocharger gas stand test code
SAE J1826. Society of Automotive Engineers Mar. 1995
(cit. on pp. 10, 18, 59, 77)

[94] **Schmitt, S., Schmid, W., Hetweck, G., Schlegl, M., and Staudacher, S.**
"High-Precision Measurements of Friction Losses in Turbochargers"
in: *Aufladetechnische Konferenz 2007*. Dresden, Germany 2007
(cit. on p. 34)

[21] **Serrano Sánchez, J.**
"Contribución a la implementación de ORCs en MCIAs"
PhD thesis. Universitat Politècnica de València 2014 (cit. on p. 5)

[22] **Serrano, J. R., Olmeda, P., Páez, A., and Vidal, F.**
"An experimental procedure to determine heat transfer properties of turbochargers"
in: *Measurement Science and Technology* 21.3 (3 2010), pp. 035–109. DOI: 10.1088/0957-0233/21/3/035109 (cit. on pp. 8, 18, 41, 68)

[1] **Serrano, J. R., Olmeda, P., Tiseira, A., García-Cuevas, L. M., and Lefebvre, A.**
"Theoretical and experimental study of mechanical losses in automotive turbochargers"
in: *Energy* 55 (2013), pp. 888–898. ISSN: 0360-5442. DOI: 10.1016/j.energy.2013.04.042 (cit. on p. vii)

[2] **Serrano, J. R., Olmeda, P., Tiseira, A., García-Cuevas, L. M., and Lefebvre, A.**
"Importance of Mechanical Losses Modeling in the Performance Prediction of Radial Turbochargers under Pulsating Flow Conditions"
in: *SAE Int. J. Engines* 6(2) (2 2013), pp. 729–738. DOI: 10.4271/2013-01-0577 (cit. on p. vii)

[12] **Serrano, J. R.**
"Análisis y modelado de transitorios de carga en MEC turboalimentados"
PhD thesis. Universitat Politècnica de València 1999 (cit. on p. 5)

[31] **Serrano, J. R., Arnau, F. J., Dolz, V., Tiseira, A., and Cervelló, C.**
"A model of turbocharger radial turbines appropriate to be used in zero- and one-dimensional gas dynamics codes for internal combustion engines modelling"
in: *Energy Conversion and Management* 49 (12 2008), pp. 3729–3745. DOI: 10.1016/j.enconman.2008.06.031 (cit. on pp. 17, 24, 161)

[40] **Serrano, J. R., Arnau, F. J., Fajardo, P., and Reyes-Belmonte, M. Á.**
"Contribution to the Modeling and Understanding of Cold Pulsating Flow Influence in the Efficiency of Small Radial Turbines for Turbochargers"
in: *Journal of Engineering for Gas Turbines and Power* 134.10 (Aug. 2012), 102701 (11 pages). DOI: 10.1115/1.4007027
(cit. on pp. 18, 71)

[41] **Serrano, J. R., Arnau, F. J., Novella, R., and Reyes-Belmonte, M. Á.**
A Procedure to Achieve 1D Predictive Modeling of Turbochargers under Hot and Pulsating Flow Conditions at the Turbine Inlet
tech. rep. 2014-01-1080. SAE International 2014. DOI: 10.4271/2014-01-1080 (cit. on p. 18)

[6] **Serrano, J. R., Margot, X., Tiseira, A., and García-Cuevas, L. M.**
"Optimization of the inlet air line of an automotive turbocharger"
in: *International Journal of Engine Research* (2012). DOI: 10.1177/1468087412449085 (cit. on p. vii)

[96] **Serrano, J. R., Olmeda, P., Arnau, F. J., Reyes-Belmonte, M. Á., and Lefebvre, A.**
"Importance of Heat Transfer Phenomena in Small Turbochargers for Passenger Car Applications"
in: *SAE Int. J. Engines* 6(2) (2 2013), pp. 716–728. DOI: 10.4271/2013-01-0576 (cit. on pp. 36, 41)

[66] **Serrano, J. R., Pla, B., Ospina, D., and Gonzalbo, R.**
Estimation of the Extended Turbine Maps for a Radial Inflow Turbine
tech. rep. 2010-01-1234. SAE International 2010. DOI: 10.4271/2010-01-1234 (cit. on p. 24)

[106] **Shaaban, S.**
"Experimental Investigation and Extended Simulation of Turbocharger Non-Adiabatic Performance"
PhD thesis. Fachbereich Maschinenbau: Universität Hannover 2004
(cit. on pp. 40, 71)

[107] **Shaaban, S., Seume, J., Berndt, R., Pucher, H., and Linnhoff, H. J.**
"Part-load performance prediction of turbocharged engines"
in: *Proceedings of 8th International Conference on Turbochargers and Turbocharging* 2006 (cit. on p. 40)

[58] **Sieros, G., Stamatis, A., and Mathioudakis, K.**
"Jet engine component maps for performance modelling and diagnosis"
in: *Journal of Propulsion and Power* 13 (1997), pp. 665–674. DOI: 10.2514/2.5218 (cit. on p. 22)

[42] **Simpson, A. T., Spence, S. W. T., and Watterson, J. K.**
"A comparison of the flow structures and losses within vaned and vaneless stators for radial turbines"
in: *Journal of Turbomachinery* 131 (2009). DOI: 10.1115/1.2988493 (cit. on pp. 19, 20)

[97] **Sjöber, E.**
Friction Characterization of Turbocharger Bearings
2013 (cit. on p. 36)

[128] *The GNU C Library (glibc)*
Last visited on 2014/10/30. URL: http://www.gnu.org/software/libc/ (cit. on p. 164)

[14] **Tiseira Izaguirre, A. O.**
"Caracterización experimental y modelado de bombeo en compresores centrífugos de sobrealimentación"
PhD thesis. Universitat Politècnica de València 2008 (cit. on pp. 5, 18, 252)

[130] **Toro, E., Spruce, M., and Speares, W.**
"Restoration of the contact surface in the HLL-Riemann solver"
English. In: *Shock Waves* 4.1 (1994), pp. 25–34. ISSN: 0938-1287. DOI: 10.1007/BF01414629 (cit. on p. 219)

[118] **Torregrosa, A. J., Olmeda, P., Martín, J., and Romero, C.**
"A Tool for Predicting the Thermal Performance of a Diesel Engine"
in: *Heat Transfer Engineering* 32 (2011), 891–904. DOI: 10.1080/01457632.2011.548639 (cit. on p. 74)

[78] **Torregrosa, A., Galindo, J., Serrano, J. R., and Tiseira, A.**
"A procedure for the unsteady characterization of turbochargers in reciprocating internal combustion engines"
in: *Fluid Machinery and Fluid Mechanics, The 4th International Symposium on Fluid Machinery and Fluid Engineering*. Beijing, China: Springer Berlin Heidelberg Nov. 2009, pp. 72–79. ISBN: 978-3-540-89748-4. DOI: 10.1007/978-3-540-89749-1_10 (cit. on p. 29)

[48] **Tousi, A. M. and Tourani, A.**
"Comparison of turbulence methods in CFD analysis of compressible flows in radial turbomachines"
in: *Aircraft Engineering and Aerospace Technology: An International Journal* (2008), pp. 657–665. ISSN: 0002-2667. DOI: 10.1108/00022660810911608 (cit. on p. 20)

[117] **United Nations Economic Comission for Europe**
E/ECE/324/Rev.2/ Add.100/Rev.3 or E/ECE/TRANS/505/Rev.2/Add.100/Rev.3 (12 April 2013), "Agreement concerning the adoption of uniform technical prescriptions for wheeled vehicles, equipment and parts which can be fitted and/or be used on wheeled vehicles and the conditions for reciprocal recognition of approvals granted on the basis of these prescriptions", Addendum 100: Regulation No. 101, Uniform provisions concerning the approval of passenger cars powered by an internal combustion engine only, or powered by a hybrid electric power train with regard to the measurement of the emission of carbon dioxide and fuel consumption and/or the measurement of electric energy consumption and electric range, and of categories M1 and N1 vehicles powered by an electric power train only with regard to the measurement of electric energy consumption and electric range.
Apr. 2013. URL: http://www.unece.org/fileadmin/DAM/trans/main/wp29/wp29regs/updates/R101r3e.pdf (cit. on p. 73)

[16] **Varnier, O.**
"Trends and Limits of Two-Stage Boosting System for Automotive Diesel Engines"
PhD thesis. Universitat Politècnica de València 2012 (cit. on p. 5)

[27] **Wallace, F. J. and Blair, G. P.**
"The pulsating-flow performance of inward radial-flow turbines"
in: *Proceedings of the ASME Gas Turbine Conference and Products Show* 1965, pp. 1–19 (cit. on p. 17)

[125] **Wasserbauer, C. A. and J., G. A.**
FORTRAN program for predicting the off-design performance of radial inflow turbines
tech. rep. NASA TN-8063. NASA 1975 (cit. on p. 154)

[60] **Watson, N. and Janota, S.**
Turbocharging the internal combustion engine
London: MacMillan Publishers Ltd. 1982 (cit. on p. 23)

[119] **Welch, P.**
"The Use of Fast Fourier Transform for the Estimation of Power Spectra: A Method Based on Time Averaging Over Short, Modified Periodograms"

in: *IEEE Transactions on Audio Electroacoustics* 15 (2 June 1967), pp. 70–73. ISSN: 0018-9278. DOI: 10.1109/TAU.1967.1161901 (cit. on pp. 91, 202, 211)

[80] **Winterbone, D. E. and Pearson, R. J.**
Theory of Engine Manifold Design: Wave Action Methods for IC Engines
Wiley-Blackwell 2000. ISBN: 1860582095 (cit. on p. 29)